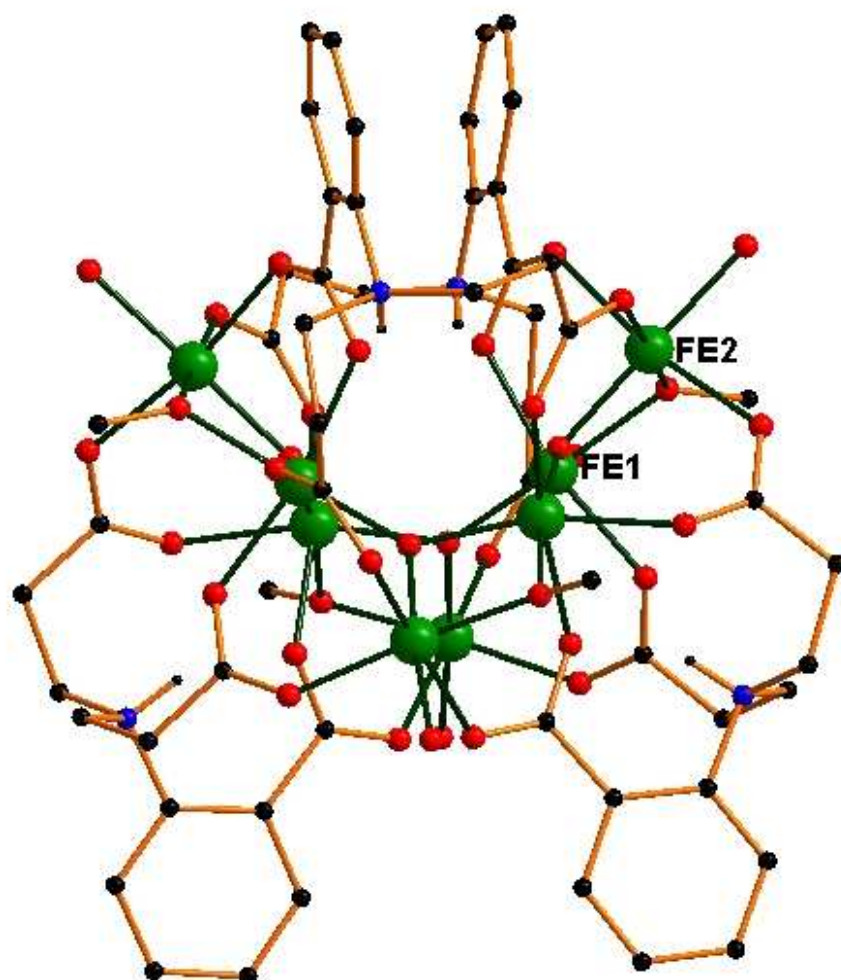


Synthesis and Characterization of Metal Aggregates with N, O-Ligands

DISSERTATION

von
Li Xue



Karlsruhe in April 2008

Synthesis and Characterization of Metal Aggregates with N, O-Ligands

**Zur Erlangung des akademischen Grades eines
DOKTORS DER NATURWISSENSCHAFTEN
(Dr. rer.nat)**

**von der Fakultät für Chemie und Biowissenschaften
der Universität Karlsruhe (TH)
angenommene**

DISSERTATION

von

**Li Xue
aus Daqing (P. R. China)**

Dekan: Prof. Dr. S. Bräse

1. Gutacher: Prof. Dr. A. K. Powell
2. Gutacher: Prof. Dr. C. Feldmann

Tag der mündlichen Prüfung: April 25, 2008

Contents

CHAPTER 1 INTRODUCTION.....	1
1.1 Ligand design	2
1.2 Synthetic strategy	4
1.3 Transition metal cluster-aggregates	5
1.3.1 Cu(II) cluster-aggregates	5
Cu(II) clusters with H ₃ cpida as ligand	5
Cu(II) clusters with H ₃ ndpa as ligand	6
Cu(II) clusters with H ₃ ntp as ligand	8
1.3.2 Fe(III) cluster-aggregates	9
Fe(III) clusters with H ₃ heidi as ligand	9
Fe(III) clusters with aromatic-H ₃ heidi-like ligands	10
A hexanuclear Fe(III) cluster	12
A nonanuclear Fe(III) cluster	12
An Fe(III) ₁₃ cluster	13
1.3.3 Co(II) and Ni(II) cluster-aggregates.....	13
Defect dicubanes Co(II) and Ni(II) clusters with H ₃ ntp as ligand	13
Cubane clusters with Co(II) ₄ and Ni(II) ₄	14
1.4 Introduction to magnetochemistry	15
1.4.1 The categories of magnetic behavior of materials.....	15
1.4.2 Magnetic susceptibility	16
1.4.3 The Brillouin function	16
1.4.4 Determination of the magnetic behavior from susceptibility.....	18
The plot of χ_m versus temperature	18
The plot of $\chi_m T$ versus temperature.....	19
The plot of χ_m^{-1} versus temperature.....	20
1.5 Magnetic properties of lanthanide cations	21
1.6 Magnetic properties of transition metal complex.....	23
1.6.1 Spin frustration	23
Large spin differences in Fe ₆ clusters with spin frustration	24
1.6.2 Single Molecule Magnets (SMMs)	24
Fe ₈ single molecule magnet with spin frustration	24
Co ₄ single molecule magnet	25
1.6.3 The magnetic properties of Cu ₄ cubanes	26
1.7 Thesis overview.....	27
CHAPTER 2 RESEARCH OBJECTIVES.....	28
CHAPTER 3 THERMOGRAVIMETRIC ANALYSIS OF THE LARGE COPPER AGGREGATE [Cu₄₄(μ_8-BR)₂(μ_3-OH)₃₆(μ-OH)₄BR₈(NTP)₁₂(H₂O)₂₈].BR₂.81H₂O	30
3.1 Background	30
3.2 Thermal analysis TGA/DTA/STA	31

3.3 Results and discussion.....	31
3.3.1 Total Thermal Analysis of $\text{Cu}_{44}\cdot 81\text{H}_2\text{O}$	31
3.3.2 Spectroscopy	33
3.3.2.1 The IR spectrum	33
3.3.2.2 X-ray powder diffraction.....	36
3.4 Summary	39
Step 1: 20°C - 184°C	39
Step 2: 184°C - 259°C.....	39
Step 3: 259°C - 597°C.....	40
Step 4: 597°C - 611°C.....	40
Step 5: 611°C - 655°C.....	41

CHAPTER 4 STRUCTURES AND MAGNETIC PROPERTIES OF COPPER (II) AND LANTHANIDE (III) 2D COORDINATION POLYMERS..... 42

4.1 The synthesis of $[\text{Cu}_2(\text{cpida})_2\text{Ln}(\text{NO}_3)(\text{H}_2\text{O})]\cdot\text{H}_2\text{O}$ (2-11)	42
4.2 The structure of $[\text{Cu}_2(\text{cpida})_2\text{Ln}(\text{NO}_3)(\text{H}_2\text{O})]\cdot\text{H}_2\text{O}$ (2-11).....	43
4.2.1 The overview of the structure of the two dimensional 2D-sheets $\{\text{Cu}_2\text{Ln}\}_x$	43
4.2.2 The coordination spheres of the metal ions.....	43
The coordination spheres of Cu(II)	43
The coordination sphere of Ln(III).....	45
4.2.3 The linkage between metals	46
The linkage between Cu(II) and Cu(II).....	46
The linkage between Cu(II) and Ln(III).....	47
The 2D-sheets formed by the linkages	48
4.2.4 The packing of the layers	49
4.3 The magnetic properties of $[\text{Cu}_2(\text{cpida})_2\text{Ln}(\text{NO}_3)(\text{H}_2\text{O})_4]\cdot\text{H}_2\text{O}$	51
4.3.1 The $\chi_m T$ product versus temperature.....	52
Ln(III) ion with f^0 , La^{3+} , 2 and f^7 , Gd^{3+} , 8 in $\{\text{Cu}_2\text{Ln}\}_x$	52
Ln(III) ions with $0 < f^n < 7$ in $\{\text{Cu}_2\text{Ln}\}_x$ (Ln = Ce, 3, Pr, 4, Nd, 5, Sm, 6, Eu, 7)	53
Ln(III) ions with $f^n > 7$ in $\{\text{Cu}_2\text{Ln}\}_x$ (Ln = Dy, 9, Ho, 10, Er, 11)	56
4.3.2 Field dependence of magnetization.....	59
Diamagnetic Ln(III) ion (Ln = La, 2).....	59
Isotropic Ln(III) ion (Ln = Gd, 8)	59
Anisotropic Ln(III) ion (Ln = Ce, 3, Pr, 4, Nd, 5, Sm, 6, Eu, 7, Dy, 9, Ho, 10, Er, 11)	
.....	60
4.3.3 The least-squares non-linear fitting of the magnetic properties of $\{\text{Cu}_2\text{La}\}_x$ and $\{\text{Cu}_2\text{Gd}\}_x$	61
The fitting of $\{\text{Cu}_2\text{La}\}_x$, 2	61
The fitting of $\{\text{Cu}_2\text{Gd}\}_x$, 8.....	62
4.4 Summary	64

CHAPTER 5 STRUCTURE AND MAGNETIC PROPERTIES OF TRANSITION METAL CLUSTERS WITH IMINO-CARBOXYLIC LIGANDS..... 65

5.1 $[\text{Fe}_8(\mu_3\text{-O})_4(\mu_2\text{-OMe})_4(\text{Hcpidp})_4(\text{H}_2\text{O})_4](\text{NO}_3)_4\cdot 10\text{H}_2\text{O}\cdot 4\text{MeOH}$, 12	65
5.1.1 Structure of $[\text{Fe}_8(\mu_3\text{-O})_4(\mu_2\text{-OMe})_4(\text{Hcpidp})_4(\text{H}_2\text{O})_4](\text{NO}_3)_4\cdot 10\text{H}_2\text{O}\cdot 4\text{MeOH}$	65
5.1.1.1 Overview of the Fe_8 structure	65
5.1.1.2 The coordination mode of the ligand cpidp^{3-}	66
5.1.1.3 The coordination spheres of the Fe(III) centres	67
5.1.1.4 The core structure of Fe_8	70
5.1.1.5 Polyhedral representation of Fe_8	72
5.1.2 The magnetic properties of Fe_8	73

5.2 The tetranuclear cubanes $[M^{II}_4(cpdeaH)_4] \cdot xH_2O$ (M = Cu, 13, Co, 14)	76
5.2.1 Molecular structures of the cubanes	76
5.2.1.1 Overview of the structures	76
5.2.1.2 The chelating mode of the ligand $(cpdeaH)^{2-}$ in the metal cubanes	77
5.2.1.3 The structures of Cu_4 and Co_4	78
The atom linkages in the Cu_4 cubane, 13	79
The atom linkages in the Co_4 cubane, 14	80
5.2.1.4 The core structures of the cubanes Cu_4 and Co_4	81
5.2.2 The hydrogen bonds in Cu_4 and Co_4	82
5.2.3 The magnetic properties of Cu_4 and Co_4	84
5.2.3.1 The temperature dependence of χT product for Cu_4 and Co_4	84
The temperature dependence of χT product for Cu_4 , 13	84
The temperature dependence of χT product for Co_4 , 14	85
5.2.3.2 The field dependence of magnetization for Cu_4 and Co_4	86
5.2.3.3 The ESR spectrum of Cu_4 , 13	87
5.2.3.4 The least-squares nonlinear fittings of the magnetic properties of Cu_4 , 13	88
5.2.3.5 The least-squares nonlinear fittings of magnetic properties of Co_4 , 14	90
5.3 Summary	91
CHAPTER 6 CONCLUSIONS	92
CHAPTER 7 EXPERIMENTAL	95
7.1 Analytical methods	95
7.1.1 NMR spectroscopy	95
7.1.2 Infra-red spectroscopy	95
7.1.3 Simultaneous Thermal Analysis (STA)	96
7.1.4 X-ray single crystal measurements	96
7.1.5 X-ray powder diffraction	97
7.1.6 Magnetic measurement	97
7.2 Synthesis	98
7.2.1 The synthesis of ligands	98
Preparation of (2-carboxylic) phenyl iminodiacetic acid (H_3cpida)	98
Preparation of (2-carboxylic) phenyl iminodipropionic acid (H_3cpidp)	98
Preparation of (2-carboxylic) phenyl diethanolamine (H_3cpdea)	99
7.2.2 Inorganic synthesis	99
Preparation of $[Cu^{II}_{44}(\mu_8-Br)_2(\mu_3-OH)_{36}(\mu-OH)_4Br_8(ntp)_{12}(H_2O)_{28}] \cdot Br_2 \cdot 81H_2O$, 1 ..	99
Preparation of $[Cu^{II}_2(cpida)_2La^{III}(NO_3)(H_2O)_4] \cdot 2H_2O$, 2	99
Preparation of $[Cu^{II}_2(cpida)_2Ln^{III}(NO_3)(H_2O)_4] \cdot H_2O$, 3-11	100
Preparation of $[Fe^{III}_8(\mu_3-O)_4(\mu-OMe)_4(Hcpidp)_4(H_2O)_4](NO_3)_4 \cdot 10H_2O \cdot 4MeOH$, 12	100
Preparation of $[Cu^{II}_4(cpdea)_4] \cdot 2H_2O$, 13	100
Preparation of $[Co^{II}_4(cpdea)_4] \cdot 3.3H_2O$, 14	100
CHAPTER 8 CRYSTAL STRUCTURE DATA	101
LIST OF ABBREVIATIONS	118
REFERENCES	119

APPENDIX	122
Plots of the field dependence of the magnetization for $\{\text{Cu}_2\text{Ln}\}_x$ (2-11).....	122
Plots of the fittings of Co_4 , 14.....	126
 ACKNOWLEDGEMENTS	 128
 CURRICULUM VITAE.....	 129

Chapter 1 Introduction

As more and more large metal clusters are synthesized, many of which show very interesting physical and chemical properties, the study into the relationship between structures and properties of large metal clusters has become an important and interesting topic. Much research is diverted towards the design and synthesis of new molecular materials which exhibit unusual chemical and physical properties, such as gas absorption^[1-4], SMM^[5-10], and catalytic behavior^[11, 12], which can be correlated with their chemical structures.

In the search for new large metal cluster molecules, the self-assembly method has been shown to be successful in that the multidentate ligands can capture the metal ions in 0-D, 1-D, 2-D or 3-D systems. The normal method used by chemists is called the bottom-up approach^[13-15], which is different from the approach of top-down^[16] which uses physical methods to break large structures into small pieces. The bottom-up approach requires that specific reaction conditions are found so that the self-assembly reaction can occur when all components meet together to give large metal cluster aggregates. Changing the reaction conditions, such as pH, solvent or stoichiometric ratio, can affect the self-assembly reaction giving metal clusters with different structures and physical and chemical properties. The 0D clusters can also be organized into 1D, 2D or 3D arrays.

In order to capture metals into large clusters, suitable ligands are required. A wide range of ligands, for example Schiff-base ligands^[17-20], amino acids^[21-24], and alcohol-based ligands^[25-28], have been shown to be able to capture transition metals and lanthanide ions. When there are carboxylic groups on the chelating ligands, the different chelating modes of the COO⁻ group can provide possibilities to capture more than one metal centers into polynuclear clusters (Fig.1.1).

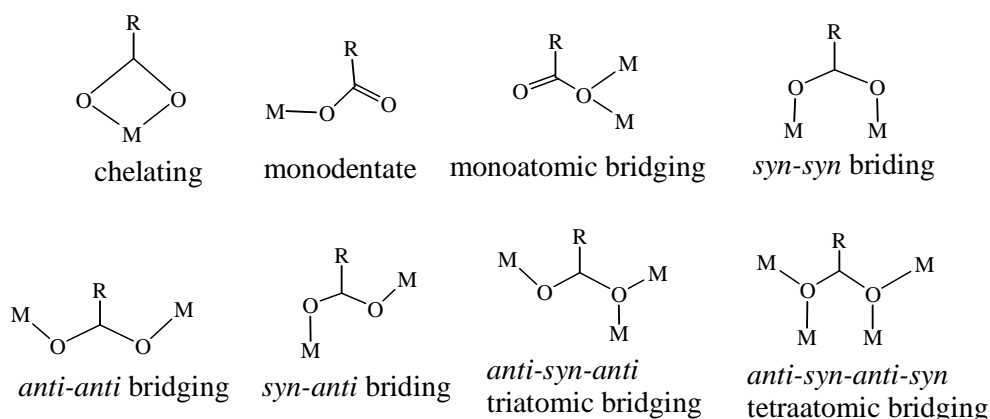


Figure 1.1 The coordination modes of the carboxylic group

Alkoxy groups, formed from the deprotonation of alcohols, are also able to coordinate to more than one metal centres to produce polynuclear compounds (Fig. 1.2).

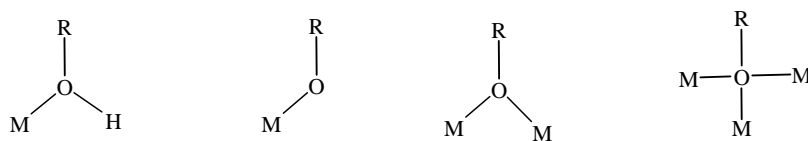
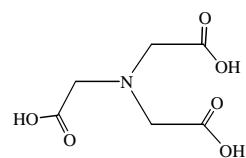


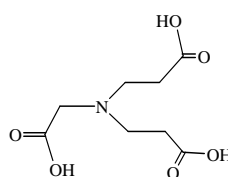
Figure 1.2 The coordination modes of the alkoxy group

After deprotonation by a base, the alkoxy group can bridge up to three metals. Another related flexible oxygen bridge is provided by hydroxo or oxo bridges formed from the deprotonation of water. These can bridge up to three (hydroxo) or six (oxo) metal centres. From this point of view, the large metal clusters are aimed to be synthesized by using chosen metals with the base in water or alcohol solvent to best form a metal-oxo core, with the ligand capturing the outer most metal centres as the outer shell to form polynuclear species.

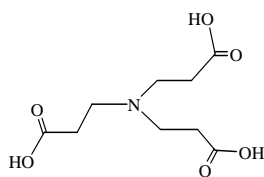
1.1 Ligand design



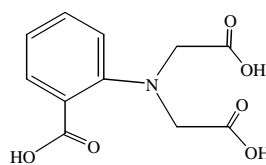
nitrilotriacetic acid
H₃nta



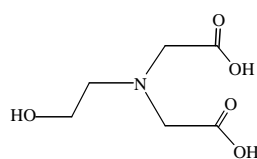
(nitrilodipropionic) acetic acid
H₃ndpa



nitrilotripropionic acid
H₃ntp



(2-carboxyphenyl)iminodiacetic acid
H₃cpida



N-(2-hydroxyethyl)imino diacetic acid
H₃heidi

Figure 1.3 Structure schemes of the ligands used in previous work

The previous research in our group showed that $NR_1R_2R_3$ type ligands are able to capture polynuclear species into very large metal clusters, such as $Cu_{44}^{[29]}$, $Fe_{19}^{[30]}$, $Fe_{13}^{[31]}$, $Cu_{12}^{[32]}$, etc. The ligands which have shown promising chelating properties are shown below in Fig.1.3.

From Fig. 1.3, ligands with different "arms" such as acetic or propionic acid showed similar coordination modes, but self-assembly reactions with the different ligands give different polynuclear clusters using similar conditions (such as $Cu_4^{[33]}$ with H_3ndpa and $Cu_{44}^{[29]}$ with H_3ntp). When the benzene ring was introduced to one of the arms, again different self-assembly reactions can occur in similar conditions (such as $Cu_{36}^{[34]}$ with H_3ndpa and $Cu_{12}^{[32]}$ with H_3cpida). When the hydroxyl group was introduced to take the place of the carboxylic group, different polynuclear clusters can result (such as $Fe_{19}^{[30]}$ with H_3heidi and $Fe_{13}^{[31]}$ with H_3ntp). From the summary of the above ligands, those chosen in this thesis for the research were based on the following two considerations: elongation of the side chain from acetic acid to propionic acid, and incorporation of hydroxyl groups into the side chains. Thus the ligands in this research are as shown in Fig 1.4:

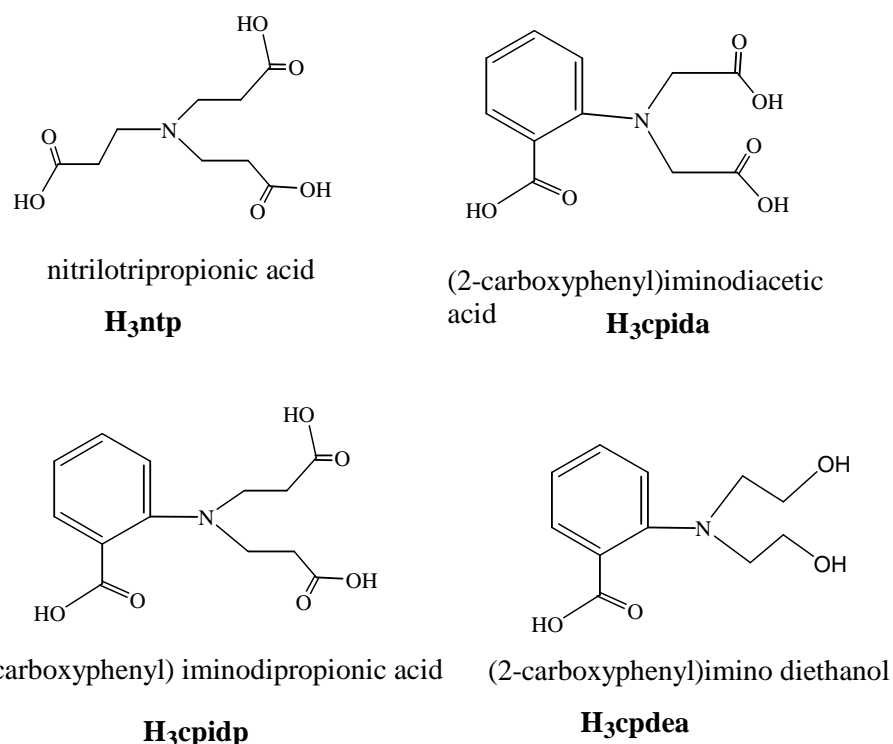


Figure 1.4 Structure schemes of the ligands used in the thesis work

1.2 Synthetic strategy

The four ligands (H₃ntp, H₃cpida, H₃cpidp and H₃cpdea) are all tetradentate with one nitrogen-donor site and three oxygen-donor sites. Normally nitrogen coordinates to only one metal atom, while the oxygen atom, whether carboxylic or hydroxyl, can link to more than one metal atom. Thus such tetradentate ligands can provide at most four coordination sites to one single metal atom. When the central metal requires five or more coordination sites, the remaining sites should be filled by donors from another tetradentate ligand or by an oxo- or hydroxo-bridge.

From this point of view, by changing solvent, the formation of oxo-bridges could be changed, thus leading to changes in metal cluster construction. By changing base, the solvent could be deprotonated to different degrees, changing from hydroxo to oxo-bridges. The ligands can also be deprotonated to different extents using different bases, thus resulting in changes in the coordination abilities of the functional groups. When alcohol-based solvents (ROH or H₂O) are used, hydrolysis reaction of solvents could be expected to dominate, which is helpful in studying the superexchange through hydroxy or oxo bridges.

Therefore by controlling the ratio of ligand: metal: base, different clusters can be accessed according to the following self-assembly scheme:



$\{M\}^{a+}$ can be transition metal or lanthanide ions, R₁, R₂, R₃ can be carboxylic groups or hydroxyl groups on the ligand arms with or without benzene rings, 'base' can be inorganic such as NaOH or KOH or organic like triethylamine or ethylenediamine. ROH is the solvent used in the self-assembly reactions with R = Me, Et or simply H to represent MeOH, EtOH and H₂O. The parameter of a⁺ and b⁻ is the electrical charge that the metal and the ligand carry, respectively. The parameters x, y, z, m, n are the numbers of each component in the final clusters. ±q is the electric charge of the final clusters which can be positive, negative, or neutral with the charge being balanced by counterions.

When the species $\{M_xL_y(O)_z(OR)_m(HOR)_n\}^{\pm q}$ is obtained in the form of a single crystal, it is possible to carry out the study on structure property relationships using X-ray diffraction and

the measurement of dc and ac magnetic susceptibility. The various magnetic exchange interactions between the paramagnetic centres can then be correlated in relation to the bridges of μ -O, μ -OR, OH-group and carboxylic COO^- groups of the ligand.

The transition metal ions Fe(III), Co(II), Ni(II), Cu(II) and lanthanide metal ions Ln(III) were chosen. One unpaired electron on the Cu(II) ions makes it possible to build simple models for explanation of magnetic interactions. Fe(III), Co(II) Ni(II) ions have more unpaired electrons in the high spin state that can give rise to large ground spin states for the cluster aggregates, which is one requirement for Single Molecule Magnet behaviour. Heterometallic complexes of transition metal and lanthanide ions could give unusual magnetic properties, as a result of the magnetic anisotropy of the lanthanides.

1.3 Transition metal cluster-aggregates

1.3.1 Cu(II) cluster-aggregates

A number of Cu(II) cluster-aggregates with various nuclearities (Cu_3 , Cu_4 , Cu_6 , Cu_9 , Cu_{12} , Cu_{36} , Cu_{44}) have been synthesized in previous research^[35]. Tetradentate ligands such as H_3ntp , H_3ndpa and H_3cpida proved to be particularly successful in creating large cluster systems. With these ligands, 1-, 2-, or 3-dimensionally linked arrays of aggregates were synthesized, which makes the magnetic studies of relevance to interactions of extended networks.

Cu(II) clusters with H_3cpida as ligand

Cu(II) and the ligand H_3cpida produces a hexanuclear Cu(II) complex $(\text{Et}_3\text{NH})_3\cdot[\text{Cu}_6\text{Na}_3(\text{cpida})_6]\cdot 7\text{MeOH}\cdot 2\text{H}_2\text{O}$ when Et_3N was used as base in MeOH solvent^[35]. When the base was changed to KOH, a nonanuclear complex $[\text{Cu}_9(\text{cpida})_6(\text{MeOH})_6]\cdot 6\text{MeOH}$ comes out in the MeOH solvent^[36] with the structure as in Fig.1.5a, the core structure in Fig. 1.5b with an $S = \frac{1}{2}$ spin ground state (Fig. 1.5c).

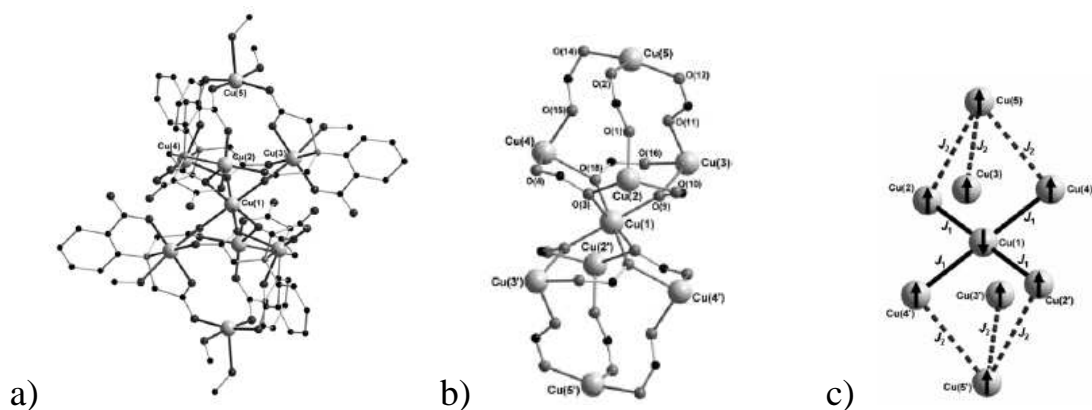


Figure 1.5 a) The structure; b) the core; c) the spin arrangement of of $[\text{Cu}_9(\text{cpida})_6(\text{MeOH})_6] \cdot 6(\text{MeOH})$.

When the ratio of the base to metal is raised in the reaction mixture, a series of dodecanuclear clusters $[\text{Cu}_{12}(\mu_3\text{-OMe})_2(\mu\text{-OMe})_6(\text{cpida})_6]^{2-}$ can be synthesized^[32]; a representative structure is shown in Fig.1.6.

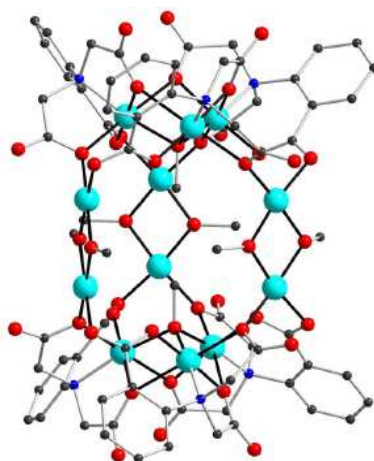


Figure 1.6 The structure of $[\text{Cu}_{12}(\mu_3\text{-OMe})_2(\mu\text{-OMe})_6(\text{cpida})_6]^{2-}$

It is noteworthy that the Cu_{12} cluster can be crystallized in a variety of arrays, from zero-dimensional species, to 1, 2, or 3-dimensional arrays of Cu_{12} building units, depending on the counteraction.

Cu(II) clusters with H_3ndpa as ligand

The self-assembly reaction of Cu(II) and the ligand H_3ndpa was found to lead to different cluster aggregates under different reaction conditions. When H_2O is used as solvent, tetranuclear cluster-aggregates were synthesized^[33]. In Fig. 1.7, the structure of one of the Cu_4 clusters is shown.

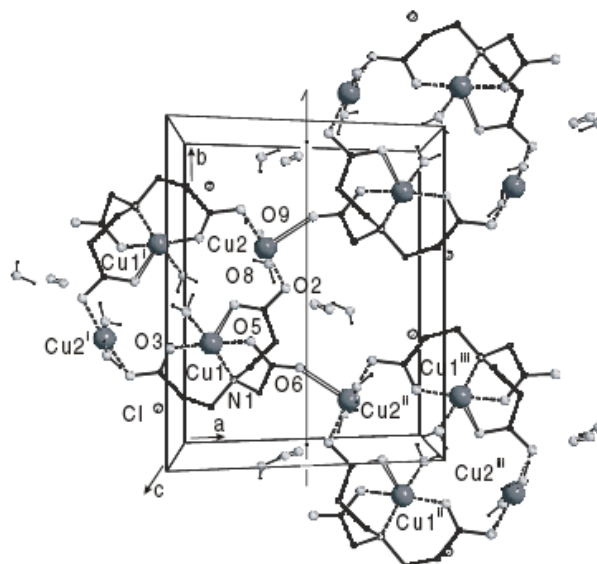


Figure 1.7 View of the unit cell of $[\text{Cu}_4(\text{ndpa})_2(\text{H}_2\text{O})_6\text{Cl}_2]\cdot 2\text{H}_2\text{O}$

In both $[\text{Cu}_4(\text{ndpa})_2(\text{NO}_3)_2(\text{H}_2\text{O})_8]\cdot 2\text{H}_2\text{O}$ and $[\text{Cu}_4(\text{ndpa})_2(\text{H}_2\text{O})_{10}]\cdot \text{SO}_4\cdot 6\text{H}_2\text{O}$ there are two syn-anti (syn(eq)-anti(ax), syn(eq)-anti(eq)) bridges, leading to overall antiferromagnetic interactions. When the above Cu_4 units are linked through anti(eq)-anti(ax) carboxylate bridges into infinite two dimensional sheets $\{[\text{Cu}_4(\text{ndpa})_2(\text{H}_2\text{O})_6]\cdot \text{Cl}_2\cdot 2\text{H}_2\text{O}\}_\infty$ and $\{[\text{Cu}_4(\text{ndpa})_2(\text{H}_2\text{O})_6]\cdot \text{Br}_2\cdot 2\text{H}_2\text{O}\}_\infty$, the intermolecule ferromagnetic interaction is of the same order of magnitude as the weak intratetramer coupling, resulting in overall ferromagnetic behaviour.

When KOH was used as base with $\text{CuCl}_2\cdot 4\text{H}_2\text{O}$ in methanolic solution, H_3ndpa captures a $\text{Cu}(\text{II})$ -oxo core into the larger cluster-aggregate Cu_{36} (Fig.1.8), which has $\{\text{KCl}_6\}^{5-}$ as template in the middle and shows antiferromagnetic interactions^[34].

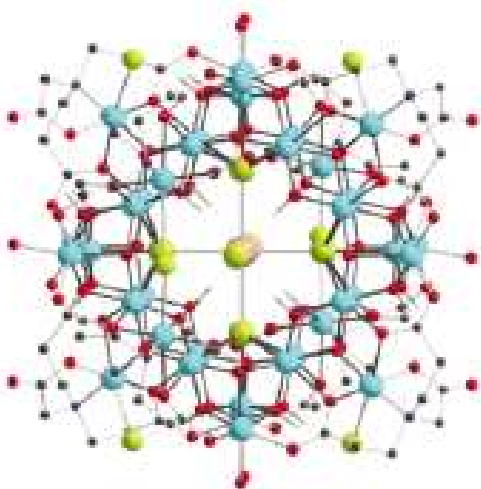


Figure 1.8 The structure of $[\text{Cu}_{36}^{\text{II}}(\mu_3\text{-OH})_{32}(\mu\text{-OR})_8(\text{ndpa})_8(\text{H}_2\text{O})_5\{\text{KCl}\}]^{3-}$

Cu(II) clusters with H₃ntp as ligand

The H₃ntp ligands captured a trinuclear Cu(II) aggregate species in water [32]. When CuSO₄ is used, a zero-dimensional species was synthesized (Fig. 1.9a), while with CuBr₂ a one-dimensional chain structure was formed (Fig. 1.9c) and with CuCl₂ or Cu(NO₃)₂ a two-dimensional pseudo-Kagome lattice structure was obtained (Fig. 1.9b).

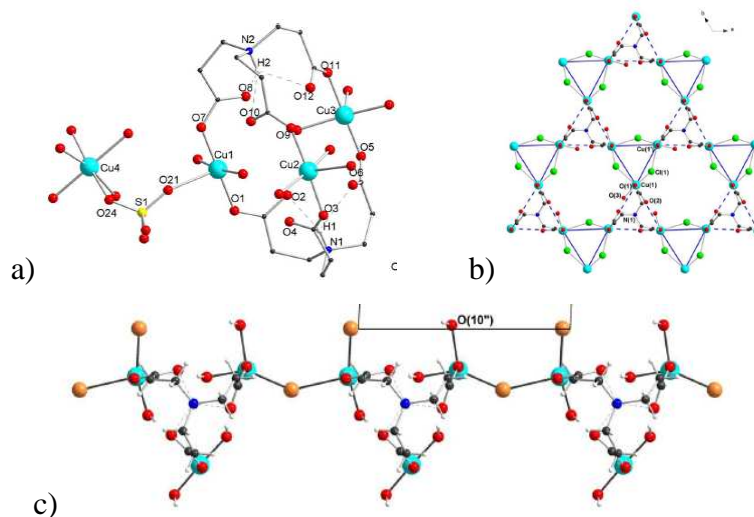


Figure 1.9 a) The structure of $[\text{Cu}_3(\text{ntp})_2(\text{H}_2\text{O})_8(\mu\text{-SO}_4)\text{Cu}(\text{H}_2\text{O})_5]^{2+}$; b) of $\{\text{Cu}_3\text{Cs}(\mu\text{-Cl})_3(\text{Hntp})_2(\text{H}_2\text{O})\}_\infty$; c) of $\{\text{Cu}_3(\text{Hntp})_2(\text{H}_2\text{O})_5\text{Br}_2\}_\infty$

There is no magnetic report for $[\text{Cu}_3(\text{ntp})_2(\text{H}_2\text{O})_8(\mu\text{-SO}_4)\text{Cu}(\text{H}_2\text{O})_5]^{2+}$, while $\{\text{Cu}_3(\text{Hntp})_2(\text{H}_2\text{O})_5\text{Br}_2\}_\infty$ shows paramagnetic behavior with dominating antiferromagnetic interactions, and $\{\text{Cu}_3\text{Cs}(\mu\text{-Cl})_3(\text{Hntp})_2(\text{H}_2\text{O})\}_\infty$ shows paramagnetic behavior with dominating ferromagnetic interactions with weaker antiferromagnetic interactions at low temperature.

When the ratio of the base (CsOH) is increased, H₃ntp captures CuBr₂ into a large Cu₄₄ aggregate (Fig. 1.10) [29].

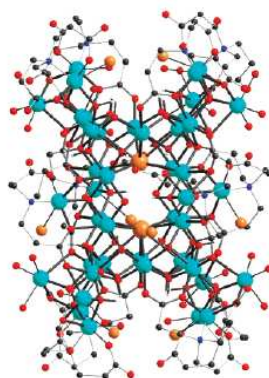


Figure 1.10 The structure of $[\text{Cu}_{44}(\mu_8\text{-Br})_2(\mu_3\text{-OH})_4(\text{ntp})_{12}\text{Br}_8(\text{H}_2\text{O})_{28}]\text{Br}_2 \cdot 81\text{H}_2\text{O}$

The structure of Cu₄₄ and the study of its thermal properties will be discussed in detail in Chapter 3.

1.3.2 Fe(III) cluster-aggregates

Since the high spin Fe(III) has $S = 5/2$, a ferromagnetic arrangement of the individual spin on the Fe clusters could provide the possibility to afford high ground spin states. However, antiferromagnetic interactions are favored by this spin-state, although large intermediate spin ground states for aggregates can be achieved. Through spin frustration effects and as a result of unequal and competing magnitudes of the pairwise coupling between paramagnetic centres, Fe₄^[37], Fe₈^[38] and Fe₉^[39] clusters, besides their high ground spin state, show SMM behavior. To date, the highest nuclear iron cluster that has displayed evidence of SMM behavior is an oxo- and hydroxo-bridged Fe₁₉^[30].

Fe(III) clusters with H₃heidi as ligand

By using the weak base, pyridine, Fe₁₇ and Fe₁₉ were crystallized from aqueous solution^[30]. The structure of Fe₁₉ (Fig.1.11) is very similar to Fe₁₇, with the exception that Fe₁₉ has two additional Fe(III) ions on opposite sides at the periphery of the molecule.

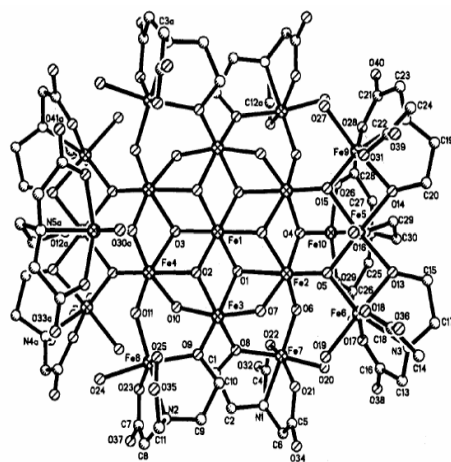


Figure 1.11 The structure of $[\text{Fe}_{19}(\mu_3\text{-O})_6(\mu_3\text{-OH})_6(\mu_2\text{-OH})_8(\text{heidi})_{10}(\text{H}_2\text{O})_{12}]^+$, Fe₁₉

The dominant magnetic properties of Fe₁₉ and F₁₇ are antiferromagnetic, but spin frustration results in a high spin ground state. It is likely that the Fe₁₉ aggregate has a ground state spin of at least 33/2.

Fe(III) clusters with aromatic-H₃heidi-like ligands

The following hda ligands R-N(CH₂CO₂H)₂ (Fig. 1.12) were used to capture iron ions into large cluster aggregates^[40].

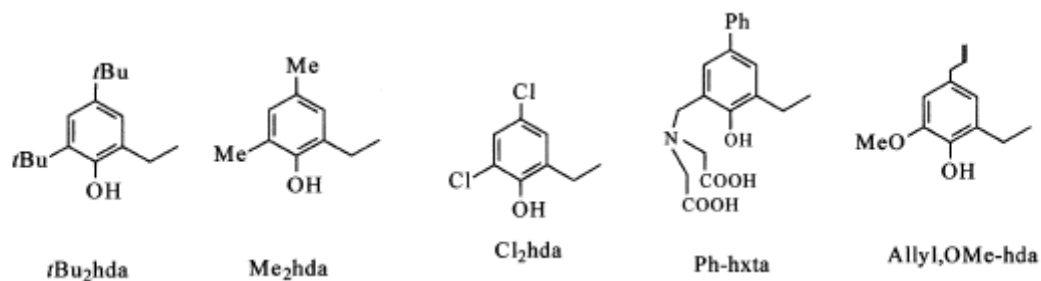


Figure 1.12 R-groups on the hda-based ligands

A monomer was obtained by using the first ligand, *t*-Bu₂hda, while the second and the third ligands, Me₂hda and Cl₂hda, capture the irons into di- or trinuclear molecules (Fig. 1.13).

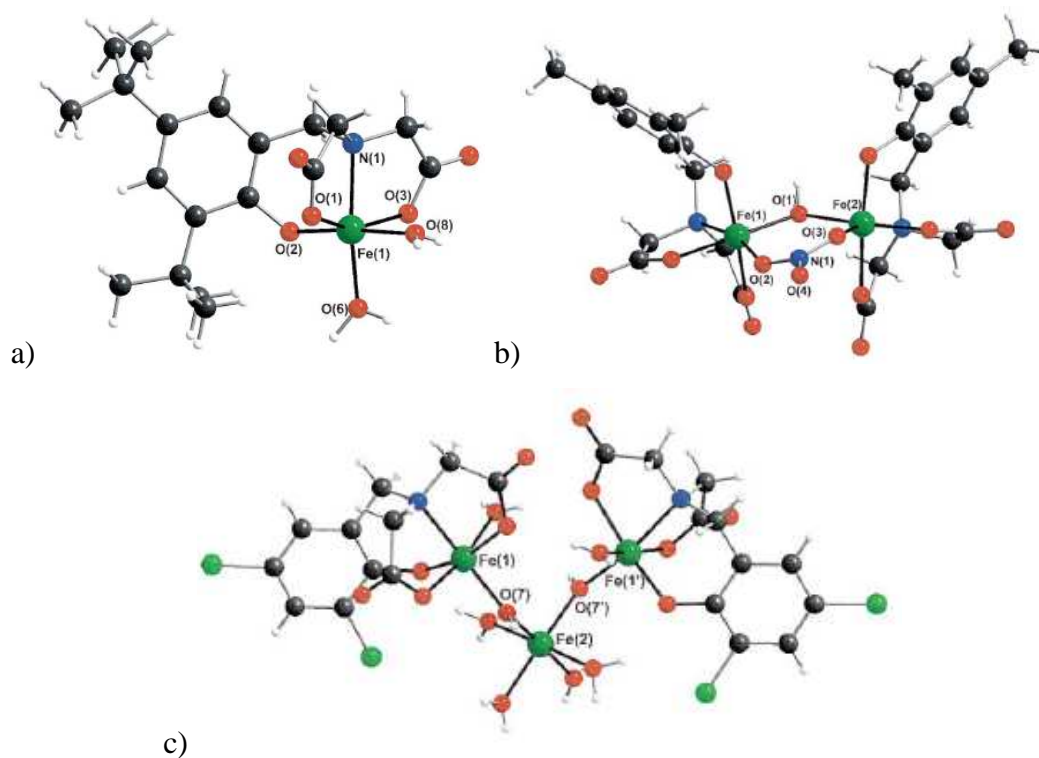


Figure 1.13 Structure a) of [(*t*-Bu₂hda)Fe(H₂O)₂]; b) of [(Me₂hda)₂Fe₂(μ-OH)(μ-NO₃)]²⁻ c) of [(Cl₂hda)₂Fe₂(μ-OH)₂Fe(H₂O)₄]⁺

The fourth ligand, 4-Ph-hxta, captures iron ions into dimeric and tetrameric cluster aggregates (Fig. 1.14) under different conditions of self-assembly reactions.

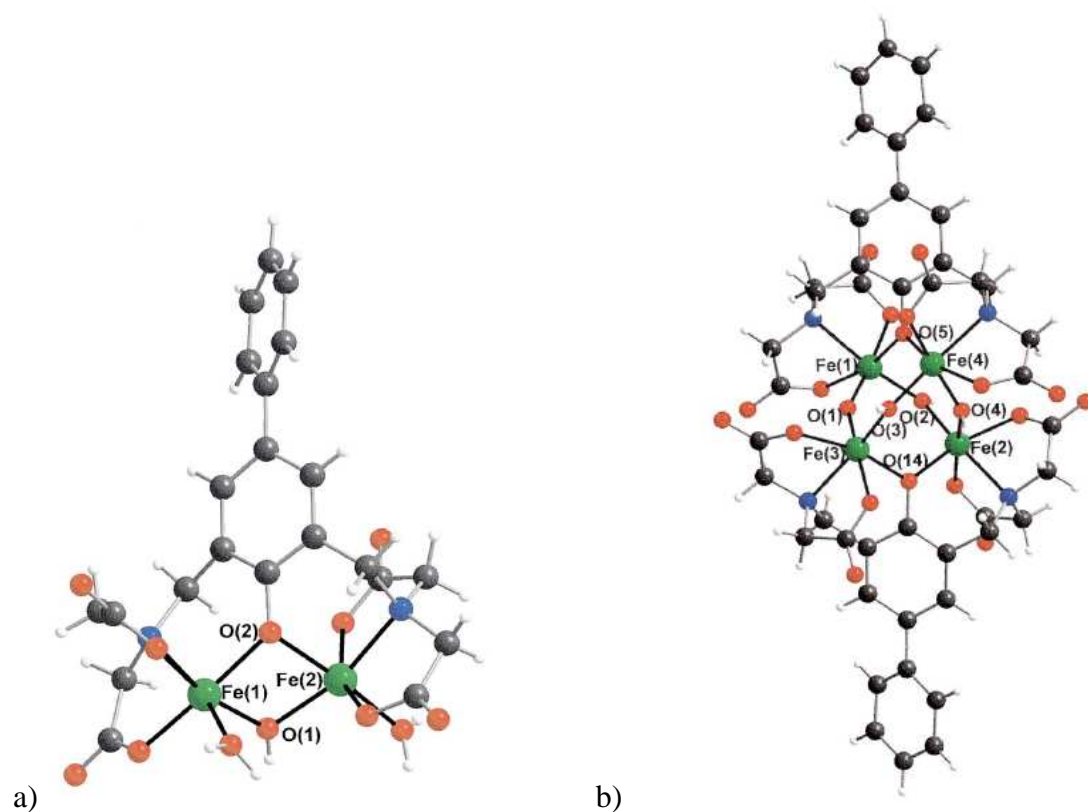


Figure 1.14 Structure a) of $[(4\text{-Ph-hxta})\text{Fe}_2(\mu\text{-OH})(\text{H}_2\text{O})_2]\cdot 6\text{H}_2\text{O}$; b) of $[(4\text{-Ph-hxta})_2\text{Fe}_4(\mu\text{-O})(\mu\text{-OH})_3]^{3-}$

A larger iron(III) aggregate, Fe_8 , was isolated when the fifth ligand, 2-allyl-4-OMe-had was used (Fig. 1.15).

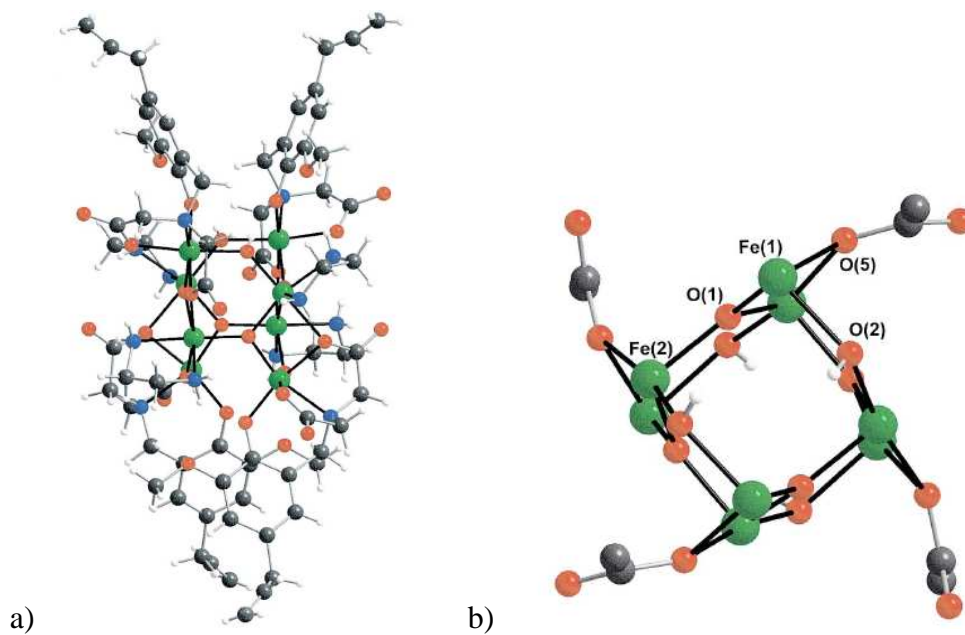


Figure 1.15 The structure a) of $[(2\text{-allyl-4-OMe-had})_4\text{Fe}_8(\mu_3\text{-O})_4(\mu\text{-OH})_4(\text{en})_4]$; b) A perspective view and a view down the molecular 4-fold axis

The cluster has an unusual core which is a sort of tetragonally compressed cube. It has an $S = 0$ ground state^[35].

A hexanuclear Fe(III) cluster

A ligand H_6L , *cis,cis*-1,3,5-cyclohexanetriamine-*N,N,N',N',N'',N''*-hexaacetic acid (Fig. 1.16a), captures irons into an $\{Fe_6\}$ cage (Fig. 1.16b), $Na_{12}[Fe_6(O)_3(CO_3)_6(L)_2] \cdot 36H_2O$ ^[41].

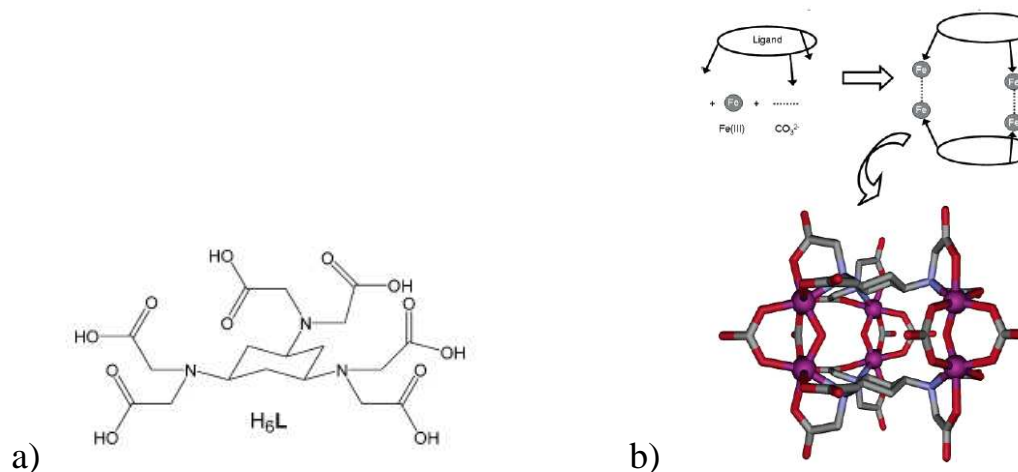


Figure 1.16 a). Structure of the ligand *cis,cis*-1,3,5-cyclohexanetriamine-*N,N,N',N',N'',N''*-hexaacetic acid; b). Schematic representation of the cluster assembly

A nonanuclear Fe(III) cluster

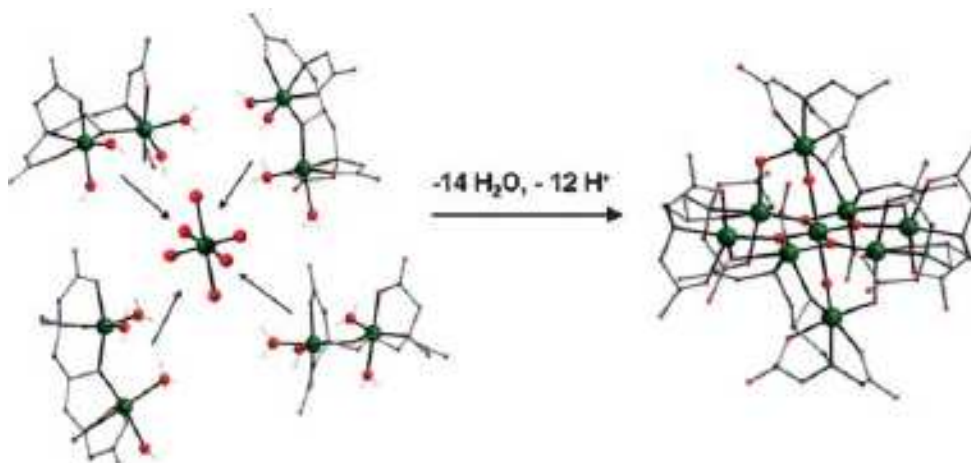


Figure 1.17 Hydrolytic encapsulation of $[Fe(H_2O)_6]^{3+}$ by four $\{Fe_2(hpdta)(H_2O)_4\}^+$ species to give $[Fe_9(\mu_3-O)_4(\mu-OH)_4(hpdta)_4]^{5-}$

Using a solvothermal synthetic method, a nonanuclear Fe(III) aggregate, $[\text{Fe}_9(\mu_3\text{-O})_4(\mu\text{-OH})_4(\text{hpdta})_4]^{5-}$ (Fig. 1.17) is formed^[42] with the ligand, 2-hydroxy-1,3-N,N,N',N'-diaminopropanetetraacetic acid (H_5hpdta).

The aggregate has a ground state spin of $S=13/2$, and hysteresis loops were observed below 1.8K.

An Fe(III)₁₃ cluster

The H_3ntp ligand captures 13 Fe^{3+} irons into $\{[\text{Fe}_{13}(\mu_3\text{-OH})_6(\mu_3\text{-O})_6(\text{H}_2\text{O})_6(\text{Hntp})_8][\text{Fe}_{13}(\mu_3\text{-OH})_6(\mu_3\text{-O})_6(\text{Hntp})_8]\}_2 \cdot (\text{NO}_3)_{15} \cdot 54\text{H}_2\text{O}$ (Fig. 1.18), the core structure of which is based on building blocks of $[\text{Fe}_3(\text{OH})_4]^{5+}$ cubanes with one Fe^{3+} corner missing^[31].

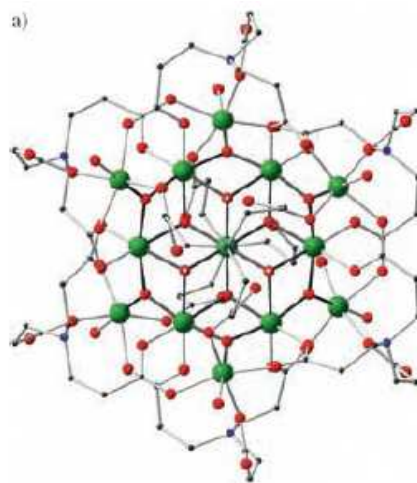


Figure 1.18 a). The structure of a Fe_{13} unit in $\{[\text{Fe}_{13}(\mu_3\text{-OH})_6(\mu_3\text{-O})_6(\text{H}_2\text{O})_6(\text{Hntp})_8][\text{Fe}_{13}(\mu_3\text{-OH})_6(\mu_3\text{-O})_6(\text{Hntp})_8]\}_2 \cdot (\text{NO}_3)_{15} \cdot 54\text{H}_2\text{O}$

The Fe_{13} units have an $S = 5/2$ ground state and hysteresis loops were observed below 1K.

1.3.3 Co(II) and Ni(II) cluster-aggregates

Defect dicubanes Co(II) and Ni(II) clusters with H_3ntp as ligand

In mixed aqueous/ethanol solution, the reaction of H_3ntp with Co^{2+} or Ni^{2+} affords tetranuclear complexes, $[\text{Co}_4(\mu_3\text{-OH})_2(\text{H}_2\text{O})_6(\text{ntp})_2] \cdot 2\text{H}_2\text{O}$ and $\{\text{Ni}_4(\text{OH})_2(\text{OR})_4\}^{2+}$ (Fig. 1.19) respectively, in which two ntp^{3-} ligands encapsulate a small portion of a metal hydroxide framework to form the defect dicubane structure^[43].

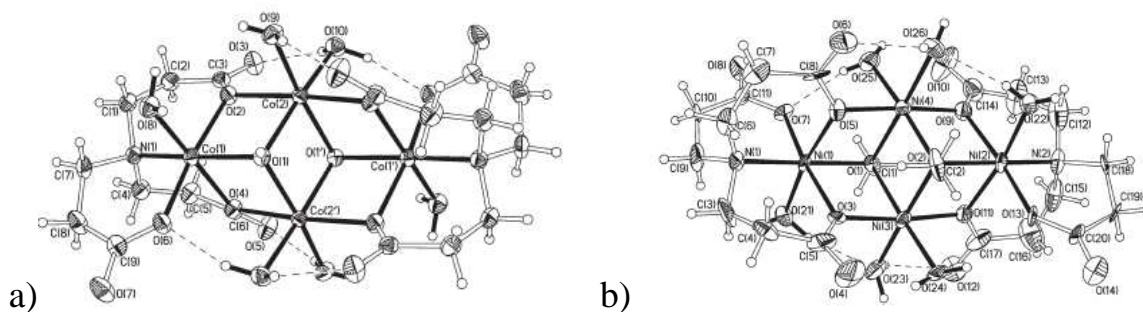


Figure 1.19 a) The structure of $[\text{Co}_4(\mu_3\text{-OH})_2(\text{H}_2\text{O})_6(\text{ntp})_2] \cdot 2\text{H}_2\text{O}$; b). The structure of $[\text{Ni}_4(\mu\text{-OMe})_2(\text{H}_2\text{O})_6(\text{ntp})_2]$

In the Co_4 cluster, four oxygen bridges lead to a competing set of antiferromagnetic and ferromagnetic interactions between $\text{Co}(\text{II})$ metal ions whereas in the Ni_4 cluster, the metal ions are ferromagnetically coupled.

Cubane clusters with $\text{Co}(\text{II})_4$ and $\text{Ni}(\text{II})_4$

In warm ethanol solvent, the cubane type structure $[\{\text{MX}(\text{L})(\text{EtOH})\}]$ (Fig. 1.20), ($\text{L} = 3,5$ -dimethyl-1-oxymethylpyrazolate), $\text{X} = \text{Cl}$ or Br ; $\text{M} = \text{Co}^{\text{II}}$ or Ni^{II}), was isolated^[44]. The oxygen atom of the ligand is able to form linkages to three different metal ions, and such behavior is also known to occur for deprotonated oxygen atoms of hydroxyl groups.

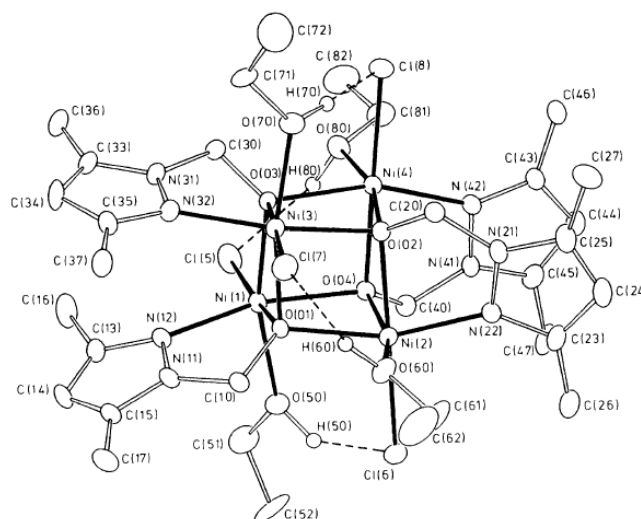


Figure 1.20 The projection view of the tetranuclear unit

The cobalt compound shows weak antiferromagnetic interactions while the nickel compound shows a ferromagnetic behavior, a phenomenon which has been observed earlier^[44].

1.4 Introduction to magnetochemistry

Magnetochemistry is the study of the magnetic properties of materials. The magnetic measurement is carried out by means of susceptometer, from which the information can be obtained whether the measured substance is attracted or repelled by a magnetic field. From this, information about magnetic exchange interactions between paramagnetic centres can be deduced^[45, 46].

1.4.1 The categories of magnetic behavior of materials

An electron in an orbital has two possible values of its spin quantum number s : $s = \pm 1/2$. These are often referred to as "spin up" and "spin down". When two electrons occupy the same orbital, one of the electrons has a spin up, and the other has a spin down state according to Hund's rule. For the metal-ligand clusters studied in this work, the electrons in the orbitals of the ligands are paired, the ligands are diamagnetic, and thus the effect of the electrons of the ligand could be considered as comparatively small. On the contrary, the $3d$ electrons on the metals, which are paramagnetic centres, become significant. With the different spin arrangements of the metal centres, the compound can be categorized into the following types.

- a. Diamagnetic – A diamagnetic compound has no unpaired electrons, thus giving a net zero ground spin state. Larger molecules are expected to have larger diamagnetic magnetism than smaller molecules. Such compounds are weakly repelled by a magnetic field.
- b. Paramagnetic – A paramagnetic compound has some paramagnetic centres with unpaired spins and the interactions between the magnetic centers are small. It is attracted by a magnetic field.
- c. Ferromagnetic – In a ferromagnetic compound, the unpaired electrons on the paramagnetic centers are arranged to have the same spin direction, all up or all down, in its ground state. Ferromagnetic compounds are strongly attracted to a magnet.
- d. Antiferromagnetic – In an antiferromagnetic compound, the unpaired electrons on the paramagnetic centers are arranged to have opposite spin directions, with the number of the spins in one direction the same as in the opposite direction, giving a net ground state of zero. Antiferromagnetic materials are strongly repelled by a magnet.
- e. Ferrimagnetic – In a ferrimagnetic compound, the unpaired electrons on the paramagnetic centers are arranged antiferromagnetically to have opposite spin

directions, with some up and some down. However the magnitudes of the spins differ and the net ground state is not zero. It is attracted to a magnet.

1.4.2 Magnetic susceptibility

The magnetic field inside a specific material, symbolized by \mathbf{B} , is the sum of the external magnetic field, symbolized by \mathbf{H} , and the magnetic field generated by the external field symbolized by \mathbf{M} . \mathbf{M} is the intrinsic property of the material itself^[45]. The relationship of the above magnetization can be formulated with the following equation:

$$\mathbf{B} = \mathbf{H} + 4\pi\mathbf{M} \quad \text{Eq. (1.1)}$$

When the equation (1.1) is often written as:

$$\mathbf{B}/\mathbf{H} = 1 + 4\pi\mathbf{M}/\mathbf{H} = 1 + 4\pi\chi \quad \text{Eq. (1.2)}$$

where the magnetic susceptibility $\chi = \mathbf{M}/\mathbf{H}$.

Many studies use χ_m , the molar magnetic susceptibility, with the units $\text{cm}^3 \text{mol}^{-1}$.

In general χ is the algebraic sum of two contributions:

$$\chi = \chi^D + \chi^P \quad \text{Eq. (1.3)}$$

where χ^D and χ^P represent respectively the diamagnetic susceptibility, which is negative, and the paramagnetic susceptibility, which is positive. Normally the diamagnetic contribution can be calculated from Pascal's constants^[47]. The magnitude of the diamagnetic contribution is usually much smaller, estimated between -1 to $-500 \times 10^{-6} \text{emu.mol}^{-1}$, than the magnitude of paramagnetic and other effects.

Further inferration about the application and the explanation of magnetic susceptibility can be found in the books or articles by Kahn^[45], Carlin^[46], O'Connor^[48], Kittel^[49], Mabbs and Machin^[50].

1.4.3 The Brillouin function

This theory was proposed by Pierre Curie and could be explained by a model of a single isolated $S=1/2$ spin.

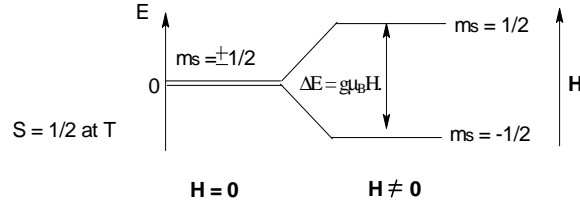


Figure 1.21 Energy diagram of an $S = 1/2$ spin in an external magnetic field along the z-axis

In zero field, the two spins $m_s = \pm 1/2$ are degenerate. When a field \mathbf{H} is applied along the positive z-axis the two levels split as illustrated in Fig. 1.21. The difference in energy between the two energy levels is $\Delta E = g\mu_B H$, with energies $-g\mu_B H/2$ for the lower level and $+g\mu_B H/2$ for the upper level.

The molar macroscopic moment of the electron is summed according to Boltzman distribution^[46], which is given as follows:

$$\mathbf{M} = N \sum \mu_n \mathbf{P}_n = N (\mu_{1/2} \mathbf{P}_{1/2} + \mu_{-1/2} \mathbf{P}_{-1/2}) \quad \text{Eq. (1.4)}$$

The population of the two spin levels at temperature T is written as follows:

$$\mathbf{P}_{\frac{1}{2}} = \frac{\exp(\frac{1}{2} g\mu_B H/k_B T)}{\exp(\frac{1}{2} g\mu_B H/k_B T) + \exp(-\frac{1}{2} g\mu_B H/k_B T)}$$

$$\mathbf{P}_{-\frac{1}{2}} = \frac{\exp(-\frac{1}{2} g\mu_B H/k_B T)}{\exp(\frac{1}{2} g\mu_B H/k_B T) + \exp(-\frac{1}{2} g\mu_B H/k_B T)}$$

Substituting for $\mathbf{P}_{1/2}$ and $\mathbf{P}_{-1/2}$, the Brillouin function is obtained as follows:

$$M = \frac{1}{2} N g \mu_B \frac{\exp(\frac{1}{2} g\mu_B H/k_B T) - \exp(-\frac{1}{2} g\mu_B H/k_B T)}{\exp(\frac{1}{2} g\mu_B H/k_B T) + \exp(-\frac{1}{2} g\mu_B H/k_B T)} \quad \text{Eq. (1.5)}$$

With the same method, similar Brillouin functions can be obtained for paramagnetic compounds with more than one electron. The Brillouin functions for various magnetic spin states are illustrated in Fig. 1.22.

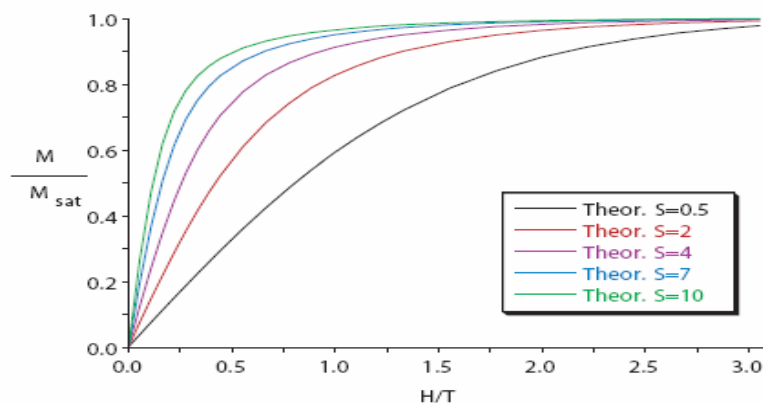


Figure 1.22 Brillouin curves for ideal paramagnets with various S values.

Magnetization normalized to the saturation magnetization is plotted against H/T . Systems with higher S values saturate more quickly in response to increasing magnetic field than those with lower values of S . Using the Brillouin analysis, the spin state of a compound can be determined without knowing the exact chemical composition of the material, since it can be determined from the magnetization as a function of applied field and the saturation magnetization of the sample.

1.4.4 Determination of the magnetic behavior from susceptibility

To determine whether a compound is paramagnetic, ferromagnetic, ferrimagnetic or antiferromagnetic, the magnetic susceptibility is useful. The plot of χ_m versus temperature (Fig. 1.23), $\chi_m T$ versus temperature (Fig. 1.24) and χ_m^{-1} versus temperature (Fig. 1.26) can all give the information to different extents.

The plot of χ_m versus temperature

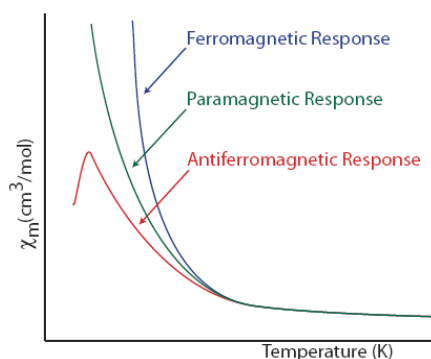


Figure 1.23 The plot of magnetic susceptibility as a function of temperature for ideal paramagnetic, ferromagnetic, and antiferromagnetic materials.

Fig. 1.23 shows the plot for magnetic susceptibility as a function of temperature for ferromagnetic, paramagnetic, and antiferromagnetic materials. From Fig. 1.23, we can easily see if the compound is antiferromagnetic.

As shown in Fig. 1.23, an antiferromagnetic compound exhibits a maximum at low temperature range, thus giving information on the strength of the magnetic interactions. A compound with stronger antiferromagnetic interactions shows the maximum at higher temperature. The shape of the maximum suggests the dimensionality of interactions: a compound with one- and two-dimensional antiferromagnetic interactions has a rounded maximum; a compound with three-dimensional antiferromagnetic interactions has a sharp peak. From this plot, information about other magnetic interactions is difficult to deduce.

The plot of $\chi_m T$ versus temperature

Fig. 1.24 shows the plot of the $\chi_m \cdot T$ product vs. T for an ideal paramagnet, ferromagnet, antiferromagnet, and ferrimagnet. The plot in Fig. 1.24 can provide information to differentiate the basic interactions in a paramagnet, ferromagnet, antiferromagnet, and ferrimagnet.

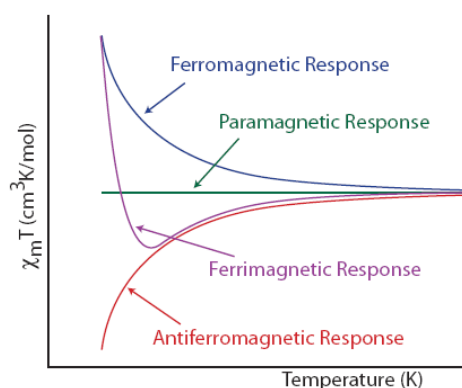


Figure 1.24 The plot of $\chi_m T$ as a function of temperature for paramagnetic, ferromagnetic, antiferromagnetic and ferromagnetic materials.

As in Fig. 1.24, the $\chi_m \cdot T$ product of a true paramagnetic material does not vary with temperature, thus giving a straight level line in the plot ($\chi_m T$ vs. T) according to the Curie-law. The deviation from the Curie law is observed in Fig. 1.25^[51]. The paramagnetic compound with a negative Weiss constant corresponds to the antiferromagnetic one while the paramagnetic compound with a positive Weiss constant corresponds to the ferromagnetic one.

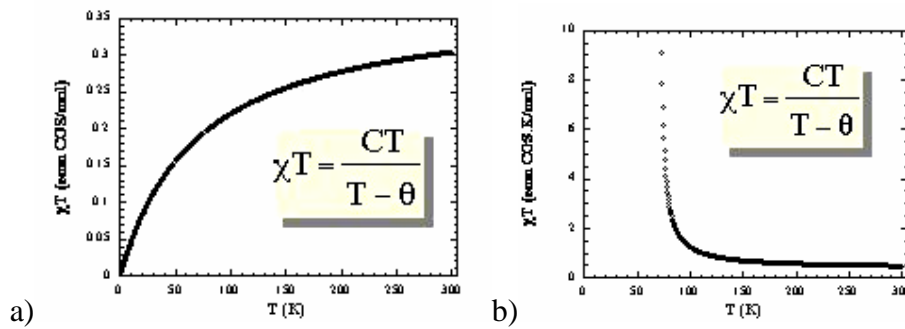


Figure 1.25 Plot of $\chi_m T$ versus temperature obeying the Curie-Weiss law a). with a negative Weiss constant, -70K ; b). with a positive Weiss constant, $+70\text{K}$.

The constant $\chi_m T$ value at higher temperatures for all types of magnetism is due to the paramagnetic behavior above their critical temperatures. A ferromagnetic compound has an upward deviation from the paramagnetic level line at lower temperatures since the ferromagnetic interaction energy overcomes thermal energy at lower temperatures. On the contrary, an antiferromagnetic compound shows a downward deviation from the paramagnetic level line at lower temperatures since more and more spins are arranged in an anti-parallel way on lowering the temperature. A ferromagnetic compound gives a similar plot to a paramagnetic material at higher temperatures (above the critical temperature) while it gives a similar plot to a ferromagnetic material at lower temperatures below the critical temperature.

The plot of χ_m^{-1} versus temperature

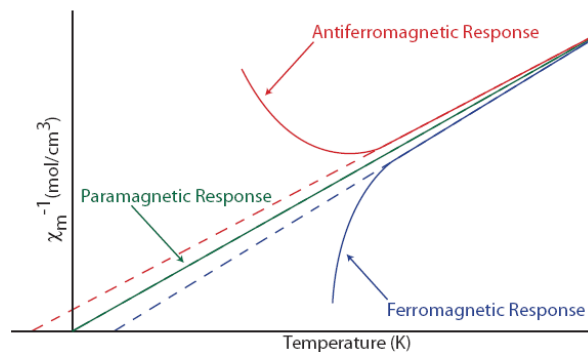


Figure 1.26 The plot of inverse susceptibility as a function of temperature for a paramagnet, a ferromagnet, and an antiferromagnet (the dotted lines indicate deviation from the Curie Law).

Fig. 1.26 is the plot of the inverse susceptibility vs. temperature. This plot could help to differentiate the three kinds of magnetic material: paramagnetic, ferromagnetic and

antiferromagnetic compounds.

An ideal paramagnet has a linear relationship between χ_m^{-1} and temperature, with the intercept at zero defined by the Curie law. The deviation from the Curie law is observed as the deviation from this linear relationship, with now a non-zero intercept, as defined by the Curie-Weiss law ^[51](Fig. 1.27).

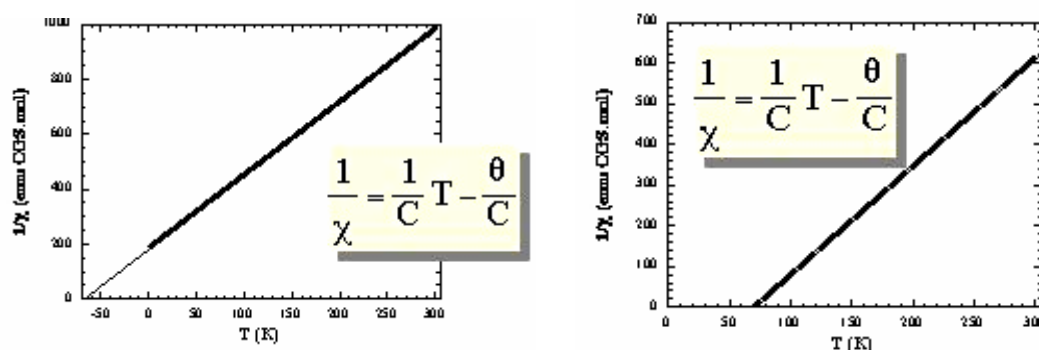


Figure 1.27 Plot of χ_m^{-1} versus temperature obeying the Curie-Weiss law a) with a negative Weiss constant, -70K; b) with a positive Weiss constant, +70K.

Compared to a paramagnetic compound, the plot for a ferromagnetic compound is shifted downwards, giving a positive intercept on the temperature axis (a positive Weiss constant), while the plot for an antiferromagnetic compound is shifted upwards and extrapolates to a negative intercept on the temperature axis (negative Weiss constant).

1.5 Magnetic properties of lanthanide cations

Rare-earth ions are characterized by strong unquenched orbital angular momentum, and thus the spin-orbit coupling is more pronounced for compounds containing the rare-earth ions than the transition-metal ions. The effect of spin-orbit coupling increases as the atomic number increases, with the exception of the $4f^7$ configuration, which has no first-order angular momentum..

The magnetic interactions between $4f$ electrons on different metal centres are expected to be much smaller than the interactions between $3d$ electrons in transition-metal complexes, since the overlap between $4f$ orbitals on different metal ions is small. In spite of the weak magnetic interactions between Ln^{3+} ions, a trinuclear Dy_3 complex shows SMM behavior^[7] (Fig 1.28).

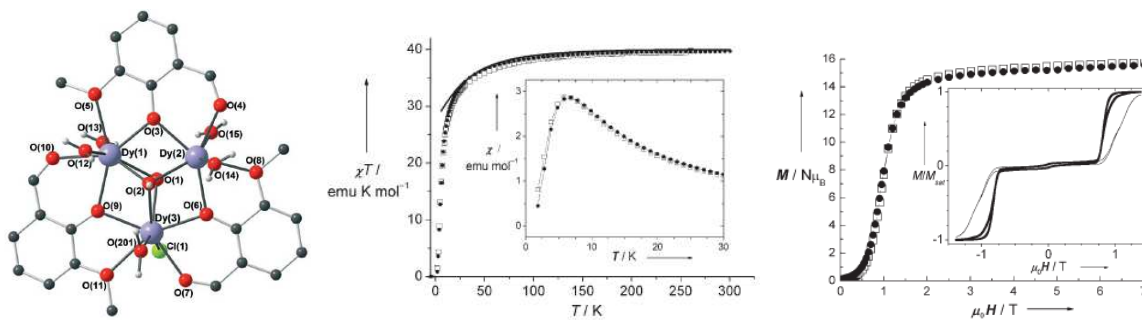


Figure 1.28 Dy₃ Structure and magnetic properties

At low temperatures, crystal-field effects split the J multiplets of the isolated ions and this splitting usually is comparable to the thermal energy. Thus a big deviation from the Curie law could be anticipated at low temperature. So lanthanide ions are unlike transition-metal ions, which have an orbitally non-degenerate ground state and are generally treated with the assumption that their magnetic moment is temperature-independent. Moreover, when a rare-earth ion is coupled to an orbitally non-degenerate transition metal ion, a deviation from the Curie law can be observed. This deviation of the magnetic susceptibility with respect to the Curie law is due to the temperature-dependence of the population of the Stark sub-levels. The $4f^n$ configuration of a Ln^{3+} ion is split into $^{2S+1}L_J$ states by the inter-electronic repulsion and the spin-orbit coupling. Each of these states is further split into Stark components (up to $2J+1$ if n is even and $J+1/2$ if n is odd) because of the crystal field perturbation. The number of Stark components depends on the field symmetry of the ion under investigation. At room temperature, all the Stark components from the ground and excited state are thermally populated. When the temperature is lowered, the higher-lying Stark components are gradually depopulated, and the susceptibility decreases in a way that depends critically on the coordination environment. For this reason, for nearly two decades, although a large number of compounds containing both lanthanide and transition metal ions were synthesized, most magnetic studies were only concerned with the cases of Gd^{3+} and Cu^{2+} .

To obtain insights into the nature of the $\text{Ln}^{\text{III}}\text{-Cu}^{\text{II}}$ interaction, some attempts have been made by experimentally using diamagnetic substitution methods. If the Cu^{2+} ion is in a square-planar environment, then replacement by the Ni^{2+} ion will give a diamagnetic metal centre, since the Ni^{2+} ion in this environment has $S = 0$.

With respect to the magnetic interaction between Gd^{3+} and Cu^{2+} , quantum-mechanical calculations^[52] showed that the magnetic properties of a Gd-Cu pair are dependent on

orbital symmetry, and there is usually ferromagnetic coupling in pseudo- C_{2v} geometry while an antiferromagnetic interaction may occur when the symmetry of the molecule is lowered.

It is worth mentioning that in the very few cases of antiferromagnetic Gd(III)-Cu(II) interactions^[53], the dihedral angle between the planes of the Cu^{2+} coordination environment and that of the Gd^{3+} plays an important role. Comparison between two similar compounds showed that the difference in magnetic behaviour depends on the dihedral angle between the Gd and Cu coordination spheres. When the dihedral angles between the planes OCuN and OGdO is as low as 6.13° , the Gd-Cu interaction is ferromagnetic and when the angle becomes greater than 39.11° , the Gd-Cu interaction becomes antiferromagnetic^[53].

With few exceptions, most Gd-Cu magnetic interactions are ferromagnetic and the explanation of the mechanism of such ferromagnetic pathway is accepted for the usual Gd(III)-Cu(II) magnetic interactions^[54].

1.6 Magnetic properties of transition metal complex

1.6.1 Spin frustration

Spin frustration is defined as the result of competing exchange interactions of comparable magnitude that prevent the preferred spin alignments. A simple example is an $Fe(III)_3$ triangle with Fe(III)-Fe(III) interactions through a μ_3-O exchange pathway in which every Fe(III)-Fe(III) magnetic interaction is antiferromagnetic. When two irons are placed anti-parallel, the spin on the third Fe(III) cannot find a direction to fulfil the requirement for the arrangement of being both anti-parallel to the former two Fe(III). In other words, the last spin is frustrated because it cannot know how to align (Fig. 1.29).

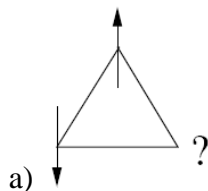


Figure 1.29 The frustration situation for the third spin carrier in the triangle.

The true classical ground state in the antiferromagnetic triangle is given by relative angles of 120° between neighboring spins (Fig.1.30).



Figure 1.30 Possible spin arrangements in the triangle with antiferromagnetic interactions.

The interactions between Fe^{III} centers are normally antiferromagnetic, but an appropriate quantity and distribution of frustrated exchange pathways in some Fe_x topologies can lead to significantly large spin ground states because of the occurrence of spin frustration effects, and further lead to SMM properties.

Large spin differences in Fe_6 clusters with spin frustration

Two Fe_6 compounds were synthesized with similar structures^[55]. One of them possesses a *trans* topology (Fig.1.31a), referring to the relative disposition of the two short, monoatomically bridged Fe_2 pairs within the triangular units, and has a ground state $S=0$; the other *cis* isomer (Fig. 1.31b) has an overall ground state of $S=5$.

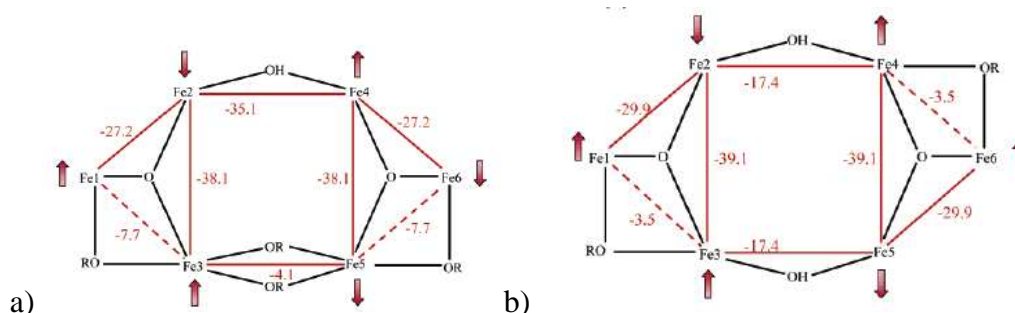


Figure 1.31 Schematic representation of the exchange interactions in the two Fe_6 clusters: a). *trans* topology with ground state $S=0$; b). complex 5A with ground state $S=5$.

This illustrates that a change in the arrangement of the bridging ligands can cause a structural change and affect the ground state spin value.

1.6.2 Single Molecule Magnets (SMMs)

Fe_8 single molecule magnet with spin frustration

The structure of $[\text{Fe}_8\text{O}_2(\text{OH})_{12}(\text{tacn})_6]^{8+}$, Fe_8 , where tacn = 1,4,7-triazacyclononane, which Wieghardt et al. originally reported as the bromide salt, Fe_8Br_8 , is shown in Fig. 1.32a^[56]. The

arrows correspond to the spin structure previously suggested from the analysis of the magnetic susceptibility^[57] and then determined from single crystal polarized neutron diffraction experiments^[58].

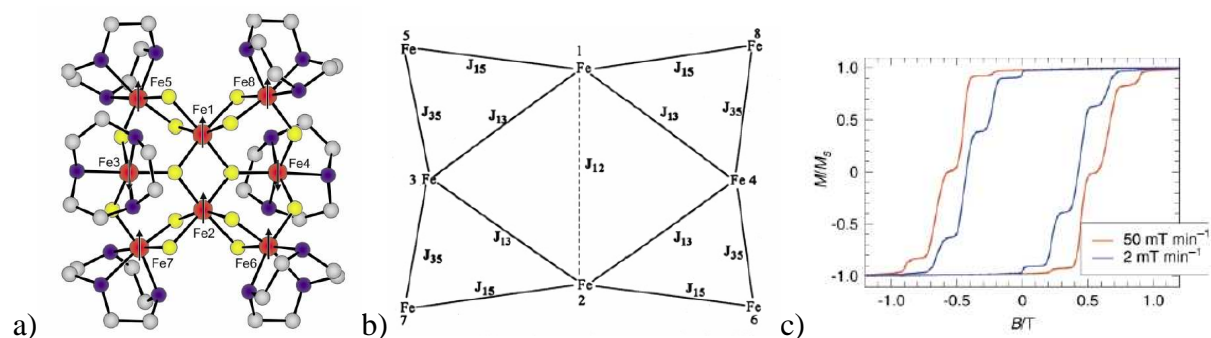


Figure 1.32 a) view of cluster $[\text{Fe}_8\text{O}_2(\text{OH})_{12}(\text{tacn})_6]^{8+}$; b) The corresponding magneto-structure; c) the hysteresis loops recorded for Fe_8Br at 0.30K and two different field scan speeds.

The analysis of the temperature dependence of the magnetic susceptibility^[57], provided evidence for a ground $S = 10$ state, which can occur if six spins are up and two down (Fig.1.32a). Since there are several triangles in the exchange pathways (Fig.5.6b) connecting the iron(III) ions spin, frustration effects can be anticipated. The stepped shape in the hysteresis loop (Fig.1.32c) is due to the tunneling of the magnetization, which occurs when two levels on the opposite sides of the barrier are brought into coincidence by sweeping the field, which accelerates the magnetic relaxation giving rise to the jumps in the magnetization.

Co₄ single molecule magnet

The compound $[\text{Co}_4(\text{hmp})_4(\text{MeOH})_4\text{Cl}_4]$ (Fig. 1.33a), where hmp- is the anion of hydroxymethylpyridine, was synthesized and shows hysteresis loops indicating single molecule magnet behavior (Fig.1.33b)^[59].

The Co₄ complex was determined to have a large ground state spin by an analysis of the two types of low-temperature, variable-field magnetization data depicted in Fig. 1.34a and Fig. 1.34b.

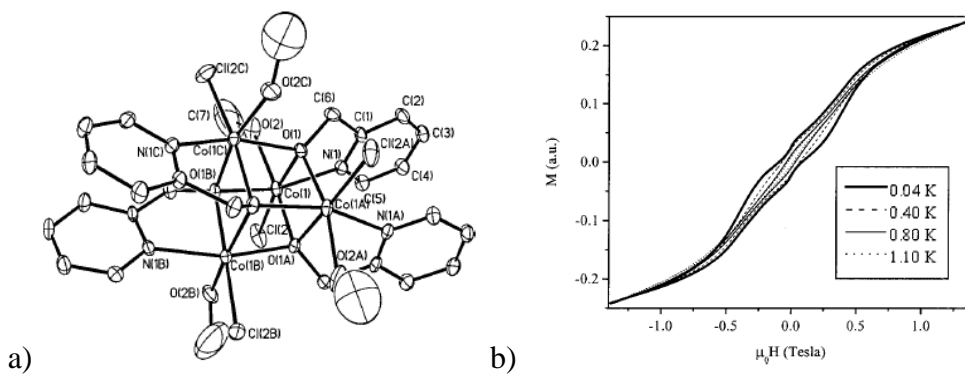


Figure 1.33 a) The structure of the $[\text{Co}_4(\text{hmp})_4(\text{MeOH})_4\text{Cl}_4]$; b) Plot of hysteresis loop with constant scanning rate (0.140 T/s) at four different temperatures

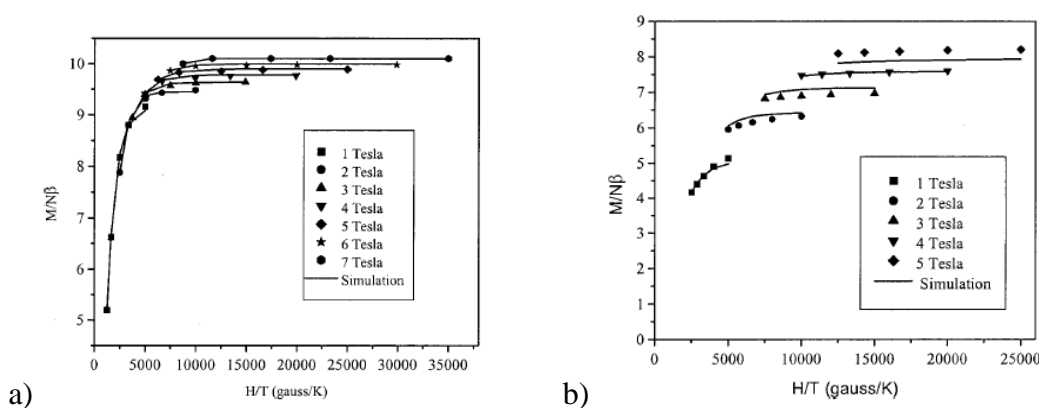


Figure 1.34 a) Plot of reduced magnetization measurement with sample aligned with magnetic field and the simulation curve; b) Plot of reduced magnetization measurement of randomly oriented powder sample and the simulation curve.

1.6.3 The magnetic properties of Cu_4 cubanes

A classification of the cubane structures can be made according to the $\text{Cu}\cdots\text{Cu}$ distance^[60]: Cu_4 with 2 short and 4 long $\text{Cu}\cdots\text{Cu}$ distances were designated as 2+4; with 4 short and 2 long $\text{Cu}\cdots\text{Cu}$ distances as 4+2; with six similar $\text{Cu}\cdots\text{Cu}$ distances as 6+0 (Fig. 1.35).

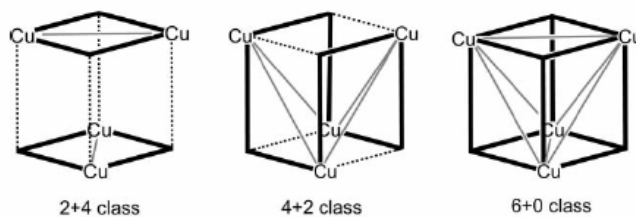


Figure 1.35 The classification of the three kinds of Cu_4 cubanes

The different classes of the Cu_4 cubanes show different magnetic properties while the compounds in the same class have similar magnetic-structures (Fig. 1.36)

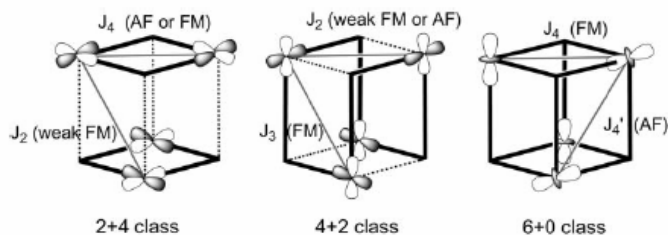


Figure 1.36 Magnetic structures for the three kinds of Cu₄ cubanes

In the cubane 2+4 complexes^[61-65], the J_2 interdinuclear interactions are weakly ferromagnetic, while the J_4 intradinuclear ones differ according to the type of the bridging, with hydroxo bridges and small Cu-O-Cu bond angles as ferromagnetic, and with alkoxo-bridges antiferromagnetic.

In the cubane 4+2 complexes^[66-75], the cubane topology requires an intradinuclear interaction (J_3) with three short and one long Cu-O bond distance and the interdinuclear interaction (J_2) with two short and two long Cu-O bond distances (Fig. 1.35). The experimentally fitted value for an interaction shows a weak antiferromagnetic interaction for J_2 and a ferromagnetic interaction for J_3 . The theoretical calculation by the method described^[60] for the two J values are both ferromagnetic, with J_2 is relatively weak while J_3 much stronger.

In the cubane 6+0 complexes^[76-78], there are two different orientations of the dz^2 orbitals thus leading to two different magnetic interaction pathway as ferromagnetic and antiferromagnetic (Fig. 1.36).

1.7 Thesis overview

In this chapter an introduction to cluster chemistry, magnetism and an overview of some clusters which have been reported in our group are presented. These clusters have been synthesized using the ligands (Fig. 1.3) similar to those in this thesis (Fig. 1.4). It shows the versatility of these ligands in the formation of nanoscale aggregates.

The following chapters will discuss the following three topics:

1. The thermal-properties of a Cu₄₄ aggregate in relation to its structure;
2. the structural features and magnetic properties of a series of lanthanide-copper compounds;
3. the structure and magnetic properties of transition metal aggregates Fe₈ and metal cubanes (Cu₄ and Co₄).

Chapter 2 Research objectives

Since the development and the application of more sensitive magnetic measurements in chemistry, increasing interest has been shown in the area of molecule based magnetism. For example, relatively large metal cluster-aggregates could provide high ground spin states which is one of the requirements for SMM behavior.

The compound $[\text{Cu}_{44}(\mu_8\text{-Br})_2(\mu_3\text{-OH})_{36}(\mu\text{-OH})_4\text{Br}_8(\text{ntp})_{12}(\text{H}_2\text{O})_{28}]\cdot\text{Br}_2\cdot 81\text{H}_2\text{O}$, shows a ground state with at least $S = 8$ and packs with large channels, which produces a nice system to study thermal decomposition properties. If this $\text{Cu}_{44}\cdot 81\text{H}_2\text{O}$ cluster could maintain its crystalline form to high temperature, its large channel cavity could make it a suitable candidate for gas absorption. Such an unusual large copper cluster is also a good model for studying the thermal decomposition properties with different metal-ligand bonds which is strongly related with the bond strength to the copper centres. To deduce the way the ligand decomposes by TGA could be helpful to understand the coordination properties in solid state.

Previous research on Ln(III)-Cu(II) cluster compounds shows that Tb(III)-Cu(II) and Dy(III)-Cu(II) interactions are often ferromagnetic and some {Tb(III)-Cu(II)} and {Dy(III)-Cu(II)} clusters have shown SMM properties. Thus synthesizing a series of Ln(III)-Cu(II) compounds could be helpful in identifying compounds with interesting magnetic properties, such as SMM behaviour. The magnetic behaviour of Gd(III)-Cu(II) compounds can often be modelled to quantify the intrinsic interactions between Gd(III) and Cu(II), and most Gd(III)-Cu(II) interactions show ferromagnetic properties with only a few antiferromagnetic examples. The whole series of Ln(III)-Cu(II) clusters could be studied on the structural basis in relation to their magnetic properties.

Since the ligand, H_3ntp , can capture Fe(III) ions into Fe_{13} cluster-aggregate, the addition of a rigid phenyl ring to the ligand could provide the possibility to modify the self-assembly reactions, thus leading to possible interesting structural arrangements which could lead to unusual magnetic properties. So the ligand, H_3cpidp , was chosen to be synthesized and reacted with Fe(III) salts to get new Fe(III) clusters.

Since the ligand, H₃heidi, captures Fe(III) ions into large Fe₁₇ and Fe₁₉ cluster-aggregates, and the ligand, H₃cpida, captures Cu(II) ions into large Cu₁₂ cluster-aggregates, the strategy of combining a phenyl ring and a hydroxyl group in a new ligand might result in new coordination modes and so to new transition metal clusters. So the ligand, H₃cpdea, was synthesized. The self-assembly reactions with various transition metals, Mn(II), Fe(II), Fe(III), Co(II), Ni(II), Cu(II), with the ligand H₃cpdea were carried out, and the structure and magnetic properties were investigated.

Chapter 3 Thermogravimetric Analysis of the large copper Aggregate $[\text{Cu}_{44}(\mu_8\text{-Br})_2(\mu_3\text{-OH})_{36}(\mu\text{-OH})_4\text{Br}_8(\text{ntp})_{12}(\text{H}_2\text{O})_{28}] \cdot \text{Br}_2 \cdot 81\text{H}_2\text{O}$

3.1 Background

$[\text{Cu}_{44}(\mu_8\text{-Br})_2(\mu_3\text{-OH})_{36}(\mu\text{-OH})_4\text{Br}_8(\text{ntp})_{12}(\text{H}_2\text{O})_{28}] \cdot \text{Br}_2 \cdot 81\text{H}_2\text{O}$ ($\text{Cu}_{44} \cdot 81\text{H}_2\text{O}$) was synthesized and characterized according to former research work^[29] by the reaction of CuBr_2 and the ligand, H_3ntp , in aqueous condition. The structure of $\text{Cu}_{44} \cdot 81\text{H}_2\text{O}$ is shown in Fig. 3.1.

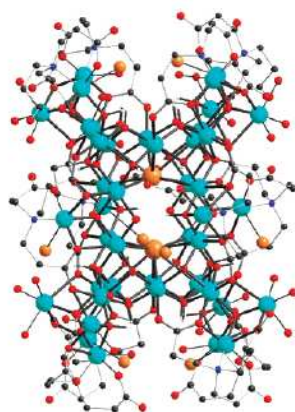


Figure 3.1 The structure of $[\text{Cu}_{44}(\mu_8\text{-Br})_2(\mu_3\text{-OH})_4(\text{ntp})_{12}\text{Br}_8(\text{H}_2\text{O})_{28}] \cdot \text{Br}_2 \cdot 81\text{H}_2\text{O}$

The X-ray single crystal measurement shows that the packing arrangement $\text{Cu}_{44} \cdot 81\text{H}_2\text{O}$ leads to very large channel cavities (Fig.3.2).

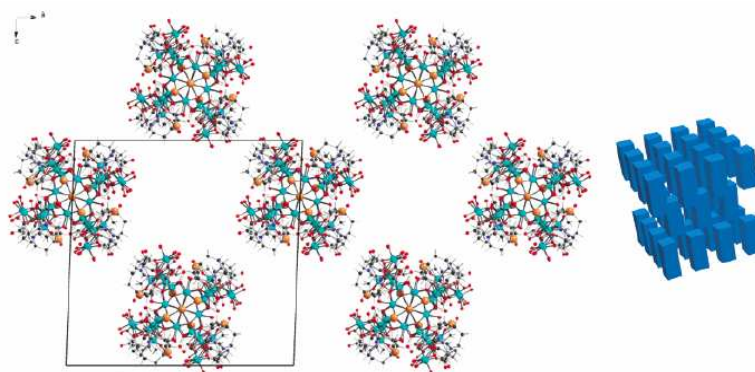


Figure 3.2 Packing diagram showing the arrangement of a layer of aggregates and cavities in the *ac*-plane and cartoon of the resulting 3D zeotypic structure

The preliminary experiment of heating the $\text{Cu}_{44}\cdot 81\text{H}_2\text{O}$ in an oven showed it has high thermal stability and keep its crystallinity until heated to 140°C ^[35]. The high thermal stability together with the large cavity dimensions, which form a zeotypic structure, giving an underlying hint that it could be suitable as storage material for gas absorption or to hold molecules such as methanol, pyridine, nitrogen, etc, which have low boiling point.

3.2 Thermal analysis TGA/DTA/STA

Thermogravimetric analysis (TGA) or thermogravimetry (TG) is a technique to measure the mass changes of a substance as a function of temperature or time while the substance is subjected to a controlled temperature program under a controlled atmosphere.

Differential Thermal Analysis (DTA) is a technique to measure the temperature difference between the substance and a reference material as a function of temperature, while the substance and reference material are subjected to a controlled temperature program under controlled atmosphere

STA refers to the application of two or more techniques on a sample at the same time. Normally STA combines the application of TGA and DTA, which can respectively give the information about the mass change and the kinetics of the thermal process.

3.3 Results and discussion

3.3.1 Total Thermal Analysis of $\text{Cu}_{44}\cdot 81\text{H}_2\text{O}$

The cluster $[\text{Cu}_{44}(\mu_8\text{-Br})_2(\mu_3\text{-OH})_{36}(\mu\text{-OH})_4\text{Br}_8(\text{ntp})_{12}(\text{H}_2\text{O})_{28}]\cdot\text{Br}_2\cdot 81\text{H}_2\text{O}$ has a molecular weight of $M_r = 9161.10$. The components that decomposed in the thermal process are listed in Table 3.1 and the corresponding mass loss calculated is listed as well.

Thus the corresponding TGA/DTA curve during the thermal process can be summarised as given in Fig. 3.3 concerning of the decomposition way of the Cu_{44} molecule.

Component.	Mass lost	Mass lost %	Driven off as
81 H ₂ O (crystalline)	1458	15.92%	81H ₂ O
2 Br ⁻ (counter anion)	162	1.77%	2HBr
8 μ-Br	648	7.07%	8HBr
18 H ₂ O (coordination)	324	3.54%	18H ₂ O
12 ntp	1212	13.23%	12NEt ₃
36 CO ₃ ²⁻	1584	17.29%	36CO ₂
2 μ ₈ -Br	162	1.77	2HBr
12 -OH	108	1.18	6H ₂ O

Table 3.1 The calculated mass loss according to the components that were decomposed in the thermal process

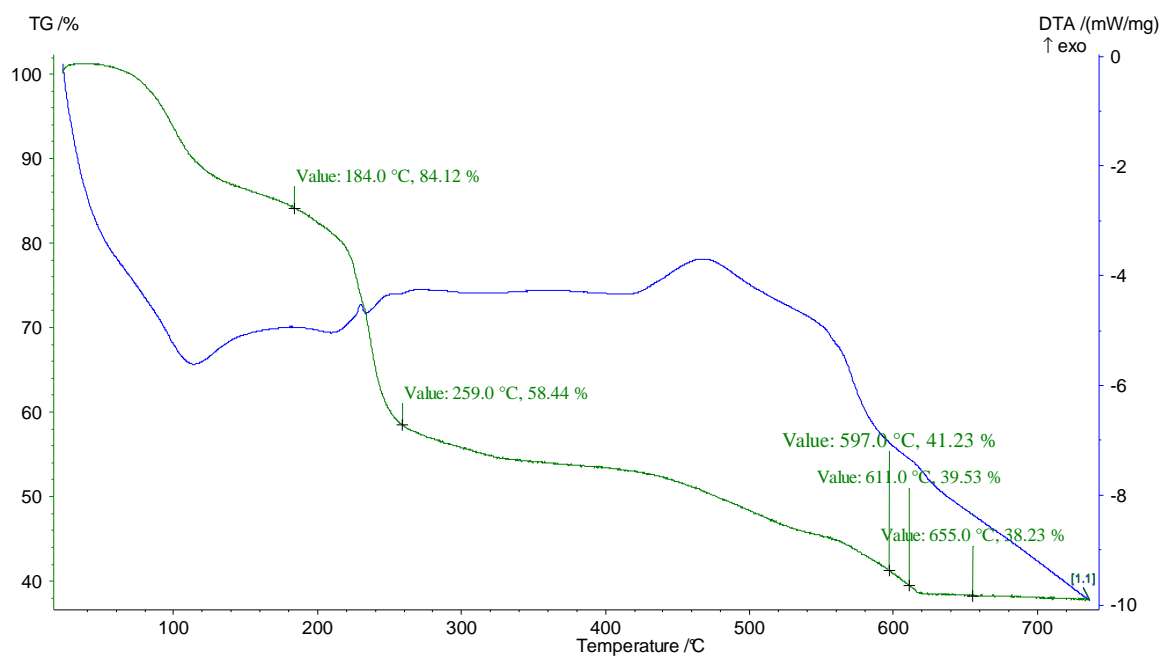


Figure. 3.3 Thermal decomposition of Cu₄₄·81H₂O in nitrogen atmosphere: TG and DTA curves for the total decomposition process

3.3.2 Spectroscopy

3.3.2.1 The IR spectrum

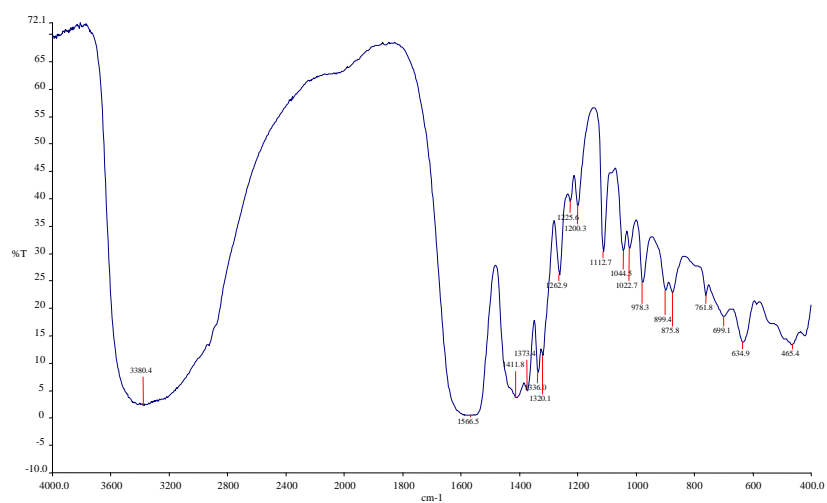


Figure 3.4 The IR of $[\text{Cu}_{44}(\mu_8\text{-Br})_2(\mu_3\text{-OH})_{36}(\mu\text{-OH})_4\text{Br}_8(\text{ntp})_{12}(\text{H}_2\text{O})_{28}] \cdot \text{Br}_2 \cdot 81\text{H}_2\text{O}$

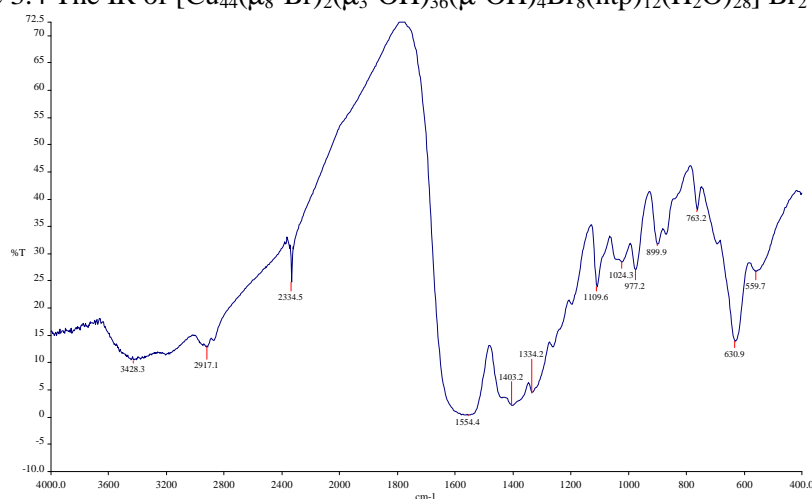


Figure 3.5 IR of thermal decomposition product of $\text{Cu}_{44} \cdot 81\text{H}_2\text{O}$ heated to 180°C

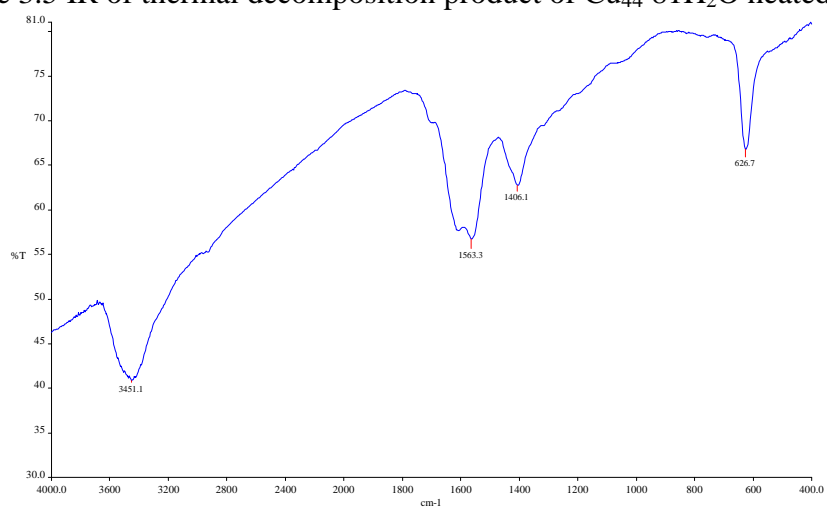


Figure 3.6 IR of thermal decomposition product of $\text{Cu}_{44} \cdot 81\text{H}_2\text{O}$ heated to 210°C

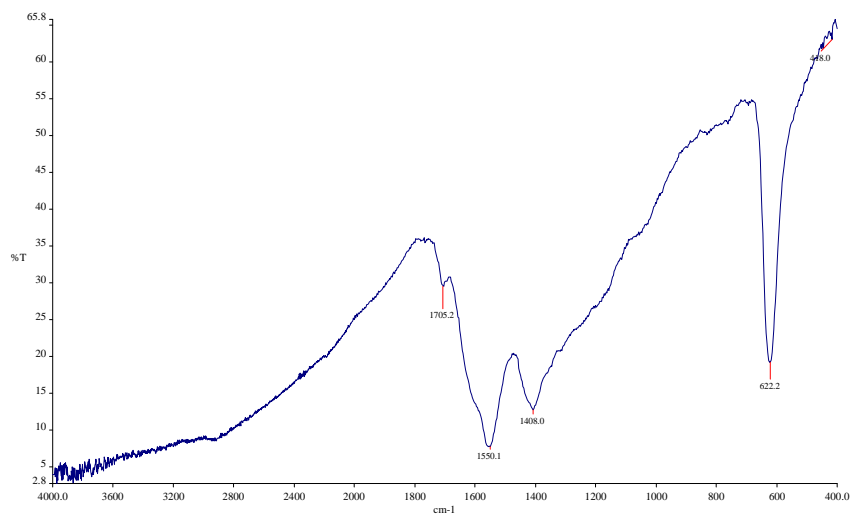


Figure 3.7 IR of thermal decomposition product of $\text{Cu}_{44}\cdot 81\text{H}_2\text{O}$ heated to 250 °C

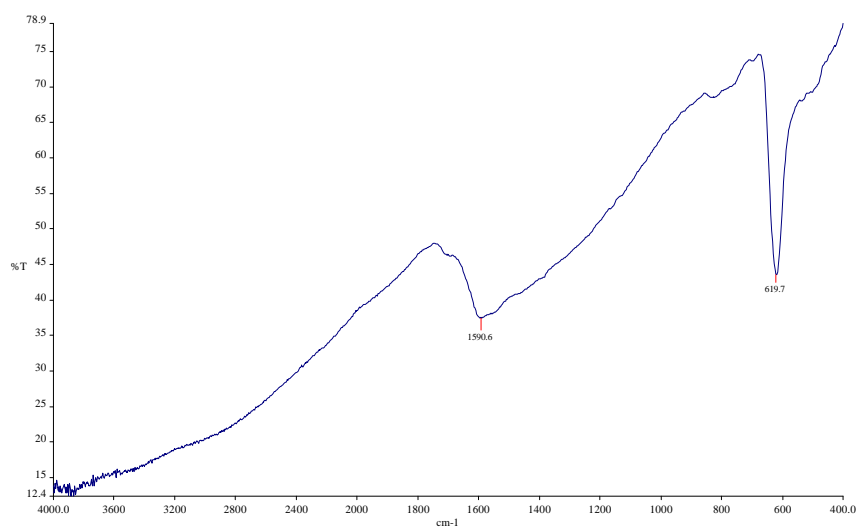


Figure 3.8 IR of thermal decomposition product of $\text{Cu}_{44}\cdot 81\text{H}_2\text{O}$ heated to 420 °C

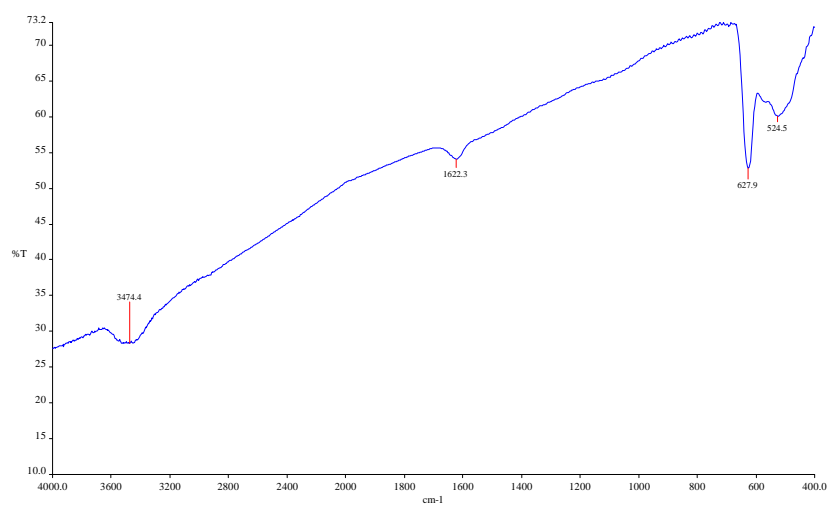
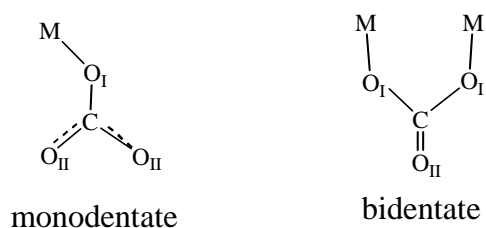


Figure 3.9 IR of thermal decomposition product of $\text{Cu}_{44}\cdot 81\text{H}_2\text{O}$ heated to 500 °C

In the IR spectrum of $[\text{Cu}_{44}(\mu_8\text{-Br})_2(\mu_3\text{-OH})_{36}(\mu\text{-OH})_4\text{Br}_8(\text{ntp})_{12}(\text{H}_2\text{O})_{28}]\cdot\text{Br}_2\cdot 81\text{H}_2\text{O}$ (Fig. 3.4) the broad band centered near 3400 cm^{-1} is due either to OH stretching or amine N-H stretching. As the ligand H_3ntp in the complex $\text{Cu}_{44}\cdot 81\text{H}_2\text{O}$ is fully deprotonated, there are no carboxylic OH and amine NH. So this ν_{OH} corresponds to the bridging $\mu_3\text{-OH}$, $\mu\text{-OH}$, coordinated and crystal water OH. The broad band centered near 1560 cm^{-1} corresponds to the stretch of COO^- in carboxylic acid salts, which is consistent with the structure that has many uncoordinated COO^- groups. The bands at the lower frequency are likely due to the organic back bone and crystalline lattice vibrations.

When the temperature is raised to 180°C (Fig. 3.5), most of the 81 crystalline waters are driven off while the coordinated water remains as seen from IR bands centred at 3428 cm^{-1} and 2917 cm^{-1} . The organic backbone vibrations are still observed below 1400 cm^{-1} .

When the temperature is raised to 210°C (Fig. 3.6), the whole crystal structure collapses into an amorphous state with the loss of crystallinity identified in IR spectrum as the disappearance of the bands at lower frequencies. The broad absorption of the carboxylic group COO^- stretching modes at around 1550 cm^{-1} has also disappeared, instead sharp peaks at 1562 cm^{-1} and 1406 cm^{-1} appear as the CO stretching mode of the $-\text{CO}_3^{2-}$ group. The vibration splitting in bidentate carbonate compounds, which is normally around 300 cm^{-1} , is larger than in monodentate carbonate compounds, which is normally around 100 cm^{-1} . The bands between 1400 cm^{-1} to 1600 cm^{-1} could be assigned to the overlaps of multidentate carbonate.



The OH stretching mode can be seen at 3451 cm^{-1} , which indicates the $\mu_3\text{-OH}$ and $\mu\text{-OH}$ stretching. The absorption at around 620 cm^{-1} could be assigned to the overlapping of bands from the deformation modes of carbonate CuO_1 stretches. The absorption of the coordinated H_2O at around 3500 cm^{-1} is still present.

When the temperature is raised to 250°C (Fig. 3.7), the absorption at around 3500 cm^{-1} disappears, whereas the absorptions for the carbonate CO_3^{2-} are still present.

When the temperature is raised to 420°C (Fig. 3.8), the absorption at around 1400cm⁻¹ disappears, as indicates that the monodentated carbonate is no longer present, whereas the absorption at around 1560cm⁻¹ indicates that the bidentate carbonate is undisturbed.

When the temperature is raised to 500°C (Fig. 3.9), the absorption at around 1560cm⁻¹ disappears and a new absorption at around 520cm⁻¹ appears, indicating that the bidentate carbonate is decomposed into a new form. The peaks at 3674cm⁻¹ and 1622cm⁻¹ could arise from H₂O in the KBr.

3.3.2.2 X-ray powder diffraction

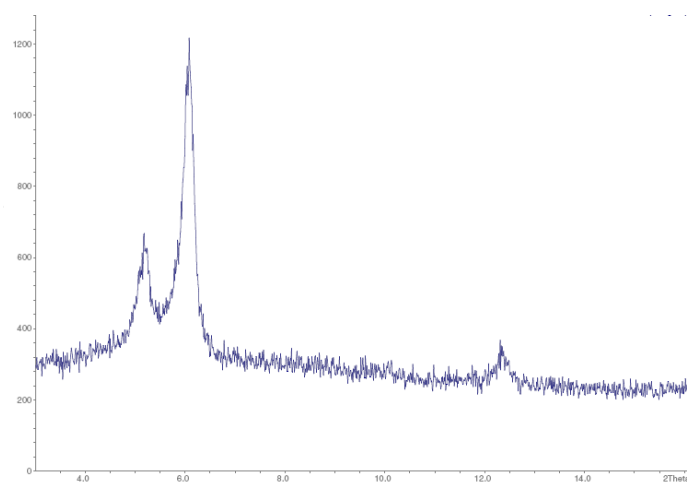


Figure 3.10 X-ray Powder Diffraction of Cu₄₄·81H₂O

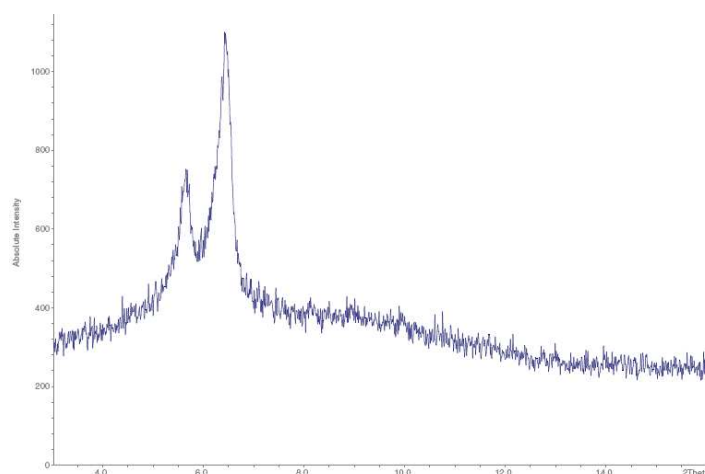


Figure 3.11 X-ray Powder Diffraction of Cu₄₄·81H₂O heated to 180°C

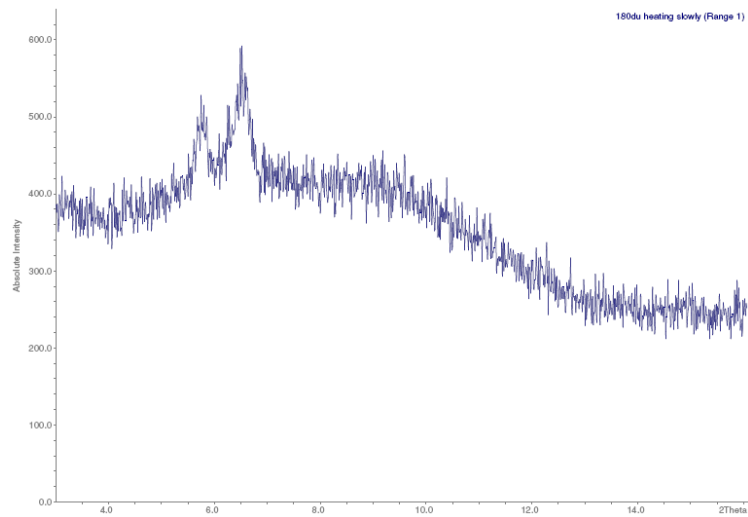


Figure 3.12 X-ray Powder Diffraction of $\text{Cu}_{44}\cdot 81\text{H}_2\text{O}$ heated to 180°C slowly

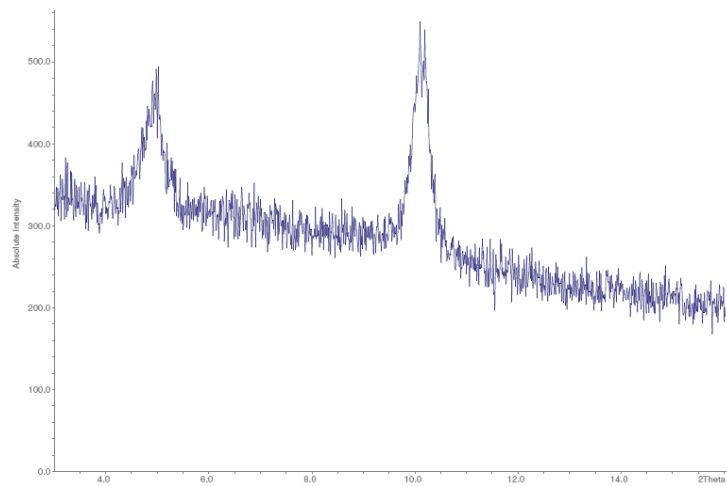


Figure 3.13 X-ray Powder Diffraction of $\text{Cu}_{44}\cdot 81\text{H}_2\text{O}$ heated to 210°C

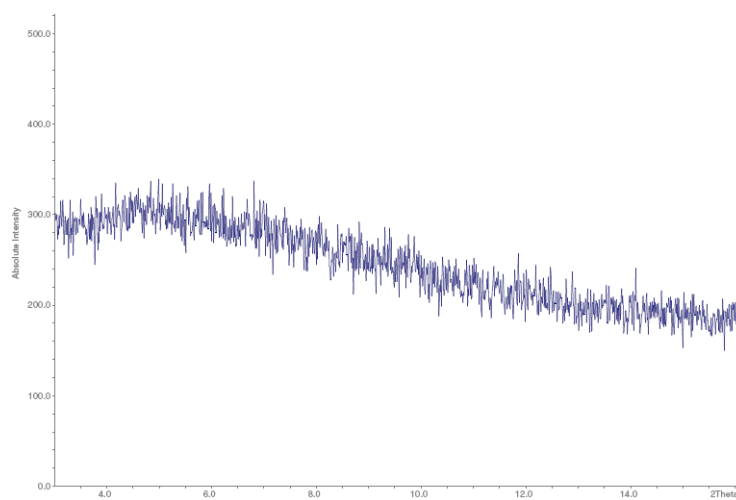


Figure 3.14 X-ray Powder Diffraction of $\text{Cu}_{44}\cdot 81\text{H}_2\text{O}$ heated to 250°C

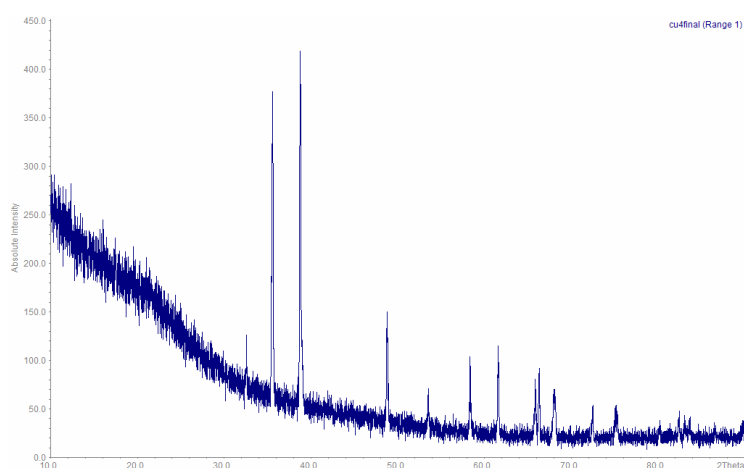


Figure 3.15 X-ray Powder Diffraction of the final product

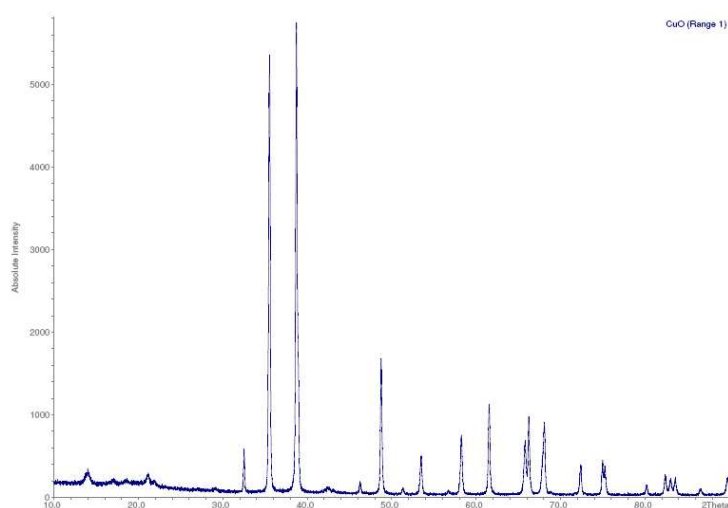


Figure 3.16 X-ray Powder Diffraction of the commercial CuO sample

From the series of XRD patterns, the decomposition of the crystalline structure of $\text{Cu}_{44}\cdot 81\text{H}_2\text{O}$ could be detected. When the temperature is raised to 180°C , only the crystal waters are driven off whereas the crystalline structure is maintained. The XRD spectrum for the heated product at 180°C (Fig. 3.11 and Fig. 3.12) is similar to that for the original $\text{Cu}_{44}\cdot 81\text{H}_2\text{O}$ (Fig. 3.10). In spite of the similarity, there is a subtle structure change when $\text{Cu}_{44}\cdot 81\text{H}_2\text{O}$ was heated to 180°C with much crystal water lost. When the temperature is raised to 210°C , the XRD pattern shows changes. The peaks at lower angles around 6° shift to around 10° (Fig. 3.13), indicating a change in crystal structure. When the temperature is raised to 250°C , all the peaks at low angles disappear (Fig. 3.14), suggesting that the whole crystalline structure is decomposed. The XRD spectrum for the final product heated to 800°C (Fig. 3.15)

corresponds to the XRD pattern for commercial CuO (Fig. 3.16). Thus the final product is assigned as CuO.

3.4 Summary

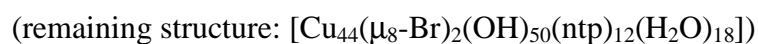
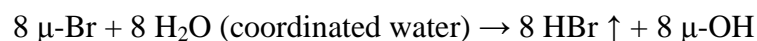
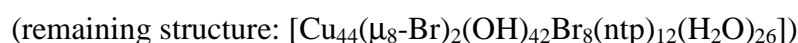
When the thermal analysis of TGA/DTA, IR and the XRD are considered altogether, the following thermal process steps can be assigned.

Step 1: 20°C - 184°C

The mass loss of 15.88% corresponds to all the 81 crystal waters (theoretically 15.92%) with an endothermic process. The IR shows the disappearance of the absorption for crystal water and XRD shows that there is no loss of crystallinity. The pattern corresponds to the structure for $[\text{Cu}_{44}(\mu_8\text{-Br})_2(\text{OH})_{40}\text{Br}_8(\text{ntp})_{12}(\text{H}_2\text{O})_{28}]\cdot\text{Br}_2$.

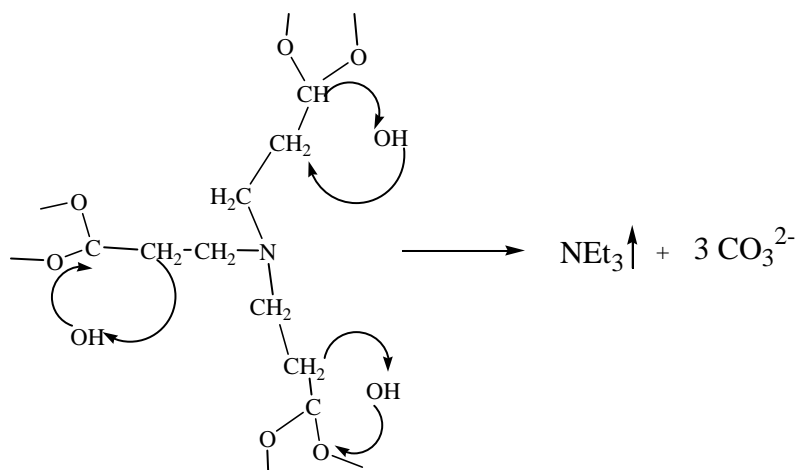
Step 2: 184°C – 259°C

The abrupt mass loss of 25.68% over a small temperature range corresponds to the breakdown of the organic backbone, the bromide anions and coordination waters (theoretically 25.61%) with a saw-shaped DTA curve. First to be lost are the bromides as shown in Scheme 3.1.



Scheme 3.1 the loss of the bromide atoms

Then follows the loss of the 18 coordinated waters. The last entity to be driven off is in the form of NEt_3 molecules possibly by the mechanism shown in Scheme 3.2.



Scheme 3.2 Proposed mechanism of the decomposition of the organic backbone

There are 12 ntp^{3-} ligands in the structure, so 36 $\mu\text{-OH}$ are required to generate 12 NEt_3 molecules and 36 CO_3^{2-} . Thus the formula is changed from $[\text{Cu}_{44}(\mu_8\text{-Br})_2(\text{OH})_{50}(\text{ntp})_{12}]$ to $[\text{Cu}_{44}(\mu_8\text{-Br})_2(\text{OH})_{14}(\text{CO}_3^{2-})_{36}]$. Both the IR and XRD show the decomposition of the organic backbone over this temperature range. Furthermore, the IR shows the appearance of the resulting carbonate CO_3^{2-} .

Step 3: 259°C – 597°C

The slow mass loss 17.21% over a large temperature range corresponds to the loss of all the 36 CO_3^{2-} (theoretically 17.29%) in two overlapping processes. The IR shows the loss of some of carbonate anions.

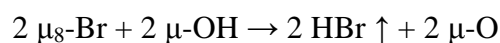


Scheme 3.3 the mechanism of the breakdown of CO_3^{2-}

The remaining structure is $[\text{Cu}_{44}(\mu_8\text{-Br})_2(\text{OH})_{14}(\text{O})_{36}]$.

Step 4: 597°C – 611°C

The mass loss of 1.70% corresponds to the loss of the last two $\mu_8\text{-Br}$ ions (theoretically 1.77%) which are buried deep inside the cluster. The mechanism is shown in Scheme 3.4, with two $\mu\text{-OH}$ is changed into $\mu\text{-O}$.



Scheme 3.4 the loss of $\mu_8\text{-Br}$

The remaining formula is $[\text{Cu}_{44}(\text{OH})_{12}(\text{O})_{38}]$.

Step 5: 611°C – 655°C

The mass loss of 1.30% corresponds to the breakdown of 12 $\mu\text{-OH}$, with 6 H_2O lost (theoretically 1.18%). The XRD shows the final product is CuO .

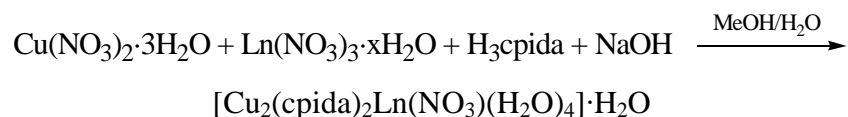
Thus the whole thermal decomposition process of $\text{Cu}_{44}\cdot 81\text{H}_2\text{O}$ is summarized as in Table 3.2.

	Temperature	Mass	%	as	Remaining formula
Step1	-184°C	1458	15.92%	81 H_2O	$[\text{Cu}_{44}(\mu_8\text{-Br})_2(\text{OH})_{40}\text{Br}_8(\text{ntp})_{12}(\text{H}_2\text{O})_{28}]\cdot\text{Br}_2$
Step2	184°C-259°C	162	1.77%	2 HBr	$[\text{Cu}_{44}(\mu_8\text{-Br})_2(\text{OH})_{42}\text{Br}_8(\text{ntp})_{12}(\text{H}_2\text{O})_{26}]$
		648	7.07%	8 HBr	$[\text{Cu}_{44}(\mu_8\text{-Br})_2(\text{OH})_{50}(\text{ntp})_{12}(\text{H}_2\text{O})_{18}]$
		324	3.54%	18 H_2O	$[\text{Cu}_{44}(\mu_8\text{-Br})_2(\text{OH})_{50}(\text{ntp})_{12}]$
		1212	13.23%	12 NEt_3	$[\text{Cu}_{44}(\mu_8\text{-Br})_2(\text{OH})_{14}(\text{CO}_3^{2-})_{36}]$
Step3	259°C-597°C	1584	17.29%	36 CO_2	$[\text{Cu}_{44}(\mu_8\text{-Br})_2(\text{OH})_{14}(\text{O})_{36}]$
Step4	597°C-610°C	162	1.77	2 HBr	$[\text{Cu}_{44}(\text{OH})_{12}(\text{O})_{38}]$
Step5	610°C-655°C	108	1.18	6 H_2O	$\text{Cu}_{44}\text{O}_{44}$ (44 CuO)

Table 3.2 The thermal process of $\text{Cu}_{44}\cdot 81\text{H}_2\text{O}$

Chapter 4 Structures and magnetic properties of copper (II) and lanthanide(III) 2D coordination polymers

4.1 The synthesis of $[\text{Cu}_2(\text{cpida})_2\text{Ln}(\text{NO}_3)(\text{H}_2\text{O})_4]\cdot\text{H}_2\text{O}$ (2-11)



Scheme 4.1 Synthetic scheme of the $\{\text{Cu}_2\text{Ln}\}_x$ 2D sheets

A series of compounds $[\text{Cu}_2(\text{cpida})_2\text{Ln}(\text{NO}_3)(\text{H}_2\text{O})_4]\cdot\text{H}_2\text{O}$ was synthesized in a mixed solvent system of water and alcohol. The self-assembly reaction is illustrated in Scheme 4.1.

When methanol was present together with water as the solvent, the evaporation rate of methanol is comparatively fast and the crystals can appear in a suitable size for the single X-ray measurement. Instead when ethanol was present together with water as solvent, the evaporation rate of ethanol is comparatively slow and crystals come out at a much slower rate, thus the green crystals achieve a large size but are not suitable for direct X-ray measurement. Thus, all the crystals of $\{\text{Cu}_2\text{Ln}\}_x$ that were measured using X-ray diffraction were synthesized in the mixed solvent system of water and methanol.

The base used in the syntheses was sodium hydroxide. The amount of base required in the synthesis increases when the atomic number of lanthanide increases. However, when more base is added, lanthanide hydroxide forms as a white powder, and this must be filtered off before the green crystals form. The time needed for the crystals to form increases steadily from two days for the La complex to more than one month for Er, and the crystal quality was also not so high with the heavier lanthanides.

Single crystals of $[\text{Cu}_2(\text{cpida})_2\text{Ln}(\text{NO}_3)(\text{H}_2\text{O})_4]\cdot\text{H}_2\text{O}$ (Ln = La, Ce, Pr, Nd, Sm, Eu, Gd, Dy, Ho, Er) were collected for further characterization such as IR, single crystal X-ray diffraction, and magnetic measurements.

4.2 The structure of [Cu₂(cpida)₂Ln(NO₃)(H₂O)]·H₂O (2-11)

All ten compounds have the general formula [Cu₂(cpida)₂Ln(NO₃)(H₂O)₄]·H₂O and crystallise as green block crystals in the monoclinic space group C2/c with Z = 4. The [Cu₂(cpida)₂Ln(NO₃)(H₂O)₄]·H₂O compound can be visualized as a layered structure, in which {Cu₂Ln} units build up layers parallel to {110}, with the water molecules between layers.

4.2.1 The overview of the structure of the two dimensional 2D-sheets {Cu₂Ln}_x

The cell parameters of the different {Cu₂Ln}_x compounds are listed in Table 4.1. The data in the table show the trend that with the increase in atomic number, the *a* edge and *c* edge of the unit cell both decrease. This is consistent with the lanthanide contraction rule that from left to right in the lanthanide row the atom radius decreases. The *b* edge of the unit cell is not subject to the lanthanide contraction because only Cu²⁺ atoms extend along this direction.

Compound	a (Å)	b (Å)	c (Å)	β(°)	V (Å ³)
{Cu ₂ La} _x , 2	17.2401(15)	9.7163(6)	18.1615(15)	103.083(7)	2963.3(4)
{Cu ₂ Ce} _x , 3	17.1998(16)	9.7028(7)	18.1090(16)	103.123(7)	2943.2(4)
{Cu ₂ Pr} _x , 4	17.1735(9)	9.6994(5)	18.0266(9)	102.837(1)	2927.7(3)
{Cu ₂ Nd} _x , 5	17.1387(7)	9.7117(4)	18.0026(7)	102.858(1)	2921.3(2)
{Cu ₂ Sm} _x , 6	17.1402(17)	9.7044(10)	17.9243(18)	102.813(2)	2907.2(5)
{Cu ₂ Eu} _x , 7	17.1217(7)	9.7075(4)	17.9010(7)	102.760(1)	2901.4(2)
{Cu ₂ Gd} _x , 8	17.1243(7)	9.7077(4)	17.8714(8)	102.812(1)	2896.9(2)
{Cu ₂ Dy} _x , 9	17.1905(6)	9.7245(4)	17.7725(7)	102.581(1)	2899.7(2)
{Cu ₂ Ho} _x , 10	17.1737(11)	9.7183(6)	17.7148(12)	102.701(1)	2884.2(3)
{Cu ₂ Er} _x , 11	17.2021(6)	9.7206(4)	17.6493(7)	102.759(1)	2878.4(2)

Table 4.1 Unit cell data for the [Cu₂(cpida)₂Ln(NO₃)(H₂O)₄]·H₂O compounds

4.2.2 The coordination spheres of the metal ions

The coordination spheres of Cu(II)

The Cu²⁺ and Ln³⁺ ions are five and ten-coordinate respectively.

The copper atom is coordinated by four carboxylic oxygen atoms and one nitrogen atom. Thus a square-based pyramidal coordination sphere is formed with three Cu-O bonds and one Cu-N bond on the plane with one Cu-O bond along the long axis (Fig. 4.1).

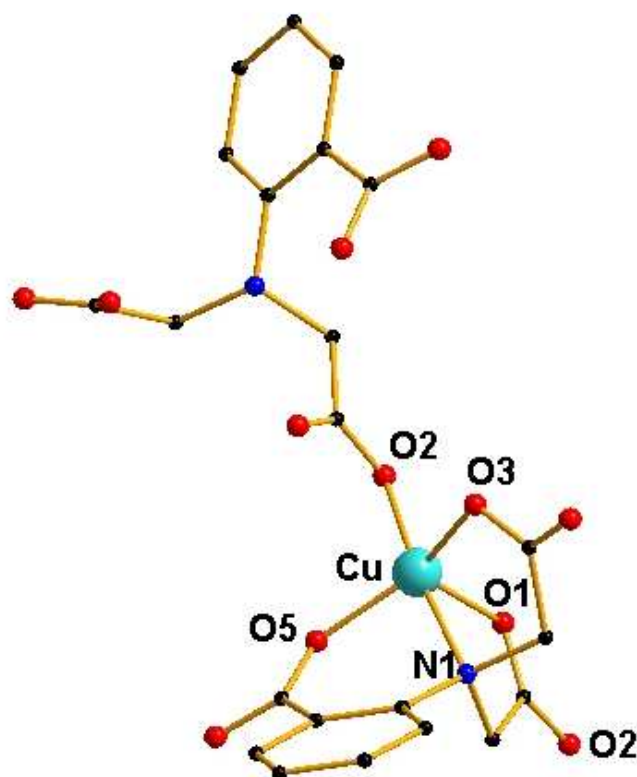


Figure 4.1 The coordination sphere of Cu cation

As shown in Fig. 4.1, the tetradentate ligand coordinates the Cu atom with the longest Cu(1)-O(1) bond length in the range of 2.175Å to 2.187Å (Table 4.2), which forms the long axis of the square-pyramidal coordination sphere. The other two Cu-O bonds, Cu(1)-O(3) and Cu(1)-O(5) are in the range of 1.957Å to 1.976Å, and the Cu-N bond is 2.031-2.036Å. The carboxylic oxygen atom O(2#) from the ligand at $\{-x+1, y, -z+1/2\}$ occupies the remaining final coordination site with Cu(1)-O(2#) bonds in the range of 1.921Å to 1.931Å.

compound	Cu(1)-O(1)	Cu(1)-O(2#)	Cu(1)-O(3)	Cu(1)-O(5)	Cu(1)-N(1)
$\{\text{Cu}_2\text{La}\}_x$, 2	2.175(2)	1.931(2)	1.964(2)	1.975(3)	2.034(3)
$\{\text{Cu}_2\text{Ce}\}_x$, 3	2.175(2)	1.926(2)	1.958(2)	1.976(2)	2.034(2)
$\{\text{Cu}_2\text{Pr}\}_x$, 4	2.175(2)	1.926(2)	1.962(2)	1.973(2)	2.033(2)
$\{\text{Cu}_2\text{Nd}\}_x$, 5	2.179(2)	1.925(2)	1.963(2)	1.969(2)	2.035(2)
$\{\text{Cu}_2\text{Sm}\}_x$, 6	2.179(2)	1.921(2)	1.963(2)	1.969(2)	2.032(2)
$\{\text{Cu}_2\text{Eu}\}_x$, 7	2.180(2)	1.922(2)	1.961(2)	1.970(2)	2.033(2)
Cu_2Gd , 8	2.181(2)	1.921(2)	1.964(2)	1.967(2)	2.034(2)
$\{\text{Cu}_2\text{Dy}\}_x$, 9	2.186(3)	1.923(3)	1.965(3)	1.965(3)	2.032(3)
$\{\text{Cu}_2\text{Ho}\}_x$, 10	2.187(3)	1.924(3)	1.963(3)	1.957(3)	2.036(3)
$\{\text{Cu}_2\text{Er}\}_x$, 11	2.188(2)	1.924(2)	1.961(2)	1.958(2)	2.031(2)

Table 4.2 The bond length of the coordination around Cu^{2+}

The coordination sphere of Ln(III)

The coordination sphere of the Ln^{3+} has crystallographic C_2 site symmetry, with the Ln^{3+} cation, and N(11) and O(12) of the nitrate ligand lying on the twofold axis (Fig. 4.2). The remaining two nitrate oxygens thus chelate the Ln^{3+} cation symmetrically. The two $(\text{cpida})^{3-}$ ligands lie to either side of the NO_3^- plane, each using the carboxylate group on the phenyl ring to chelate Ln^{3+} . These two carboxylate groups are approximately *trans* to each other. The four coordinated water molecules lie below the plane defined by O(5) and O(6) and their symmetry equivalents, completing the ten-fold coordination sphere of the Ln^{3+} .

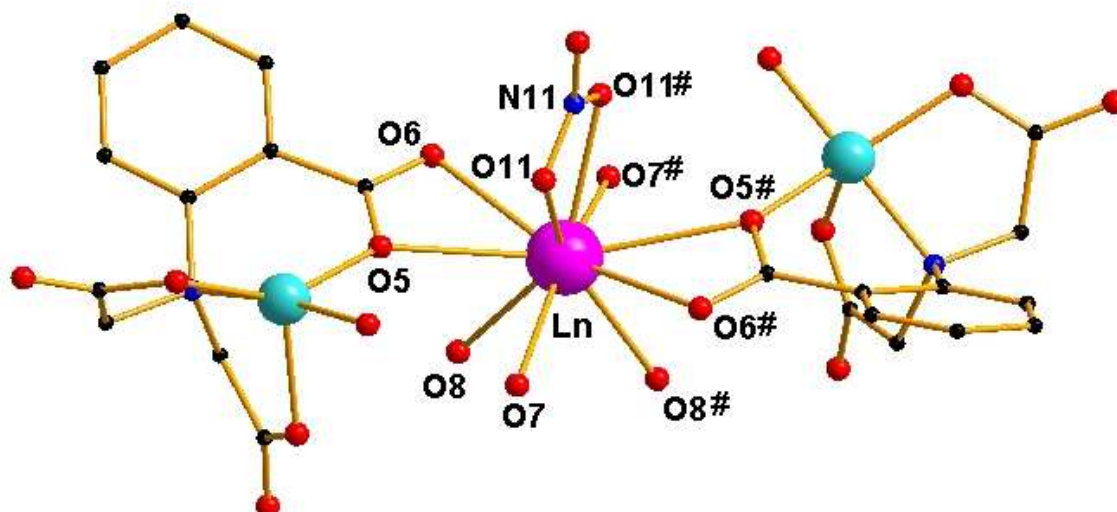


Figure 4.2 The coordination of Ln^{3+} cation (the atoms with symmetric operation of $\{-x+1, y, -z+0.5\}$ are marked with #)

The carboxylic group from the benzene ring chelates Ln^{3+} and bridges to the Cu^{2+} , with one stronger Ln-O bond and one weaker Ln-O bond. As seen in Table 4.3, the Ln(1)-O(5) bond is the longest and longer than the normal Ln-O bond, which corresponds to a weaker Ln-O bonding, whereas the bond of Ln(1)-O(6) lies in the range of the normal Ln-O bond, which corresponds to a stronger bonding. The coordinated nitrate oxygen atoms form two Ln(1)-O(11) bonds with the bond length in the range of 2.43Å to 2.60Å. The four water molecules coordinate to Ln^{3+} with Ln(1)-O(7) and Ln(1)-O(8) bonding in the range of 2.42Å to 2.60Å.

compound	Ln-O(5)	Ln-O(6)	Ln-O(7)	Ln-O(8)	Ln-O(11)
{Cu ₂ La} _x , 2	2.774(2)	2.586(3)	2.514(3)	2.595(3)	2.592(3)
{Cu ₂ Ce} _x , 3	2.757(2)	2.563(2)	2.492(2)	2.573(2)	2.568(2)
{Cu ₂ Pr} _x , 4	2.754(2)	2.550(2)	2.473(2)	2.549(2)	2.551(3)
{Cu ₂ Nd} _x , 5	2.743(2)	2.534(2)	2.461(2)	2.532(2)	2.533(2)
{Cu ₂ Sm} _x , 6	2.742(2)	2.508(2)	2.432(2)	2.503(2)	2.506(2)
{Cu ₂ Eu} _x , 7	2.736(2)	2.495(2)	2.421(2)	2.487(2)	2.492(2)
Cu ₂ Gd _x , 8	2.737(2)	2.483(2)	2.410(2)	2.470(2)	2.483(2)
{Cu ₂ Dy} _x , 9	2.766(3)	2.456(3)	2.380(3)	2.449(4)	2.452(3)
{Cu ₂ Ho} _x , 10	2.766(3)	2.440(3)	2.363(3)	2.428(3)	2.436(3)
{Cu ₂ Er} _x , 11	2.773(2)	2.421(2)	2.356(2)	2.414(2)	2.424(2)

Table 4.3 Bond length of the coordination around Ln³⁺

The bond length of Ln-O decreases from the lower to the higher members of the lanthanide series in accordance with the lanthanide contraction (Table. 4.3 and Fig. 4.3).

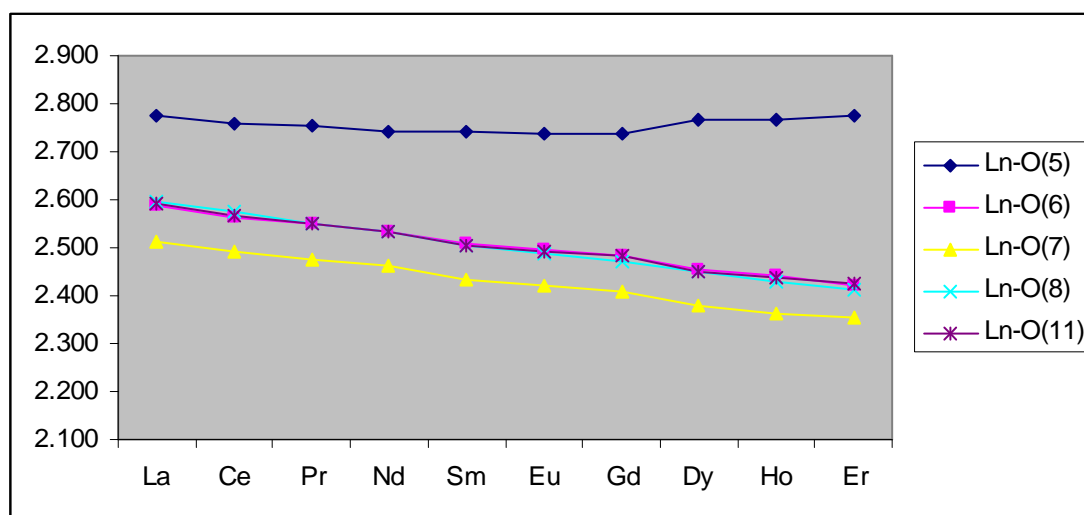


Figure 4.3 Graph showing the decreasing trend of Ln-O bond length

4.2.3 The linkage between metals

The linkage between Cu(II) and Cu(II)

Each Cu²⁺ has two ligands coordinated, with one of the ligands acting as a chelate to occupy four coordination sites and the other playing a linking role to occupy the fifth coordination site thus forming chains of coppers. The carboxylate group on one of the acetate arms of cpida³⁻ uses O(1) to coordinate to the chelated Cu²⁺, and O(2) to coordinate to the next Cu²⁺ in the chain, forming a *syn(ax)-anti(eq)* bridge (Fig. 4.4). The zig-zag chains run parallel to the crystal *b*-axis.

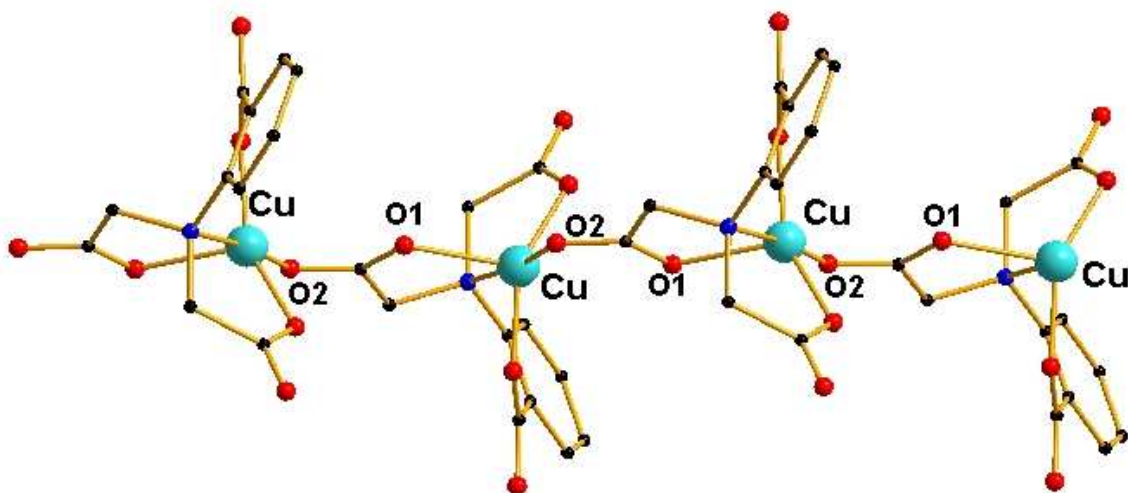


Figure 4.4 The linkage between copper atoms

The linkage between Cu(II) and Ln(III)

Adjacent parallel copper chains are held together by lanthanide cations that link the two chains. The carboxylic group on the benzene ring plays the linking role using both of its oxygen atoms. Cu^{2+} and Ln^{3+} are directly linked by O(5) and O(6) which form a *syn-anti* carboxylate bridge. Since the Ln-O(5) bond is significantly (*ca.* 0.21 Å) longer than Ln-O(6) (Table 4.3), the linkage may perhaps be best described as a *syn-anti* bridge with additional weaker Cu-O-Ln bonding (Fig. 4.4). Since the Ln-O(5) bond length is rather independent of the lanthanide (unlike the other Ln-O distances, Table 4.3) it is perhaps likely that the Ln-O(5) interaction is indeed rather weak.

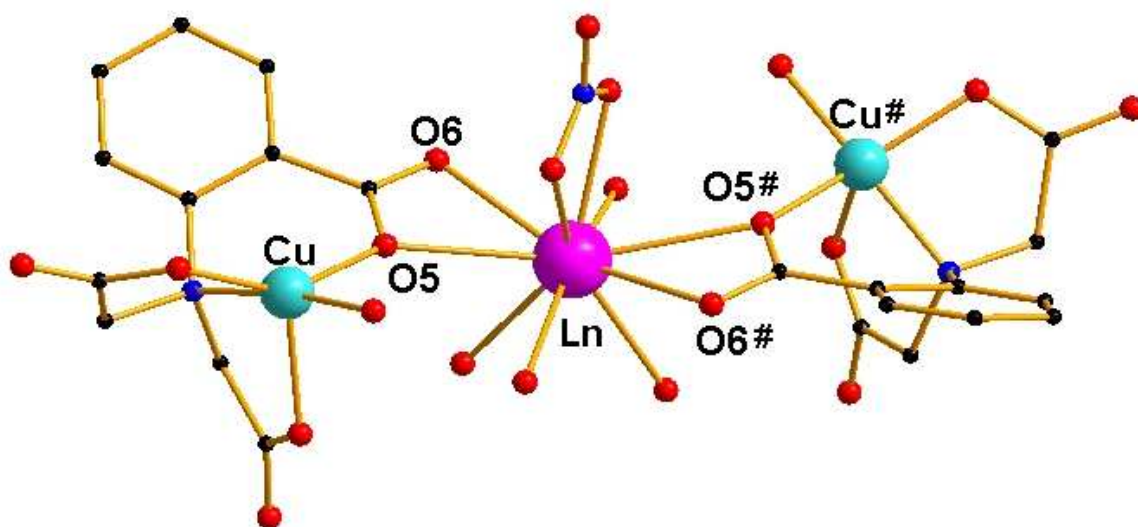


Figure 4.5 the linkage between copper and lanthanide cations

The angle Cu(1)-O(5)-Ln(1) increases from the lower to the higher analogues, as shown in Table 4.4. The angle increases by 4.7° on going from La to Er.

Angle	La	Ce	Pr	Nd	Sm	Eu	Gd	Dy	Ho	Er
Cu(1)-O(5)-Ln(1)	144.3(2)	144.7(9)	145.2(9)	145.5(9)	146.2(9)	146.4(9)	146.9(7)	147.9(2)	148.5(2)	149.0(2)

Table 4.4 Angles of Cu-O(5)-Ln

The 2D-sheets formed by the linkages

The chains of Cu²⁺ ions extend parallel to the *b* axis and coordinate Ln³⁺ ions in the *a* axis direction. The Ln³⁺ ions further coordinate via the ligand to another Cu²⁺ ion along the *a* axis. Each Cu²⁺ ion coordinates two Cu²⁺ ions along the *b* axis and one Ln³⁺ ion along the *a* axis, while each Ln³⁺ ion coordinates two Cu²⁺ ions along the *a* axis. This results in the formation of square windows as shown in Fig. 4.6.

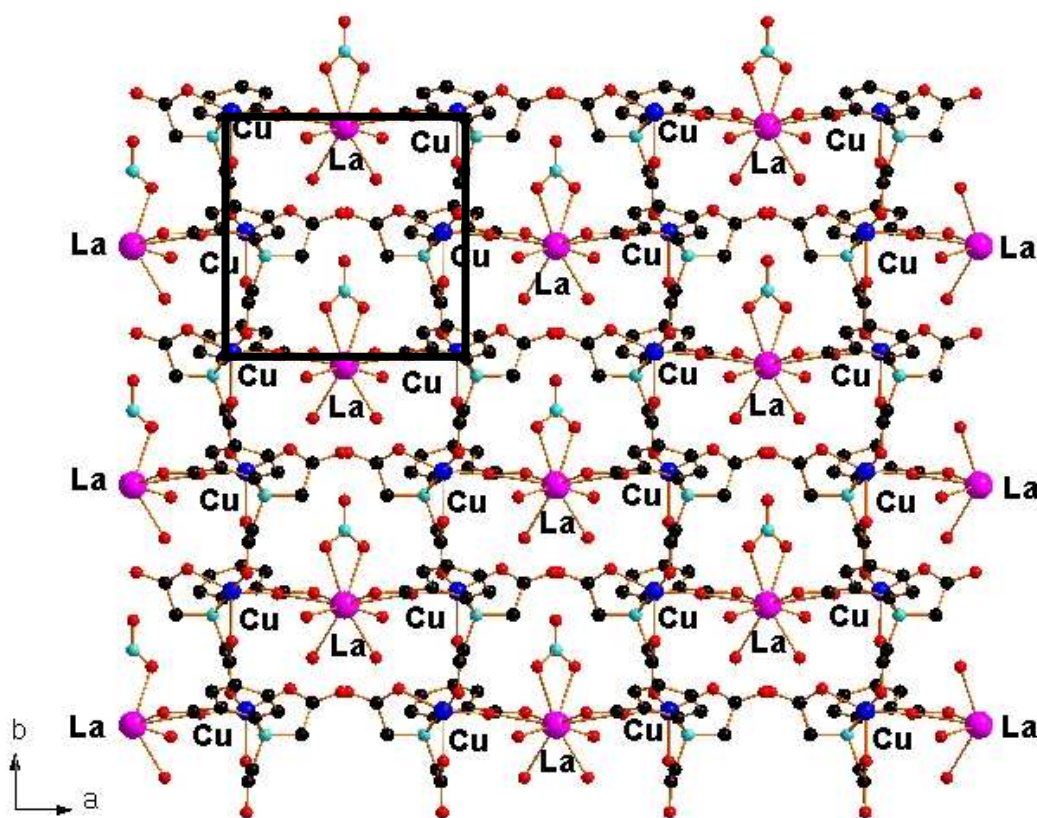


Figure 4.6 The perspective view along *c* axis

Each of these square windows has four Cu²⁺ at the four corners while two Cu²⁺ ions are along the edges of the *b* axis direction and two Ln³⁺ ions along the edges of the *a* axis direction. The four Cu²⁺ ions at the four corners behave as the corner of the next square window along the *b*

axis, thus extending the pattern along this direction. The two Cu^{2+} ions on the two opposite edges of the square window behave as the corner of the next square windows along the a axis, thus extending the pattern along this direction. This results in a network sheet with square windows (Fig. 4.6). The metal distances in the square windows are listed in Table 4.5, with d_1 as $\text{Cu}\cdots\text{Cu}$ distance between two consecutive coppers along the b axis; d_2 as $\text{Cu}\cdots\text{Ln}$ distance between the nearest Cu^{2+} and Ln^{3+} along the a axis; d_3 as $\text{Cu}\cdots\text{Cu}$ distance between two coppers connected by Ln cations.

compound	$d_1(\text{\AA})$	$d_2(\text{\AA})$	$d_3(\text{\AA})$
$\{\text{Cu}_2\text{La}\}_x$, 2	5.1576(4)	4.5266(6)	8.9823(12)
$\{\text{Cu}_2\text{Ce}\}_x$, 3	5.1452(4)	4.5160(5)	8.9607(10)
$\{\text{Cu}_2\text{Pr}\}_x$, 4	5.1371(3)	4.5174(4)	8.9664(2)
$\{\text{Cu}_2\text{Nd}\}_x$, 5	5.1384(3)	4.5058(4)	8.9434(7)
$\{\text{Cu}_2\text{Sm}\}_x$, 6	5.1276(5)	4.5131(5)	8.9585(11)
$\{\text{Cu}_2\text{Eu}\}_x$, 7	5.1258(3)	4.5103(4)	8.9534(8)
$\text{Cu}_2\text{Gd}\}_x$, 8	5.1221(2)	4.5129(3)	8.9591(7)
$\{\text{Cu}_2\text{Dy}\}_x$, 9	5.1248(3)	4.5523(5)	9.0383(10)
$\{\text{Cu}_2\text{Ho}\}_x$, 10	5.1179(4)	4.5503(6)	9.0344(12)
$\{\text{Cu}_2\text{Er}\}_x$, 11	5.1140(3)	4.5641(4)	9.0625(7)

Table 4.5 The metal distances on the 2-D sheet

As seen in Table 4.5, d_1 decreases continuously while d_2 and d_3 decrease at first then increase again from lower to higher members of the lanthanide series. Changing the lanthanide thus has an effect on the $\text{Cu}\cdots\text{Cu}$ distance, and although the effect on the $\text{Cu}\cdots\text{Cu}$ magnetic interaction may be small, we cannot assume that it will remain exactly the same in the compounds with different lanthanides. Access to the Cu_2Y and Cu_2Lu analogues in addition to Cu_2La would have allowed us to quantify any changes in J_{CuCu} across the series, but it was unfortunately not possible to crystallise these complexes.

4.2.4 The packing of the layers

The π - π stacking can be seen clearly from the perspective view along the a axis (Fig. 4.7), and the overlapping of the benzene ring from the neighboring layers can also be clearly seen, which helps the π - π stacking to stabilize this compact structure. Between the hydrophobic benzene rings, two crystal waters are dispersed between the two neighboring layers. These two crystal waters belong to the two layers and form an intra-molecular hydrogen bond to the carboxylic oxygen. The distance between O(31) (crystal water) and O(6) (carboxylic oxygen), 2.995 Å, is characteristic of weak hydrogen bonding. The two O(6) atoms which coordinate to the Ln^{3+} ion in $\{\text{Cu}_2\text{Ln}\}_x$ unit further stabilize two crystal waters.

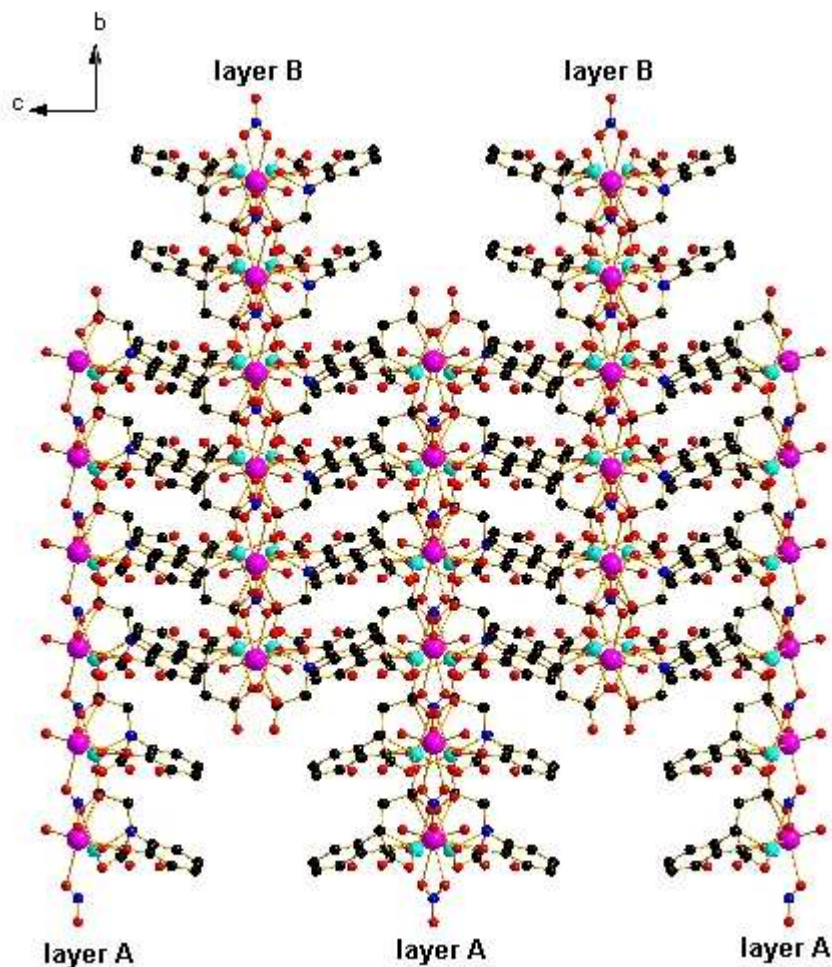


Figure 4.7 the perspective view along a axis

The benzene rings on every layer A tilt towards the $-b$ axis direction while the benzene rings on every layer B tilt towards the $+b$ axis direction. Thus the benzene rings on the neighboring layer A and layer B overlap each other to a much higher extent while maintaining the compact nature of the structure.

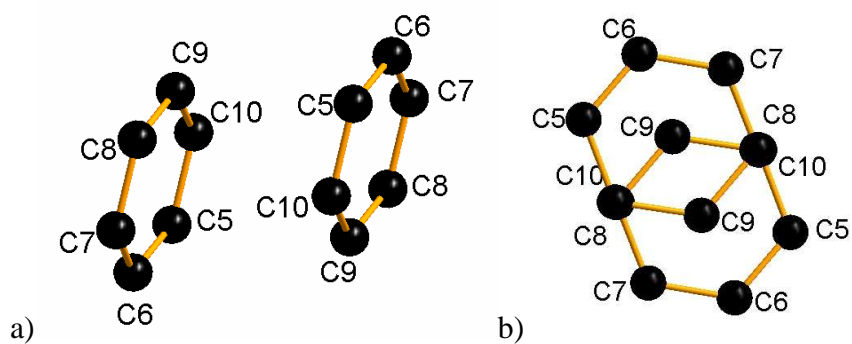


Figure 4.8 a) the two parallel benzene rings on the neighboring layers; b) Projection of the two parallel benzene rings along the axis perpendicular to the benzene plane.

A π - π interaction can be regarded as resulting when the distance between the two benzene rings is between 3.3 Å to 3.7 Å and the corresponding bond strength is 1 to 50 kJ·mol⁻¹[79]. The benzene rings of the neighboring layers in {Cu₂Ln} are parallel and stagger to some extent (Fig. 4.8 a). When the two benzene rings are viewed perpendicular to their molecular planes, it can be seen that the C(9) atom lies nearly at the centre of the other parallel benzene ring while the C(8) and C(10) atoms from different rings almost overlap each other. So the distance between C(8) and C(10) (from the overlapping benzene rings) can be considered more or less as the distance between two parallel benzenes. Taking {Cu₂La} as an example, the C(8)···C(10) distance is 3.35 Å which lies within the expected range of 3.3 Å to 3.7 Å and means there is a strong π - π interaction between the benzene rings.

4.3 The magnetic properties of [Cu₂(cpida)₂Ln(NO₃)(H₂O)₄]·H₂O

In order to check for the presence of ferromagnetic impurities in compounds, the magnetization as a function of the field at 100 K was performed. For paramagnetic or diamagnetic systems, a perfect straight line is expected. No presence of ferromagnetic impurities is seen in the field dependence of the magnetization for all cases of the {Cu₂Ln}_x series at 100 K (see Fig. 4.9).

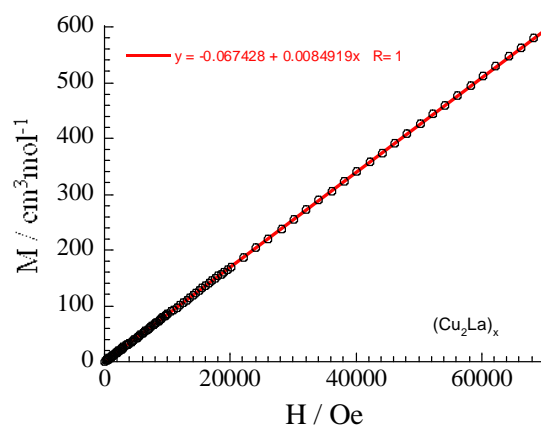


Figure 4.9 The magnetization as a function of the field at 100 K for {Cu₂La}_x

The susceptibility, which is the slope of the straight line ({Cu₂La}_x is taken as an example (Fig. 4.9)). At 100 K the values are 0.0085, 0.0161, 0.0198, 0.0206, 0.0096, 0.015, 0.0899, 0.1338, 0.1276 and 0.1106 cm³ mol⁻¹ for {Cu₂La}_x, {Cu₂Ce}_x, {Cu₂Pr}_x, {Cu₂Nd}_x, {Cu₂Sm}_x, {Cu₂Eu}_x, {Cu₂Gd}_x, {Cu₂Dy}_x, {Cu₂Ho}_x and {Cu₂Er}_x respectively. They are in good agreement with the susceptibility measurements done at 1000 Oe and 1 T (see below).

4.3.1 The $\chi_m T$ product versus temperature

Ln(III) ion with f^0 , La^{3+} , 2 and f^7 , Gd^{3+} , 8 in $\{\text{Cu}_2\text{Ln}\}_x$

$\{\text{Cu}_2\text{La}\}_x$ --- At room temperature, the χT product is $0.86 \text{ cm}^3 \text{ K mol}^{-1}$. This value is in good agreement with the expected value for two octahedral Cu(II) metal ions ($S = 1/2$, $g = 2.14$: $C = 0.43 \text{ cm}^3 \text{ K mol}^{-1}$ of Cu(II)). Decreasing the temperature, the χT product is almost temperature independent till around 15 K, and then rapidly decreases to reach $0.68 \text{ cm}^3 \text{ K mol}^{-1}$ at 1.8 K indicating dominant antiferromagnetic interactions within the Cu(II) spin carriers.

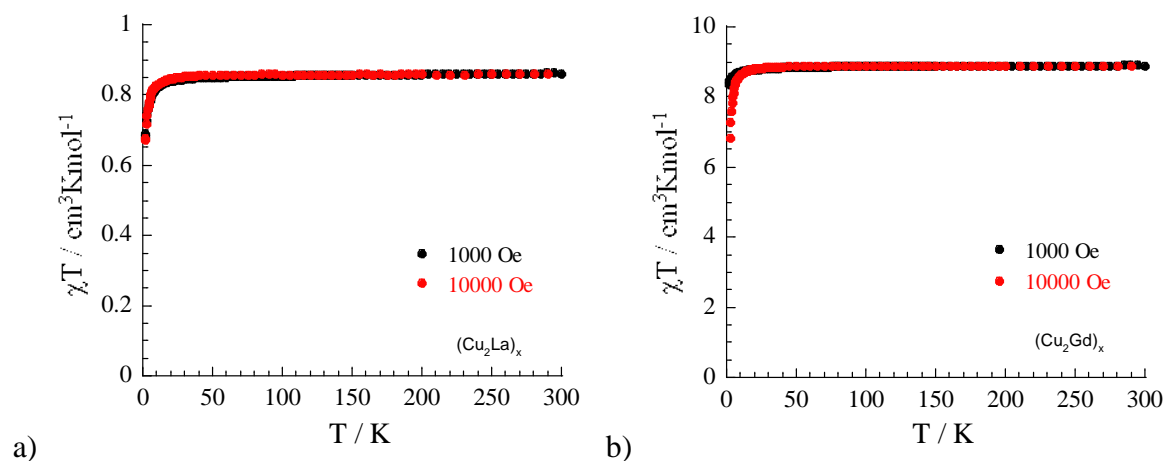


Figure 4.10 Temperature dependence of the χT product at 0.1 and 1T: a) for $\{\text{Cu}_2\text{La}\}_x$, **2**; b) for $\{\text{Cu}_2\text{Gd}\}_x$, **8**

$\{\text{Cu}_2\text{Gd}\}_x$ --- At room temperature, the χT product is $8.92 \text{ cm}^3 \text{ K mol}^{-1}$. This value is in good agreement with the expected value ($8.74 \text{ cm}^3 \text{ K mol}^{-1}$) for the presence of two octahedral Cu(II) metal ions ($S = 1/2$, taking $g = 2.14$ observed for $\{\text{Cu}_2\text{La}\}_x$: $C = 0.43 \text{ cm}^3 \text{ K mol}^{-1}$ of Cu(II)) and one Gd(III) ion ($S = 7/2$, $C = 7.875 \text{ cm}^3 \text{ K mol}^{-1}$ expected for $g = 2.0$ ^[54]). On decreasing the temperature, the χT product stays constant until 12 K and then slightly decreases to reach $8.45 \text{ cm}^3 \text{ K mol}^{-1}$ (at 1000 Oe) at 1.8 K. As the Gd(III) ion has an $^8\text{S}_{7/2}$ ground term, it has no orbital contribution and therefore can be considered as an isotropic $S = 7/2$ spin. Therefore the decrease of χT product at low temperature indicates dominant antiferromagnetic interactions. Fitting the experimental data to a Curie-Weiss law above 1.8 K leads to the following Curie and Weiss constants: $8.84 \text{ cm}^3 \text{ K mol}^{-1}$ and -0.11 K , respectively as shown in Fig. 4.11.

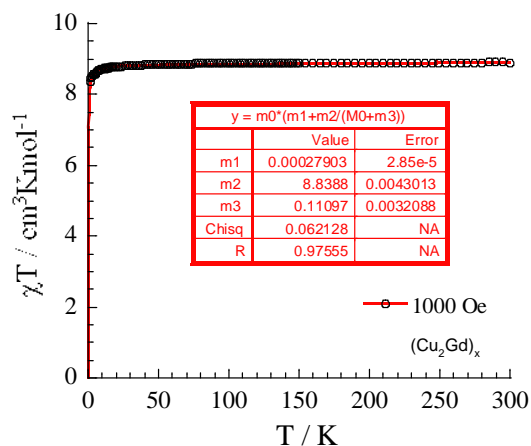


Figure. 4.11 Curie-Weiss fit of $\{\text{Cu}_2\text{Gd}\}_x$, **8**

As expected the Curie constant is close to the value of $8.63 \text{ cm}^3 \text{ K mol}^{-1}$ required for two Cu(II) metal ions and one Gd(III) ion. The negative Weiss constant suggests the presence of very small interactions between spin carriers with a dominating antiferromagnetic contribution. Considering that the Cu(II)-Gd(III) interactions are almost always of ferromagnetic nature^[54], the antiferromagnetic Cu(II)-Cu(II) interaction should be discussed, i.e. whether it is through the *syn-anti eq-axial* carboxylate bridges (evaluated at about -0.36 K in the $\{\text{Cu}_2\text{La}\}_x$ analogue) and dominates the magnetic behavior of this compound.

Ln(III) ions with $0 < f^n < 7$ in $\{\text{Cu}_2\text{Ln}\}_x$ (Ln = Ce, 3, Pr, 4, Nd, 5, Sm, 6, Eu, 7)

$\{\text{Cu}_2\text{Ce}\}_x$ --- At room temperature, the χT product is $1.74 \text{ cm}^3 \text{ K mol}^{-1}$. This value is in good agreement with the expected value ($1.66 \text{ cm}^3 \text{ K mol}^{-1}$) for the presence of two octahedral Cu(II) metal ions ($S = 1/2$, taking $g = 2.14$ observed for Cu_2La : $C = 0.43 \text{ cm}^3 \text{ K mol}^{-1}$ of Cu(II)) and one Ce(III) ion ($S = 1/2$, $L = 2$, $^2F_{5/2}$: $C = 0.80 \text{ cm}^3 \text{ K mol}^{-1}$ [54]). The profile of the χT vs T plot does not allow for the determination of the Cu(II)-Ce(III) magnetic interactions. Indeed the Stark sublevels (of the $^2F_{5/2}$ ground state or low-lying first excited states) of the Ce(III) ions are thermally depopulated when the temperature is lowered resulting in a decrease of the χT vs T plot^[80]. Therefore even if the χT product decreases with the temperature and reaches $0.93 \text{ cm}^3 \text{ K mol}^{-1}$ at 1.8 K it is not possible to be sure that this behavior is associated with dominant antiferromagnetic interactions within the complex.

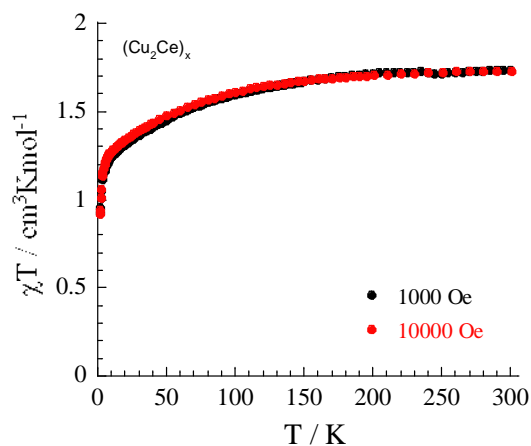


Figure 4.12 Temperature dependence of the χT product per $\{\text{Cu}_2\text{Ce}\}_x$, **3** at 0.1 and 1T

$\{\text{Cu}_2\text{Pr}\}_x$ --- At room temperature, the χT product is $2.21 \text{ cm}^3 \text{ K mol}^{-1}$. This value is in good agreement with the expected value ($2.46 \text{ cm}^3 \text{ K mol}^{-1}$) for the presence of two octahedral Cu(II) metal ions ($S = 1/2$, taking $g = 2.14$ observed for Cu_2La : $C = 0.43 \text{ cm}^3 \text{ K mol}^{-1}$ of Cu(II)) and one Pr(III) ion ($S = 1$, $L = 3$, $^3\text{H}_4$: $C = 1.60 \text{ cm}^3 \text{ K mol}^{-1}$ expected for $g = 4/5$ [54]). As in the Ce(III) compound, the profile of the χT vs T plot does not allow for the determination of the Cu(II)-Pr(III) magnetic interactions. The Stark sublevels (of the $^3\text{H}_4$ ground state or low-lying first excited states) of the Pr(III) ions are thermally depopulated when the temperature is lowered resulting in a decrease of the χT vs T plot^[80]. Therefore even if the χT product decreases with the temperature and reaches $0.69 \text{ cm}^3 \text{ K mol}^{-1}$ at 1.8 K it is not possible to be sure that this thermal behavior is associated with dominant antiferromagnetic interactions within the complex.

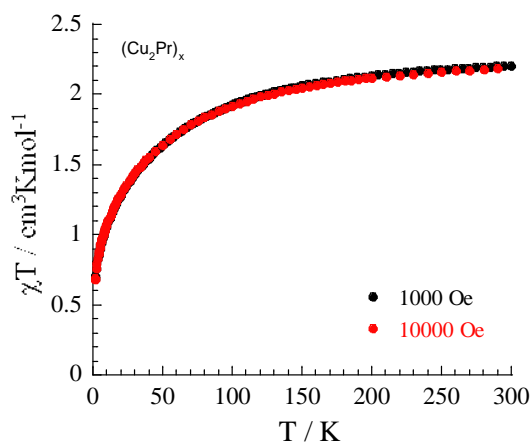


Figure 4.13 Temperature dependence of the χT product per $\{\text{Cu}_2\text{Pr}\}_x$, **4** at 0.1 and 1T

$\{\text{Cu}_2\text{Nd}\}_x$ --- At room temperature, the χT product is $2.28 \text{ cm}^3 \text{ K mol}^{-1}$. This value is in good agreement with the expected value ($2.50 \text{ cm}^3 \text{ K mol}^{-1}$) for the presence of two octahedral

Cu(II) metal ions ($S = 1/2$, taking $g = 2.14$ observed for Cu_2La : $C = 0.43 \text{ cm}^3 \text{ K mol}^{-1}$ of Cu(II)) and one Nd(III) ion ($S = 3/2$, $L = 3$, ${}^4\text{I}_{9/2}$, $C = 1.64 \text{ cm}^3 \text{ K mol}^{-1}$ expected for $g = 8/11$ [54]). On decreasing the temperature, the χT product continuously decreases to reach $1.10 \text{ cm}^3 \text{ K mol}^{-1}$ at 1.8 K. As in the Ce(III) and Pr(III) compounds, the profile of the χT vs T plot does not allow for the determination of the Cu(II)-Nd(III) magnetic interactions. As explained before, the Stark sublevels (of the ${}^4\text{I}_{9/2}$ ground state or low-lying first excited states) of the Nd(III) ions are thermally depopulated when the temperature is lowered resulting in a decrease of the χT vs T plot [80]. Therefore even if the χT product decreases with the temperature, it is not possible to be sure that this behavior is associated with dominant antiferromagnetic interactions within the complex.

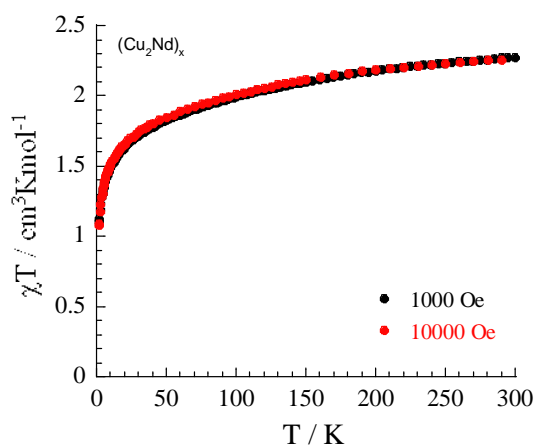


Figure 4.14 Temperature dependence of the χT product per $\{\text{Cu}_2\text{Nd}\}_x$, **5** at 0.1 and 1T

$\{\text{Cu}_2\text{Sm}\}_x$ --- At room temperature, the χT product is $1.04 \text{ cm}^3 \text{ K mol}^{-1}$. This value is in good agreement with the expected value ($0.95 \text{ cm}^3 \text{ K mol}^{-1}$) for the presence of two octahedral Cu(II) metal ions ($S = 1/2$, taking $g = 2.14$ observed for Cu_2La : $C = 0.43 \text{ cm}^3 \text{ K mol}^{-1}$ of Cu(II)) and one Sm(III) ion ($S = 5/2$, $L = 0$, ${}^5\text{H}_{5/2}$, $C = 0.09 \text{ cm}^3 \text{ K mol}^{-1}$ expected for $g = 2/7$ [54]). On decreasing the temperature, the χT product steadily decreases to reach $0.86 \text{ cm}^3 \text{ K mol}^{-1}$ at 15 K and then rapidly drops down to $0.62 \text{ cm}^3 \text{ K mol}^{-1}$ at 1.8 K. As in the Ce(III), Pr(III) and Nd(III) compounds, the profile of the χT vs T plot does not allow for the determination of the Cu(II)-Sm(III) magnetic interactions. As explained before, the Stark sublevels (of the ${}^5\text{H}_{5/2}$ ground state or low-lying first excited states) of the Sm(III) ions are thermally depopulated when the temperature is lowered resulting in a decrease of the χT vs T plot [80]. Therefore even if the χT product decreases with the temperature, it is not possible to be sure that this behavior is associated with dominant antiferromagnetic interactions within the complex.

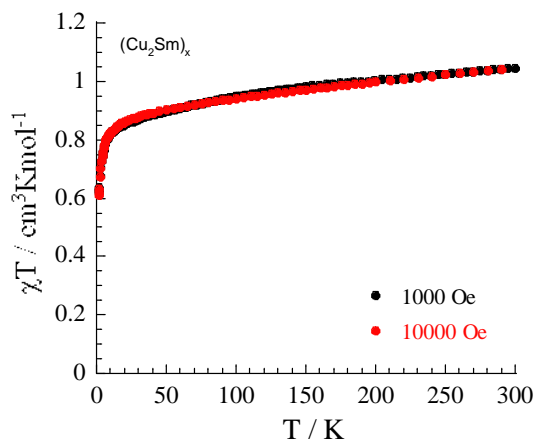


Figure 4.15 Temperature dependence of the χT product per $\{\text{Cu}_2\text{Sm}\}_x$, **6** at 0.1 and 1T

$\{\text{Cu}_2\text{Eu}\}_x$ --- At room temperature, the χT product is $2.21 \text{ cm}^3 \text{ K mol}^{-1}$. This value is higher than the expected value ($0.86 \text{ cm}^3 \text{ K mol}^{-1}$) for the presence of two octahedral Cu(II) metal ions ($S = 1/2$, $g = 2.14$: $C = 0.43 \text{ cm}^3 \text{ K mol}^{-1}$ of Cu(II)) and one diamagnetic Eu(III) ion ($S = 0$, ${}^7\text{F}_0$, [54, 80]). On decreasing the temperature, the χT product continuously decreases to reach $0.63 \text{ cm}^3 \text{ K mol}^{-1}$ at 1.8 K indicating dominant antiferromagnetic interactions within the spin carrier.

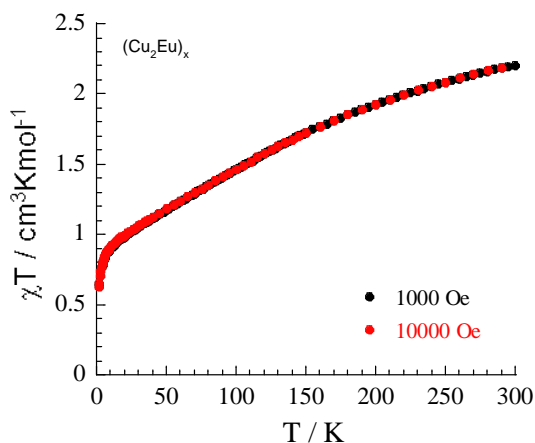


Figure 4.16 Temperature dependence of the χT product per $\{\text{Cu}_2\text{Eu}\}_x$, **7** at 0.1 and 1T

Ln(III) ions with $f^n > 7$ in $\{\text{Cu}_2\text{Ln}\}_x$ (Ln = Dy, **9**, Ho, **10**, Er, **11**)

$\{\text{Cu}_2\text{Dy}\}_x$ --- At room temperature, the χT product is $13.5 \text{ cm}^3 \text{ K mol}^{-1}$. This value is slightly lower than the expected value ($15.03 \text{ cm}^3 \text{ K mol}^{-1}$) for the presence of two octahedral Cu(II) metal ions ($S = 1/2$, taking $g = 2.14$ observed for Cu_2La : $C = 0.43 \text{ cm}^3 \text{ K mol}^{-1}$ of Cu(II)) and one Dy(III) ion ($S = 5/2$, $L = 5$, ${}^6\text{H}_{15/2}$, $C = 14.17 \text{ cm}^3 \text{ K mol}^{-1}$ expected for $g = 4/3$ [54]). As in

the other Ln(III) compounds, the profile of the χT vs T plot does not allow for the determination of the Cu(II)-Dy(III) magnetic interactions. The Stark sublevels (of the ${}^6\text{H}_{15/2}$ ground state or low-lying first excited states) of the Dy(III) ions are thermally depopulated when the temperature is lowered resulting in a decrease of the χT vs T plot^[80, 81]. Therefore even if the χT product decreases with the temperature and reaches $9.20 \text{ cm}^3 \text{ K mol}^{-1}$ at 1.8 K it is not possible to be sure that this thermal behavior is associated with dominant antiferromagnetic interactions within the complex.

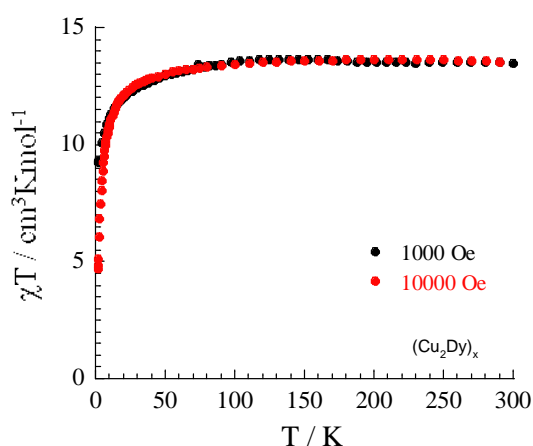


Figure 4.17 Temperature dependence of the χT product per $\{\text{Cu}_2\text{Dy}\}_x$, **9** at 0.1 and 1T

$\{\text{Cu}_2\text{Ho}\}_x$ --- At room temperature, the χT product is $13.4 \text{ cm}^3 \text{ K mol}^{-1}$. This value is slightly lower than the expected value ($14.93 \text{ cm}^3 \text{ K mol}^{-1}$) for the presence of two octahedral Cu(II) metal ions ($S = 1/2$, taking $g = 2.14$ observed for Cu_2La : $C = 0.43 \text{ cm}^3 \text{ K mol}^{-1}$ of Cu(II)) and one Ho(III) ion ($S = 2$, $L = 6$, ${}^5\text{I}_8$: $C = 14.07 \text{ cm}^3 \text{ K mol}^{-1}$ expected for $g = 5/4$ ^[54]). As in the other Ln(III) compounds, the profile of the χT vs T plot does not allow for the determination of the Cu(II)-Ho(III) magnetic interactions. The Stark sublevels (of the ${}^5\text{I}_8$ ground state or low-lying first excited states) of the Ho(III) ions are thermally depopulated when the temperature is lowered resulting in a decrease of the χT vs T plot^[81]. Therefore even if the χT product decreases with the temperature and reaches $4.93 \text{ cm}^3 \text{ K mol}^{-1}$ at 1.8 K it is not possible to be sure that this thermal behavior is associated with dominant antiferromagnetic interactions within the complex.

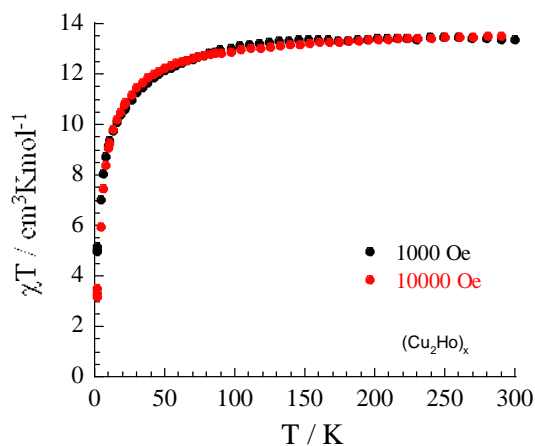


Figure 4.18 Temperature dependence of the χT product per $\{\text{Cu}_2\text{Ho}\}_x$, **10** at 0.1 and 1T

$\{\text{Cu}_2\text{Er}\}_x$ --- At room temperature, the χT product is $11.4 \text{ cm}^3 \text{ K mol}^{-1}$. This value is slightly lower than the expected value ($12.36 \text{ cm}^3 \text{ K mol}^{-1}$) for the presence of two octahedral Cu(II) metal ions ($S = 1/2$, taking $g = 2.14$ observed for Cu_2La : $C = 0.43 \text{ cm}^3 \text{ K mol}^{-1}$ of Cu(II)) and one Er(III) ion ($S = 3/2$, $L = 6$, ${}^4\text{I}_{15/2}$, $C = 11.5 \text{ cm}^3 \text{ K mol}^{-1}$ expected for $g = 6/5$ [54]). As in the other Ln(III) compounds, the profile of the χT vs T plot does not allow for the determination of the Cu(II)-Ho(III) magnetic interactions. The Stark sublevels (of the ${}^4\text{I}_{15/2}$ ground state or low-lying first excited states) of the Er(III) ions are thermally depopulated when the temperature is lowered resulting in a decrease of the χT vs T plot^[80]. Therefore even if the χT product decreases with the temperature and reaches $7.22 \text{ cm}^3 \text{ K mol}^{-1}$ at 1.8 K it is not possible to be sure that this thermal behavior is associated with dominant antiferromagnetic interactions within the complex.

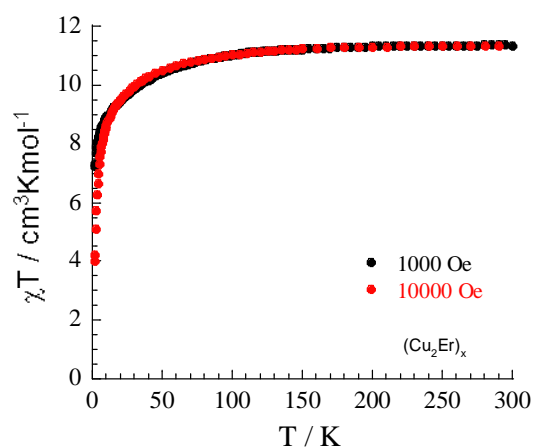


Figure 4.19 Temperature dependence of the χT product per $\{\text{Cu}_2\text{Er}\}_x$, **11** at 0.1 and 1T

4.3.2 Field dependence of magnetization

Diamagnetic Ln(III) ion (Ln = La, 2)

For the compound $\{\text{Cu}_2\text{La}\}_x$, the field dependence of magnetization at low temperatures reveals a true saturation above 7 T indicative of weak or absence of magnetic anisotropy. This result has been confirmed by the M versus H/T plots as the data are roughly all superposed on a single master-curve as expected for isotropic system. The saturation of M at $2.1 \mu_B$ is very close to the value of $2.0 \mu_B$ expected for two Cu(II) ions ($S = 1/2$) for $\{\text{Cu}_2\text{La}\}_x$ if the spins are uncoupled, decoupled or ferromagnetically coupled. As suggested before by the presence of weak Cu(II)-Cu(II) antiferromagnetic interactions in these compounds, we are clearly in the situation where these interactions are overcome by the applied magnetic field.

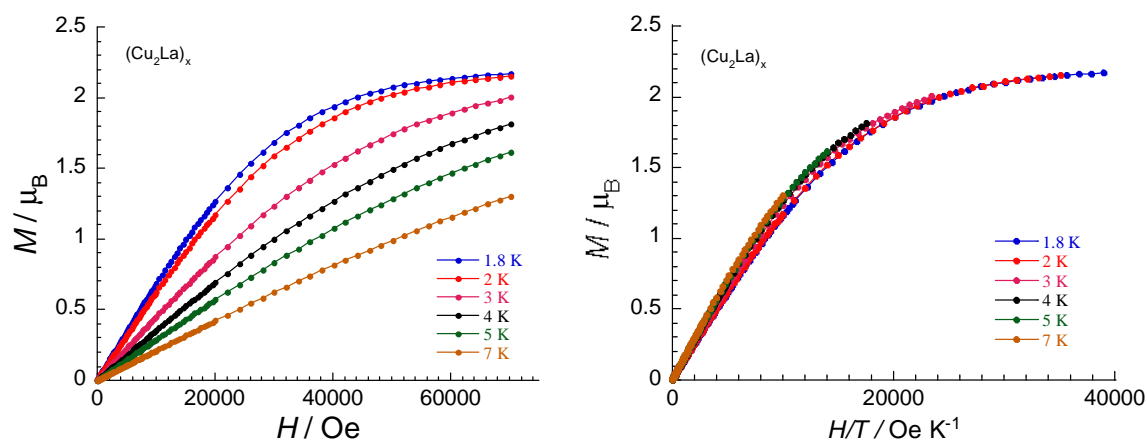


Figure 4.20 The field dependence of magnetization for $\{\text{Cu}_2\text{La}\}_x$, 2

Isotropic Ln(III) ion (Ln = Gd, 8)

For the compound $(\text{Cu}_2\text{Gd})_x$, the field dependence of magnetization at low temperatures reveals a true saturation above 7 T and 6 T indicative of weak or absence of magnetic anisotropy. This result has been confirmed by the M vs H/T plots as the data are roughly all superposed on a single master-curve as expected for isotropic systems. This is, indeed, not surprising considering that the Gd(III) and the Cu(II) ions are very weakly anisotropic metal ions. The saturation of M at $9.2 \mu_B$ is very close to the value of $9.0 \mu_B$ expected for two Cu(II) ions ($S = 1/2$) and one Gd(III) ion ($S = 7/2$) for $(\text{Cu}_2\text{Gd})_x$ if the spins are uncoupled, decoupled or ferromagnetically coupled. As suggested before by the presence of weak Cu(II)-Ln(III) and

Cu(II)-Cu(II) antiferromagnetic interaction in these compounds, we are clearly in the situation where these interactions are overcome by the applied magnetic field.

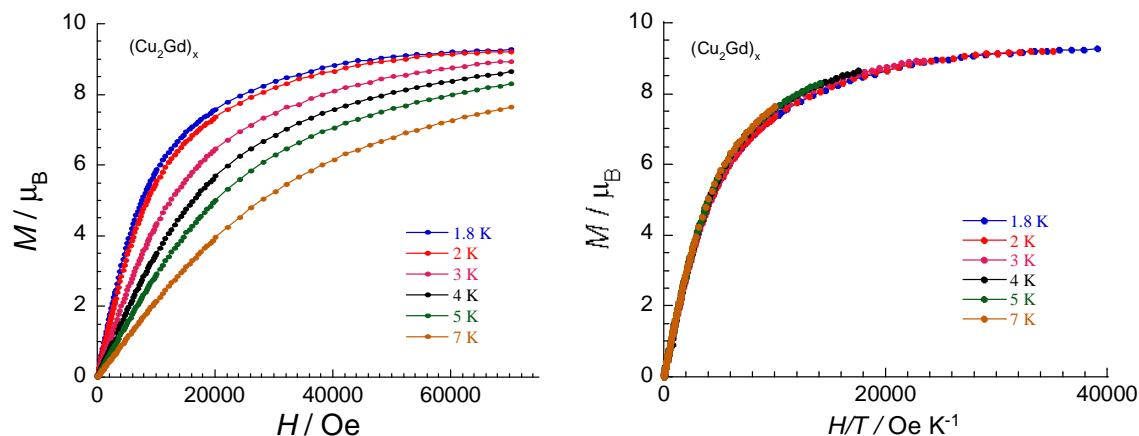


Figure 4.21 the field dependence of magnetization for $\{\text{Cu}_2\text{Gd}\}_x$, **8**

Anisotropic Ln(III) ion (Ln = Ce, **3**, Pr, **4**, Nd, **5**, Sm, **6**, Eu, **7**, Dy, **9**, Ho, **10**, Er, **11**)

For compounds $(\text{Cu}_2\text{Ce})_x$, $(\text{Cu}_2\text{Pr})_x$, $(\text{Cu}_2\text{Nd})_x$, $(\text{Cu}_2\text{Sm})_x$, $(\text{Cu}_2\text{Eu})_x$, $(\text{Cu}_2\text{Dy})_x$, $(\text{Cu}_2\text{Ho})_x$ and $(\text{Cu}_2\text{Er})_x$, the field dependence of the magnetization at low temperatures shows that the magnetization smoothly increases with the applied dc field without saturation even at 7 T at which it reaches the values of 3.3, 2.4, 3.5, 2.2, 2.3, 7.9, 7.3 and 6.6 μ_B for compound **3**, **4**, **5**, **6**, **7**, **9**, **10**, **11**, respectively (take Cu_2Dy as example in Fig. 4.25). This behavior indicates the lack of any well-defined ground state and thus suggests the presence of low-lying excited states that might be populated when a field is applied. This hypothesis is in good agreement with the expected weak Cu(II)-Ln(III) and Cu(II)-Cu(II) interactions. Moreover, while plotting the M vs H/T at different fields (see Fig. 4.22), the curves are not all superposed on a single master-curve as expected for isotropic system further indicating the presence of magnetic anisotropy or low lying excited states.

In agreement with the M vs H data at 1.8 K that do not show any sign of slow relaxation i.e. hysteresis effect, the ac susceptibility of all compounds in zero dc field shows a complete absence of out-of-phase component above 1.8 K.

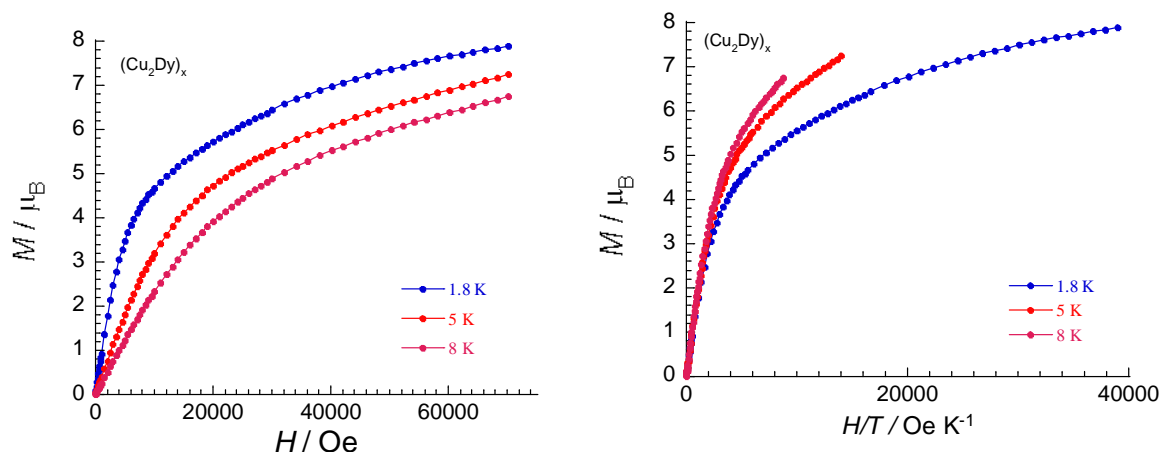


Figure 4.22 the field dependence of magnetization for $\{\text{Cu}_2\text{Dy}\}_x$

4.3.3 The least-squares non-linear fitting of the magnetic properties of $\{\text{Cu}_2\text{La}\}_x$ and $\{\text{Cu}_2\text{Gd}\}_x$

The fitting of $\{\text{Cu}_2\text{La}\}_x$, 2

Based on the structure, because of the diamagnetic La(III) ion in the complex center, the trinuclear unit can be magnetically viewed as dimer of $S = 1/2$ Cu(II) with interactions mediated by the diamagnetic La(III) ion or most likely by *syn-anti* carboxylate bridge. Therefore application of the van Vleck equation^[82] to Kambe's vector coupling scheme^[83] allows us to determine an analytical expression of the magnetic susceptibility from the following spin Hamiltonian:

$$H = -2J \{S_{\text{Cu}1} \bullet S_{\text{Cu}2}\} \quad \text{Eq. (4.1)}$$

where S_i and S_j are the spin operators [$S = 1/2$ for Cu(1) and Cu(2)], J_1 is the exchange coupling between the two Cu(II) centers. The best set of parameters obtained using this model (see Fig. 4.23a) is $J_1/k_B = -0.7(1)$ K, and $g = 2.14(1)$. The interaction parameter, J_1 , is in good agreement with what is expected for *syn-anti eq-axial* carboxylate bridges^[84].

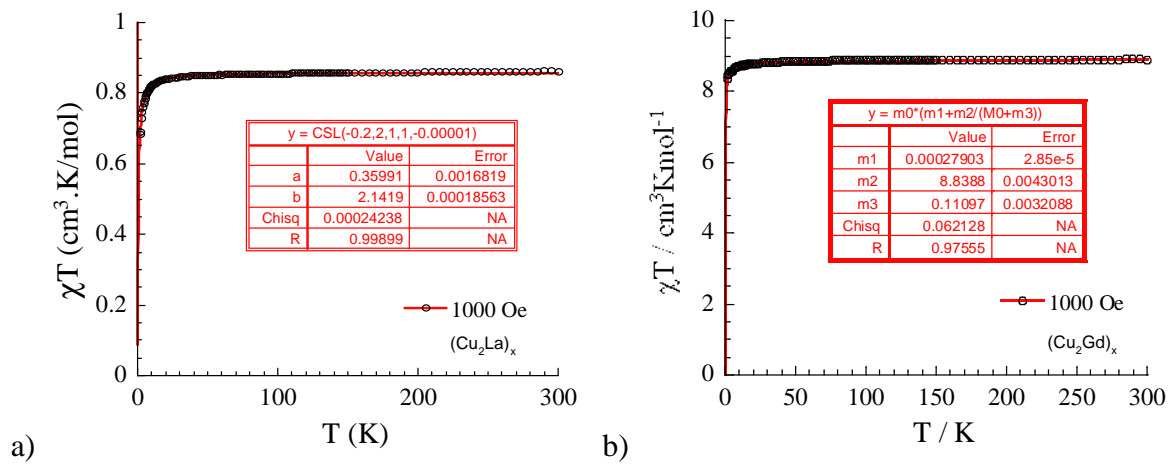


Figure 4.23 The simulation of χT product versus temperature: a) for Cu_2La ; b) for Cu_2Gd

The fitting of $\{\text{Cu}_2\text{Gd}\}_x$, 8

Considering only the Cu(II)-Ln(III) interactions leads to a trinuclear Cu-Gd-Cu model. The magnetic behaviour can be analyzed by using a simple isotropic Heisenberg Hamiltonian:

$$\mathbf{H} = -J_2 \mathbf{S}_{\text{Gd}} (\mathbf{S}_{\text{Cu1}} + \mathbf{S}_{\text{Cu2}}) \quad \text{Eq. (4.2)}$$

where \mathbf{S}_i the spin operators ($S = 1/2$ for the Cu^{II} ions and $S = 7/2$ for Gd^{III}) and J the magnetic interaction between Cu and Gd metal ions. The application of the van Vleck equation^[82] to Kambe's vector coupling scheme^[83] allows to determine the analytical expression of the magnetic susceptibility in the low field approximation:

$$\chi T = \frac{Ng^2\mu_B^2}{2k_B} \frac{(35 + 84(\exp(9J/k_B T) + \exp(7J/k_B T)) + 165\exp(16J/k_B T))}{(6 + 8(\exp(9J/k_B T) + \exp(7J/k_B T)) + 10\exp(16J/k_B T))} \quad \text{Eq. (4.3)}$$

The experimental data are well fitted to this Heisenberg model (see Fig. 4.23b) with $g = 2.02(1)$ and $J_2/k_B = -0.06$ K. $|J_2/k_B|$ should be lower than the calculated value 0.06 K as will be discussed as below.

The magnetic properties of compounds are highly structure related. The structure described as in 4.3.3 shows that along b axis there are only Cu atoms coordinated by syn-anti carboxylic groups forming copper chains. Thus along b axis there is only Cu-Cu magnetic interactions (Fig. 4.25) by super-exchange pathway of Cu-O-C-O-Cu, with Cu...Cu separation around 5.1 Å, which indicates that the magnetic interaction along the b axis is weakly antiferromagnetic.

Along the a axis there are no other connections but Cu^{2+} and Ln^{3+} , with the $\text{Cu}\cdots\text{Ln}$ separation around 4.5 Å. The magnetic interactions along the a axis can be considered as a separated $\{\text{Cu}_2\text{Ln}\}$ unit with Ln^{3+} inbetween (Fig. 4.23). Since the two copper atoms are in a C_2 symmetry about Ln^{3+} , the interactions between Ln^{3+} and the two Cu^{2+} are the same and can be considered as one Cu-Ln interaction.

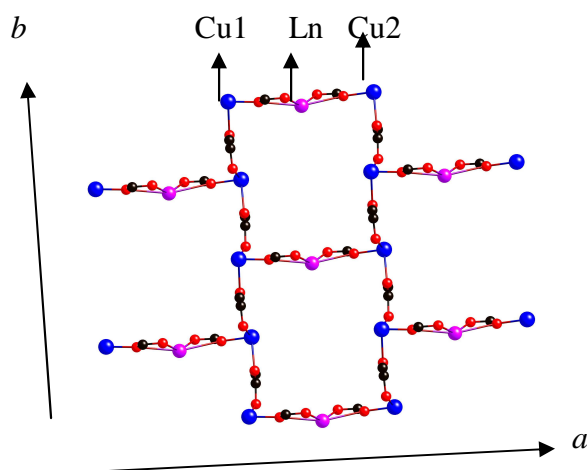


Figure 4.24 The arrangement of metal interactions

Since $|J_2/k_B|$ is lower than 0.06K, it could be considered that there is no magnetic interaction between Gd^{3+} and Cu^{2+} pairs, or another hypothesis is that a ferromagnetic interaction counteracts the antiferromagnetic interaction.

In the other Cu_2Ln compounds, it is not possible to determine the magnitude of the $\text{Cu}\cdots\text{Ln}$ interaction, as the effects of the splitting of the Stark sub-levels are difficult to quantify. In some systems it is possible to replace the Cu^{2+} with a diamagnetic metal ion without changing the geometry around the lanthanide cation, and so to establish the contribution of this sub-level splitting to the overall magnetic behavior.

In the complexes $[\text{Cu}_2(\text{cpida})_2\text{Ln}(\text{NO}_3)(\text{H}_2\text{O})]\cdot 2\text{H}_2\text{O}$, the Cu^{2+} is five coordinated and the corresponding Ni compound $[\text{Ni}_2(\text{cpida})_2\text{Ln}(\text{NO}_3)(\text{H}_2\text{O})]\cdot 2\text{H}_2\text{O}$ and Zn compound $[\text{Zn}_2(\text{cpida})_2\text{Ln}(\text{NO}_3)(\text{H}_2\text{O})]\cdot 2\text{H}_2\text{O}$ with the same structure is not possible to synthesize because the instability of 5-coordinated Ni^{2+} and Zn^{2+} compared with 4-coordinated and 6-coordinated Ni^{2+} and Zn^{2+} . Thus the synthesis of Ni-substituted and Zn-substituted compounds was not possible.

4.4 Summary

2D sheets of $[\text{Cu}_2(\text{cpida})_2\text{Ln}(\text{NO}_3)(\text{H}_2\text{O})_4]\cdot 2\text{H}_2\text{O}$ extend along the b axis with copper-copper connections by syn-anti carboxylic bridges while along the a axis with copper-lanthanide connection by oxygen Cu-O-Ln and syn-anti carboxylic bridges. Along the c axis the layers of the sheets stack in a compact way by π - π stacking.

Due to the lanthanide contraction, the Ln-O bond lengths in the $\{\text{Cu}_2\text{Ln}\}_x$ complexes decrease as the atomic number of the lanthanides increases, as expected. However, the Cu \cdots Cu distance between the carboxylate-bridged Cu^{2+} centres also decreases significantly on going across the lanthanide series from left to right.

By least-squares nonlinear fitting, weak antiferromagnetic interactions between Cu^{2+} and Cu^{2+} along the b axis were found to occur in the $\{\text{Cu}_2\text{La}\}_x$ compound. There is no significant magnetic interaction, or there is a counteraction of antiferromagnetic and ferromagnetic interactions, between Gd^{3+} and Cu^{2+} in the $\{\text{Cu}_2\text{Gd}\}_x$ compound.

Chapter 5 Structure and magnetic properties of transition metal clusters with imino-carboxylic ligands

5.1 $[\text{Fe}_8(\mu_3\text{-O})_4(\mu_2\text{-OMe})_4(\text{Hcpidp})_4(\text{H}_2\text{O})_4](\text{NO}_3)_4 \cdot 10\text{H}_2\text{O} \cdot 4\text{MeOH}$, 12

5.1.1 Structure of $[\text{Fe}_8(\mu_3\text{-O})_4(\mu_2\text{-OMe})_4(\text{Hcpidp})_4(\text{H}_2\text{O})_4](\text{NO}_3)_4 \cdot 10\text{H}_2\text{O} \cdot 4\text{MeOH}$

5.1.1.1 Overview of the Fe_8 structure

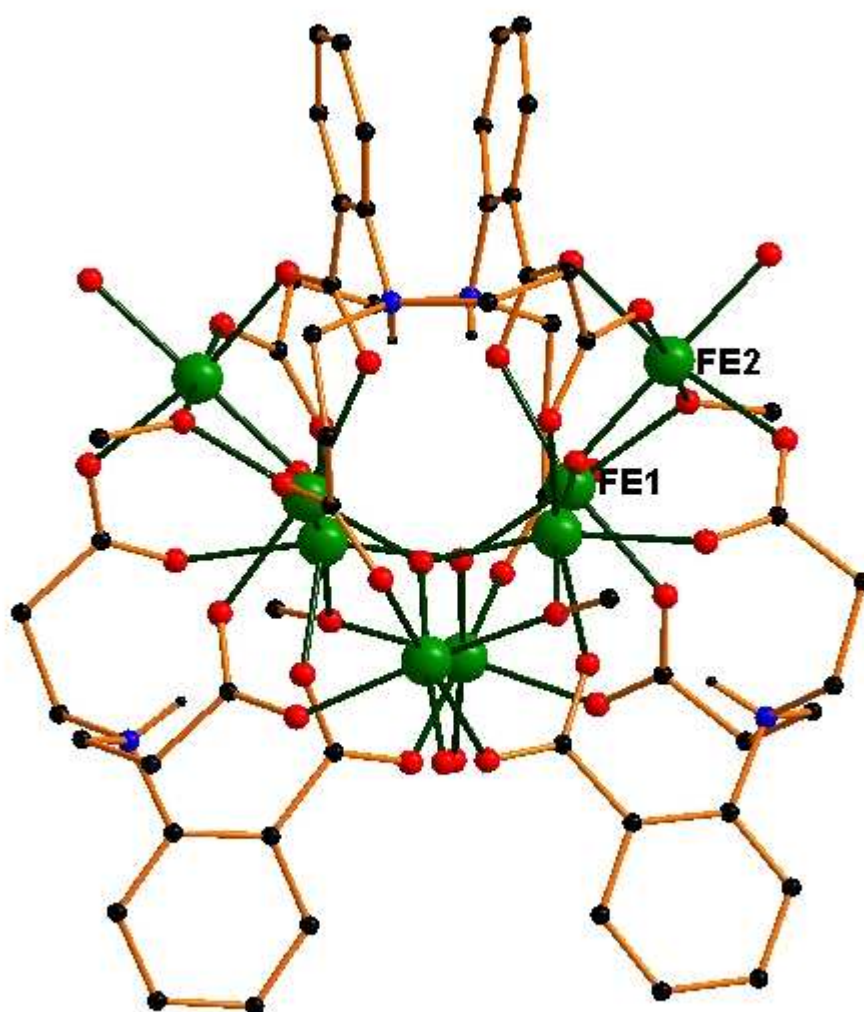


Figure 5.1 Structure of the complex 12

The complex crystallizes in the tetragonal space group $I\bar{4}c2$ and the structure of the Fe_8 complex is shown in Fig.5.1. The complex possesses an imposed S_4 symmetry and therefore has two unique Fe^{III} ions in the asymmetric unit.

5.1.1.2 The coordination mode of the ligand cpidp³⁻

The coordination mode of the ligand with two long propionate acid arms will first be described. It has three carboxylate groups, one of them on the benzene ring and the other two on the propionate arms, and one nitrogen atom, which gives a maximum possible tetradentate coordination system. In forming this Fe₈ cluster, all of the carboxylate groups adopt *syn, syn* coordination modes bridging two atoms. However, the nitrogen is protonated and does not coordinate, but forms an intraligand hydrogen bond to O(3). The ligand coordination mode is shown in Fig. 5.2.

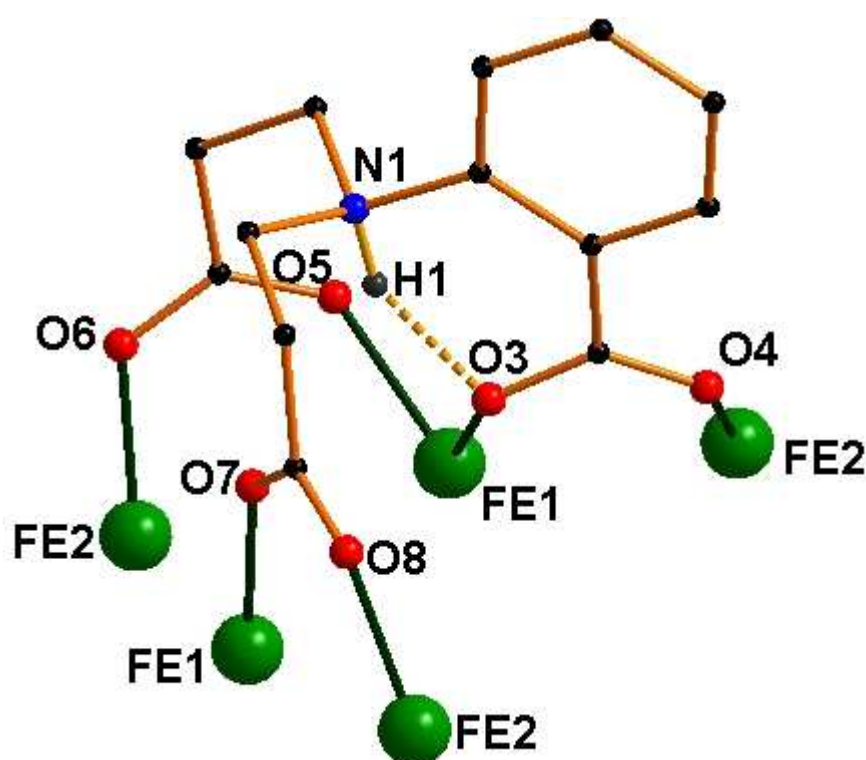


Figure 5.2 The coordination mode of the ligand cpidp³⁻

The carboxylate group on the phenyl ring (abbreviated as Ph-COO⁻) coordinates Fe(1) and Fe(2) by a *syn, syn* $\eta^1:\eta^1:\mu_2$ PhCOO²⁻ bridging mode, which contains the atoms O(3) and O(4), with O(3) to Fe(1) and O(4) to Fe(2) respectively. The two carboxylic groups on the two propionic arms (abbreviated as R-COO⁻) also have a *syn, syn* $\eta^1:\eta^1:\mu_2$ coordination mode, with one R-COO⁻ group coordinating to Fe(1) and a second Fe(2) by O(5) and O(6) respectively, the other R-COO⁻ group coordinating to a second Fe(1) and a third Fe(2) by O(7) and O(8) respectively. Altogether one ligand coordinates to five Fe(III) atoms, two Fe(1) and three Fe(2) atoms, through all the carboxylate oxygens (Fig. 5.2). The intraligand

hydrogen bond N(1)–H(1)⋯O(3) (N(1)–H(1) = 0.912Å, H(1)⋯O(3) = 1.773Å) helps to stabilise the whole structure.

5.1.1.3 The coordination spheres of the Fe(III) centres

The iron atoms occupy two different crystallographic sites and are octahedrally coordinated by oxygen atoms. A representation of the local connectivity of Fe(1) is shown in Fig. 5.3, and that of Fe(2) is shown in Fig.5.4.

For clarity the atoms with different symmetry operations are defined as follows: (-0.5+y, 0.5-x, 0.5-z) as #1, (0.5-y, 0.5+x, 0.5-z) as #2, and (-x, 1-y, z) as #3.

The coordination spheres of Fe(1)

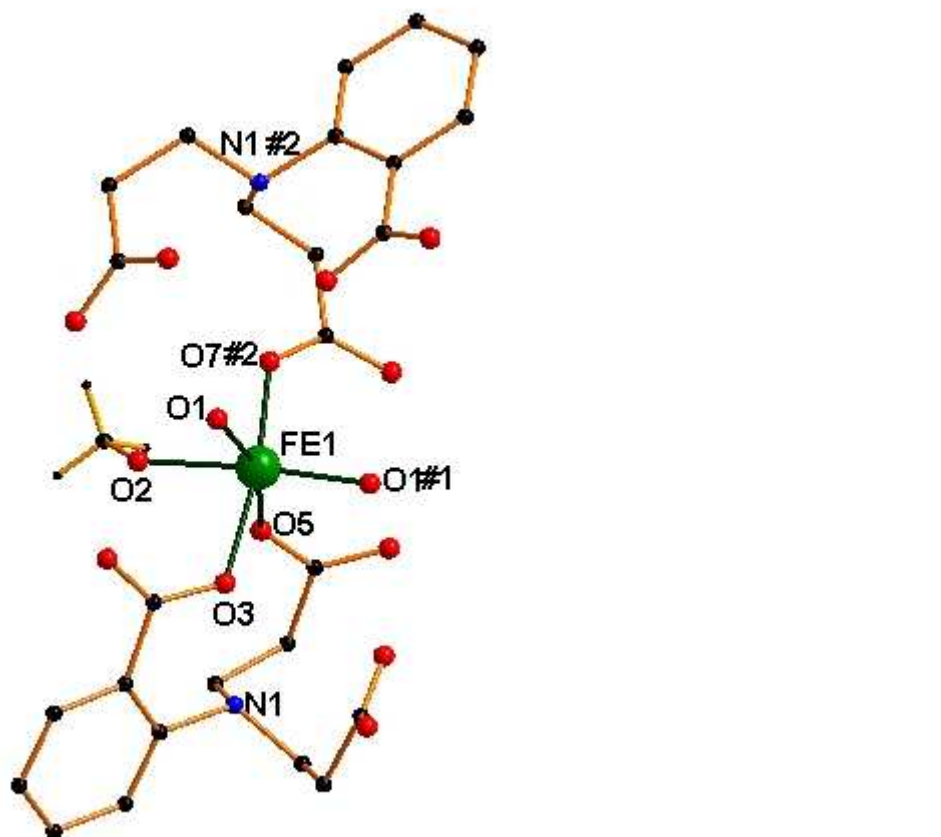


Figure 5.3 Coordination spheres of the Fe(1) atom

For Fe(1) (Fig. 5.3), there are two cpdp³⁻ ligands coordinating to it, one of which chelates Fe(1) with two carboxylate groups, PhCOO⁻ with O(3) as the coordination atom and R-COO⁻

with O(5) as the coordination atom. The other ligand uses RCOO⁻ with O(7)#2 occupying the coordination site *trans* to O(3) of PhCOO⁻. The other three coordination sites are occupied by two μ_3 -O (O(1)) and one μ -OMe (O(2)), with O(1) and O(5), O(2) and O(1)#1 opposite each other in the pair respectively.

The octahedral environment of Fe(1) is rather distorted, with two short Fe-O bond distances Fe(1)-O(1)#1 = 1.866(3) Å, Fe(1)-O(1) = 1.941(3) Å, three medium ones Fe(1)-O(5) = 2.092(3) Å, Fe(1)-O(7)#2 = 2.050(3) Å, Fe(1)-O(2) = 2.031(3) Å, and one long bond Fe(1)-O(3) = 2.123(3) Å. The mean Fe-O distance 2.02 Å is typical for Fe(III). The bond between Fe(1) and O(3) which comes from the PhCOO⁻ is the weakest with bond length over 2.1 Å.

Bond	Length (Å)	Bond	Length (Å)
Fe(1)-O(1)	1.941(3)	Fe(1)-O(7)#2	2.050(3)
Fe(1)-O(3)	2.123(3)	Fe(1)-O(2)	2.031(3)
Fe(1)-O(5)	2.092(3)	Fe(1)-O(1)#1	1.866(3)

Table 5.1 Bond length around Fe(1)

Table 5.2 shows that the O-Fe-O angles in the octahedral coordination sphere of Fe(1) deviate markedly from 90° or 180°. The angles involving pairs of *trans* oxygens are 172.3°, 165.7° and 160.7°, deviating much from 180°, while the angles involving *cis*-oxygens range between 79.7° and 106.9°. This is not unusual for Fe(III).

Bond	Angle (°)	Bond	Angle (°)
O(1)-Fe(1)-O(1)#1	106.9	O(3)-Fe(1)-O(1)	91.8
O(2)-Fe(1)-O(1)#1	172.3	O(7)#2-Fe(1)-O(2)	85.8
O(7)#2-Fe(1)-O(1)#1	95.8	O(5)-Fe(1)-O(2)	81.3
O(5)-Fe(1)-O(1)#1	91.0	O(3)-Fe(1)-O(2)	82.8
O(3)-Fe(1)-O(1)#1	94.5	O(5)-Fe(1)-O(7)#2	90.2
O(2)-Fe(1)-O(1)	80.5	O(3)-Fe(1)-O(7)#2	165.7
O(7)#2-Fe(1)-O(1)	94.9	O(3)-Fe(1)-O(5)	79.7
O(5)-Fe(1)-O(1)	160.7		

Table 5.2 Selected angles (°) for the coordination sphere of Fe(1)

The coordination spheres of Fe(2)

Bond	Length (Å)	Bond	Length (Å)
Fe(2)-O(1)	1.944 (3)	Fe(2)-O(6)#2	2.045(4)
Fe(2)-O(2)	1.938(3)	Fe(2)-O(8)#3	2.011(3)
Fe(2)-O(4)	2.104(4)	Fe(2)-O(9)	2.056(4)

Table 5.3 Bond lengths around Fe(2)

For Fe(2) (Fig. 5.4), there are three ligands coordinating to it, and each of the three ligands uses one carboxylate group on the arm to coordinate to Fe(2) with bonds shown in Table 5.3.

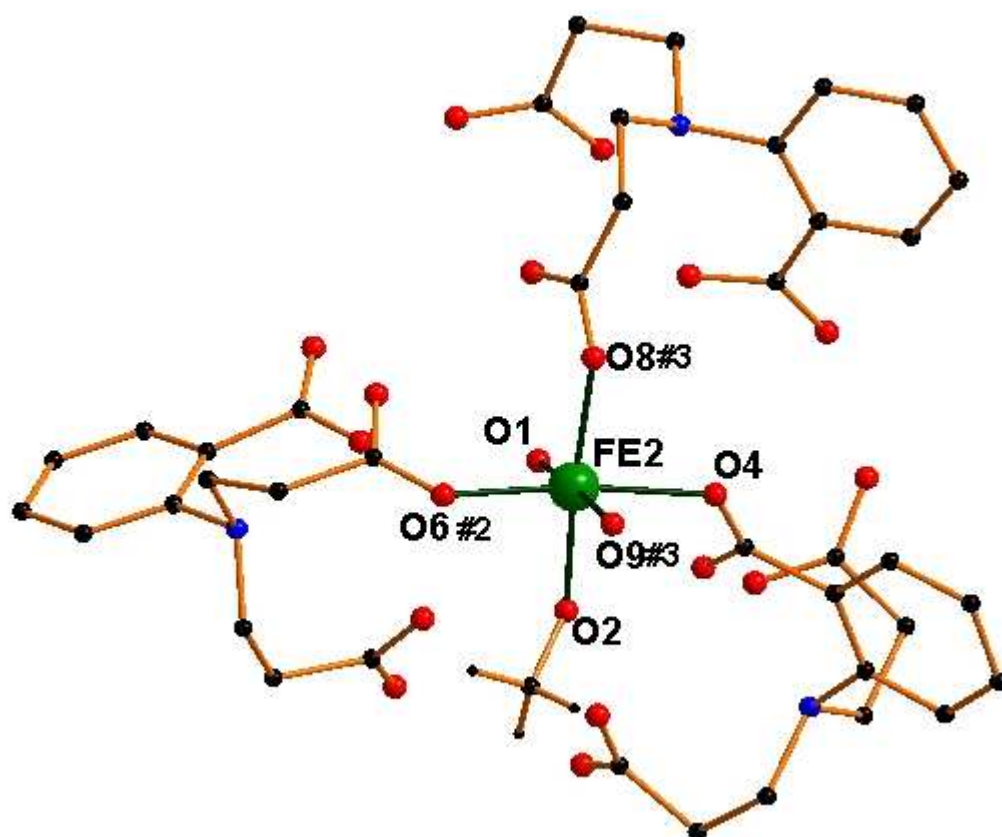


Figure 5.4 The coordination sphere of the Fe(2) atom

One of the ligands is the one that uses two carboxylate groups (Ph-COO⁻ and R-COO⁻) chelating the Fe(1) atom and here uses the other oxygen atom O(4) on Ph-COO⁻ to coordinate Fe(2). The second ligand is the one that uses one carboxylate group (R-COO⁻) to coordinate Fe(1) and here uses another carboxyl group (R-COO⁻) with O(7) to coordinate to Fe(2) occupying the coordination site *trans* to O(4) of PhCOO⁻. The third ligand has no coordination to the former Fe(1) and uses one carboxylate group (R-COO⁻) with O(8)#3 to coordinate Fe(2). The other three coordination sites are occupied by one μ_3 -O (O(1)), one μ_2 -OMe (O(2)), and one coordination water (O(9)#3). O(1) *trans* to O(9), and O(2) *trans* to O(8)#3.

Compared with Fe(1), Fe(2) has a less distorted octahedral geometry, with two short bonds Fe(2)-O(1) = 1.944(3)Å, Fe(2)-O(2) = 1.938(3)Å, three medium bonds Fe(2)-O(6)#2 = 2.045(4)Å, Fe(2)-O(8)#3 = 2.011(3)Å, Fe(2)-O(9)#3 = 2.056(4)Å, and one long bond Fe(2)-O(4) = 2.104(4)Å. The bonds between Fe(1) and the bridging oxygen atoms, μ_3 -O (O1) and

μ_2 -OMe, are the shortest with bond length less than 2.0 Å. As with Fe(2), the bond between Fe(2) and O(4) which comes from the PhCOO⁻ is the weakest with bond length over 2.1 Å.

Bond	Angle (°)	Bond	Angle (°)
O(1)-Fe(2)-O(2)	82.9	O(1)-Fe(2)-O(4)	93.9
O(2)-Fe(2)-O(8)#3	175.0	O(6)#2-Fe(2)-O(8)#3	95.0
O(2)-Fe(2)-O(6)#2	90.2	O(8)#3-Fe(2)-O(9)#3	87.3
O(2)-Fe(2)-O(9)#3	92.9	O(4)-Fe(2)-O(8)#3	88.7
O(2)-Fe(2)-O(4)	86.3	O(6)#2-Fe(2)-O(9)#3	84.2
O(1)-Fe(2)-O(8)#3	97.1	O(4)-Fe(2)-O(6)#2	168.5
O(1)-Fe(2)-O(6)#2	96.6	O(4)-Fe(2)-O(9)#3	85.2
O(1)-Fe(2)-O(9)#3	175.7		

Table 5.4 Selected angles (°) for the coordination spheres of Fe(2)

Table 5.4 shows that the octahedral sphere of Fe(2) is less distorted than that of Fe(1), with the O-Fe-O angles deviating less from 180° or 90°.

5.1.1.4 The core structure of Fe₈

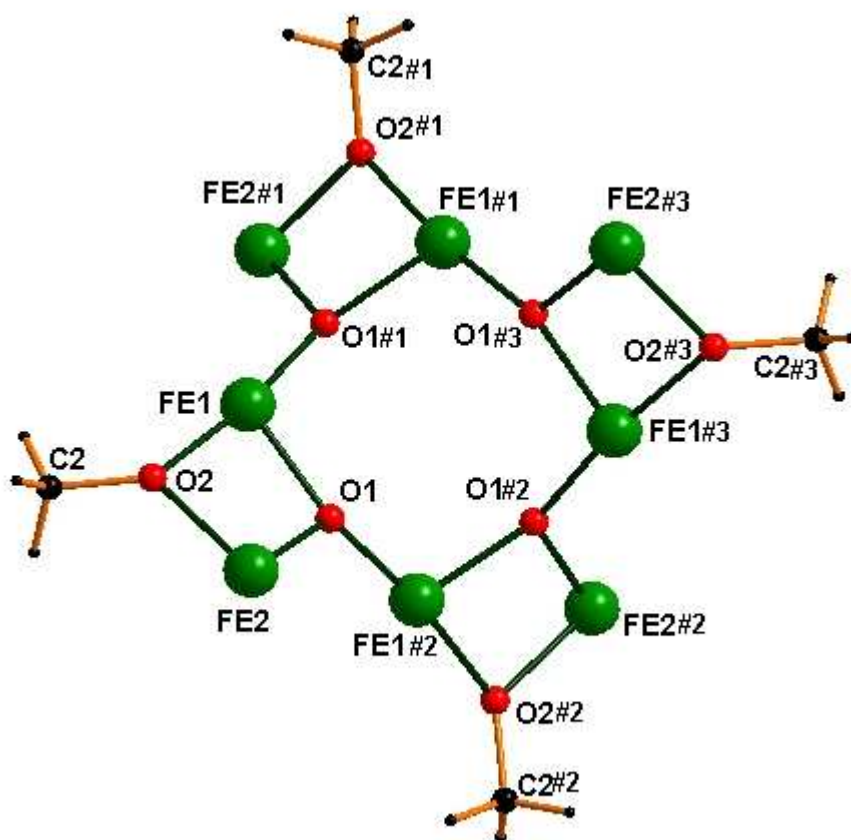


Figure 5.5 The core structure of Fe₈ with μ_3 -O and μ_2 -OMe bridges

The complex as a whole contains eight iron atoms (Fig.5.5), with four of them (Fe(1) with its symmetry equivalents) on a ring bridged by the μ_3 -oxo oxygen atoms O(1). These μ_3 -oxo oxygen atoms further point outwards to bridge the other four iron atoms Fe(2).

The arrangement of the atoms in the central core $\{\text{Fe}_8\text{O}_4\}^{16+}$ as ‘saddle’ shape is shown in Fig. 5.5. The four Fe(1) atoms are arranged in a nearly planar configuration, with Fe(1) and Fe(1)#3 0.326 Å above the plane, and Fe(1)#1 and Fe(1)#2 0.326 Å below the mean plane defined by Fe(1), Fe(1)#1, Fe(1)#2 and Fe(1)#3. The oxygen atom O(1) and Fe(2), and their C_2 symmetry-related atoms Fe(2)#3 and O(1)#3, are situated above this plane, while their S_4 symmetry-related atoms Fe(2)#1, O(1)#1, Fe(2)#2 and O(1)#2 are below the Fe_4 least-squares plane. Consequently Fe(2) and its symmetry equivalents are displaced 2.060 Å out of this plane.

Atoms	Deviation (Å)	Atoms	Deviation(Å)
Fe(1)	-0.326(8)	Fe(1)#1	0.326(8)
Fe(2)	-2.060(1)	Fe(2)#1	2.060(1)
O(1)	-0.664(4)	O(1)#1	0.664(4)
Fe(1)#3	-0.326(8)	Fe(1)#2	0.326(8)
Fe(2)#3	-2.060(1)	Fe(2)#2	2.060(1)
O(1)	-0.664(4)	O(1)#2	0.664(4)

Table 5.5 Deviations of the atoms from the least-squares plane defined by Fe(1)-Fe(1)#1-Fe(1)#2-Fe(1)#3

The dihedral angle of the plane defined by Fe(1)-Fe(2)-Fe(1)#1 with the least-squares Fe_4 plane is 53.4° . The μ_3 -oxide in each triangle unit is slightly out of the plane formed by the three Fe atoms (Fe(1)-Fe(2)-Fe(1)) by 0.250(7) Å.

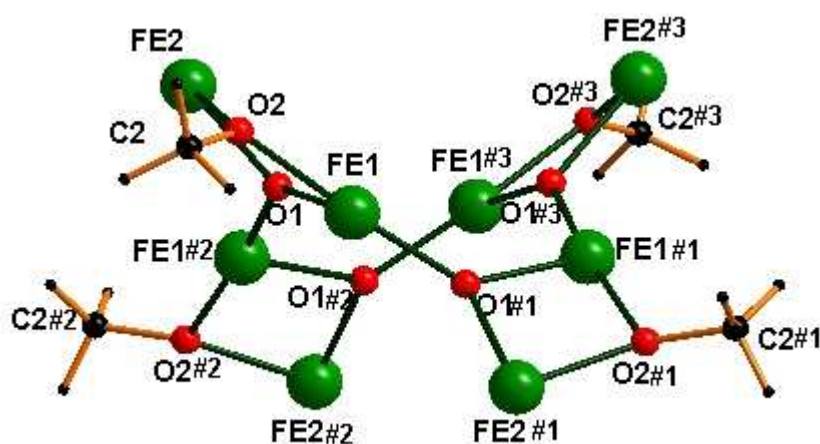


Fig. 5.6 The core structure of Fe_8 showing Fe(2) and Fe(2)#3 above, Fe(2)#1 and Fe(2)#2 below the Fe_4 plane

The μ_3 -oxo oxygen atom O(1) bridges between the three iron atoms Fe(1), Fe(2), Fe(1)#2. Within the Fe^{III}_3 triangle, the μ_3 -O bridge is unsymmetrical, as a result of the different bridges along each Fe...Fe edge.

Bond	Bond length (Å)	Bond	Angle (°)
Fe(1)–O(1)	1.940(8)	Fe(1)–O(1)–Fe(2)	98.5
Fe(2)–O(1)	1.943(8)	Fe(1)–O(1)–Fe(1)#2	135.9
Fe(1)#2–O(1)	1.866(2)	Fe(2)–O(1)–Fe(1)#2	120.3

Table 5.6 Bond lengths and angles in the $\text{Fe}^{\text{III}}_3(\mu_3\text{-O})$ triangle

Fe(1) and Fe(2) are bridged by μ_2 -OMe, μ_3 -O and one *syn-syn* carboxylate group, resulting in a short Fe(1)...Fe(2) distance (2.941(1)Å) and a small angle Fe(1)-O(1)-Fe(2) (98.5°). The longest edge of this triangle is defined by Fe(1) and Fe(1)#1, bridged only by μ_3 -O, thus giving a long Fe...Fe distance of 3.528(1)Å and a large angle Fe(1)-O(1)-Fe(1) of 135.9°. Fe(1) and Fe(2)#2 are bridged by μ_3 -O and two *syn, syn* carboxylate groups, so that the distance Fe(1)...Fe(2)#1 (3.303(1)Å) and the angle Fe(2)-O(1)-Fe(1)#2 (120.3°) are intermediate. The three inequivalent Fe...Fe distances within this triangular subunit therefore result in a strongly scalene triangle.

5.1.1.5 Polyhedral representation of Fe_8

The metal oxide framework can be described as eight groups of edge-sharing and corner-sharing FeO_6 octahedra (as is shown in Fig. 5.7). The octahedral pair of the two irons with the same symmetry operation (Fe(1) and Fe(2), etc), $\{\text{Fe}(1)\text{O}_6\}$ and $\{\text{Fe}(2)\text{O}_6\}$ share a common edge which is formed by μ_3 -O (O(1)) and μ_2 -OCH₃ (O(2)) bridges, with O(1) towards the inside and O(2) towards the outside of the molecule.

When the two irons belong to two different asymmetric units, the octahedron formed around them only share one corner, μ_3 -O (O(1)). Thus in the way described above, the four edge-sharing octahedral unit pairs are linked into a tilting square with four groups of units (Fig. 5.7),

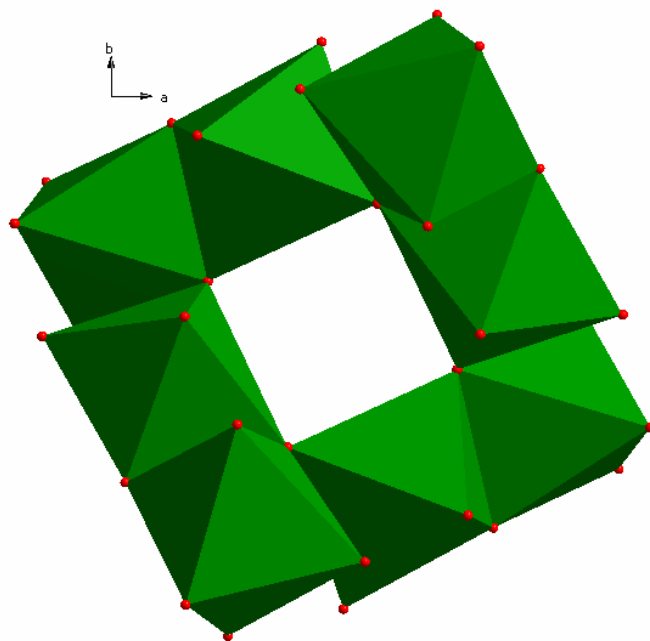


Figure 5.7 A polyhedral representation of the complex **12**

5.1.2 The magnetic properties of Fe_8

Variable-temperature, solid-state magnetic susceptibility measurements were performed on microcrystalline samples of Fe_8 at 0.1 T in the 2.0-300 K temperature range. The obtained data are shown in Fig. 5.8 as χT product per Fe_8 versus T.

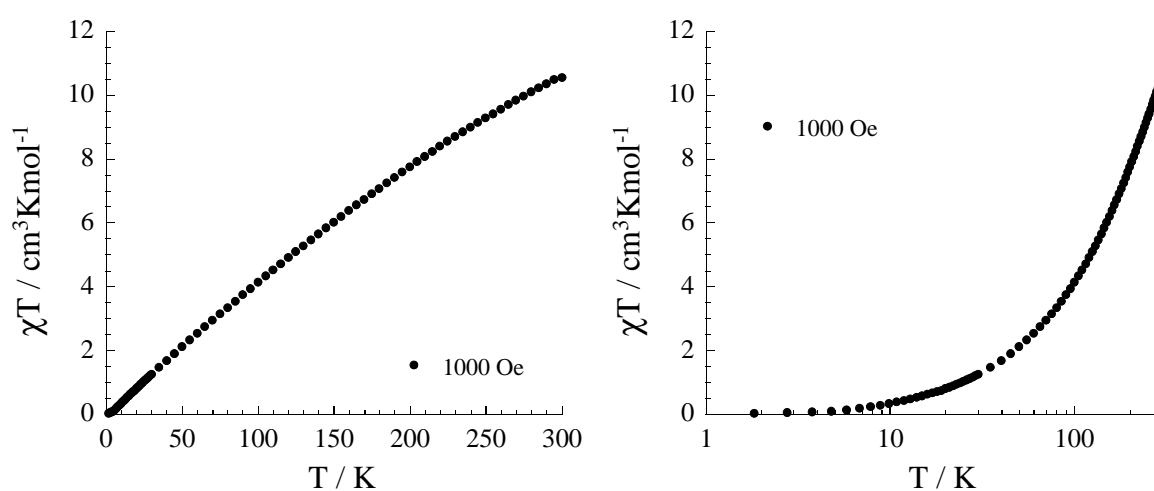


Figure 5.8 Temperature dependence of the χT product per Fe_8 at 0.1 T

At room temperature, the χT product is $10.58 \text{ cm}^3 \text{ K mol}^{-1}$. This value is much lower than the expected value ($35.0 \text{ cm}^3 \text{ K mol}^{-1}$) for the presence of eight isolated high-spin Fe(III) ions ($S = 5/2$, $C = 4.375 \text{ cm}^3 \text{ K mol}^{-1}$) taking into account a g value of 2.0. This type of behaviour indicates very strong overall antiferromagnetic interactions within this Fe_8 complex. As can be seen on the χT vs T semi-log plot shown above, the χT product decreases to zero below 7 K indicating an $S = 0$ ground state. This hypothesis is qualitatively supported by the field dependence of the magnetization at 1.8 K (Fig. 5.9), in which the magnetization is only slightly populated with the increase of field up to 7 T.

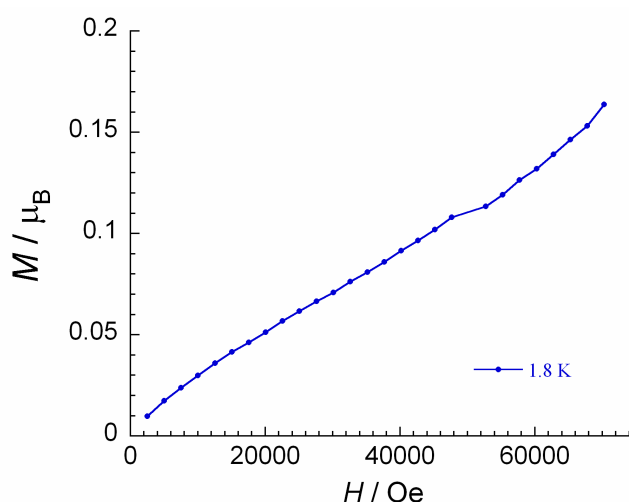
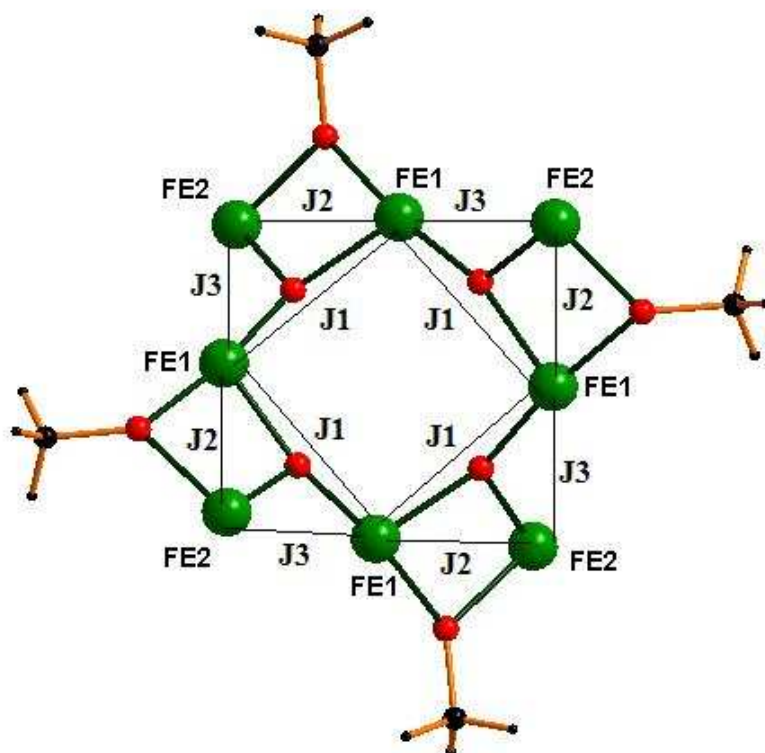


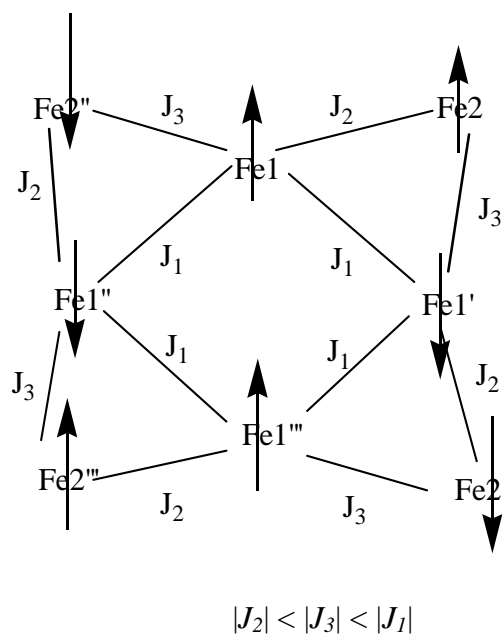
Figure 5.9 The field dependence of magnetization for Fe_8 at 1.8K



Scheme 5.1 Schematic representation of the exchange interactions in Fe_8

The Fe₈ complex has an S₄ symmetry axis, so that the magnetic interaction pathways are as shown in Scheme 5.1. J_1 is defined as the interactions by μ_3 -O between two Fe(1) and Fe(1); J_2 is defined as the interactions by μ_3 -O, μ_2 -OMe, and one carboxylate group between the Fe(1) and Fe(2) in the same asymmetric unit; J_3 is defined as the interactions by μ_3 -O, two carboxylate groups between Fe(1) and Fe(2) in different asymmetric units.

Using the magneto-structural correlation proposed for oxygen-bridged Fe(III) systems by Christou *at al.*^[55], it is probable that all three of the interactions are antiferromagnetic, with $|J_2| < |J_3| < |J_1|$. The Fe^{III}₃(μ_3 -O) triangles will therefore be spin-frustrated, with one spin antiparallel to the other two, which then have to be parallel to each other. The two parallel spins are then likely to be those with the weakest antiferromagnetic interaction between them, in this case J_2 . Therefore the magnetic spin structure in Scheme 5.2 can be proposed, which is consistent with the $S = 0$ ground state determined from the experimental data. Because there are too many parameters, it is not possible to model the data with three different J values.



Scheme 5.2 Schematic representation of the magnetic structure within Fe₈ in the diamagnetic ground state

5.2 The tetranuclear cubanes $[M^{II}_4(\text{cpdeaH})_4] \cdot x\text{H}_2\text{O}$ ($M = \text{Cu}$, 13, Co , 14)

5.2.1 Molecular structures of the cubanes

5.2.1.1 Overview of the structures

The complexes $[\text{Cu}^{II}_4(\text{cpdeaH})_4] \cdot 2\text{H}_2\text{O}$ and $[\text{Co}^{II}_4(\text{cpdeaH})_4] \cdot 3.2\text{H}_2\text{O}$ crystallize isomorphously in the monoclinic space group $C2/c$. The crystal water molecules are found in the area between the cluster aggregates. Examination of the crystal packing indicates that the Cu_4 and Co_4 molecules are reasonably well isolated, taking Co_4 as an example in Fig. 5.9 (Cu_4 has the same packing). The cell parameters for Cu_4 are $a = 21.6055 \text{ \AA}$, $b = 15.354 \text{ \AA}$, $c = 17.1037 \text{ \AA}$, $\beta = 126.892^\circ$ while for Co_4 are $a = 21.7852 \text{ \AA}$, $b = 15.5860 \text{ \AA}$, $c = 17.2027 \text{ \AA}$, $\beta = 127.364^\circ$. The asymmetric unit contains one half of the tetranuclear cubane cluster. The cubane as a whole has C_2 symmetry.

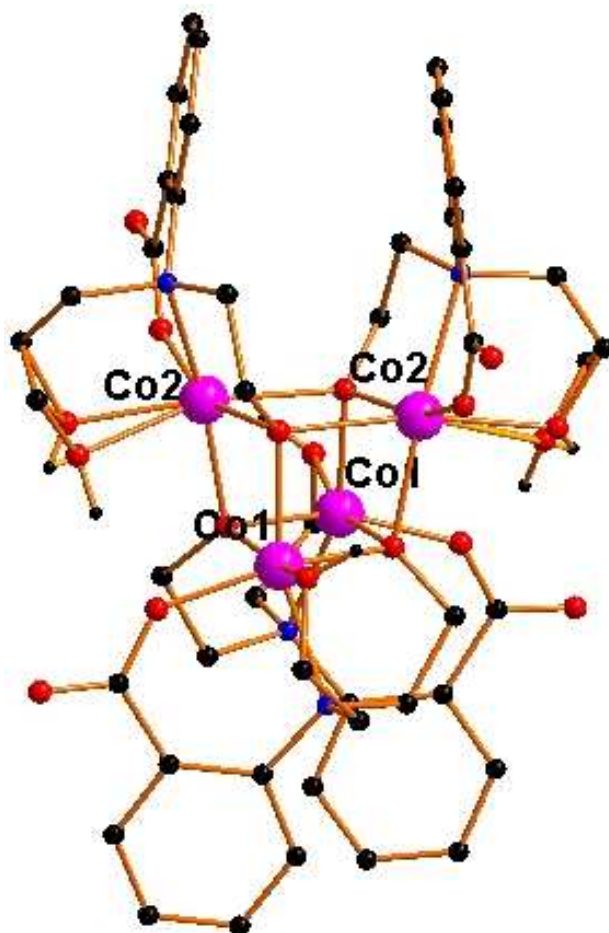
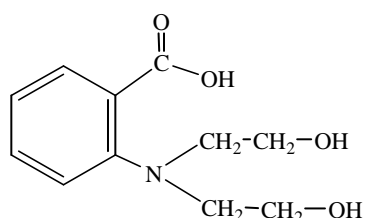


Figure 5.10 Molecular structure for $[\text{Co}^{II}_4(\text{cpdeaH})_4] \cdot 3.2\text{H}_2\text{O}$

5.2.1.2 The chelating mode of the ligand (cpdeaH)²⁻ in the metal cubanes

The ligand that chelates the copper and cobalt atoms in Cu₄ and Co₄ is *N*-(2-carboxyphenyl)diethanolamine, cpdeaH₃. The structure of cpdeaH₃ (Scheme 5.3) is similar to H₃cpidp but with two –OH instead of –COOH groups.



Scheme 5.3 The structure of the ligand *N*-(2-carboxyphenyl)diethanolamine (cpdeaH₃)

Under the reaction conditions used, the carboxylic acid group and one of the hydroxyl groups have been deprotonated while the second hydroxyl group remains protonated and the ligand is tetradentate. The carboxylate group, nitrogen atom and both the deprotonated and protonated hydroxyl groups chelate round one copper atom while the deprotonated hydroxyl group bridges to a further two metal centres, forming a threefold bridge between a triangle of Cu atoms (Fig. 5.11).

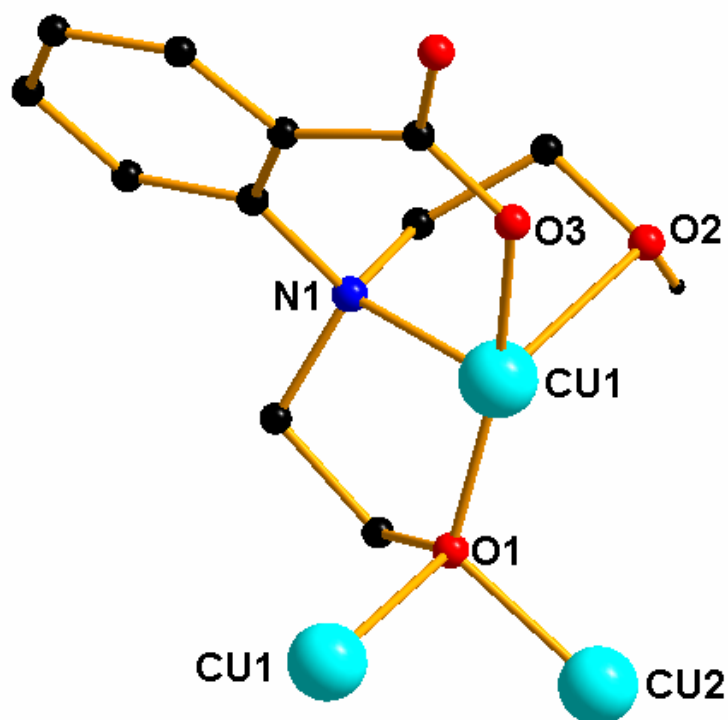


Fig. 5.11 the chelating mode of the Hcpdea²⁻ ligand

5.2.1.3 The structures of Cu₄ and Co₄

The angles and bond lengths of Cu₄ and Co₄ are listed respectively in Table 5.7 and Table 5.8.

Cu ₄ , 13		Co ₄ , 14	
Bonds	Angles (°)	Bonds	Angles (°)
O(3)-Cu(1)-O(1)	164.4	O(3)-Co(1)-O(1)	157.1
O(5)#-Cu(1)-O(1)	87.0	O(5)#-Co(1)-O(1)	84.8
N(1)-Cu(1)-O(1)	87.7	N(1)-Co(1)-O(1)	83.6
O(2)-Cu(1)-O(1)	113.6	O(2)-Co(1)-O(1)	110.9
O(1)#-Cu(1)-O(1)	79.8	O(1)#-Co(1)-O(1)	78.3
O(5)#-Cu(1)-O(3)	93.1	O(5)#-Co(1)-O(3)	108.2
N(1)-Cu(1)-O(3)	94.4	N(1)-Co(1)-O(3)	88.2
O(2)-Cu(1)-O(3)	82.1	O(2)-Co(1)-O(3)	88.6
O(1)#-Cu(1)-O(3)	85.5	O(1)#-Co(1)-O(3)	85.5
N(1)-Cu(1)-O(5)#	170.1	N(1)-Co(1)-O(5)#	160.7
O(2)-Cu(1)-O(5)#	94.5	O(2)-Co(1)-O(5)#	89.9
O(1)#-Cu(1)-O(5)#	70.9	O(1)#-Co(1)-O(5)#	79.5
O(2)-Cu(1)-N(1)	80.1	O(2)-Co(1)-N(1)	80.0
O(1)#-Cu(1)-N(1)	116.4	O(1)#-Co(1)-N(1)	113.1
O(1)#-Cu(1)-O(2)	160.2	O(1)#-Co(1)-O(2)	165.5
Cu(2)-O(1)-Cu(1)	112.0	Co(2)-O(1)-Co(1)	102.1
Cu(1)#-O(1)-Cu(1)	100.0	Co(1)#-O(1)-Co(1)	101.7
Cu(1)#-O(1)-Cu(2)	86.4	Co(1)#-O(1)-Co(2)	90.7
O(5)-Cu(2)-O(7)	167.7	O(5)-Co(2)-O(7)	158.0
O(1)-Cu(2)-O(7)	94.9	O(1)-Co(2)-O(7)	108.3
N(2)-Cu(2)-O(7)	91.2	N(2)-Co(2)-O(7)	86.4
O(6)-Cu(2)-O(7)	97.9	O(6A)-Co(2)-O(7)	85.8
O(5)#-Cu(2)-O(7)	91.0	O(5)#-Co(2)-O(7)	88.5
O(1)-Cu(2)-O(5)	89.2	O(1)-Co(2)-O(5)	86.7
N(2)-Cu(2)-O(5)	86.8	N(2)-Co(2)-O(5)	82.4
O(6)-Cu(2)-O(5)	93.8	O(6A)-Co(2)-O(5)	110.2
O(5)#-Cu(2)-O(5)	79.4	O(5)#-Co(2)-O(5)	78.7
N(2)-Cu(2)-O(1)	169.5	N(2)-Co(2)-O(1)	162.5
O(6)-Cu(2)-O(1)	91.2	O(6A)-Co(2)-O(1)	93.4
O(5)#-Cu(2)-O(1)	70.4	O(5)#-Co(2)-O(1)	78.0
O(6)-Cu(2)-N(2)	79.5	O(6A)-Co(2)-N(2)	77.8
O(5)#-Cu(2)-N(2)	118.3	O(5)#-Co(2)-N(2)	113.0
O(5)#-Cu(2)-O(6)	160.2	O(5)#-Co(2)-O(6A)	167.5
		O(6B)-Co(2)-O(7)	103.8
		O(6B)-Co(2)-O(5)	93.6
		O(6B)-Co(2)-O(1)	84.7
		O(6B)-Co(2)-N(2)	82.5
		O(5)#-Co(2)-O(6B)	161.3

Table 5.8 Selected angles for Cu₄ and Co₄

Cu ₄ , 13		Co ₄ , 14	
Bond	Distance(Å)	Bond	Distance(Å)
Cu(1) – O(1)	1.907(5)	Co(1) – O(1)	1.996(8)
Cu(1) – O(3)	1.919(9)	Co(1) – O(3)	1.969(6)
Cu(1) – O(5)#	1.958(4)	Co(1) – O(5)#	2.056(3)
Cu(1) – N(1)	2.072(4)	Co(1) – N(1)	2.245(9)
Cu(1) – O(2)	2.445(7)	Co(1) – O(2)	2.170(4)
Cu(1) – O(1)#	2.658(2)	Co(1) – O(1)#	2.297(4)
Cu(2) – O(7)	1.910(1)	Co(2) – O(7)	1.958(1)
Cu(2) – O(5)	1.928(5)	Co(2) – O(5)	2.000(3)
Cu(2) – O(1)	1.970(1)	Co(2) – O(1)	2.064(5)
Cu(2) – N(2)	2.066(0)	Co(2) – N(2)	2.273(8)
Cu(2) – O(5)#	2.572(5)	Co(2) – O(5)#	2.274(3)
Cu(2) – O(6)	2.414(6)	Co(2) – O(6A)	2.122(8)
		Co(2) – O(6B)	2.242(0)
Cu(1)···Cu(2)	3.213(6)	Co(1)···Co(2)	3.158(7)
Cu(1)···Cu(1)#	3.521(4)	Co1···Co1'	3.334(3)
Cu(1)···Cu(2)#	3.205(3)	Co(1)···Co(2)#	3.105(3)
Cu(2)···Cu(2)#	3.473(4)	Co(2)···Co(2)#	3.310(6)

Table 5.7 Selected bond lengths for Cu₄ and Co₄

The atom linkages in the Cu₄ cubane, 13

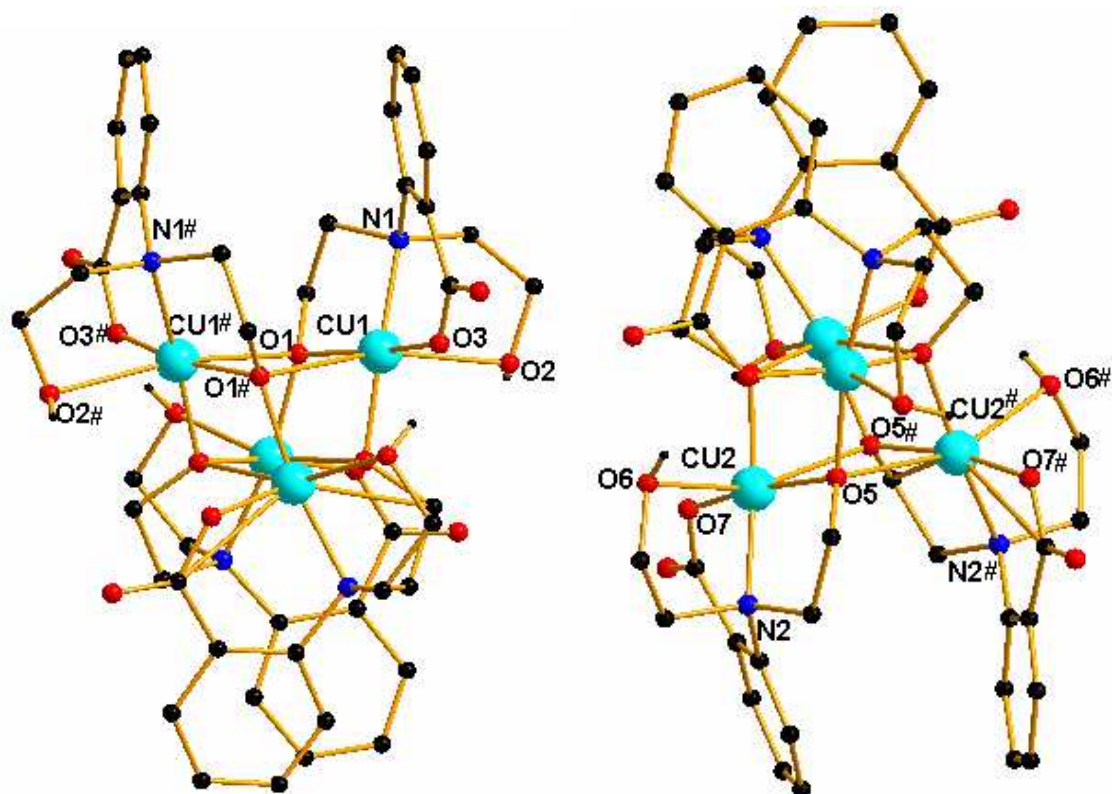


Figure 5.12 Two views of the structure of the Cu₄ cubane

Each Cu(II) is captured by one ligand, with the bonds to deprotonated hydrogen oxygen (Cu(1)-O(1) = 1.907(5)Å, Cu(2)-O(5) = 1.928(5)Å) and carboxylate oxygen (Cu(1)-O(3) = 1.919(9)Å, Cu(2)-O(7) = 1.910(1)Å) shorter and bonds to amino nitrogen (Cu(1)-N(1) = 2.072(4)Å, Cu(2)-N(2) = 2.066(0)Å) and protonated oxygen (Cu(1)-O(2) = 2.445(7)Å, Cu(2)-O(6) = 2.414(6)Å) longer. The two remaining coordination sites are occupied by a deprotonated oxygen, which is from the ligand capturing the unsymmetric Cu(II), with shorter bond (Cu(1)-O(5)# = 1.958(4) Å, Cu(2)-O(1) = 1.970(1)Å) and a deprotonated hydrogen oxygen, which is from the ligand capturing the C₂ symmetric Cu(II), with longer bonds (Cu(1)-O(1)# = 2.658(2) Å, Cu(2)-O(5)# = 2.572(5) Å) (Fig. 5.13).

The whole Cu₄ structure is formed by rotating the half molecule around the C₂ axis along the *b* axis. Both Cu(1) and Cu(2) atoms have distorted octahedral topology, or more like square pyramidal environment, with O(2) and O(1)# on the Jahn-Teller elongation apical axis of Cu(1), O(6) and O(5)# on the Jahn-Teller elongation apical axis of Cu(2).

The atom linkages in the Co₄ cubane, 14

Co₄ and Cu₄ have isomorphous crystal structure, so that the connectivities around the Cu or Co ions are the same, but with different metal-ligand bond lengths and angles (Table 5.7). In Cu₄, the two pairs of Cu-O bonds, Co(1)-O(2) and Co(1)-O(1)#, and Co(1)-O(2) and Co(1)-O(1)#, respectively, define the Jahn-Teller elongation apical axes. In Co₄ these Co-O bonds are still the longest ones, although not as long as in Cu₄. The corresponding Cu-O bonds are longer than the Co-O bonds. However, in Co₄ the Co-N bonds are also lengthened, unlike the Cu-N bonds and they become the second longest bonds in Co₄. The distortions of the octahedral coordination geometries in Co₄ are thus not a simple 4+2 as in Cu₄, but instead there are three *mer*-orientated long bonds and three *mer*-related short ones.

The whole Co₄ structure is formed by rotating the half molecule around C₂ axis along *b* axis. Co(II) has less distorted octahedral topology than Cu(II) in that the bond lengths along the apical axis of the tetrahedron are shorter in Co₄ than that in Cu₄, while the bond lengths on the plane of the tetrahedron are longer in Co₄ than that in Cu₄. But the apical axes do not change in Co₄, still is defined by O(2) and O(1)# for Co(1) atoms, O(6) and O(5)# for Co(2) atoms.

5.2.1.4 The core structures of the cubanes Cu_4O_4 and Co_4O_4

With alternating metal and oxygen atoms, the cubic core Cu_4O_4 is more distorted than Co_4O_4 (Fig. 5.13).

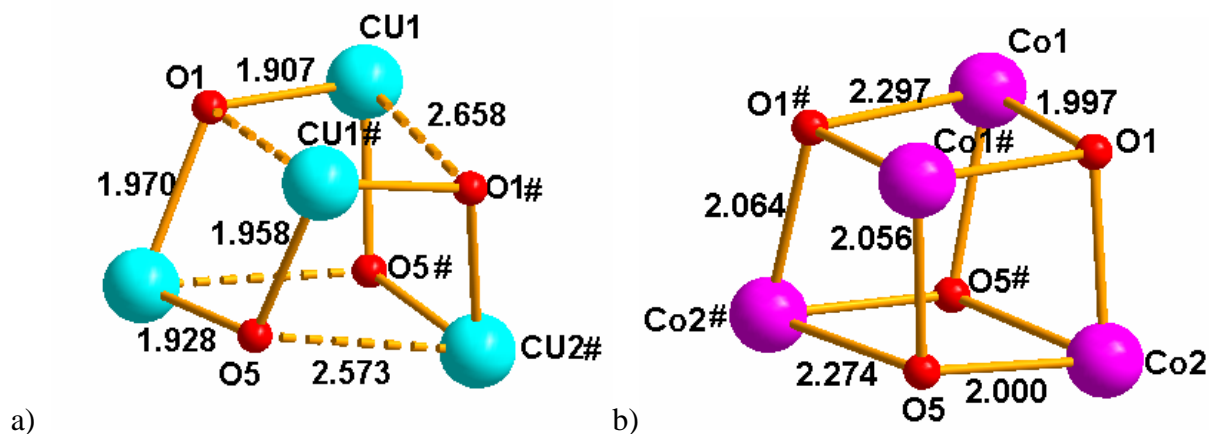


Figure 5.13 The cubic core structures: a) of Cu_4O_4 ; b) of Co_4O_4

In Cu_4O_4 , there are three $\text{Cu}^*(\text{O}(5))$ bonds with length as 2.573Å , 1.958Å , 1.928Å and three $\text{Cu}^*(\text{O}(1))$ bonds with length as 2.658Å , 1.970Å , 1.907Å . The cubane structure of Cu_4O_4 can be regarded as a pseudo dimeric structure, separated by the medium length of the Cu-O bond, two $\text{Cu}(1)\text{-O}(5)$ bonds 1.958Å and two $\text{Cu}(2)\text{-O}(1)$ bonds 1.970Å . Thus the intra dimeric bonds and angles are respectively 2.573Å for $\text{Cu}(2)\text{-O}(5)\#$ and $\text{Cu}(2)\#\text{-O}(5)$, 1.928Å for $\text{Cu}(2)\text{-O}(5)$ and $\text{Cu}(2)\#\text{-O}(5)\#$, 100.1° for $\text{Cu}(2)\#\text{-O}(5)\text{-Cu}(2)$, 79.4° for $\text{O}(5)\text{-Cu}(2)\text{-O}(5)\#$ on the plane of $\text{Cu}(2)\text{-O}(2)\text{-Cu}(2)\#\text{-O}(2)\#$. The intra dimeric bonds and angles are respectively 2.658Å for $\text{Cu}(1)\text{-O}(1)\#$ and $\text{Cu}(1)\#\text{-O}(1)$, 1.907Å for $\text{Cu}(1)\text{-O}(1)$ and $\text{Cu}(1)\#\text{-O}(1)\#$, 99.7° for $\text{Cu}(1)\#\text{-O}(1)\text{-Cu}(1)$, 79.8° for $\text{O}(1)\text{-Cu}(1)\text{-O}(1)\#$ on the plane of $\text{Cu}(1)\text{-O}(1)\text{-Cu}(1)\#\text{-O}(1)\#$.

	Bonds	Angles ($^\circ$)	bonds	Angles ($^\circ$)
Cu_4O_4	$\text{O}(5)\#\text{-Cu}(1)\text{-O}(1)$	87.1	$\text{Cu}(2)\text{-O}(1)\text{-Cu}(1)$	112.0
	$\text{O}(1)\#\text{-Cu}(1)\text{-O}(1)$	79.8	$\text{Cu}(1)\#\text{-O}(1)\text{-Cu}(1)$	100.0
	$\text{O}(1)\#\text{-Cu}(1)\text{-O}(5)\#$	70.9	$\text{Cu}(1)\#\text{-O}(1)\text{-Cu}(2)$	86.4
	$\text{O}(1)\text{-Cu}(2)\text{-O}(5)$	89.2	$\text{Cu}(1)\#\text{-O}(5)\text{-Cu}(2)$	111.1
	$\text{O}(5)\#\text{-Cu}(2)\text{-O}(5)$	79.4	$\text{Cu}(2)\#\text{-O}(5)\text{-Cu}(2)$	100.1
	$\text{O}(5)\#\text{-Cu}(2)\text{-O}(1)$	70.4	$\text{Cu}(2)\#\text{-O}(5)\text{-Cu}(1)\#$	89.3
Co_4O_4	$\text{O}(5)\#\text{-Co}(1)\text{-O}(1)$	84.8	$\text{Co}(2)\text{-O}(1)\text{-Co}(1)$	102.1
	$\text{O}(1)\#\text{-Co}(1)\text{-O}(1)$	78.3	$\text{Co}(1)\#\text{-O}(1)\text{-Co}(1)$	101.7
	$\text{O}(1)\#\text{-Co}(1)\text{-O}(5)\#$	79.5	$\text{Co}(1)\#\text{-O}(1)\text{-Co}(2)$	90.7
	$\text{O}(1)\text{-Co}(2)\text{-O}(5)$	86.7	$\text{Co}(1)\#\text{-O}(5)\text{-Co}(2)$	99.9
	$\text{O}(5)\#\text{-Co}(2)\text{-O}(5)$	78.7	$\text{Co}(2)\#\text{-O}(5)\text{-Co}(2)$	101.4
	$\text{O}(5)\#\text{-Co}(2)\text{-O}(1)$	78.0	$\text{Co}(2)\#\text{-O}(5)\text{-Co}(1)\#$	93.6

Table 5.9 The angles in the cubic cores for Cu_4O_4 and Co_4O_4

In Co_4O_4 , there are three Co-O(5) bonds with lengths of 2.274Å, 2.056Å, 2.000Å and three Co-O1 bonds with lengths of 2.297Å, 2.064Å, 1.997Å. The long Co-O bonds (2.274Å and 2.297Å) are much shorter than the corresponding long Cu-O bonds (2.573Å and 2.658Å), whilst the medium and short Co-O bonds (2.056Å, 2.064Å, 2.000Å, 1.997Å) are much longer than the corresponding Cu-O bonds (1.958Å, 1.970Å, 1.928Å, 1.970Å, 1.907Å). Thus all Co-O bond lengths tend to be similar and the cubane is much less distorted than the Cu_4O_4 cubane. This also reflected by the angles in the Co_4O_4 core (Table. 5.9).

5.2.2 The hydrogen bonds in Cu_4 and Co_4

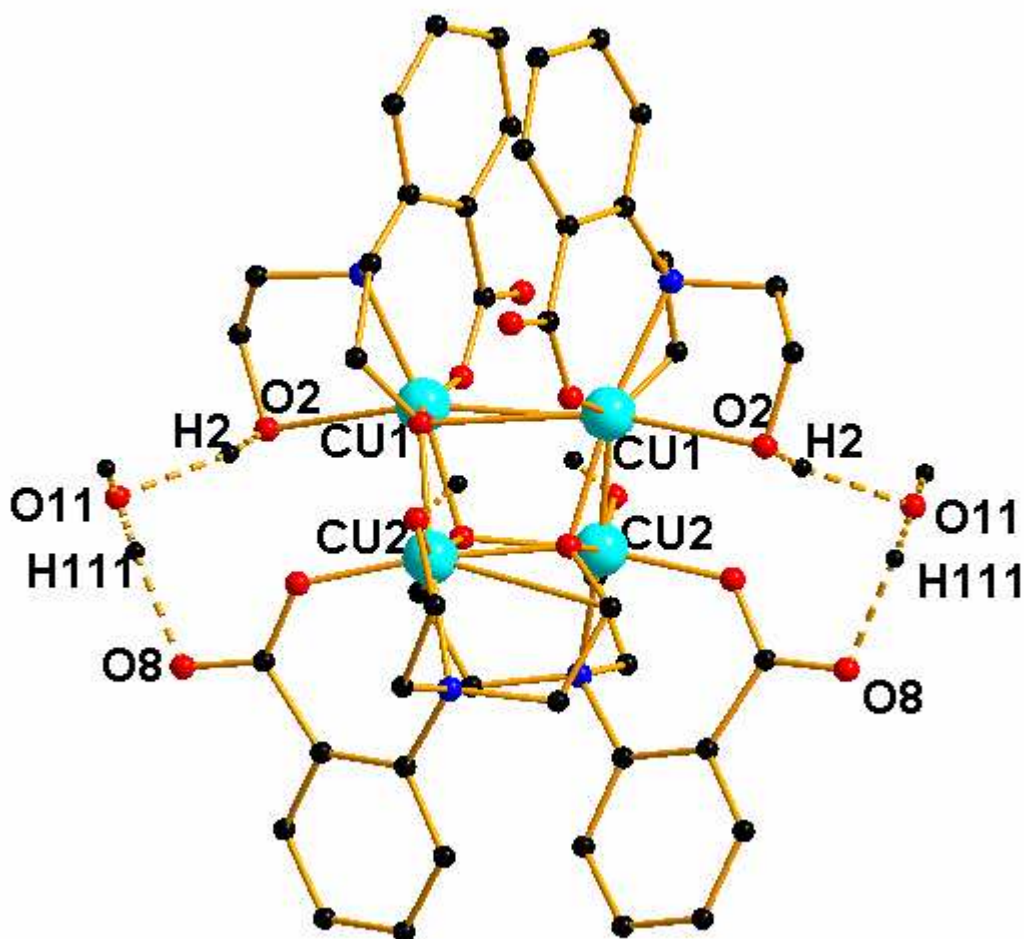


Figure 5.14 The hydrogen bonds in the cluster of $[\text{Cu}^{\text{II}}_4(\text{cpdeaH})_4] \cdot 2\text{H}_2\text{O}$, **13**

In the cubane cluster of $[\text{Cu}^{\text{II}}_4(\text{cpdeaH})_4] \cdot 2\text{H}_2\text{O}$, two crystal water molecules are symmetry related. The oxygen atom of the water, O(11) acting as an electron donor, forms a hydrogen

bond with the hydrogen atom of the protonated hydroxyl group. The hydrogen atom of the water, H(111) acting as an electron acceptor, forms a hydrogen bond with the oxygen atom of the carboxylate group that does not coordination to the copper atom (Fig. 5.14).

The water labelled as O(11) not only forms hydrogen bonds within the cluster, but also forms a hydrogen bond with the second cluster, involving the hydrogen atom of water, H(111) and the oxygen atom of the carboxylate group, O(4) (Fig. 5.15).

The corresponding hydrogen bonds O \cdots H and associated angles of hydrogen bonds H-O \cdots H for Cu₄ are listed in Table 5.10.

Cu ₄	Angle	Degree (°)	Hydrogen Bond	Length (Å)	O \cdots O distance	Length (Å)
intra	O(2)-H(2) \cdots O(11)	164.9	H(2) \cdots O(11)	1.883(6)	O2 \cdots O11	2.662(5)
	O(11)-H(111) \cdots O(8)	175.3	H(111) \cdots O(8)	1.834(3)	O(11) \cdots O(8)	2.686(6)
inter	O(11)-H(112) \cdots O(4)	172.4	H(112) \cdots O(4)	1.903(5)	O(11) \cdots O(4)	2.729(7)

Table 5.10 The hydrogen bond lengths and the associated angles in Cu₄, **13**

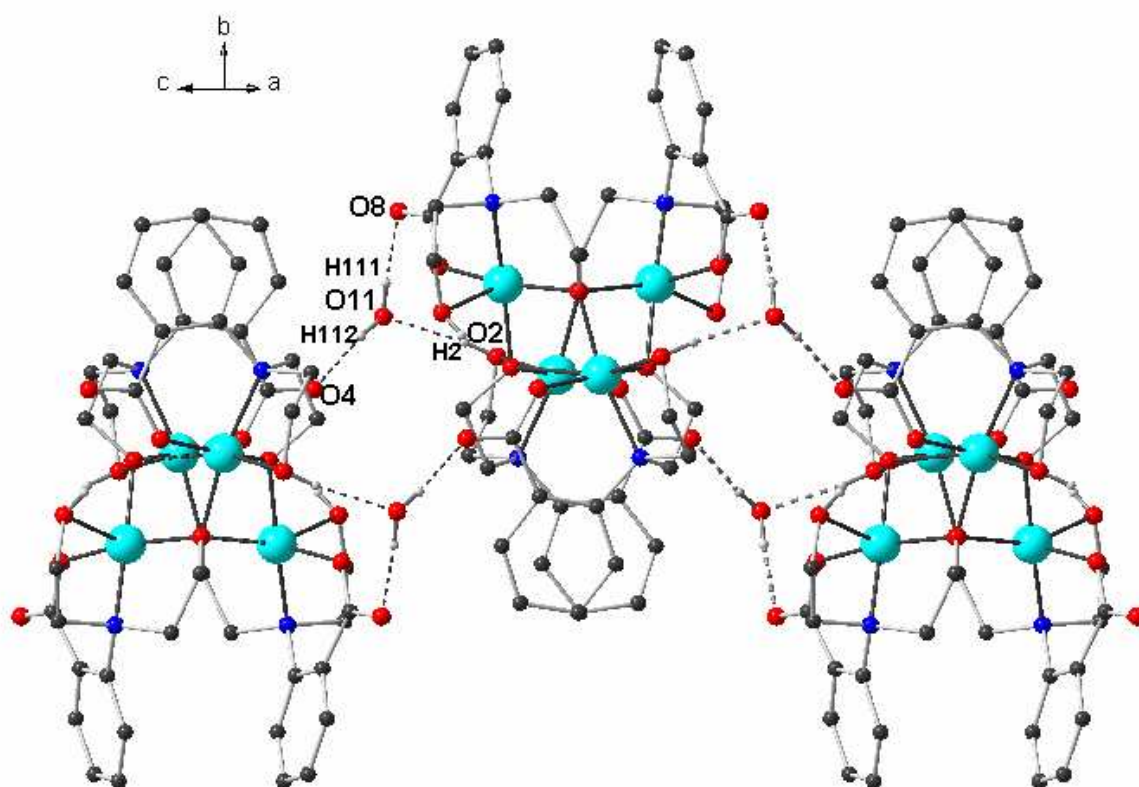


Fig. 5.15 The hydrogen bonds between the cluster of [Cu^{II}₄(cpdeaH)₄] \cdot 2H₂O, **13**

The bond lengths of O \cdots H are around 1.8 Å, the distances of O \cdots O are around 2.7 Å, and the angles are nearly 180°, all of them are characteristic of typical hydrogen bonds.

The Co₄ cluster has two hydrogen bonds in the cluster, centered on the waters labeled as O(11) and O(12A). The linkage between Co₄ is similar to that of Cu₄. The corresponding hydrogen bonds O···H and associated angles of hydrogen bonds H-O···H for Co₄ are listed in Table 5.11.

	Angle	Degree (°)	Hydrogen Bond	Length	O···O distance	Length (Å)
Co ₄ (intra)	O(2)-H(2)···O(11)	156.0	H(2)···O(11)	1.817(6)	O(2)···O(11)	2.671(2)
	O(12A)-H(6A)···O(6A)	150.0	H(6A)···O(12A)	1.811(9)	O(12A)···O(6A)	2.650(8)
	O(11)-H(112)···O(8)	170.8	H(112)···O(8)	1.902(4)	O(11)···O(8)	2.808(1)
	O(12A)-H(121)···O(4)	170.5	H(121)···O(4)	2.054(6)	O(12A)···O(4)	2.939(2)
(inter)	O(11)-H(111)···O(4)	163.5	H(111)···O(4)	1.835(4)	O(11)···O(4)	2.764(4)

Table 5.11 The hydrogen bond lengths and the associated angles in Co₄, **14**

Most of the bond lengths of O···H are around 1.8 Å, the distances of O···O are around 2.7 Å, and the angles are nearly 180°. The exception is the hydrogen bond formed between water molecule O(12A) and carboxylate group, with O···H 2.054(6) Å, O···O 2.939(2) Å, which shows rather a weak hydrogen bond.

5.2.3 The magnetic properties of Cu₄ and Co₄

5.2.3.1 The temperature dependence of χT product for Cu₄ and Co₄

The molar magnetic susceptibilities χ_M were measured on crystalline samples of Cu₄ and Co₄ in the temperature range 2-300K under applied magnetic field of 0.1T and 1T, and the results are shown in Fig. 5.15 for Cu₄ and Fig. 5.16 for Co₄ in the form of χT versus T.

The temperature dependence of χT product for Cu₄, 13

At room temperature, the χT product is 1.38 cm³ K mol⁻¹. This value is in agreement with the expected value for the presence of four isolated Cu(II) ions ($S = 1/2$, $C = 0.41$ cm³ K mol⁻¹) taking into account a g value of 2.1. When the temperature is lowered, the χT product at 1000 Oe increases continuously to reach a round maximum of 3.26 cm³ K mol⁻¹ around 15 K indicating dominant ferromagnetic interactions within the complex.

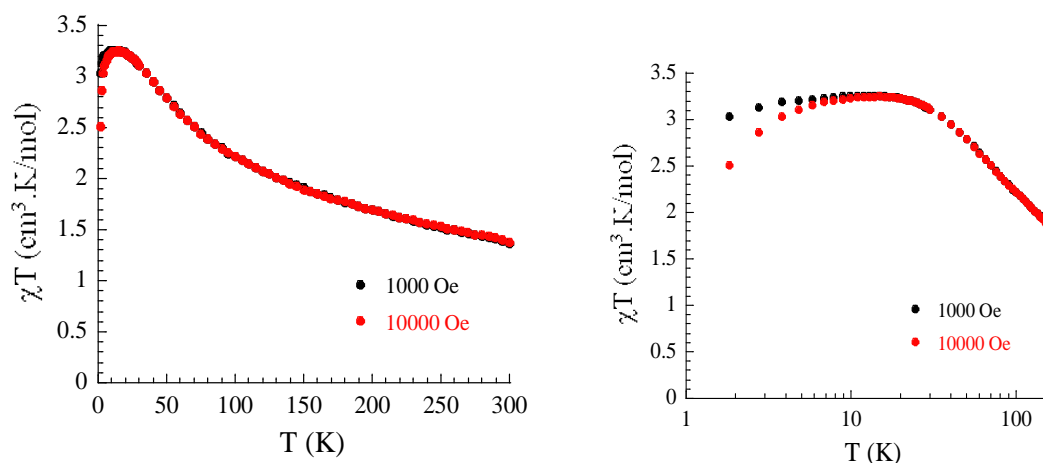


Figure 5.16 The temperature dependence of χT product at 0.1T and 1T for Cu_4 , **13**

Below 15 K, the χT product drops down to $3.05 \text{ cm}^3 \text{ K mol}^{-1}$ at 1.8 K suggesting the presence of weak antiferromagnetic interactions and/or a significant magnetic anisotropy. The experimental $(\chi T)_{max}$ at 15 K suggests that the total spin ground state of this compound is $S_T = 2$ with the four Cu(II) ions ferromagnetically arranged. The $S_T = 2$ ground state is also supported by the field dependence of the magnetization at low temperatures (see Fig. 5.18) at which the magnetization at 7 T and 1.8 K reaches $4.1 \mu_B$, and can be fit by a simple $S = 2$ Brillouin function.

The temperature dependence of χT product for Co_4 , 14

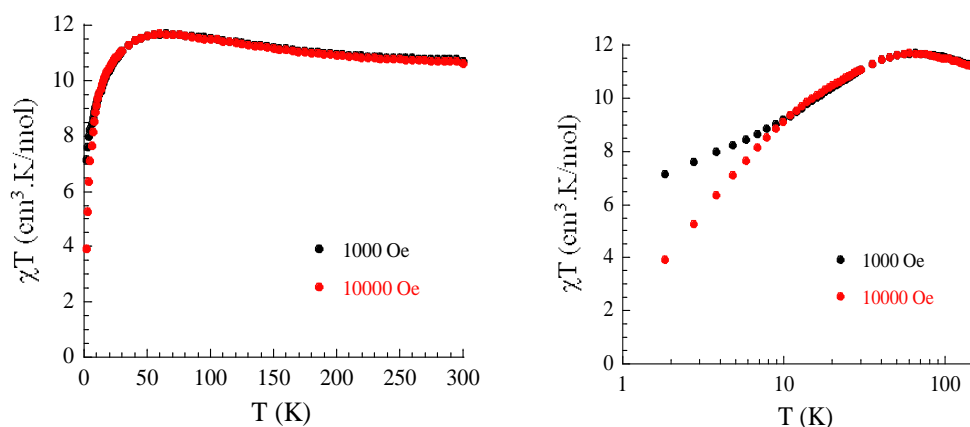


Figure 5.17 The temperature dependence of χT product for Co_4 at 0.1T and 1T for Co_4 , **14**

At room temperature, the χT product is $10.7 \text{ cm}^3 \text{ K mol}^{-1}$. This value is in good agreement with the expected value for the presence of four HS isolated Co(II) ions ($S = 3/2$, $C = 2.675 \text{ cm}^3 \text{ K mol}^{-1}$) taking into account a g value of $g_{\text{Co}} = 2.38$. When the temperature is lowered, the χT product at 1000 Oe increases steadily to reach the maximum of $11.75 \text{ cm}^3 \text{ K mol}^{-1}$

around 60 K and then continuously decreases to $7.17 \text{ cm}^3 \text{ K mol}^{-1}$ at 1.8 K. This behavior suggests ferromagnetic interactions are dominant between magnetic centers.

5.2.3.2 The field dependence of magnetization for Cu_4 and Co_4

The field dependence of magnetization for Cu_4 at 1.8 K reveals a true saturation above 3 T indicative of a weak or the absence of magnetic anisotropy. This is indeed not surprising considering that Cu(II) ions are weakly anisotropic metal ions. The saturation of M at $4.1 \mu_{\text{B}}$ is very close to the expected value of $4 \mu_{\text{B}}$ for four Cu(II) ($S = 1/2$) ions ferromagnetically coupled. It is worth noting that the fit of the M vs H data at 1.8 K by an $S = 2$ Brillouin function works well with a g value of 2.1, in very good agreement with χT vs T fit.

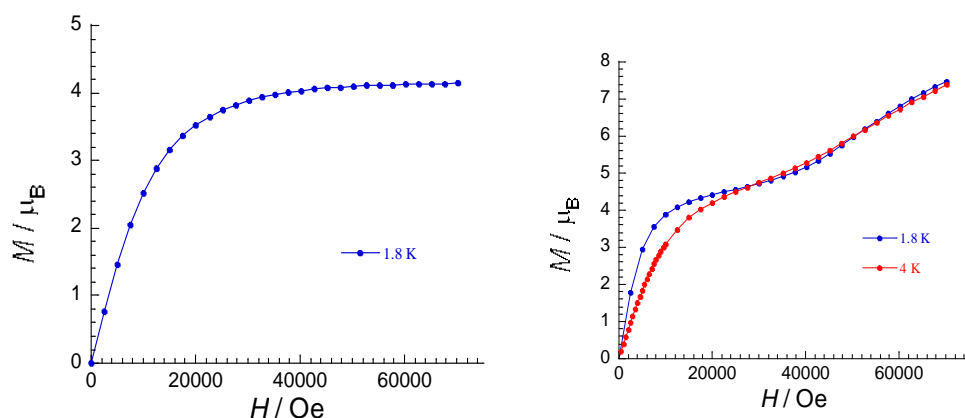


Figure 5.18 The field dependence of magnetization: a) for Cu_4 , **13**, at 1.8 K; b) for Co_4 , **14**, at 1.8 K and 4 K

The field dependence of the magnetization for Co_4 at 1.8 and 4 K shows that the magnetization abruptly increases to $3.9 \mu_{\text{B}}$ with the applied dc field up to 1 T. When the field is increased, the magnetization gradually reaches $4.7 \mu_{\text{B}}$ at 3 T. With the further increase of the field, the magnetization is going up again to reach $7.5 \mu_{\text{B}}$ at 7 T without saturation. This sigmoidal shape of magnetization indicates that the low-lying excited states are clearly populated when a dc field is applied. With the 1.8 K measurement there is a nearly constant magnetization value of $4 \mu_{\text{B}}$ which corresponds to the saturation of $S = 2$ from 1 T to 3 T. There are four Co^{2+} in the cubane and each of them can be in $S = 1/2$ (low spin) or $S = 3/2$ (high spin) states. So $4 \mu_{\text{B}}$ ($S = 2$) is consistent with four $S = 1/2$ low spins. With the field raised higher, the spins of some or all Co^{2+} ions cross the energy barrier to crossover from the low spin to the high spin state, as the magnetization is raised further. There is no step at $S = 3$

since this state is not stable for the cubane structure. To see whether there is step for $S = 4$, $S = 5$, $S = 6$, a broader field scan should be taken such as 0-20 T or 0-50 T instead of the routine program 0-7 T.

Although this system possesses a significant amount of magnetic anisotropy, the ac susceptibility shows no out-of-phase signal above 1.8 K.

5.2.3.3 The ESR spectrum of Cu_4 , 13

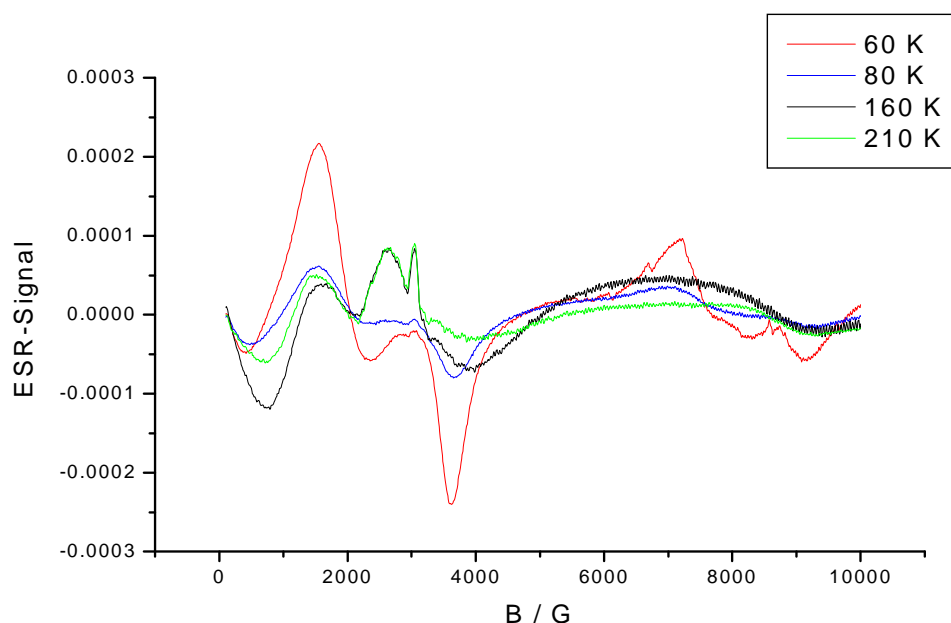


Figure 5.19 The ESR spectrum for Cu_4 at temperatures of 60K, 80K, 160K and 210K

The ESR spectrum of crystalline sample at 210K, 160K, 80K and 60K (Fig. 5.19) shows a broad isotropic copper(II) signal centered around a g value of 2.1.

The intensity of the ESR increases with the temperature decrease and multiple peaks appear at high temperature while two pronounced positive and negative appear at low temperature. This confirms that the ground state manifold is paramagnetic suggesting that the intracluster exchange couplings are predominantly ferromagnetic.

5.2.3.4 The least-squares nonlinear fittings of the magnetic properties of Cu₄, 13

Four metal ions Cu1, Cu2, Cu1', Cu2' occupy the vertices of a regular tetrahedron bridged by the O1, O5, O1', O5', which occupy the second regular tetrahedron thus forming a 4+2 type cubane (Fig. 5.20a).

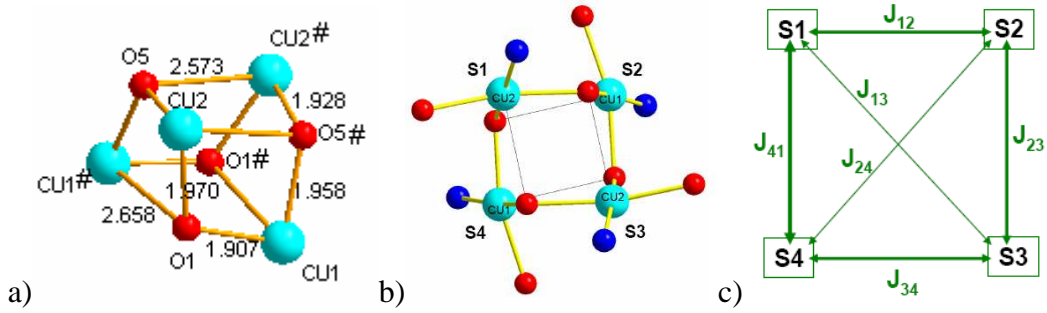


Figure 5.20 a) The cubane structure of Cu₄; b) Scheme of the spin topology for Cu₄; c) the interactions between spins

The four Cu(II) ions in the topology as Fig 5.20 b interact each other in the way shown in Fig.5.19c. Thus the Hamiltonian in zero field is as in Equation (5.2)

$$H = -J_{12} \cdot S_1 \cdot S_2 - J_{23} \cdot S_2 \cdot S_3 - J_{34} \cdot S_3 \cdot S_4 - J_{14} \cdot S_1 \cdot S_4 - J_{13} \cdot S_1 \cdot S_3 - J_{24} \cdot S_2 \cdot S_4 \quad \text{Eq. (5.2)}$$

When considering the similarity of bond lengths and angles, the approximation can be made that the interactions between two Cu ions with short Cu...Cu distance are the same, defined as J' and the interactions between two Cu ions (Cu1 with S2 and Cu1' with S4, Cu2 with S1 and Cu2' with S3) with long Cu...Cu distance are the same defined as J . Then

$$J_{13} = J_{24} = J, \quad J_{12} = J_{23} = J_{34} = J_{14} = J'$$

It is clear that J is much larger than J' . The zero-field spin Hamiltonian is then

$$H = -J (S_1 \cdot S_3 + S_2 \cdot S_4) - J' (S_1 \cdot S_2 + S_2 \cdot S_3 + S_3 \cdot S_4 + S_1 \cdot S_4) \quad \text{Eq. (5.3)}$$

or

$$H = -[(J - J')/2] \cdot (S_{AB}^2 + S_{CD}^2 - S_1^2 - S_2^2 - S_3^2 - S_4^2) - (J'/2) \cdot (S_T^2 - S_1^2 - S_2^2 - S_3^2 - S_4^2) \quad \text{Eq. (5.4)}$$

with

$$S_{AB} = S_1 + S_3, S_{CD} = S_2 + S_4, S_T = S_A + S_B$$

The energy of E (S_T, S_{AB}, S_{CD}) is expressed as

$$E(S_T, S_{AB}, S_{CD}) = -[(J - J')/2] \cdot [S_{AB}(S_{AB} + 1) + S_{CD}(S_{CD} + 1)] - (J'/2) \cdot S_T(S_T + 1) \quad \text{Eq. (5.5)}$$

With $E(0, 0, 0) = 0$ as the energy origin, it follows that:

$$\begin{aligned} E(0, 0, 0) &= 0, & E(1, 0, 1) &= -J, & E(1, 1, 0) &= -J, \\ E(0, 1, 1) &= -2J + 2J', & E(1, 1, 1) &= -2J + J', & E(2, 1, 1) &= -2J - J' \end{aligned}$$

Raising the energy to $2J$ higher, then

$$\begin{aligned} E(0, 0, 0) &= 2J, & E(1, 0, 1) &= J, & E(1, 1, 0) &= J, \\ E(0, 1, 1) &= 2J', & E(1, 1, 1) &= J', & E(2, 1, 1) &= -J' \end{aligned}$$

Then the magnetic susceptibility can be calculated from the common Van Vleck equation

$$\chi = \frac{N\mu_B^2 g^2}{4KT} \cdot \frac{10e^{\frac{J'}{kT}} + 2e^{\frac{-J'}{kT}} + 4e^{\frac{-J}{kT}}}{5e^{\frac{J'}{kT}} + 3e^{\frac{-J'}{kT}} + e^{\frac{-2J'}{kT}} + 6e^{\frac{-J}{kT}} + e^{\frac{-2J}{kT}}} \quad \text{Eq. (5.6)}$$

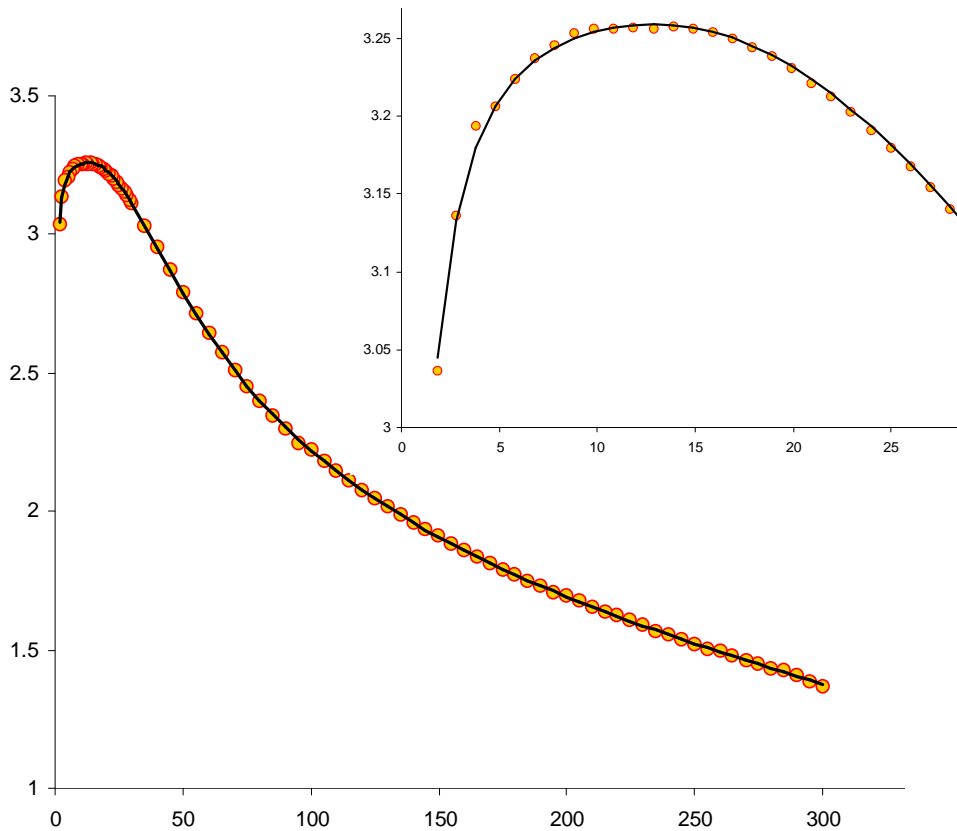


Figure 5.21 The fitting of χT versus temperature for Cu_4 , **13**

The best fit (Fig. 5.21) was obtained for the following parameters set: $g = 2.11$, $J = 37.53 \text{ cm}^{-1}$ and $J' = -4.26 \text{ cm}^{-1}$. The agreement factor R is 1.1×10^{-6} ($R = \sum[(\chi_M)^{\text{obs}} - (\chi_M)^{\text{calc}}]^2 /$

$[(\chi_M)^{\text{obs}}]^2$). The positive J value reveals strong ferromagnetic interactions between two intra-dimeric Cu(II) ions and the small negative J' value shows the weak antiferromagnetic interactions between two inter-dimeric Cu(II) ions.

The best fit for the M vs. H at 1.8K with an $S = 2$ Brillouin function (Fig. 5.22) is working very well and the obtained g value 2.07 is consistent with the value 2.11 obtained in the simulation of χT vs. temperature.

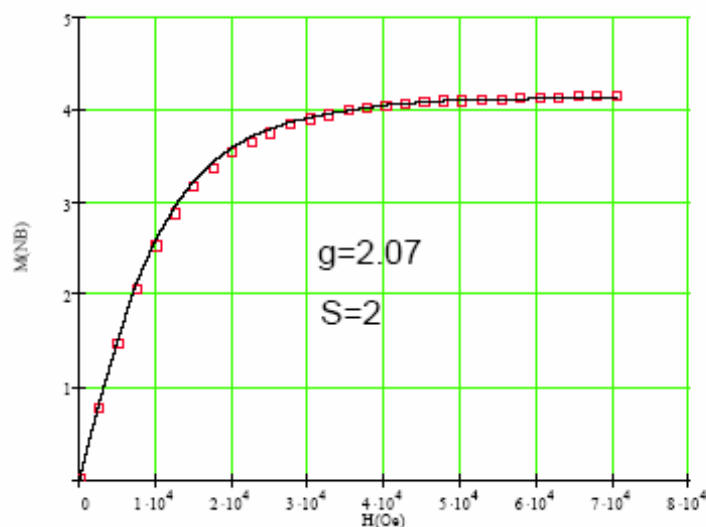


Figure 5.22 the fit of the M vs. H at 1.8K for Cu₄, 13

5.2.3.5 The least-squares nonlinear fittings of magnetic properties of Co₄, 14

As expected for Co(II) systems, clearly no one model is able to reproduce even the simple temperature dependence of the χT product (see Appendix). The data could not be fitted below 70K since it is generally a very hard task to model exchange coupling, spin-orbit coupling and zero-field splitting effects unambiguously when these effects are of similar magnitude.

A Brillouin function for each of the ground states (see Appendix) is not working well even at low fields. The reason for it is that Co(II) is an anisotropic spin (possibly Ising type) and thus does not follow a Brillouin function.

5.3 Summary

The ligand, H₃cpidp, captures Fe(III) ions into Fe₈ clusters with a high symmetry of S₄. The nitrogen atoms on the ligands were not involved in the chelating mode, while all the carboxylate groups take part in chelating. The four Fe(III) ions and four μ-O₃ atoms form an eight-membered ring and each of the μ-O₃ atom on the ring extend to link the other four Fe(III) ions. This high symmetry structure resulted in disappointing magnetic properties since it has an S = 0 ground spin state.

The ligand, H₃cpdea, captures Cu(II) and Co(II) into M₄ cubane structures. The deprotonated hydroxyl oxygens coordinate to three transition metals sitting on the alternate edges of the cubane. Cu₄ and Co₄ have similar core structures with Cu₄ more distorted than Co₄ as a normal cubane, thus Cu₄ was also considered as a pseudo-dimeric molecule. The crystal waters in Cu₄ form intra-molecule hydrogen bonds while the crystal waters in Co₄ form inter-molecule hydrogen bonds along the *c* axis in addition to the intra-molecule bonds. The magnetic interaction between Cu-Cu inside the pseudo-dimer is ferromagnetic while that between Cu-Cu between the pseudo-dimer is antiferromagnetic. Thus Cu₄ reaches its ground spin state of S = 2 at low temperatures while the spin state of Co₄ is difficult to obtain and seems to involve a spin-crossover from S = 3/2 to S = 1/2 on the individual Co(II) centres.

Chapter 6 Conclusions

The work is composed of three parts, each of which focused on illustrating one kind of cluster aggregate. **Chapter 3** describes the thermal behaviour of $\text{Cu}_{44}\cdot 81\text{H}_2\text{O}$, which had been originally obtained by a former member of the research group. **Chapter 4** describes a series of analogous Ln-Cu 2-D coordination polymers, which could be synthesized with most of the lanthanide(III) ions. **Chapter 5** describes the synthesis and magnetic behaviour of transition metal aggregates which were obtained from self-assembly reactions, in which the ligands had been modified by adding a phenyl ring and hydroxyl groups.

In **Chapter 3**, the large cluster $\text{Cu}_{44}\cdot 81\text{H}_2\text{O}$ was obtained in high yield according to the former recipe with the ligand H_3ntp .

With the help of the TGA curve, Cu_{44} was found to partially maintain its crystalline structure at the high temperature of 180°C after the lattice waters had been driven off, while the coordinated waters remain and maintain the stability of the structure. The crystalline stability of Cu_{44} at high temperatures indicates that it might be a good candidate for guest-absorption systems especially given the large cavities in the structure.

The 81 crystal waters were lost at the lowest temperature range in an endothermic process. In the second step, several components were lost. In this second step, the two Br^- counterions were lost at first as HBr , then the eight μ -coordinated Br as HBr (8 H atoms are taken from 8 coordinated waters), then the last 18 coordinated waters, then 12 NEt_3 from the decomposition of the organic backbone. In the third step, the carboxylic groups are decomposed to give 36CO_2 . In the fourth step at a temperature around 600°C , the two μ_8 - Br atoms are driven out as HBr (two H atoms are taken from two μ - OH). In the last fifth step, the μ - OH network is broken to give 44CuO .

The above thermal process was followed using IR and X-ray powder diffraction.

In **Chapter 4**, the series of compounds $[\text{Cu}_2\text{Ln}(\text{cpida})_2(\text{NO}_3)(\text{H}_2\text{O})_4]\cdot\text{H}_2\text{O}$ was obtained using the ligand, H_3cpida , to capture copper(II) and lanthanide(III) nitrate salts in aqueous solvent. Compounds of this type could be obtained with La^{3+} , Ce^{3+} , Pr^{3+} , Nd^{3+} , Sm^{3+} , Eu^{3+} , Gd^{3+} ,

Dy³⁺, Ho³⁺, Er³⁺. The lanthanide contraction has an effect on the Ln-N and Ln-O bond lengths, which decrease with the increasing atomic number along the lanthanide(III) series.

The phenyl ring on the ligand helps to produce a 2D-dimensional sheet {Cu₂Ln}_x by π - π stacking between the phenyl rings in the neighboring layers. The π - π interaction is rather strong with a very short ring distance of 3.35 Å (normally 3.3-3.7 Å). The 2D {Cu₂Ln}_x sheet extends in the way that along the *b* axis there are only Cu-Cu connections while along the *a* axis only Cu-Gd connections.

The magnetic interactions can be directly detected by DC measurements for {Cu₂Ln} and {Cu₂Gd}, in which there are weak antiferromagnetic Cu-Cu interactions along *b* axis and no Gd-Cu interactions along *a* axis.

In **Chapter 5**, two kinds of cluster were synthesized, one of which is an Fe₈ cluster and the other is an M₄ (M = Cu²⁺ or Co²⁺) cubane cluster. The structure of Fe₈ is new while the structure of M₄ is similar to many literature examples of Cu₄ and Co₄ cubanes.

In the Fe₈ cluster, there are two chemically-distinct Fe(III), with four Fe(III) ions belonging to each of them. The inner four Fe(III) ions are linked to each other by μ_3 -O ligands, thus the four Fe³⁺ and four O form an eight-membered ring. The four μ_3 -O extend outwards to bridge to the remaining four Fe³⁺ ions, so that the structure can be considered as a cyclic system of four corner-sharing Fe₃O triangles. Because of the high symmetry of the Fe₈, it shows an S = 0 ground spin state.

Since the ligand, H₃cpidp, was not fully deprotonated and the nitrogen atom was not involved in the coordination, there could be room for using H₃cpidp to capture irons into more versatile larger structures.

The core structure of the Cu₄ cubane is more distorted than that of the Co₄ cubane, showing a Jahn-Teller elongation axis for the Cu(II) ions. The Cu₄ can also be regarded as two linked pseudo-dimers. There are two long Cu-O bonds and two short Cu-O bonds within the pseudo-dimer, and between two pseudo-dimers there are four medium length Cu-O bonds. The Cu-Cu interactions in the pseudo-dimers are ferromagnetic. The Cu-Cu interactions between the pseudo-dimers are anti-ferromagnetic. Cu₄ has an S = 2 ground spin state.

The Co-O bonds in Co_4 are all similar at around 2.0 \AA , thus forming a less distorted cubane than for Co_4 . The higher temperature behavior of χT versus temperature indicates dominant ferromagnetic interactions, while at lower temperatures the effect of a weak antiferromagnetic interaction or anisotropic effect can be seen. There is a stepwise increase of magnetization, with a transition at a constant value at $S = 2$, which indicates a spin-crossover phenomenon.

Chapter 7 Experimental

To characterize the compounds and investigate the chemical and physical properties, the following analytical techniques have been carried out. For different experimental aims, not every analytical experiment is applied to all of the compounds.

7.1 Analytical methods

7.1.1 NMR spectroscopy

The ^1H NMR and ^{13}C NMR were used to identify the ligands that were synthesized throughout the whole thesis work. The organic ligands were analyzed on the Bruker AC 250 spectrometer at the department of inorganic chemistry at Karlsruhe University. The deuterium solvents were chosen as D_2O or DMSO-D_6 according to the polarity of the ligands.

7.1.2 Infra-red spectroscopy

Infra-red spectroscopy was applied to identify the organic ligands and the metal-ligand clusters. As a "fingerprinting" method, IR was routinely used, especially to identify whether the same ligand captures the metal ions into the same structure with different metals or by different inorganic synthetic methods.

A small amount of the sample to be measured was ground together with absolutely dry KBr into fine powder. This was then pressed into a transparent disk by evacuated pumping under a force of 10 N.

Fourier Transform IR measurements were carried out on a Perkin-Elmer Spectrum instrument. The spectra were taken in the normal range between 4000 cm^{-1} and 400 cm^{-1} using 16 scans at a resolution of 4 cm^{-1} .

7.1.3 Simultaneous Thermal Analysis (STA)

The combination of a NETZSCH thermobalance with a DTA measuring head makes up the simultaneous thermal analyzer. The mass change and the temperature difference are measured. The advantage is that both signals from the same sample are measured under exactly the same conditions at the same time.

About 20mg crystalline sample was taken on one of the measuring heads with NaCl powder on the other measuring head as reference. The heating program was set at the step of 10°C/min in the range of 20-800°C under N₂ atmosphere. The TGA and DTA measurement were carried out simultaneously.

7.1.4 X-ray single crystal measurements

Single crystal X-ray structure analysis is one of the most powerful and useful methods for analyzing the structure of molecules in the single crystal form. The data were collected using Stoe IPDS I and IPDS II imaging plates, either a Stoe STADI-4 four circle detector, or area-detector diffractometer, a Bruker SMART Apex CCD detector. Then they are refined using SHELXTL software.

To check the obtained structure from the program of SHELXTL, the following factors are important.

First, the residual factors. R_1 is defined as:

$$R_1 = \{ \sum | |F_o| - |F_c| | \} / \{ \sum |F_o| \}$$

Traditional calculation of R_1 only takes account of the data with $|F_o| \geq 4\sigma(|F_o|)$, σ is the standard uncertainty. $|F_o|$ is the data of the diffraction intensity, background exposure time and others from the raw data after the process of data collection, data reduction and correction. $|F_c|$ is the corresponding calculated data after structure analyzing. $R_1 < 0.05$ normally indicates good structure analysis.

wR_2 is defined as:

$$wR_2 = \{ \sum [w(F_o^2 - F_c^2)^2] / \sum [w(F_o^2)^2] \}^{1/2}$$

The value w is the weight for each diffraction point. According to the weighting scheme, w is defined as:

$$w = 1/\sigma^2$$

wR_2 is sensitive to the little difference for the structure analysis, such as the disorder of atoms and the defined H atoms. Normally wR_2 can be lower than 0.15 when the data is nice, but 0.2 is still acceptable.

Then another important guideline for the quality of the structure analysis is the goodness-of-fit which is defined as:

$$S = \{ \sum | [w(F_o^2 - F_c^2)^2] / (n - p) \}^{1/2}$$

where n and p are the number of the unique reflections and the number of parameters that involves in the structure refinement. When S is far from 1.0, it indicates that the weighting scheme could be wrong and should be made better if the collected data is fine.

7.1.5 X-ray powder diffraction

The PXRD in this thesis research was applied to identify the purity of the sample ($\text{Cu}_{44}\cdot 81\text{H}_2\text{O}$), detect the thermo-decomposition process and identify the end-product CuO of the decomposition process. With this simple purpose the diffraction intensity was not indexed with hkl.

The samples are ground into fine powder, and mounted on a round disk with grease between two plastic sheets and placed on the STOE STADI P X-ray powder diffractometer. The measurements were made using the Cu- $K\alpha_1$ radiation with $\lambda = 1.5406\text{\AA}$. The collected data were analyzed with the software WinX^{Pow} which gives out the graph with diffraction intensities and the 2θ values.

7.1.6 Magnetic measurement

This method is used to search into the magnetostructures of the compounds, such as the intra-magnetic interactions, inter-magnetic interactions. The measurements were taken on a Superconducting Quantum Interference Devices (SQUID) with direct currents or DC fields.

The polycrystalline samples are ground into a fine powder, weighed exactly to 0.1 mg and mounted on the Quantum Design MPMS-XL magnetometer with maximum external field of 7 T.

7.2 Synthesis

The synthesis had two aspects. One is the synthesis of the organic ligands, while the other is synthesizing the metal clusters with the selected transition metal or lanthanide ions and the ligands. One of the four ligands used in the work, H₃ntp, was commercially obtained while the other three ligands, H₃cpida, H₃cpidp and H₃cpdea, were synthesized using amino acids. Using these four ligands, different metal clusters are obtained.

7.2.1 The synthesis of ligands

Preparation of (2-carboxylic) phenyl iminodiacetic acid (H₃cpida)

The compounds chloroacetic acid (9.45g, 0.1mol), anthranilic acid (6.86g, 0.05mol), and sodium hydroxide (10g, 0.25mol) were dissolved in water (70ml). The mixture was heated on an oil bath under reflux for 24 hours, then was allowed to cool to room temperature. The solution was acidified with concentrated HCl to pH = 2 and the yellow powder was collected as the final product in 53% yield.

Preparation of (2-carboxylic) phenyl iminodipropionic acid (H₃cpidp)

A solution of anthranilic acid (13.71g, 0.1mol) and NaOH (4g, 0.1mol) in H₂O (20ml) was heated to 70°C using an oil bath. With the temperature kept constant at 70°C, a solution of 3-bromopropionic acid (22g, 0.202mol) and NaHCO₃ (17g, 0.202mol) in H₂O (30ml) was added in small portions into the anthranilic-NaOH-H₂O solution while adding an aqueous solution (20ml) of NaOH (8g, 0.2mol) to keep the pH ~11. The resulting solution was allowed to cool to room temperature and stirred for a further 48 hours. Then the solution was acidified to pH = 2 with concentrated HCl and left undisturbed to stand overnight. White needle shaped crystals were collected in 15% yield. ¹H NMR (DMSO-d₆): 2.53ppm (t, 4H, 2CH₂), 3.86ppm

(t, 4H, 2CH₂), 7.58ppm (m, 1H, C₆H₄), 7.70ppm (m, 2H, C₆H₄), 8.06ppm (m, 1H, C₆H₄); ¹³C NMR (DMSO-d⁶): 29.76ppm (2CH₂), 53.98ppm (2CH₂), 121.86ppm (C₆H₄), 127.81ppm (C₆H₄), 130.50ppm (C₆H₄), 131.30ppm (C₆H₄), 134.43ppm (C₆H₄), 138.85ppm (C₆H₄), 171.21ppm (COOH), 173.71ppm (2COOH).

Preparation of (2-carboxylic) phenyl diethanolamine (H₃cpdea)

To a solution of anthranilic acid (13.71g, 0.10mol) and KOH (5.67g, 0.101mol) in 30 ml water, 2-bromo-ethanol (14ml, 0.20mol) was added. The mixture was kept heated on an oil bath under reflux. A solution of KOH (16.83g, 3mol) in H₂O (60ml) was added in small portions over 30 minutes. Then 3ml 2-bromo-ethanol (2ml, 0.03mol) was added in two portions over the following one hour. The mixture was cooled to room temperature and the byproduct extracted using diethyl ether. Then the pH was adjusted to pH = 2 using concentrated HBr, and the solution was left to stand for one week. The product was collected as white needle crystals, and recrystallised from acetone in 30% yield.

7.2.2 Inorganic synthesis

Preparation of [Cu^{II}₄₄(μ₈-Br)₂(μ₃-OH)₃₆(μ-OH)₄Br₈(ntp)₁₂(H₂O)₂₈].Br₂·81H₂O, 1

The compound was prepared as described previously^[35].

Preparation of [Cu^{II}₂(cpida)₂La^{III}(NO₃)(H₂O)₄].2H₂O, 2

To a mixed MeOH/H₂O (3ml : 3ml) solution of Cu(NO₃)₃·3H₂O (0.046 g, 0.19 mmol) and La(NO₃)₃·6H₂O (0.028 g, 0.065 mmol), a solution of H₃cpida (0.048 g, 0.19 mmol) and NaOH (0.012 g, 0.3 mmol) in MeOH (3 ml) / H₂O (3 ml) was added with stirring. The clear blue solution was left to stand. After two days green block shaped crystals of [Cu₂(cpida)₂La(NO₃)(H₂O)₄].2H₂O appear. Yield: 42%

Preparation of [Cu^{II}₂(cpida)₂Ln^{III}(NO₃)(H₂O)₄]·H₂O, 3-11

The preparation of [Cu^{II}₂(cpida)₂Ln^{III}(NO₃)(H₂O)₄]·2H₂O (Ln = Ce, Pr, Nd, Sm, Eu, Gd, Dy, Ho, Er) was the same with that of [Cu^{II}₂(cpida)₂La^{III}(NO₃)(H₂O)₄]·H₂O. Ln = Ce, Pr, Nd, Sm, Eu, Gd, Dy, Ho, Er correspond to **3, 4, 5, 6, 7, 8, 9, 10, 11** respectively.

Preparation of [Fe^{III}₈(μ₃-O)₄(μ-OMe)₄(Hcpidp)₄(H₂O)₄](NO₃)₄·10H₂O·4MeOH, 12

To a solution of Fe(NO₃)₃·9H₂O (0.202 g, 0.50 mmol) in MeOH (15 ml), a solution of H₃cpidp (0.062 g, 0.25 mmol) and KOH (0.042 g, 0.75 mmol) in MeOH (15 ml) was added slowly with stirring. The above solution was further stirred for one hour, then left to stand undisturbed. After 15 days, orange block crystals [Fe^{III}₈(μ₃-O)₄(μ-OMe)₄(Hcpidp)₄(H₂O)₄](NO₃)₄·10H₂O·4MeOH had formed. Yield: 34%

Preparation of [Cu^{II}₄(cpdea)₄]·2H₂O, 13

To a solution of Cu(NO₃)₂·3H₂O (0.242 g, 1 mmol) in the solvent mixture CH₃OH (15 ml) and H₂O (5 ml), a solution of H₃cpdea (0.181 g, 1 mmol) and Et₃N (0.42 ml, 3 mmol) in the solvent mixture CH₃OH (15 ml) and H₂O (5 ml) was added with stirring. The resulting clear sky blue solution was filtered and left to stand undisturbed. After two days blue block crystals [Cu^{II}₄(cpdea)₄]·2H₂O appeared. Yield: 47%.

Preparation of [Co^{II}₄(cpdea)₄]·3.3H₂O, 14

To a solution of CoCl₂·6H₂O (0.120 g, 0.5 mmol) in the solvent mixture EtOH (24 ml) and H₂O (6 ml), a solution of H₃cpdea (0.112 g, 0.5 mmol) and Et₃N (0.350 ml, 2.5 mmol) in the solvent mixture EtOH (20 ml) and H₂O (5 ml) was added with stirring. The resulting solution was filtered and the resulting pink-violet solution was left to stand undisturbed. After two weeks pink-orange colored block shaped crystals [Co^{II}₄(cpdea)₄]·3.3H₂O appeared. Yield: 32%

Chapter 8 Crystal structure data

The information about the crystal measurement and the resulted structure data, such as selected bond lengths and angles for compound 2 to 14 are listed here. The structure data for compound 1 could be found in the former thesis^[35].

Compound	2	3	4	5
Formula	C ₂₂ H ₂₈ Cu ₂ LaN ₃ O ₂₁	C ₂₂ H ₂₈ Cu ₂ CeN ₃ O ₂₁	C ₂₂ H ₂₈ Cu ₂ PrN ₃ O ₂₁	C ₂₂ H ₂₈ Cu ₂ NdN ₃ O ₂₁
Formula Weight	936.46	937.67	938.47	941.80
Crystal System	Monoclinic	Monoclinic	Monoclinic	Monoclinic
Space Group	C 2/c	C 2/c	C 2/c	C 2/c
a / Å	17.2401(15)	17.1998(16)	17.1735(9)	17.1387(7)
b / Å	9.7163(6)	9.7028(7)	9.6994(5)	9.7117(4)
c / Å	18.1615(15)	18.1090(16)	18.0266(9)	18.0026(7)
α / °	90	90	90	90
β / °	103.083(7)	103.123(7)	102.837(1)	102.858(1)
γ / °	90	90	90	90
V / Å ³	2963.3(4)	2943.2(4)	2927.7(3)	2921.3(2)
Z	4	4	4	4
T / K	150	150	100	100
F (000)	1816	1820	1824	1828
D _c / mg·m ⁻³	2.059	2.075	2.088	2.100
μ (Mo-K α)/mm ⁻¹	2.934	3.049	3.175	3.291
Crystal Size/mm	0.35×0.29×0.25	0.32×0.27×0.19	0.26×0.23×0.19	0.25×0.23×0.21
Diffractometer	Stoe IPDS II	Stoe IPDS II	Bruker SMART Apex	Bruker SMART Apex
Measurement	Area detector	Area detector	CCD detector	CCD detector
Data Measured	10501	11484	8863	6739
Unique Data	2857	3115	3337	3249
R _{int}	0.0476	0.0202	0.0219	0.0158
gt (I>2 σ (I))	2600	2845	3071	2928
Completeness 2 θ →50°	99.6%	99.1%	99.7%	99.4%
wR ₂ (all data)	0.1065	0.0806	0.0695	0.0667
S (all data)	1.053	1.038	1.048	1.043
R _I (gt)	0.0388	0.0291	0.0282	0.0257
Para./restr.	235/6	236/6	235/6	235/6
max.peak/hole	+0.76/-1.63	+1.00/-0.99	+0.81/-0.59	+0.86/-0.52
Appearance	Green block	Green block	Green block	Green block

Compound	6	7	8	9
Formula	C ₂₂ H ₂₈ Cu ₂ SmN ₃ O ₂₁	C ₂₂ H ₂₈ Cu ₂ EuN ₃ O ₂₁	C ₂₂ H ₂₈ Cu ₂ GdN ₃ O ₂₁	C ₂₂ H ₂₈ Cu ₂ DyN ₃ O ₂₁
Formula Weight	947.92	949.52	954.81	960.06
Crystal System	Monoclinic	Monoclinic	Monoclinic	Monoclinic
Space Group	C 2/c	C 2/c	C 2/c	C 2/c
a / Å	17.1402(17)	17.1217(7)	17.1243(7)	17.1905(6)
b / Å	9.7044(10)	9.7075(4)	9.7077(4)	9.7245(4)
c / Å	17.9243(18)	17.9010(7)	17.8714(8)	17.7725(7)
α / °	90	90	90	90
β / °	102.813	102.760(1)	102.812(1)	102.581(1)
γ / °	90	90	90	90
V / Å ³	2907.2(5)	2901.4(2)	2896.9(2)	2899.67(19)
Z	4	4	4	4
T / K	100	100	100	100
F (000)	1836	1840	1844	1852
D _c / mg·m ⁻³	2.125	2.132	2.148	2.158
μ(Mo-Kα)/mm ⁻¹	3.541	3.686	3.816	4.102
Crystal Size/mm	0.36×0.33×0.29	0.27×0.24×0.22	0.24×0.21×0.19	0.26×0.21×0.15
Diffractionmeter	Bruker SMART Apex	Bruker SMART Apex	Bruker SMART Apex	Bruker SMART Apex
Measurement	CCD detector	CCD detector	CCD detector	CCD detector
Data Measured	9940	7216	9897	7144
Unique Data	3314	3278	3301	3237
R _{int}	0.0180	0.0190	0.0183	0.0177
gt (I>2σ(I))	3182	3015	3141	3076
Completeness 2θ→50°	99.7%	99.9%	99.8%	99.2%
wR ₂ (all data)	0.0631	0.0655	0.0520	0.0834
S (all data)	1.059	1.041	1.042	1.079
R _I (gt)	0.0248	0.0253	0.0203	0.0344
Para./restr.	235/6	235/6	235/6	235/6
max.peak/hole	+1.21/-0.46	+1.08/-0.44	+0.78/-0.41	+1.65/-0.90
Appearance	Green block	Green block	Green block	Green block

Compound	10	11	12	13
Formula	$C_{22}H_{28}Cu_2HoN_3O_{21}$	$C_{22}H_{28}Cu_2ErN_3O_{21}$	$C_{60}H_{108}Fe_8N_8O_{62}$	$C_{44}H_{56}Cu_4N_4O_{18}$
Formula Weight	962.49	964.82	2380.34	1183.09
Crystal System	Monoclinic	Monoclinic	tetragonal	Monoclinic
Space Group	C 2/c	C 2/c	I-4c2	C 2/c
a / Å	17.1737(11)	17.2021(6)	18.3508(8)	21.6055(14)
b / Å	9.7183(6)	9.7206(4)	18.3508(8)	15.3540(10)
c / Å	17.7148(12)	17.6493(7)	26.8560(13)	17.1037(11)
$\alpha / ^\circ$	90	90	90	90
$\beta / ^\circ$	102.701(1)	102.759	90	126.892(1)
$\gamma / ^\circ$	90	90	90	90
V / Å ³	2884.2(3)	2878.35(19)	9043.8(7)	4537.7(5)
Z	4	4	4	4
T / K	100	100	150	100
F (000)	1856	1860	4912	2432
D _c / mg·m ⁻³	2.175	2.185	1.748	1.732
μ (Mo-K α)/mm ⁻¹	4.277	4.452	1.364	1.933
Crystal Size/mm	0.12×0.06×0.03	0.15×0.08×0.03	0.17×0.15×0.11	0.42×0.34×0.23
Diffractionmeter	Bruker SMART Apex	Bruker SMART Apex	Stoe IPDS II	Bruker SMART Apex
Measurement	CCD detector	CCD detector	Area detector	CCD detector
Data Measured	7096	9812	24359	13547
Unique Data	3226	3228	4815	5134
R _{int}	0.0371	0.0220	0.0405	0.0334
gt (I>2 σ (I))	2820	3037	4360	4233
Completeness 2 θ →50°	99.8%	99.6%	99.6%	99.8%
wR ₂ (all data)	0.0833	0.0564	0.1387	0.0720
S (all data)	1.040	1.038	1.053	0.993
R _f (gt)	0.0356	0.0241	0.0549	0.0329
Para./restr.	235/6	235/6	313/19	328/4
max.peak/hole	+1.56/-0.89	+0.90/-0.52	+0.77/-0.84	+0.53/-0.36
Appearance	Green block	Green block	Orange block	Blue block

Compound	14
Formula	$C_{44}H_{58.6}Co_4N_4O_{19.3}$
Formula Weight	1188.08
Crystal System	Monoclinic
Space Group	$C 2/c$
$a / \text{\AA}$	21.7852(15)
$b / \text{\AA}$	15.5860(12)
$c / \text{\AA}$	17.2027(12)
$\alpha / ^\circ$	90
$\beta / ^\circ$	127.364(4)
$\gamma / ^\circ$	90
$V / \text{\AA}^3$	4642.5(6)
Z	4
T / K	150
F (000)	2456
$D_c / \text{mg}\cdot\text{m}^{-3}$	1.702
$\mu(\text{Mo-K}\alpha)/\text{mm}^{-1}$	1.490
Crystal Size/mm	0.19×0.15×0.08
Diffractometer	Stoe IPDS II
Measurement	Area detector
Data Measured	14270
Unique Data	4900
R_{int}	0.0418
gt ($I > 2\sigma(I)$)	4009
Completeness $2\theta \rightarrow 50^\circ$	99.5%
wR_2 (all data)	0.1151
S (all data)	0.991
R_j (gt)	0.0437
Para./restr.	365/7
max.peak/hole	+0.59/-0.90
Appearance	Pinkish orange block

Table A-1. Selected bond lengths [Å] and angles [°] for compound 2

La(1)-O(7)#1	2.514(1)	La(1)-O(11)	2.592(3)	Cu(1)-O(1)	2.175(2)
La(1)-O(7)	2.514(1)	La(1)-O(8)#1	2.595(3)	Cu(1)-O(2)#2	1.931(2)
La(1)-O(6)#1	2.586(1)	La(1)-O(8)	2.595(3)	Cu(1)-O(3)	1.943(2)
La(1)-O(6)	2.586(1)	La(1)-O(5)#1	2.774(2)	Cu(1)-O(5)	1.975(3)
La(1)-O(11)#1	2.592(3)	La(1)-O(5)	2.774(2)	Cu(1)-N(1)	2.034(3)
O(7)-La(1)-O(7)#1	158.3(2)	O(11)-La(1)-O(5)	68.6(7)	O(5)-Cu(1)-N(1)	90.0(5)
O(7)-La(1)-O(6)#1	69.1(1)	O(11)-La(1)-O(5)#1	93.52(2)	O(5)-Cu(1)-O(1)	94.5(0)
O(7)-La(1)-O(6)	115.4(3)	O(8)-La(1)-O(8)#1	68.9(5)	O(5)-Cu(1)-O(1)#2	89.3(3)
O(7)-La(1)-O(11)#1	124.8(5)	O(8)-La(1)-O(5)	66.7(8)	O(5)-Cu(1)-O(7)	54.4(9)
O(7)-La(1)-O(11)	76.8(1)	O(8)-La(1)-O(5)#1	131.8(8)	O(5)-Cu(1)-O(4)	143.7(4)
O(7)-La(1)-O(8)#1	84.8(2)	O(5)-La(1)-O(5)	160.9(2)	N(1)-Cu(1)-O(1)	80.2(1)
O(7)-La(1)-O(8)	77.3(1)	O(2)#2-Cu(1)-O(3)	94.6(7)	N(1)-Cu(1)-O(1)#2	138.6(1)
O(7)-La(1)-O(5)	68.0(9)	O(2)#2-Cu(1)-O(5)	93.8(4)	N(1)-Cu(1)-O(7)	124.0(2)
O(7)-La(1)-O(5)#1	115.8(3)	O(2)#2-Cu(1)-N(1)	172.5(8)	N(1)-Cu(1)-O(4)	64.3(7)
O(6)-La(1)-O(6)#1	157.6(7)	O(2)#2-Cu(1)-O(1)	93.1(8)	O(1)-Cu(1)-O(1)#2	141.0(6)
O(6)-La(1)-O(11)#1	72.8(8)	O(2)#2-Cu(1)-O(1)#2	47.8(8)	O(1)-Cu(1)-O(7)	63.8(5)
O(6)-La(1)-O(11)	86.6(3)	O(2)#2-Cu(1)-O(7)	54.5(3)	O(1)-Cu(1)-O(4)	105.1(0)
O(6)-La(1)-O(8)#1	129.5(6)	O(2)#2-Cu(1)-O(4)	114.7(4)	O(1)#2-Cu(1)-O(7)	88.0(0)
O(6)-La(1)-O(8)	71.4(8)	O(3)-Cu(1)-O(5)	148.9(0)	O(1)#2-Cu(1)-O(4)	93.8(0)
O(6)-La(1)-O(5)	47.9(3)	O(3)-Cu(1)-N(1)	85.1(6)	O(7)-Cu(1)-O(4)	161.6(1)
O(6)-La(1)-O(5)#1	127.2(9)	O(3)-Cu(1)-O(1)	114.8(0)	Cu(1)-O(1)-Cu(1)#2	168.9(4)
O(11)-La(1)-O(11)#1	48.4(2)	O(3)-Cu(1)-O(1)#2	74.6(8)	Cu(1)-O(5)-La(1)	144.2(7)
O(11)-La(1)-O(8)#1	143.8(0)	O(3)-Cu(1)-O(7)	147.7(5)		
O(11)-La(1)-O(8)	134.1(8)	O(3)-Cu(1)-O(4)	21.1(6)		

Symmetry transformation used to generate equivalent atoms: #1(1-x, y, 0.5-z);
#2 (0.5-x, 0.5+y, 0.5-z)

Table A-2. Selected bond lengths [\AA] and angles [$^\circ$] for compound 3

Ce(1)-O(7)#1	2.492(2)	Ce(1)-O(11)	2.568(2)	Cu(1)-O(1)	2.175(2)
Ce(1)-O(7)	2.492(2)	Ce (1)-O(8)#1	2.573(2)	Cu(1)-O(2)#2	1.926(2)
Ce(1)-O(6)#1	2.563(2)	Ce (1)-O(8)	2.573(2)	Cu(1)-O(3)	1.958(2)
Ce(1)-O(6)	2.563(2)	Ce (1)-O(5)#1	2.757(2)	Cu(1)-O(5)	1.976(2)
Ce(1)-O(11)#1	2.568(2)	Ce (1)-O(5)	2.757(2)	Cu(1)-N(1)	2.034(2)
O(7)-Ce(1)-O(7)#1	157.4(6)	O(11)- Ce (1)-O(5)	68.5(0)	O(5)-Cu(1)-N(1)	89.9(8)
O(7)- Ce (1)-O(6)#1	69.3(3)	O(11)- Ce (1)-O(5)#1	93.8(0)	O(5)-Cu(1)-O(1)	94.2(1)
O(7)- Ce (1)-O(6)	115.4(6)	O(8)- Ce (1)-O(8)#1	69.0(7)	O(5)-Cu(1)-O(1)#2	89.3(5)
O(7)- Ce (1)-O(11)#1	125.5(5)	O(8)- Ce (1)-O(5)	131.7(6)	O(5)-Cu(1)-O(7)	53.9(1)
O(7)- Ce (1)-O(11)	76.9(6)	O(8)- Ce (1)-O(5)#1	66.7(9)	O(5)-Cu(1)-O(4)	143.8(5)
O(7)- Ce (1)-O(8)#1	84.3(0)	O(5)- Ce (1)-O(5)	161.0(0)	N(1)-Cu(1)-O(1)	80.1(6)
O(7)- Ce (1)-O(8)	77.1(3)	O(2)#2-Cu(1)- O(3)	94.6(1)	N(1)-Cu(1)-O(1)#2	138.3(3)
O(7)- Ce (1)-O(5)	67.9(4)	O(2)#2-Cu(1)- O(5)	93.8(3)	N(1)-Cu(1)-O(7)	123.5(5)
O(7)- Ce (1)-O(5)#1	116.1(1)	O(2)#2-Cu(1)-N(1)	172.5(8)	N(1)-Cu(1)-O(4)	64.4(2)
O(6)- Ce (1)-O(6)#1	157.3(4)	O(2)#2-Cu(1)-O(1)	93.2(0)	O(1)-Cu(1)-O(1)#2	141.4(1)
O(6)- Ce (1)-O(11)#1	72.6(8)	O(2)#2-Cu(1)- O(1)#2	48.2(1)	O(1)-Cu(1)-O(7)	63.8(1)
O(6)- Ce (1)-O(11)	86.5(7)	O(2)#2-Cu(1)- O(7)	54.9(7)	O(1)-Cu(1)-O(4)	105.1(5)
O(6)- Ce (1)-O(8)#1	129.9(0)	O(2)#2-Cu(1)- O(4)	114.7(5)	O(1)#2-Cu(1)- O(7)	88.4(1)
O(6)- Ce (1)-O(8)	71.4(8)	O(3)-Cu(1)-O(5)	149.2(3)	O(1)#2-Cu(1)-O(4)	93.7(1)
O(6)- Ce (1)-O(5)	48.1(3)	O(3)-Cu(1)-N(1)	85.2(8)	O(7)-Cu(1)-O(4)	162.0(2)
O(6)- Ce (1)-O(5)#1	127.0(6)	O(3)-Cu(1)-O(1)	114.7(5)	Cu(1)-O(1)-Cu(1)#2	168.9(3)
O(11)- Ce (1)-O(11)#1	48.9(9)	O(3)-Cu(1)-O(1)#2	74.6(8)	Cu(1)-O(5)- Ce (1)	144.6(8)
O(11)- Ce (1)-O(8)#1	143.5(2)	O(3)-Cu(1)-O(7)	148.1(3)		
O(11)- Ce (1)-O(8)	134.0(5)	O(3)-Cu(1)-O(4)	21.2(0)		

Symmetry transformation used to generate equivalent atoms: #1(1-x, y, 0.5-z);
#2 (0.5-x, 0.5+y, 0.5-z)

Table A-3. Selected bond lengths [\AA] and angles [$^\circ$] for compound 4

Pr(1)-O(7)#1	2.473(2)	Pr (1)-O(11)	2.551(3)	Cu(1)-O(1)	2.175(2)
Pr (1)-O(7)	2.473(2)	Pr (1)-O(8)#1	2.549(2)	Cu(1)-O(2)#2	1.926(2)
Pr (1)-O(6)#1	2.550(2)	Pr (1)-O(8)	2.549(2)	Cu(1)-O(3)	1.962(2)
Pr (1)-O(6)	2.550(2)	Pr (1)-O(5)#1	2.754(2)	Cu(1)-O(5)	1.973(2)
Pr (1)-O(11)#1	2.551(3)	Pr (1)-O(5)	2.754(2)	Cu(1)-N(1)	2.033(2)
O(7)-Pr(1)-O(7)#1	157.9(1)	O(11)- Pr (1)-O(5)	67.7(3)	O(5)-Cu(1)-N(1)	90.0(7)
O(7)- Pr (1)-O(6)#1	69.4(2)	O(11)- Pr (1)-O(5)#1	95.0(6)	O(5)-Cu(1)-O(1)	93.9(0)
O(7)- Pr (1)-O(6)	115.5(0)	O(8)- Pr (1)-O(8)#1	69.6(2)	O(5)-Cu(1)-O(1)#2	89.0(2)
O(7)- Pr (1)-O(11)#1	125.3(9)	O(8)- Pr (1)-O(5)	131.6(6)	O(5)-Cu(1)-O(7)	53.2(9)
O(7)- Pr (1)-O(11)	76.6(3)	O(8)- Pr (1)-O(5)#1	66.3(1)	O(5)-Cu(1)-O(4)	144.1(0)
O(7)- Pr (1)-O(8)#1	84.4(2)	O(5)- Pr (1)-O(5)	161.5(8)	N(1)-Cu(1)-O(1)	80.1(1)
O(7)- Pr (1)-O(8)	77.4(5)	O(2)#2-Cu(1)- O(3)	94.6(7)	N(1)-Cu(1)-O(1)#2	137.9(7)
O(7)- Pr (1)-O(5)	67.7(4)	O(2)#2-Cu(1)- O(5)	93.3(4)	N(1)-Cu(1)-O(7)	123.8(1)
O(7)- Pr (1)-O(5)#1	116.1(1)	O(2)#2-Cu(1)-N(1)	172.9(3)	N(1)-Cu(1)-O(4)	64.4(6)
O(6)- Pr (1)-O(6)#1	156.1(8)	O(2)#2-Cu(1)-O(1)	93.4(7)	O(1)-Cu(1)-O(1)#2	141.8(6)
O(6)- Pr (1)-O(11)#1	73.1(1)	O(2)#2-Cu(1)- O(1)#2	48.4(0)	O(1)-Cu(1)-O(7)	64.4(1)
O(6)- Pr (1)-O(11)	85.1(7)	O(2)#2-Cu(1)- O(7)	54.6(3)	O(1)-Cu(1)-O(4)	105.2(3)
O(6)- Pr (1)-O(8)#1	130.7(2)	O(2)#2-Cu(1)- O(4)	115.0(1)	O(1)#2-Cu(1)- O(7)	87.9(3)
O(6)- Pr (1)-O(8)	71.7(3)	O(3)-Cu(1)-O(5)	149.7(5)	O(1)#2-Cu(1)-O(4)	93.8(2)
O(6)- Pr (1)-O(5)	48.2(2)	O(3)-Cu(1)-N(1)	85.4(3)	O(7)-Cu(1)-O(4)	162.4(6)
O(6)- Pr (1)-O(5)#1	126.8(9)	O(3)-Cu(1)-O(1)	114.6(4)	Cu(1)-O(1)-Cu(1)#2	168.7(2)
O(11)- Pr(1)-O(11)#1	49.4(8)	O(3)-Cu(1)-O(1)#2	74.9(3)	Cu(1)-O(5)- Pr (1)	145.2(3)
O(11)- Pr (1)-O(8)#1	144.0(8)	O(3)-Cu(1)-O(7)	147.9(6)		
O(11)- Pr (1)-O(8)	132.9(6)	O(3)-Cu(1)-O(4)	21.2(8)		

Symmetry transformation used to generate equivalent atoms: #1(1-x, y, 0.5-z);
#2 (0.5-x, 0.5+y, 0.5-z)

Table A-4. Selected bond lengths [\AA] and angles [$^\circ$] for compound 5

Nd(1)-O(7)#1	2.461(2)	Nd (1)-O(11)	2.533(2)	Cu(1)-O(1)	2.179(2)
Nd (1)-O(7)	2.461(2)	Nd (1)-O(8)#1	2.532(2)	Cu(1)-O(2)#2	1.925(2)
Nd (1)-O(6)#1	2.534(2)	Nd (1)-O(8)	2.532(2)	Cu(1)-O(3)	1.963(2)
Nd (1)-O(6)	2.534(2)	Nd (1)-O(5)#1	2.743(2)	Cu(1)-O(5)	1.969(2)
Nd(1)-O(11)#1	2.533(2)	Nd (1)-O(5)	2.743(2)	Cu(1)-N(1)	2.035(2)
O(7)-Nd(1)-O(7)#1	156.3(3)	O(11)- Nd (1)-O(5)	67.6(5)	O(5)-Cu(1)-N(1)	90.0(7)
O(7)- Nd (1)-O(6)#1	69.6(3)	O(11)- Nd (1)-O(5)#1	95.2(7)	O(5)-Cu(1)-O(1)	93.7(5)
O(7)- Nd (1)-O(6)	115.7(7)	O(8)- Nd (1)-O(8)#1	69.6(0)	O(5)-Cu(1)-O(1)#2	89.0(9)
O(7)- Nd (1)-O(11)#1	126.3(8)	O(8)- Nd (1)-O(5)	66.3(9)	O(5)-Cu(1)-O(7)	52.9(6)
O(7)- Nd (1)-O(11)	77.2(2)	O(8)- Nd (1)-O(5)#1	131.4(3)	O(5)-Cu(1)-O(4)	144.1(9)
O(7)- Nd (1)-O(8)#1	83.5(5)	O(5)- Nd (1)-O(5)	161.7(0)	N(1)-Cu(1)-O(1)	80.0(1)
O(7)- Nd (1)-O(8)	77.0(2)	O(2)#2-Cu(1)- O(3)	94.6(3)	N(1)-Cu(1)-O(1)#2	137.7(2)
O(7)- Nd (1)-O(5)	67.6(9)	O(2)#2-Cu(1)- O(5)	93.2(3)	N(1)-Cu(1)-O(7)	123.2(9)
O(7)- Nd (1)-O(5)#1	116.4(2)	O(2)#2-Cu(1)-N(1)	173.1(8)	N(1)-Cu(1)-O(4)	64.4(9)
O(6)- Nd (1)-O(6)#1	155.5(6)	O(2)#2-Cu(1)-O(1)	93.8(0)	O(1)-Cu(1)-O(1)#2	142.2(1)
O(6)- Nd (1)-O(11)#1	72.6(9)	O(2)#2-Cu(1)- O(1)#2	48.4(0)	O(1)-Cu(1)-O(7)	64.1(7)
O(6)- Nd (1)-O(11)	85.0(5)	O(2)#2-Cu(1)- O(7)	55.2(1)	O(1)-Cu(1)-O(4)	105.2(3)
O(6)- Nd (1)-O(8)#1	131.0(9)	O(2)#2-Cu(1)- O(4)	114.9(8)	O(1)#2-Cu(1)- O(7)	88.5(8)
O(6)- Nd (1)-O(8)	71.9(6)	O(3)-Cu(1)-O(5)	149.8(3)	O(1)#2-Cu(1)-O(4)	93.6(6)
O(6)- Nd (1)-O(5)	48.5(9)	O(3)-Cu(1)-N(1)	85.4(4)	O(7)-Cu(1)-O(4)	162.6(5)
O(6)- Nd (1)-O(5)#1	126.4(5)	O(3)-Cu(1)-O(1)	114.6(9)	Cu(1)-O(1)-Cu(1)#2	168.7(4)
O(11)- Nd (1)-O(11)#1	49.8(7)	O(3)-Cu(1)-O(1)#2	74.8(1)	Cu(1)-O(5)- Nd(1)	145.5(3)
O(11)- Nd (1)-O(8)#1	143.8(2)	O(3)-Cu(1)-O(7)	148.4(1)		
O(11)- Nd (1)-O(8)	133.0(1)	O(3)-Cu(1)-O(4)	21.2(7)		

Symmetry transformation used to generate equivalent atoms: #1(1-x, y, 0.5-z);
#2 (0.5-x, 0.5+y, 0.5-z)

Table A-5. Selected bond lengths [Å] and angles [°] for compound 6

Sm(1)-O(7)#1	2.432(2)	Sm (1)-O(11)	2.506(2)	Cu(1)-O(1)	2.179(2)
Sm (1)-O(7)	2.432(2)	Sm (1)-O(8)#1	2.503(2)	Cu(1)-O(2)#2	1.921(2)
Sm (1)-O(6)#1	2.508(2)	Sm (1)-O(8)	2.503(2)	Cu(1)-O(3)	1.963(2)
Sm (1)-O(6)	2.508(2)	Sm (1)-O(5)#1	2.742(2)	Cu(1)-O(5)	1.969(2)
Sm(1)-O(11)#1	2.506(2)	Sm (1)-O(5)	2.742(2)	Cu(1)-N(1)	2.032(2)
O(7)-Sm(1)-O(7)#1	155.3(6)	O(11)- Sm (1)-O(5)	67.3(3)	O(5)-Cu(1)-N(1)	90.0(2)
O(7)- Sm (1)-O(6)#1	70.0(9)	O(11)- Sm (1)-O(5)#1	96.0(5)	O(5)-Cu(1)-O(1)	93.2(8)
O(7)- Sm (1)-O(6)	115.8(1)	O(8)- Sm (1)-O(8)#1	69.9(7)	O(5)-Cu(1)-O(1)#2	88.9(4)
O(7)- Sm (1)-O(11)#1	127.1(5)	O(8)- Sm (1)-O(5)	66.2(1)	O(5)-Cu(1)-O(7)	51.9(5)
O(7)- Sm (1)-O(11)	77.4(0)	O(8)- Sm (1)-O(5)#1	131.0(8)	O(5)-Cu(1)-O(4)	144.3(2)
O(7)- Sm (1)-O(8)#1	82.7(1)	O(5)- Sm (1)-O(5)	162.1(9)	N(1)-Cu(1)-O(1)	80.0(8)
O(7)- Sm (1)-O(8)	77.1(3)	O(2)#2-Cu(1)- O(3)	94.6(1)	N(1)-Cu(1)-O(1)#2	137.2(0)
O(7)- Sm (1)-O(5)	67.5(0)	O(2)#2-Cu(1)- O(5)	93.1(4)	N(1)-Cu(1)-O(7)	122.8(7)
O(7)- Sm (1)-O(5)#1	116.6(6)	O(2)#2-Cu(1)-N(1)	173.5(4)	N(1)-Cu(1)-O(4)	64.3(6)
O(6)- Sm (1)-O(6)#1	154.3(2)	O(2)#2-Cu(1)-O(1)	94.1(2)	O(1)-Cu(1)-O(1)#2	142.7(0)
O(6)- Sm (1)-O(11)#1	72.4(4)	O(2)#2-Cu(1)- O(1)#2	48.5(9)	O(1)-Cu(1)-O(7)	64.3(7)
O(6)- Sm (1)-O(11)	84.2(5)	O(2)#2-Cu(1)- O(7)	55.8(6)	O(1)-Cu(1)-O(4)	105.3(0)
O(6)- Sm (1)-O(8)#1	132.1(7)	O(2)#2-Cu(1)- O(4)	115.0(6)	O(1)#2-Cu(1)- O(7)	88.7(6)
O(6)- Sm (1)-O(8)	72.1(2)	O(3)-Cu(1)-O(5)	150.2(8)	O(1)#2-Cu(1)-O(4)	93.8(1)
O(6)- Sm (1)-O(5)	48.7(4)	O(3)-Cu(1)-N(1)	85.3(6)	O(7)-Cu(1)-O(4)	163.4(6)
O(6)- Sm (1)-O(5)#1	126.2(0)	O(3)-Cu(1)-O(1)	114.6(7)	Cu(1)-O(1)-Cu(1)#2	168.4(6)
O(11)-Sm (1)-O(11)#1	50.5(9)	O(3)-Cu(1)-O(1)#2	75.1(1)	Cu(1)-O(5)- Sm (1)	146.2(5)
O(11)- Sm (1)-O(8)#1	143.5(1)	O(3)-Cu(1)-O(7)	149.1(2)		
O(11)- Sm (1)-O(8)	132.6(5)	O(3)-Cu(1)-O(4)	21.2(9)		

Symmetry transformation used to generate equivalent atoms: #1(1-x, y, 0.5-z);
#2 (0.5-x, 0.5+y, 0.5-z)

Table A-6. Selected bond lengths [\AA] and angles [$^\circ$] for compound 7

Eu(1)-O(7)#1	2.421(2)	Eu (1)-O(11)	2.492(2)	Cu(1)-O(1)	2.180(2)
Eu (1)-O(7)	2.421(2)	Eu (1)-O(8)#1	2.487(2)	Cu(1)-O(2)#2	1.922(2)
Eu (1)-O(6)#1	2.495(2)	Eu (1)-O(8)	2.487(2)	Cu(1)-O(3)	1.961(2)
Eu (1)-O(6)	2.495(2)	Eu (1)-O(5)#1	2.736(2)	Cu(1)-O(5)	1.970(2)
Eu (1)-O(11)#1	2.492(2)	Eu (1)-O(5)	2.736(2)	Cu(1)-N(1)	2.033(2)
<hr/>					
O(7)-Eu(1)-O(7)#1	155.1(4)	O(11)- Eu (1)-O(5)	67.1(4)	O(5)-Cu(1)-N(1)	89.8(1)
O(7)- Eu (1)-O(6)#1	70.2(2)	O(11)- Eu (1)-O(5)#1	96.6(7)	O(5)-Cu(1)-O(1)	92.9(8)
O(7)- Eu (1)-O(6)	115.8(8)	O(8)- Eu (1)-O(8)#1	70.1(1)	O(5)-Cu(1)-O(1)#2	89.0(7)
O(7)- Eu (1)-O(11)#1	127.3(7)	O(8)- Eu (1)-O(5)	66.0(3)	O(5)-Cu(1)-O(7)	51.6(3)
O(7)- Eu (1)-O(11)	77.3(8)	O(8)- Eu(1)-O(5)#1	130.7(9)	O(5)-Cu(1)-O(4)	144.2(8)
O(7)- Eu (1)-O(8)#1	82.3(8)	O(5)- Eu (1)-O(5)	162.6(4)	N(1)-Cu(1)-O(1)	80.0(1)
O(7)- Eu (1)-O(8)	77.3(0)	O(2)#2-Cu(1)- O(3)	94.6(7)	N(1)-Cu(1)-O(1)#2	137.0(3)
O(7)- Eu (1)-O(5)	67.4(3)	O(2)#2-Cu(1)- O(5)	93.1(2)	N(1)-Cu(1)-O(7)	122.7(1)
O(7)- Eu (1)-O(5)#1	116.6(7)	O(2)#2-Cu(1)-N(1)	173.7(1)	N(1)-Cu(1)-O(4)	64.3(3)
O(6)- Eu (1)-O(6)#1	153.6(7)	O(2)#2-Cu(1)-O(1)	94.2(7)	O(1)-Cu(1)-O(1)#2	142.9(4)
O(6)- Eu (1)-O(11)#1	72.4(6)	O(2)#2-Cu(1)- O(1)#2	48.6(8)	O(1)-Cu(1)-O(7)	64.5(2)
O(6)- Eu (1)-O(11)	83.7(0)	O(2)#2-Cu(1)- O(7)	55.9(3)	O(1)-Cu(1)-O(4)	105.3(1)
O(6)- Eu (1)-O(8)#1	132.6(8)	O(2)#2-Cu(1)- O(4)	115.2(6)	O(1)#2-Cu(1)- O(7)	88.7(8)
O(6)- Eu (1)-O(8)	72.2(4)	O(3)-Cu(1)-O(5)	150.5(5)	O(1)#2-Cu(1)-O(4)	93.8(7)
O(6)- Eu (1)-O(5)	48.8(3)	O(3)-Cu(1)-N(1)	85.4(4)	O(7)-Cu(1)-O(4)	163.8(0)
O(6)- Eu (1)-O(5)#1	126.1(2)	O(3)-Cu(1)-O(1)	114.6(5)	Cu(1)-O(1)-Cu(1)#2	168.3(4)
O(11)- Eu (1)-O(11)#1	50.9(7)	O(3)-Cu(1)-O(1)#2	75.1(7)	Cu(1)-O(5)- Eu(1)	146.4(2)
O(11)- Eu (1)-O(8)#1	143.5(3)	O(3)-Cu(1)-O(7)	149.2(7)		
O(11)- Eu (1)-O(8)	132.3(6)	O(3)-Cu(1)-O(4)	21.3(9)		

Symmetry transformation used to generate equivalent atoms: #1(1-x, y, 0.5-z);
#2 (0.5-x, 0.5+y, 0.5-z)

Table A-7. Selected bond lengths [\AA] and angles [$^\circ$] for compound 8

Gd(1)-O(7)#1	2.410(2)	Gd (1)-O(11)	2.483(2)	Cu(1)-O(1)	2.181(2)
Gd (1)-O(7)	2.410(2)	Gd (1)-O(8)#1	2.470(2)	Cu(1)-O(2)#2	1.921(2)
Gd (1)-O(6)#1	2.483(2)	Gd (1)-O(8)	2.470(2)	Cu(1)-O(3)	1.964(2)
Gd (1)-O(6)	2.483(2)	Gd (1)-O(5)#1	2.737(2)	Cu(1)-O(5)	1.967(2)
Gd(1)-O(11)#1	2.483(2)	Gd (1)-O(5)	2.737(2)	Cu(1)-N(1)	2.034(2)
O(7)-Gd(1)-O(7)#1	154.9(0)	O(11)- Gd (1)-O(5)	66.8(6)	O(5)-Cu(1)-N(1)	89.8(1)
O(7)- Gd (1)-O(6)#1	115.9(4)	O(11)- Gd (1)-O(5)#1	97.1(9)	O(5)-Cu(1)-O(1)	92.8(1)
O(7)- Gd (1)-O(6)	70.4(0)	O(8)- Gd (1)-O(8)#1	70.2(6)	O(5)-Cu(1)-O(1)#2	89.0(0)
O(7)- Gd (1)-O(11)#1	77.3(3)	O(8)- Gd (1)-O(5)	65.9(2)	O(5)-Cu(1)-O(7)	51.2(4)
O(7)- Gd (1)-O(11)	127.6(5)	O(8)- Gd (1)-O(5)#1	130.6(3)	O(5)-Cu(1)-O(4)	144.3(5)
O(7)- Gd (1)-O(8)#1	77.3(4)	O(5)- Gd (1)-O(5)	162.9(0)	N(1)-Cu(1)-O(1)	80.1(1)
O(7)- Gd (1)-O(8)	82.1(8)	O(2)#2-Cu(1)- O(3)	94.6(1)	N(1)-Cu(1)-O(1)#2	136.6(8)
O(7)- Gd (1)-O(5)	116.7(9)	O(2)#2-Cu(1)- O(5)	93.0(2)	N(1)-Cu(1)-O(7)	122.6(7)
O(7)- Gd (1)-O(5)#1	67.2(9)	O(2)#2-Cu(1)-N(1)	174.0(1)	N(1)-Cu(1)-O(4)	64.3(4)
O(6)- Gd (1)-O(6)#1	152.8(4)	O(2)#2-Cu(1)-O(1)	94.4(6)	O(1)-Cu(1)-O(1)#2	143.2(0)
O(6)- Gd (1)-O(11)#1	72.3(4)	O(2)#2-Cu(1)- O(1)#2	48.7(5)	O(1)-Cu(1)-O(7)	64.6(7)
O(6)- Gd (1)-O(11)	83.1(3)	O(2)#2-Cu(1)- O(7)	56.1(2)	O(1)-Cu(1)-O(4)	105.4(4)
O(6)- Gd (1)-O(8)#1	133.2(1)	O(2)#2-Cu(1)- O(4)	115.2(2)	O(1)#2-Cu(1)- O(7)	88.8(2)
O(6)- Gd (1)-O(8)	72.5(1)	O(3)-Cu(1)-O(5)	150.5(4)	O(1)#2-Cu(1)-O(4)	93.7(7)
O(6)- Gd (1)-O(5)	48.9(8)	O(3)-Cu(1)-N(1)	85.4(5)	O(7)-Cu(1)-O(4)	164.1(3)
O(6)- Gd (1)-O(5)#1	125.9(1)	O(3)-Cu(1)-O(1)	114.8(5)	Cu(1)-O(1)-Cu(1)#2	168.2(6)
O(11)- Gd (1)-O(11)#1	51.4(3)	O(3)-Cu(1)-O(1)#2	75.0(8)	Cu(1)-O(5)-Gd (1)	146.7(6)
O(11)- Gd (1)-O(8)#1	143.5(5)	O(3)-Cu(1)-O(7)	149.4(9)		
O(11)- Gd (1)-O(8)	132.0(2)	O(3)-Cu(1)-O(4)	21.4(0)		

Symmetry transformation used to generate equivalent atoms: #1(1-x, y, 0.5-z);
#2 (0.5-x, 0.5+y, 0.5-z)

Table A-8. Selected bond lengths [\AA] and angles [$^\circ$] for compound 9

Dy(1)-O(7)#1	2.380(3)	Dy (1)-O(11)	2.452(3)	Cu(1)-O(1)	2.186(3)
Dy (1)-O(7)	2.380(3)	Dy (1)-O(8)#1	2.449(4)	Cu(1)-O(2)#2	1.923(3)
Dy (1)-O(6)#1	2.456(3)	Dy (1)-O(8)	2.449(4)	Cu(1)-O(3)	1.965(3)
Dy (1)-O(6)	2.456(3)	Dy (1)-O(5)#1	2.766(3)	Cu(1)-O(5)	1.965(3)
Dy 1)-O(11)#1	2.452(3)	Dy (1)-O(5)	2.766(3)	Cu(1)-N(1)	2.032(3)
O(7)-Dy(1)-O(7)#1	155.0(2)	O(11)- Dy (1)-O(5)	66.5(2)	O(5)-Cu(1)-N(1)	89.6(4)
O(7)- Dy (1)-O(6)#1	71.0(6)	O(11)- Dy (1)-O(5)#1	98.3(2)	O(5)-Cu(1)-O(1)	92.1(7)
O(7)- Dy (1)-O(6)	115.3(5)	O(8)- Dy (1)-O(8)#1	70.6(2)	O(5)-Cu(1)-O(1)#2	88.4(0)
O(7)- Dy (1)-O(11)#1	127.7(4)	O(8)- Dy (1)-O(5)	65.5(3)	O(5)-Cu(1)-O(7)	49.8(4)
O(7)- Dy (1)-O(11)	77.1(0)	O(8)- Dy (1)-O(5)#1	130.1(3)	O(5)-Cu(1)-O(4)	144.7(0)
O(7)- Dy (1)-O(8)#1	82.0(0)	O(5)- Dy (1)-O(5)	163.7(7)	N(1)-Cu(1)-O(1)	80.1(1)
O(7)- Dy (1)-O(8)	77.6(7)	O(2)#2-Cu(1)- O(3)	94.9(0)	N(1)-Cu(1)-O(1)#2	136.2(0)
O(7)- Dy (1)-O(5)	66.7(7)	O(2)#2-Cu(1)- O(5)	92.5(3)	N(1)-Cu(1)-O(7)	122.2(9)
O(7)- Dy (1)-O(5)#1	117.0(9)	O(2)#2-Cu(1)-N(1)	174.6(9)	N(1)-Cu(1)-O(4)	64.4(5)
O(6)- Dy (1)-O(6)#1	152.3(0)	O(2)#2-Cu(1)-O(1)	94.9(5)	O(1)-Cu(1)-O(1)#2	143.6(9)
O(6)- Dy (1)-O(11)#1	72.8(7)	O(2)#2-Cu(1)- O(1)#2	48.7(8)	O(1)-Cu(1)-O(7)	65.3(6)
O(6)- Dy (1)-O(11)	82.2(0)	O(2)#2-Cu(1)- O(7)	56.4(1)	O(1)-Cu(1)-O(4)	105.4(8)
O(6)- Dy (1)-O(8)#1	134.0(0)	O(2)#2-Cu(1)- O(4)	115.5(0)	O(1)#2-Cu(1)- O(7)	88.1(8)
O(6)- Dy (1)-O(8)	72.3(1)	O(3)-Cu(1)-O(5)	151.2(5)	O(1)#2-Cu(1)-O(4)	94.3(7)
O(6)- Dy (1)-O(5)	48.8(2)	O(3)-Cu(1)-N(1)	85.4(7)	O(7)-Cu(1)-O(4)	165.1(9)
O(6)- Dy (1)-O(5)#1	126.2(1)	O(3)-Cu(1)-O(1)	114.7(3)	Cu(1)-O(1)-Cu(1)#2	167.3(5)
O(11)- Dy (1)-O(11)#1	52.0(1)	O(3)-Cu(1)-O(1)#2	76.0(1)	Cu(1)-O(5)- Dy (1)	147.8(6)
O(11)- Dy (1)-O(8)#1	143.6(1)	O(3)-Cu(1)-O(7)	150.2(0)		
O(11)- Dy (1)-O(8)	131.4(4)	O(3)-Cu(1)-O(4)	21.3(0)		

Symmetry transformation used to generate equivalent atoms: #1(1-x, y, 0.5-z);
#2 (0.5-x, 0.5+y, 0.5-z)

Table A-9. Selected bond lengths [\AA] and angles [$^\circ$] for compound 10

Ho(1)-O(7)#1	2.363(3)	Ho (1)-O(11)	2.436(3)	Cu(1)-O(1)	2.187(3)
Ho (1)-O(7)	2.363(3)	Ho (1)-O(8)#1	2.428(3)	Cu(1)-O(2)#2	1.924(3)
Ho (1)-O(6)#1	2.440(3)	Ho (1)-O(8)	2.428(3)	Cu(1)-O(3)	1.963(3)
Ho (1)-O(6)	2.440(3)	Ho (1)-O(5)#1	2.766(3)	Cu(1)-O(5)	1.957(3)
Ho 1)-O(11)#1	2.436(3)	Ho (1)-O(5)	2.766(3)	Cu(1)-N(1)	2.036(3)
O(7)-Ho(1)-O(7)#1	155.2(2)	O(11)- Ho (1)-O(5)	66.2(6)	O(5)-Cu(1)-N(1)	89.6(0)
O(7)- Ho (1)-O(6)#1	71.34(4)	O(11)- Ho (1)-O(5)#1	99.0(1)	O(5)-Cu(1)-O(1)	91.9(3)
O(7)- Ho (1)-O(6)	115.24(1)	O(8)- Ho (1)-O(8)#1	70.9(1)	O(5)-Cu(1)-O(1)#2	88.3(4)
O(7)- Ho (1)-O(11)#1	127.8(8)	O(8)- Ho (1)-O(5)	65.2(7)	O(5)-Cu(1)-O(7)	49.2(2)
O(7)- Ho (1)-O(11)	76.7(3)	O(8)- Ho (1)-O(5)#1	129.9(4)	O(5)-Cu(1)-O(4)	144.8(0)
O(7)- Ho (1)-O(8)#1	82.0(3)	O(5)- Ho (1)-O(5)	164.2(3)	N(1)-Cu(1)-O(1)	80.0(5)
O(7)- Ho (1)-O(8)	77.8(3)	O(2)#2-Cu(1)- O(3)	94.9(2)	N(1)-Cu(1)-O(1)#2	135.9(3)
O(7)- Ho (1)-O(5)	66.4(5)	O(2)#2-Cu(1)- O(5)	92.2(5)	N(1)-Cu(1)-O(7)	122.3(1)
O(7)- Ho (1)-O(5)#1	117.2(9)	O(2)#2-Cu(1)-N(1)	174.9(6)	N(1)-Cu(1)-O(4)	64.3(5)
O(6)- Ho (1)-O(6)#1	151.2(5)	O(2)#2-Cu(1)-O(1)	95.2(0)	O(1)-Cu(1)-O(1)#2	144.0(1)
O(6)- Ho (1)-O(11)#1	72.7(0)	O(2)#2-Cu(1)- O(1)#2	48.8(6)	O(1)-Cu(1)-O(7)	65.9(2)
O(6)- Ho (1)-O(11)	81.5(0)	O(2)#2-Cu(1)- O(7)	56.3(1)	O(1)-Cu(1)-O(4)	105.3(5)
O(6)- Ho (1)-O(8)#1	134.7(0)	O(2)#2-Cu(1)- O(4)	115.8(1)	O(1)#2-Cu(1)- O(7)	87.8(8)
O(6)- Ho (1)-O(8)	72.6(1)	O(3)-Cu(1)-O(5)	151.6(4)	O(1)#2-Cu(1)-O(4)	94.5(4)
O(6)- Ho (1)-O(5)	48.9(6)	O(3)-Cu(1)-N(1)	85.6(4)	O(7)-Cu(1)-O(4)	165.7(2)
O(6)- Ho (1)-O(5)#1	126.0(5)	O(3)-Cu(1)-O(1)	114.6(2)	Cu(1)-O(1)-Cu(1)#2	166.8(6)
O(11)- Ho (1)-O(11)#1	52.6(6)	O(3)-Cu(1)-O(1)#2	76.1(0)	Cu(1)-O(5)- Ho (1)	148.4(6)
O(11)- Ho (1)-O(8)#1	143.5(8)	O(3)-Cu(1)-O(7)	150.2(2)		
O(11)- Ho (1)-O(8)	130.9(6)	O(3)-Cu(1)-O(4)	21.5(4)		

Symmetry transformation used to generate equivalent atoms: #1(1-x, y, 0.5-z);
#2 (0.5-x, 0.5+y, 0.5-z)

Table A-10. Selected bond lengths [\AA] and angles [$^\circ$] for compound 11

Er(1)-O(7)#1	2.356(2)	Er (1)-O(11)	2.424(2)	Cu(1)-O(1)	2.188(2)
Er (1)-O(7)	2.356(2)	Er (1)-O(8)#1	2.414(2)	Cu(1)-O(2)#2	1.924(2)
Er (1)-O(6)#1	2.421(2)	Er (1)-O(8)	2.414(2)	Cu(1)-O(3)	1.961(2)
Er (1)-O(6)	2.421(2)	Er (1)-O(5)#1	2.773(2)	Cu(1)-O(5)	1.958(2)
Er (1)-O(11)#1	2.424(2)	Er (1)-O(5)	2.773(2)	Cu(1)-N(1)	2.031(2)
O(7)-Er(1)-O(7)#1	155.4(9)	O(11)- Er (1)-O(5)	65.9(6)	O(5)-Cu(1)-N(1)	89.4(0)
O(7)- Er (1)-O(6)#1	71.5(3)	O(11)- Er (1)-O(5)#1	99.8(8)	O(5)-Cu(1)-O(1)	91.52(0)
O(7)- Er (1)-O(6)	115.1(7)	O(8)- Er (1)-O(8)#1	71.0(0)	O(5)-Cu(1)-O(1)#2	88.2(9)
O(7)- Er (1)-O(11)#1	127.6(4)	O(8)- Er (1)-O(5)	65.0(2)	O(5)-Cu(1)-O(7)	48.6(7)
O(7)- Er (1)-O(11)	76.6(7)	O(8)- Er (1)-O(5)#1	129.5(4)	O(5)-Cu(1)-O(4)	145.0(0)
O(7)- Er (1)-O(8)#1	81.9(6)	O(5)- Er (1)-O(5)	164.8(7)	N(1)-Cu(1)-O(1)	80.0(3)
O(7)- Er (1)-O(8)	78.1(3)	O(2)#2-Cu(1)- O(3)	95.0(1)	N(1)-Cu(1)-O(1)#2	135.5(6)
O(7)- Er (1)-O(5)	66.2(1)	O(2)#2-Cu(1)- O(5)	92.1(8)	N(1)-Cu(1)-O(7)	122.2(6)
O(7)- Er (1)-O(5)#1	117.3(5)	O(2)#2-Cu(1)-N(1)	175.2(5)	N(1)-Cu(1)-O(4)	64.5(1)
O(6)- Er (1)-O(6)#1	150.4(0)	O(2)#2-Cu(1)-O(1)	95.4(5)	O(1)-Cu(1)-O(1)#2	144.4(0)
O(6)- Er (1)-O(11)#1	72.9(9)	O(2)#2-Cu(1)- O(1)#2	49.0(2)	O(1)-Cu(1)-O(7)	66.3(2)
O(6)- Er (1)-O(11)	80.5(0)	O(2)#2-Cu(1)- O(7)	56.3(4)	O(1)-Cu(1)-O(4)	105.4(0)
O(6)- Er (1)-O(8)#1	135.2(9)	O(2)#2-Cu(1)- O(4)	115.7(9)	O(1)#2-Cu(1)- O(7)	87.6(2)
O(6)- Er (1)-O(8)	72.8(7)	O(3)-Cu(1)-O(5)	151.9(2)	O(1)#2-Cu(1)-O(4)	94.5(8)
O(6)- Er (1)-O(5)	49.0(7)	O(3)-Cu(1)-N(1)	85.6(5)	O(7)-Cu(1)-O(4)	166.1(0)
O(6)- Er (1)-O(5)#1	126.0(1)	O(3)-Cu(1)-O(1)	114.6(9)	Cu(1)-O(1)-Cu(1)#2	166.4(6)
O(11)- Er (1)-O(11)#1	52.8(2)	O(3)-Cu(1)-O(1)#2	76.3(1)	Cu(1)-O(5)- Er (1)	148.9(8)
O(11)- Er (1)-O(8)#1	143.9(7)	O(3)-Cu(1)-O(7)	150.4(5)		
O(11)- Er (1)-O(8)	130.5(1)	O(3)-Cu(1)-O(4)	21.4(2)		

Symmetry transformation used to generate equivalent atoms: #1(1-x, y, 0.5-z);
#2 (0.5-x, 0.5+y, 0.5-z)

Table A-11. Selected bond lengths [Å] and angles [°] for compound 12

Fe(1)-O(1)#1	1.866(1)	Fe(1)-O(5)	2.091(8)	Fe(2)-O(8)#3	2.011(5)
Fe(1)-O(1)	1.940(8)	Fe(1)-O(3)	2.122(9)	Fe(2)-O(6)#2	2.045(4)
Fe(1)-O(2)	2.031(2)	Fe(2)-O(2)	1.937(6)	Fe(2)-O(9)	2.055(1)
Fe(1)-O(7)#2	2.050(2)	Fe(2)-O(1)	1.943(8)	Fe(2)-O(4)	2.104(0)
O(1)#1-Fe(1)-O(1)	106.8(9)	O(2)-Fe(2)-O(4)	86.2(8)	C(9)-O(3)-Fe(1)	124.4(3)
O(1)#1-Fe(1)-O(2)	172.2(5)	O(1)-Fe(2)-O(8)#3	97.0(4)	C(8)-O(3)-Fe(1)	147.0(9)
O(1)#1-Fe(1)-O(7)#2	95.7(7)	O(1)-Fe(2)-O(6)#2	96.5(3)	C(3)-O(3)-Fe(1)	141.5(4)
O(1)#1-Fe(1)-O(5)	91.0(9)	O(1)-Fe(2)-O(9)	175.6(4)	C(9)-O(4)-Fe(2)	121.4(9)
O(1)#1-Fe(1)-O(3)	94.5(2)	O(1)-Fe(2)-O(4)	93.8(5)	C(8)-O(4)-Fe(2)	144.1(7)
O(1)-Fe(1)-O(2)	80.5(0)	O(8)#3-Fe(2)-O(6)#2	94.9(1)	C(7)-O(4)-Fe(2)	152.0(9)
O(1)-Fe(1)-O(7)#2	94.8(6)	O(8)#3-Fe(2)-O(9)	87.2(0)	C(12)-O(5)-Fe(1)	134.2(0)
O(1)-Fe(1)-O(5)	160.7(0)	O(8)#3-Fe(2)-O(4)	88.7(1)	C(11)-O(5)-Fe(1)	153.2(3)
O(1)-Fe(1)-O(3)	91.7(3)	O(6)#2-Fe(2)-O(9)	84.1(2)	C(10)-O(5)-Fe(1)	130.7(5)
O(2)-Fe(1)-O(7)#2	85.7(7)	O(6)#2-Fe(2)-O(4)	168.5(0)	C(2)-O(5)-Fe(1)	72.4(3)
O(2)-Fe(1)-O(5)	81.2(9)	O(9)-Fe(2)-O(4)	85.1(6)	C(12)-O(6)-Fe(2)#1	123.6(6)
O(2)-Fe(1)-O(3)	82.7(3)	Fe(1)#2-O(1)-Fe(1)	135.9(0)	C(11)-O(6)-Fe(2)#1	154.3(1)
O(7)#2-Fe(1)-O(5)	90.1(3)	Fe(1)#2-O(1)-Fe(2)	120.2(2)	C(15)-O(7)-Fe(1)#1	130.8(5)
O(7)#2-Fe(1)-O(3)	165.6(2)	Fe(1)-O(1)-Fe(2)	98.4(3)	C(14)-O(7)-Fe(1)#1	164.9(5)
O(5)-Fe(1)-O(3)	79.6(5)	Fe(1)-O(2)-Fe(2)	95.6(1)	C(13)-O(7)-Fe(1)#1	161.0(8)
O(2)-Fe(2)-O(1)	82.8(2)	C(2)-O(2)-Fe(2)	130.2(1)	C(15)-O(8)-Fe(2)#3	131.9(0)
O(2)-Fe(2)-O(8)#3	174.9(6)	C(2)-O(2)-Fe(1)	126.9(3)	C(14)-O(8)-Fe(2)#3	164.5(3)
O(2)-Fe(2)-O(6)#2	90.1(1)	C(9)-O(2)-Fe(2)	73.1(7)		
O(2)-Fe(2)-O(9)	92.8(7)	C(9)-O(2)-Fe(1)	74.9(3)		

Symmetry transformation used to generate equivalent atoms: #1 (-0.5+y, 0.5-x, 0.5-z); #2 (0.5-y, 0.5+x, 0.5-z); #3 (-x, 1-y, z)

Table A-12. Selected bond lengths [Å] and angles [°] for compound 13

Cu(1)-O(1)	1.907(5)	Cu(1)-O(2)	2.445(7)	Cu(2)-O(1)	1.970(0)
Cu(1)-O(3)	1.919(9)	Cu(1)-O(1)#	2.658(2)	Cu(2)-N(2)	2.066(0)
Cu(1)-O(5)#	1.958(5)	Cu(2)-O(7)	1.910(2)	Cu(2)-O(6)	2.414(6)
Cu(1)-N(1)	2.072(4)	Cu(2)-O(5)	1.928(4)	Cu(2)-O(5)#	2.572(5)
O(1)-Cu(1)-O(3)	164.3(3)	O(7)-Cu(2)-O(5)#	91.0(4)	C(2)-O(1)-Cu(1)#	120.5(9)
O(1)-Cu(1)-O(5)#	87.0(1)	O(5)-Cu(2)-O(1)	89.1(5)	C(1)-O(1)-Cu(1)	81.3(2)
O(1)-Cu(1)-N(1)	87.6(7)	O(5)-Cu(2)-N(2)	86.7(1)	C(1)-O(1)-Cu(2)	161.7(7)
O(1)-Cu(1)-O(2)	113.6(0)	O(5)-Cu(2)-O(6)	93.7(4)	C(1)-O(1)-Cu(1)#	104.2(7)
O(1)-Cu(1)-O(1)#	79.7(4)	O(5)-Cu(2)-O(5)#	79.3(3)	C(4)-O(2)-Cu(1)	99.7(0)
O(3)-Cu(1)-O(5)#	93.0(7)	O(1)-Cu(2)-N(2)	169.4(8)	C(3)-O(2)-Cu(1)	74.8(0)
O(3)-Cu(1)-N(1)	94.3(1)	O(1)-Cu(2)-O(6)	91.1(8)	C(11)-O(3)-Cu(1)	128.3(9)
O(3)-Cu(1)-O(2)	82.0(3)	O(1)-Cu(2)-O(5)#	70.3(1)	C(10)-O(3)-Cu(1)	96.1(8)
O(3)-Cu(1)-O(1)#	85.4(8)	N(2)-Cu(2)-O(6)	79.4(5)	C(13)-O(5)-Cu(2)	110.6(1)
O(5)#-Cu(1)-N(1)	170.0(8)	N(2)-Cu(2)-O(5)#	118.2(5)	C(13)-O(5)-Cu(1)#	117.2(7)
O(5)#-Cu(1)-O(2)	94.4(1)	O(6)-Cu(2)-O(5)#	160.1(6)	C(13)-O(5)-Cu(2)#	126.0(3)
O(5)#-Cu(1)-O(1)#	70.8(5)	Cu(1)-O(1)-Cu(2)	111.9(3)	C(12)-O(5)-Cu(2)	81.9(5)
N(1)-Cu(1)-O(2)	80.0(9)	Cu(1)-O(1)-Cu(1)#	99.6(3)	C(12)-O(5)-Cu(1)#	153.2(9)
N(1)-Cu(1)-O(1)#	116.3(3)	Cu(2)-O(1)-Cu(1)#	86.3(2)	C(12)-O(5)-Cu(2)#	111.9(8)
O(2)-Cu(1)-O(1)#	160.1(5)	Cu(1)#-O(5)-Cu(2)	111.1(0)	C(15)-O(6)-Cu(2)	106.1(9)
O(7)-Cu(2)-O(5)	167.6(5)	Cu(2)-O(5)-Cu(2)#	100.0(3)	C(14)-O(6)-Cu(2)	73.8(5)
O(7)-Cu(2)-O(1)	94.9(0)	Cu(1)#-O(5)-Cu(2)#	89.2(8)	C(22)-O(7)-Cu(2)	125.7(2)
O(7)-Cu(2)-N(2)	91.1(5)	C(2)-O(1)-Cu(1)	109.9(8)	C(21)-O(7)-Cu(2)	95.0(2)
O(7)-Cu(2)-O(6)	97.8(2)	C(2)-O(1)-Cu(2)	124.3(0)		

Symmetry transformation used to generate equivalent atoms: # (-x, y, 0.5-z)

Table A-13. Selected bond lengths [Å] and angles [°] for compound 14

Co(1)-O(1)	1.996(8)	Co (1)-O(2)	2.170(4)	Co (2)-O(1)	2.064(5)
Co (1)-O(3)	1.969(6)	Co (1)-O(1)#	2.297(4)	Co (2)-N(2)	2.273(8)
Co (1)-O(5)#	2.056(3)	Co (2)-O(7)	1.958(1)	Co (2)-O(5)#	2.274(3)
Co (1)-N(1)	2.245(9)	Co (2)-O(5)	2.000(0)	Co (2)-O(6a)	2.122(8)
				Co (2)-O(6b)	2.242(0)
O(1)-Co(1)-O(3)	157.0(8)	O(5)-Co(2)-N(2)	82.3(7)	C(1)-O(1)-Co(1)	83.6(4)
O(1)-Co(1)-O(5)#	84.7(9)	O(5)-Co(2)-O(6a)	110.1(4)	C(1)-O(1)-Co(2)	158.4(4)
O(1)-Co(1)-N(1)	83.6(1)	O(5)-Co(2)-O(6b)	93.5(7)	C(1)-O(1)-Co(1)#	108.7(4)
O(1)-Co(1)-O(2)	110.8(1)	O(5)-Co(2)-O(5)#	78.6(2)	C(4)-O(2)-Co(1)	107.8(2)
O(1)-Co(1)-O(1)#	78.3(0)	O(1)-Co(2)-N(2)	162.4(9)	C(3)-O(2)-Co(1)	83.1(4)
O(3)-Co(1)-O(5)#	108.1(3)	O(1)-Co(2)-O(6a)	93.3(5)	C(11)-O(3)-Co(1)	135.7(1)
O(3)-Co(1)-N(1)	88.1(3)	O(1)-Co(2)-O(6b)	84.6(6)	C(10)-O(3)-Co(1)	102.8(6)
O(3)-Co(1)-O(2)	88.5(8)	O(1)-Co(2)-O(5)#	77.9(3)	C(13)-O(5)-Co(2)	111.2(4)
O(3)-Co(1)-O(1)#	85.4(1)	N(2)-Co(2)-O(6a)	77.7(9)	C(13)-O(5)-Co(1)#	120.5(4)
O(5)#-Co(1)-N(1)	160.6(6)	N(2)-Co(2)-O(6b)	82.4(5)	C(13)-O(5)-Co(2)#	125.8(3)
O(5)#-Co(1)-O(2)	89.8(6)	N(2)-Co(2)-O(5)#	112.9(4)	C(12)-O(5)-Co(2)	84.9(0)
O(5)#-Co(1)-O(1)#	79.4(9)	O(6A)-Co(2)-O(5)#	167.4(8)	C(12)-O(5)-Co(1)#	154.4(7)
N(1)-Co(1)-O(2)	79.9(2)	O(6B)-Co(2)-O(5)#	161.2(3)	C(12)-O(5)-Co(2)#	110.2(2)
N(1)-Co(1)-O(1)#	113.0(5)	Co(1)-O(1)-Co(2)	102.1(0)	C(15a)-O(6a)-Co(2)	109.9(6)
O(2)-Co(1)-O(1)#	165.4(6)	Co(1)-O(1)-Co(1)#	101.6(5)	C(15b)-O(6a)-Co(2)	114.2(4)
O(7)-Co(2)-O(5)	157.9(1)	Co(2)-O(1)-Co(1)#	90.6(2)	C(14)-O(6a)-Co(2)	86.2(6)
O(7)-Co(2)-O(1)	108.2(2)	Co(1)#-O(5)-Co(2)	99.9(0)	C(15a)-O(6b)-Co(2)	89.4(4)
O(7)-Co(2)-N(2)	86.4(0)	Co(2)-O(5)-Co(2)#	101.3(3)	C(15b)-O(6b)-Co(2)	113.5(9)
O(7)-Co(2)-O(6a)	85.7(8)	Co(1)#-O(5)-Co(2)#	93.5(3)	C(14)-O(6b)-Co(2)	78.3(1)
O(7)-Co(2)-O(6b)	103.7(7)	C(2)-O(1)-Co(1)	110.5(1)	C(22)-O(7)-Co(2)	135.1(7)
O(7)-Co(2)-O(5)#	88.4(5)	C(2)-O(1)-Co(2)	123.9(6)	C(21)-O(7)-Co(2)	103.2(5)
O(5)-Co(2)-O(1)	86.6(7)	C(2)-O(1)-Co(1)#	123.8(4)		

Symmetry transformation used to generate equivalent atoms: # (-x, y, 0.5-z)

List of abbreviations

Et	=	Ethyl
Me	=	Methyl
Ph	=	Phenyl
L	=	Ligand
H ₃ nta	=	nitrilotriacetic acid
H ₃ ndpa	=	nitrilo(dipropionic)acetic acid
H ₃ ntp	=	nitrilotripropionic acid
H ₃ cpida	=	(2-carboxyphenyl)iminodiacetic acid
H ₃ heidi	=	hydroxyethyl iminodiacetic acid
H ₃ cpidp	=	(2-carboxyphenyl)iminodipropionic acid
H ₃ cpdea	=	(2-carboxyphenyl) diethanol amin
H ₅ hpda	=	2-hydroxy-1,3-N,N,N',N'-diamino-propanetetraacetic acid
EtOH	=	ethanol
MeOH	=	methanol
DMSO	=	dimethyl sulphoxide
Et ₃ N	=	triethylene amine
en	=	ethylenediamin
t-Bu	=	tert-butyl
R	=	alkyl
FTIR	=	Fourier Transform Infrared
NMR	=	Nuclear Magnetic Resonance
s, d, t, m	=	Singlet, Doublet, Triplet, Multiplet
ESR	=	Electron Spin Resonance
SQUID	=	Super-conducting Quantum Interference Device

References

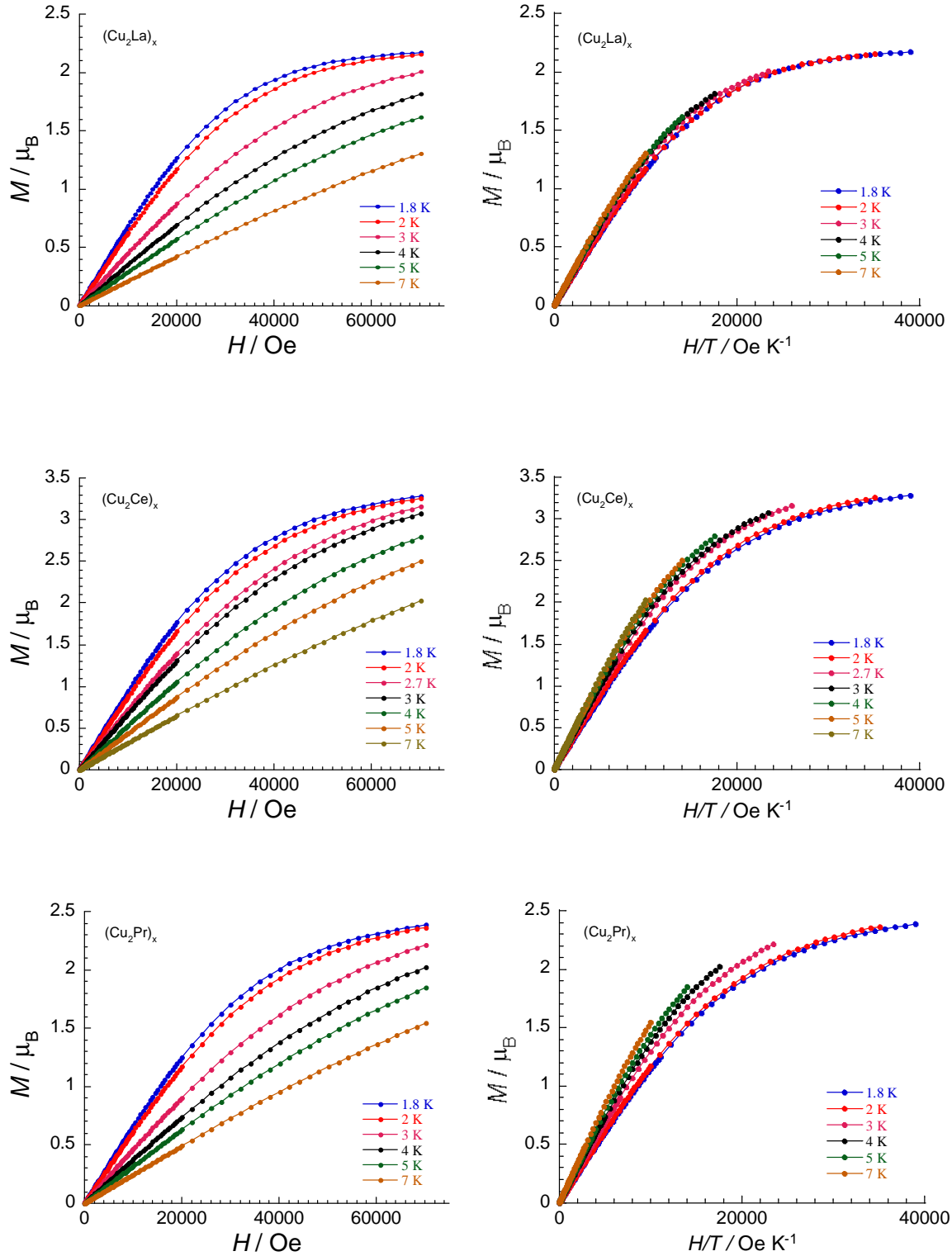
- [1] H. -K. Liu, W. -Y. Sun, D. -J. Ma, K. -B. Yu, W. -X. Tang, *Chem. Commun.* **2000**, 591.
- [2] H. Li, M. Eddaoudi, T. L. Groy, O. M. Yaghi, *J. Am. Chem. Soc.* **1998**, *120*, 8571.
- [3] K. Biradha, Y. Hongo, M. Fujita, *Angew. Chem.* **2002**, *114*, 3545.
- [4] M. Eddaoudi, J. Kim, N. Rosi, D. Vodak, J. Wachter, M. O'keeffe, O. M. Yaghi, *Science* **2002**, *295*, 469.
- [5] C. Aronica, G. Pilet, G. Chastanet, W. Wernsdorfer, J. -F. Jacquot, D. Luneau, *Angew. Chem. Int. Ed.* **2006**, *45*, 4659.
- [6] A. J. Tasiopoulos, A. Vinslava, W. Wernsdorfer, K. A. Abboud, G. Christou, *Angew. Chem.* **2004**, *116*, 2169.
- [7] J. K. Tang, I. Hewitt, N. T. Madhu, G. Chastanet, W. Wernsdorfer, C. E. Anson, C. Benelli, R. Sessoli, A. K. Powell, *Angew. Chem. Int. Ed.* **2006**, *45*, 1729.
- [8] M. Murugesu, M. Habrych, W. Wernsdorfer, K. A. Abboud, G. Christou, *J. Am. Chem. Soc.* **2004**, *126*, 4766.
- [9] R. Sessoli, D. Gatteschi, A. Caneschi, M. A. Novak, *Nature* **1993**, *365*, 141.
- [10] W. Wernsdorfer, N. Allaga-Alcalde, D. N. Hendrickson, G. Christou, *Nature* **2002**, *416*, 406.
- [11] G. Trettenhahn, M. Nagel, N. Neuwirth, V. B. Arion, W. Jary, P. Poehlauer, W. Schmid, *Angew. Chem. Int. Ed.* **2006**, *45*, 2794.
- [12] J. S. Seo, D. Whang, H. Lee, S. I. Jun, J. Oh, Y. J. Jeon, K. Kim, *Nature* **2000**, *404*, 982.
- [13] Banglin Chen, M. Eddaoudi, S. T. Hyde, M. O'Keeffe, O. M. Yaghi, *Science* **2001**, *291*, 1021.
- [14] H. Li, M. Eddaoudi, M. O'Keeffe, O. M. Yaghi, *Nature* **1999**, *402*, 276.
- [15] S. S. -Y. Chi, S. M. -F. Lo, J. P. H. Charmant, A. G. Orpen, I. D. Williams, *Science* **1999**, *283*, 1148.
- [16] W. Schmitt, J. P. Hill, M. P. Juanico, A. Caneschi, F. Costantino, C. E. Anson, A. K. Powell, *Angew. Chem. Int. Ed.* **2005**, *44*, 4187.
- [17] B. Chiari, O. Piovesana, T. Tarantelli, P. R. Zanazzi, *Inorg. Chem.* **1982**, *21*, 2444.
- [18] H. Miyasaka, N. Matsumoto, H. Okawa, N. Re, E. Gallo, C. Floriani, *J. Am. Chem. Soc.* **1996**, *118*, 981.
- [19] R. Karmakar, C. R. Choudhury, G. Bravic, J. -P. Sutter, S. Mitra, *Polyhedron* **2004**, *23*, 949.
- [20] T. Glaser, M. Heidemeier, T. Weyhermueller, R. -D. Hoffman, H. Rupp, P. Mueller, *Angew. Chem. Int. Ed.* **2006**, *45*, 6033.
- [21] A. -C. Wang, C. -H. Yang, C. -H. Lee, G.-H. Lee, *Inorg. Chem.* **2002**, *41*, 429.
- [22] C. Chatterjee, R. S. Singh, A. Phulambrikar, S. Das, *J. Chem. Soc. Dalton Trans.* **1988**, 159.
- [23] E. R. Souaya, W. G. Hanna, N. E. Milad, E. H. Ismail, *J. Coord. Chem.* **2002**, *55*, 999.
- [24] H. -Y. An, E. -B. Wang, D. -R. Xiao, Y. -G. Li, Z. -M. Su, L. Xu, *Angew. Chem. Int. Ed.* **2006**, *45*, 904.
- [25] I. A. Koval, M. Huisman, A. F. Stassen, P. Gamez, M. Lutz, A. L. Spek, J. Reedij, *Eur. J. Inorg. Chem.* **2004**, 591.
- [26] S. Mukhopadhyay, D. Mandal, P. B. Chatterjee, C. Desplanches, J. -P. Sutter, M. Chaudhury, *Inorg. Chem.* **2004**, *43*, 8501.
- [27] T. C. Stamatatos, K. A. Abboud, W. Wernsdorfer, G. Christou, *Angew. Chem. Int. Ed.* **2006**, *45*, 4134.

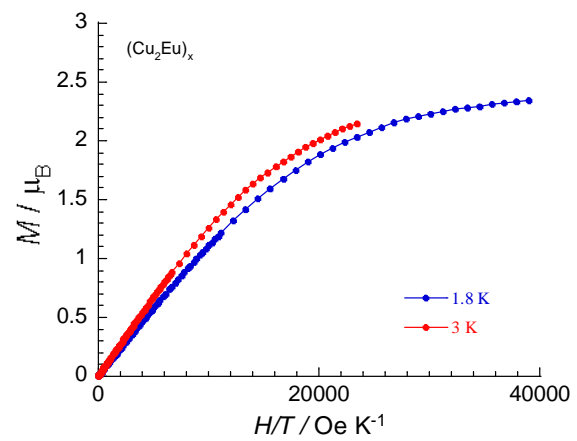
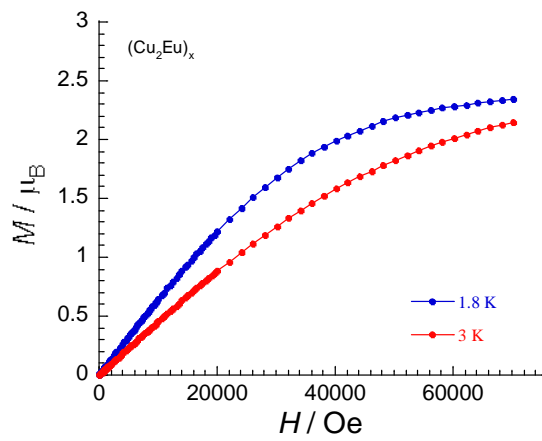
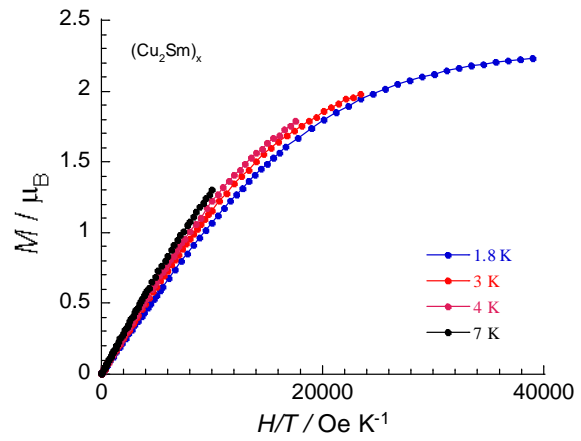
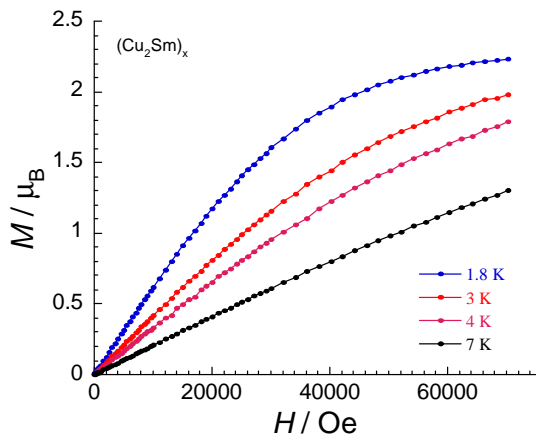
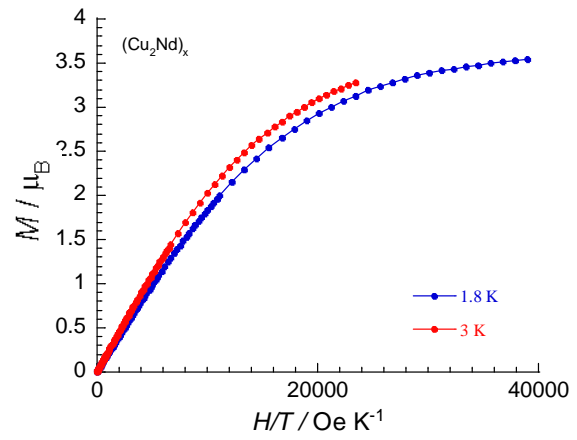
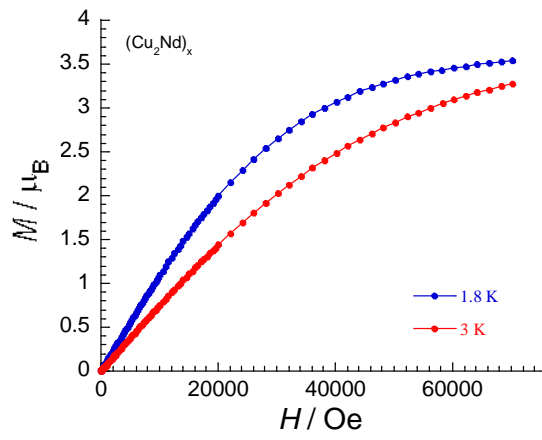
- [28] T. Schnepfensieper, G. Liehr, R. van Eldik, J. Ensling, P. Guetlich, *Inorg. Chem.* **2000**, *39*, 5565.
- [29] M. Murugesu, R. Clerac, C. E. Anson, A. K. Powell, *Inorg. Chem.* **2004**, *43*, 7269.
- [30] A. K. Powell, S. L. Heath, D. Gatteschi, L. Pardi, R. Sessoli, G. Spina, F. Del Giallo, F. Pieralli, *J. Am. Chem. Soc.* **1995**, *117*, 2491.
- [31] M. Murugesu, R. Clerac, W. Wernsdorfer, C. E. Anson, A. K. Powell, *Angew. Chem. Ent. Ed.* **2005**, *44*, 6678.
- [32] M. Murugesu, R. Clerac, C. E. Anson, A. K. Powell, *J. Phys. Chem. Solids* **2004**, *65*, 667.
- [33] Y. Boudam, G. Fischer, J. Hagel, E. Herrling, B. Pilawa, C. E. Anson, M. Murugesu, A. K. Powell, *J. Phys.: Condens. Matter* **2003**, *25*, 4477.
- [34] M. Murugesu, R. Clerac, C. E. Anson, A. K. Powell, *Chem. Commun.* **2004**, 1598.
- [35] M. Murugesu, *Ph.D thesis*, University of Karlsruhe, Karlsruhe, **2002**.
- [36] M. Murugesu, P. King, R. Clerac, C. E. Anson, A. K. Powell, *Chem. Commun.* **2004**, 740.
- [37] H. Oshio, N. Hoshino, T. Ito, *J. Am. Chem. Soc.* **2000**, *122*, 12602.
- [38] K. Wieghardt, K. Pohl, I. Jibril, G. Huttner, *Angew. Chem. Int. Ed. Engl.* **1984**, *23*, 77.
- [39] A. K. Boudalis, B. Donnadieu, V. Nastopoulos, J. M. Clemente-Juan, Y. S. A. Mari, J. -P. Tuchagues, S. P. Perlepes, *Angew. Chem. Int. Ed.* **2004**, *43*, 2266.
- [40] W. Schmitt, M. Murugesu, J. C. Goodwin, J. P. Hill, A. Mandel, R. Bhalla, C. E. Anson, S. L. Heath, A. K. Powell, *Polyhedron* **2001**, *20*, 1687.
- [41] G. J. T. Cooper, H. Abbas, P. Koegerler, L. D. -L, L. Cronin, *Inorg. Chem.* **2004**, *43*, 7266.
- [42] W. Schmitt, C. E. Anson, W. Wernsdorfer, A. K. Powell, *Chem. Commun.* **2005**, 2098.
- [43] P. King, R. Clerac, W. Wernsdorfer, C. E. Anson, A. K. Powell, *J. Chem. Soc. Dalton Trans.* **2004**, 2670.
- [44] F. Paap, E. Bouwman, W. L. Driessen, R. A. G. de Graaff, J. Reedijk, *J. Chem. Soc. Dalton Trans.* **1985**, 737.
- [45] O. Kahn, *Molecular Magnetism*, VCH Publi. Inc., **1993**.
- [46] R. L. Carlin, *Magnetochemistry*, Springer-Verlag, **1986**.
- [47] E. A. Boudreaux, L. N. Mulay, *Theory and applications of Molecular Paramagnetism*, J. Wiley & Sons, New York, **1976**.
- [48] C. J. O'Connor, *Prog. Inorg. Chem.* **1982**, *29*, 203.
- [49] C. Kittel, *Introduction to Solid State Physics*, Second ed., J. Wiley and Sons Publ. Inc. , New York, **1953**.
- [50] R. E. Mabbs, D. J. Machin, *Magnetism and Transition Metal Complexes*, Chapman and Hall, **1973**.
- [51] F. Palacio, *Introduction to Physical Techniques in Molecular Magnetism*, University of Zaragoza, Zaragoza, **1999**.
- [52] J. Paulovic, F. Cimpoesu, M. Ferbinteanu, K. Hirao, *J. Am. Chem. Soc.* **2004**, *126*, 3321.
- [53] J. -P. Costes, F. Dahan, A. Dupuis, J.-P. Laurent, *Inorg. Chem.* **2000**, *39*, 169.
- [54] C. Benelli, D. Gatteschi, *Chem. Rev.* **2002**, *102*, 2369.
- [55] C. Canada-Vilalta, T. A. O'Brien, E. K. Brechin, M. Pink, E. R. Davidson, G. Christou, *Inorg. Chem.* **2004**, *43*, 5505.
- [56] D. Gatteschi, R. Sessoli, A. Cornia, *Chem. Commun.* **2000**, 725.
- [57] C. Delfs, D. Gatteschi, L. Pardi, R. Sessoli, K. Wieghardt, D. Hanke, *Inorg. Chem.* **1993**, *32*, 3099.
- [58] Y. Pontillon, A. Caneschi, D. Gatteschi, R. Sessoli, E. Ressouche, J. Schweizer, E. Lelievre-Berna, *J. Am. Chem. Soc.* **1999**, *121*, 5342.

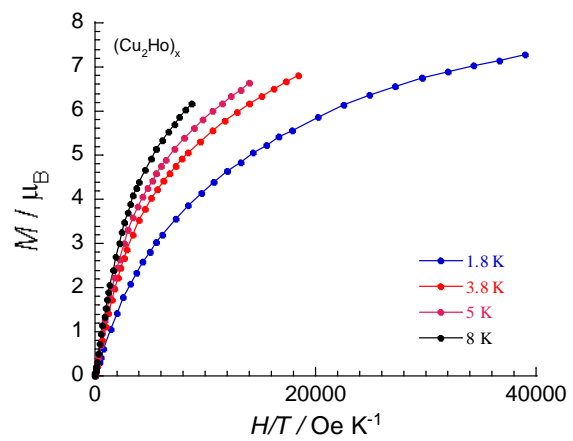
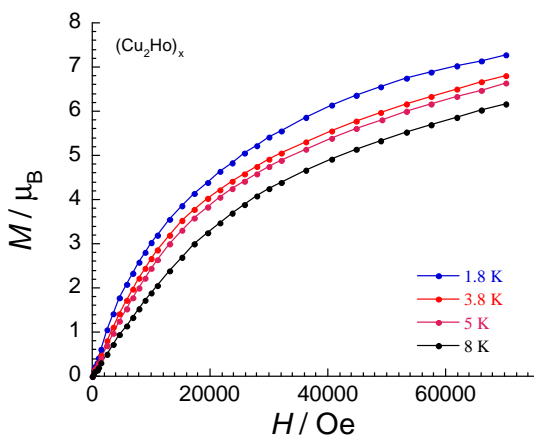
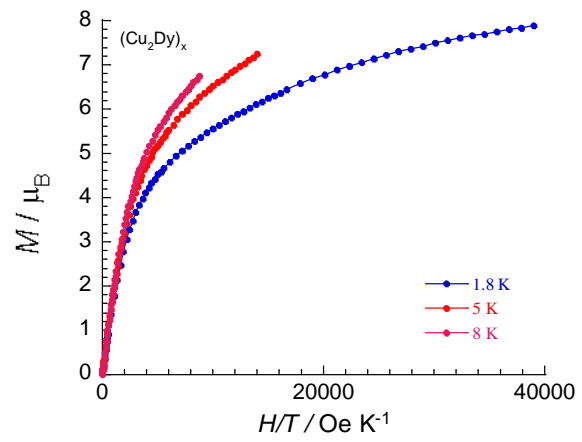
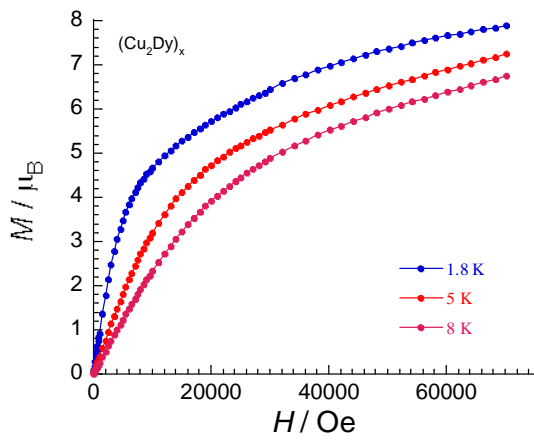
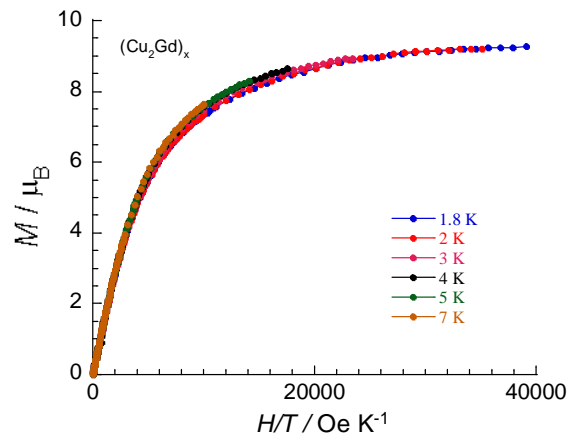
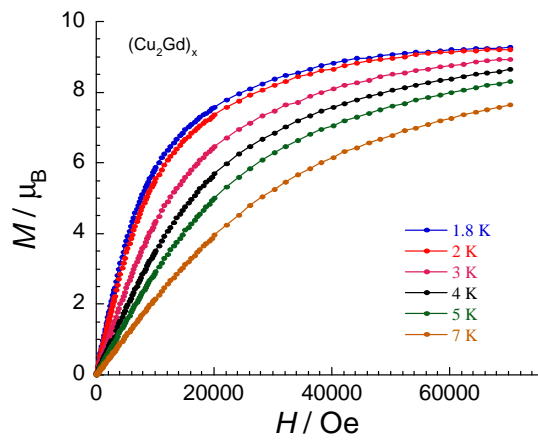
- [59] E. Yang, D. N. Hendrickson, *J. Appl. Phys.* **2002**, *91*, 7382.
- [60] J. Tercero, E. Ruiz, S. Alvarez, A. Rodriguez-Rortea, P. Alemany, *J. Mater. Chem* **2006**, *16*, 2729.
- [61] G. D. Fallon, B. Moubaraki, K. S. Murray, A. M. van der Bergen, B. O. West, *Polyhedron* **1993**, *12*, 1989.
- [62] J. K. Eberhardt, T. Glaser, R. D. Hoffmann, R. Froehlick, E. U. Wuersthwein, *Eur. J. Inorg. Chem.* **2005**, 1175.
- [63] J. Sletten, A. Sorensen, M. Julve, Y. Journaux, *Inorg. Chem.* **1990**, *29*, 5054.
- [64] S. Wang, J. C. Zheng, J. R. Hall, L. K. Thompson, *Polyhedron* **1994**, *13*, 1039.
- [65] Y. Xie, W. Bu, X. Xu, H. Jiang, Q. Liu, Y. Xue, Y. Fan, *Chem. Commun.* **2001**, *4*, 558.
- [66] A. Mukherjee, M. Nethaji, A. R. Chakravarty, *Angew. Chem. Int. Ed.* **2004**, *43*, 87.
- [67] A. Mukherjee, R. Raghunathan, M. K. Saha, M. Nethaji, S. Ramasesha, A. R. Chakravarty, *Chem. –Eur. J.* **2005**, *11*, 3087.
- [68] E. A. Buvaylo, V. N. Kokozay, O. Y. Vassilyeva, B. W. Skellton, J. Jezierska, L. C. Brunel, A. Ozarowski, *Inorg. Chem.* **2005**, *44*, 206.
- [69] H. Astheimer, F. Nepveu, L. Walz, W. Haase, *J. Chem. Soc. Dalton Trans.* **1985**, 315.
- [70] H. Oshio, Y. Saito, T. Ito, *angew. Chem. Int. Ed.* **1997**, *36*, 2673.
- [71] L. Walz, H. Paulus, W. Haase, H. Langhof, F. Nepveu, *J. Chem. Soc. Dalton Trans.* **1983**, 657.
- [72] R. Mergehenn, L. Merz, W. Haase, *J. Chem. Soc. Dalton Trans.* **1980**, 1703.
- [73] R. Wegner, M. Gottschaldt, H. Gorls, E. G. Jager, D. Klemm, *Chem.-Eur.J.* **2001**, *7*, 2143.
- [74] W. H. Gu, X. Y. Chen, L. H. Yin, A. Yu, X. Q. Fu, P. Cheng, *Inorg. Chim. Acta* **2004**, *357*, 4085.
- [75] X. S. Tan, Y. Fujii, R. Nukada, M. Mikuriya, Y. Nakano, *J. Chem. Soc. Dalton Trans.* **1999**, 2415.
- [76] L. Merz, W. Haase, *J. Chem. Soc. Dalton Trans.* **1978**, 1594.
- [77] L. Schwabe, W. Haase, *J. Chem. Soc. Dalton Trans.* **1985**, 1909.
- [78] N. Matsumoto, I. Ueda, Y. Nishida, S. Kida, *Bull. Chem. Soc. Jpn.* **1976**, *49*, 1308.
- [79] X. M. Chen, J. W. Cai, *The Structural Analysis of the X-ray Single Crystal*, Science Publ. , Beijing, **2003**.
- [80] M. L. Kahn, J. -P. Sutter, S. Golhen, P. Guionneau, L. Ouahao, O. Kahn, D. Chasseau, *J. Am. Chem. Soc* **2000**, *122*, 3413.
- [81] M. L. Kahn, R. Ballou, P. Porcher, O. Kahn, J.-P. Sutter, *Chem. Eur. J.* **2002**, *8*, 525.
- [82] J. H. v. Vleck, *The Theory of Electric and Magnetic Susceptibility*, Oxford University Press, **1932**.
- [83] K. Kambe, *J. Phys. Soc. Jpn.* **1950**, *5*, 48.
- [84] M. Murugesu, R. Clerac, B. Pilawa, A. Mandel, C. E. Anson, A. K. Powell, *Inorg. Chim. Acta* **2002**, *337*, 328.

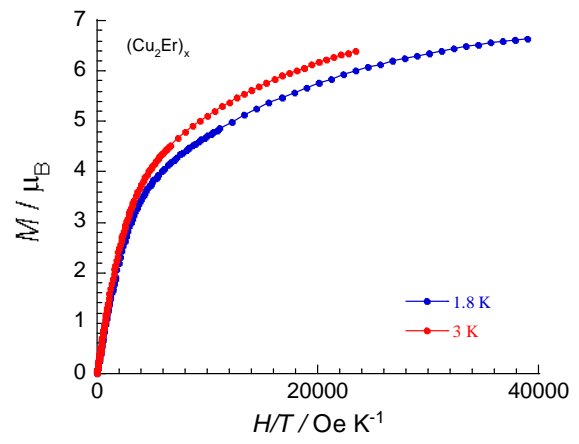
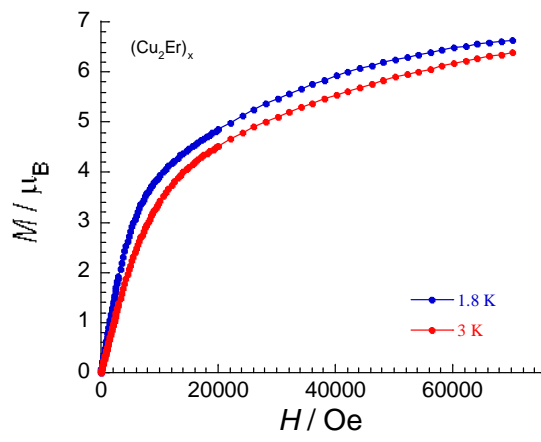
Appendix

Plots of the field dependence of the magnetization for $\{\text{Cu}_2\text{Ln}\}_x$ (2-11)

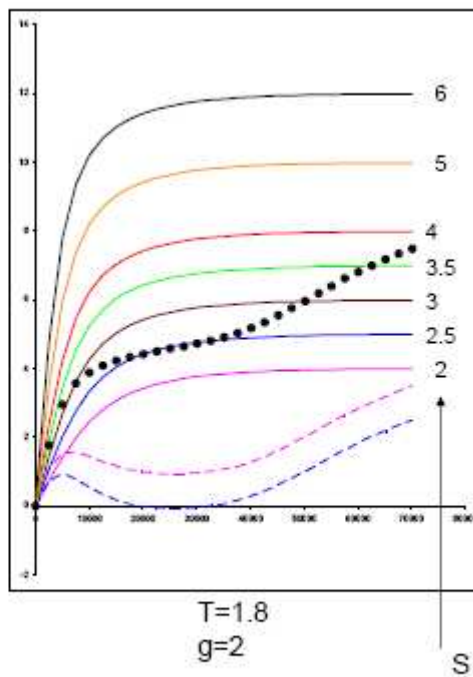
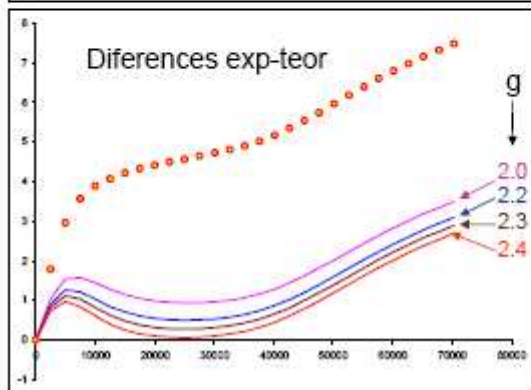
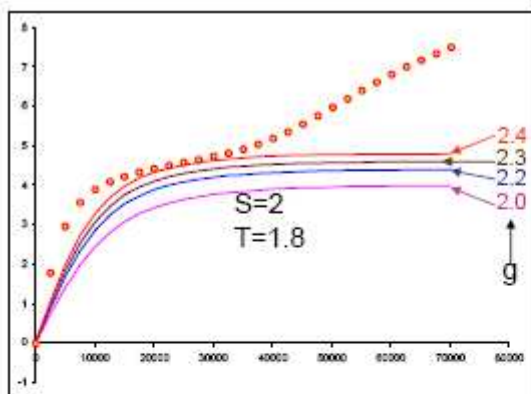
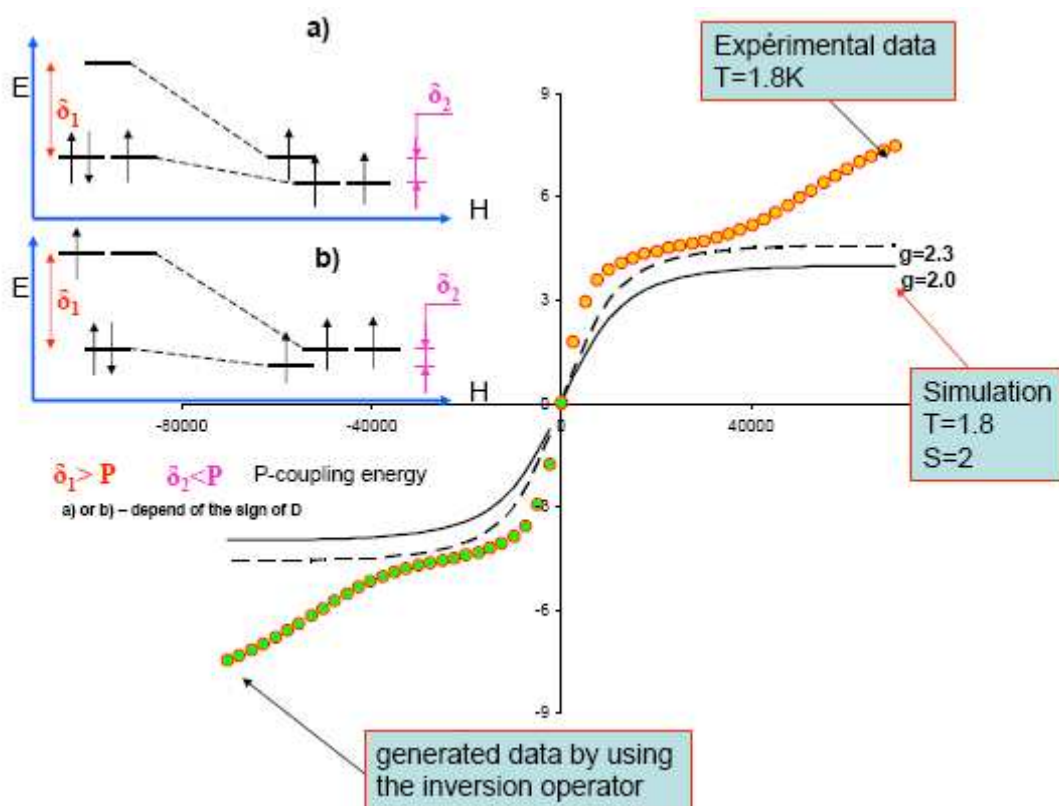


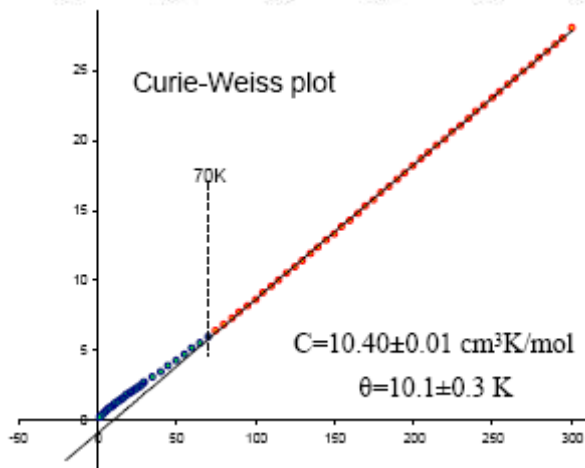
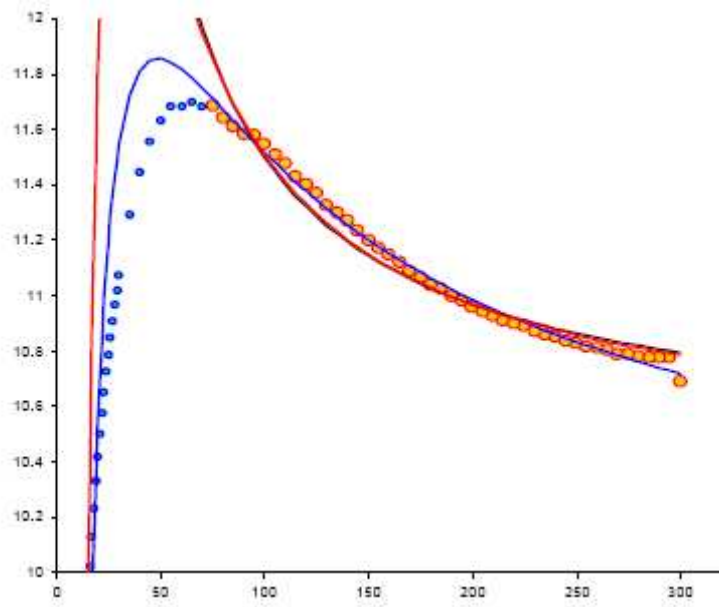






Plots of the fittings of Co₄, 14





Acknowledgements

On this page I would like to take the opportunity to thank the following people for the help and support in my doctorate studies.

First, I must thank Prof. Dr. Annie. Powell for the opportunity to come and study in Karlsruhe and for providing the creative freedom throughout studies, the guidance on my research and teaching me the chemistry about supermolecular and magnetic chemistry that I know. Many thanks to Dr. Chris Anson for undertaking all of the X-ray single crystal measurement and persistent refinement of the crystallographic data presented here. Also Chris helped me much in this thesis correction.

I would like to thank Dr. Yangguang Li, who taught me all about what magnetism is and how to measure it on a SQUID, Dr. Yanhua Lan for performing the SQUID measurements on all the microcrystals presented here. Thanks to Dr. Rodolphe Clérac (université Bordeaux, CNRS) for patient explanation of the magnetic interpretation of the compounds in this work. Thanks to Dr. Ghenadie Novitchi for the least-square simulation of the cubane compounds. With regard to the measurement of ESR on the copper cubane, I would like to thank Dr. Bernd Pilawa (Physicalisches Institute, Universität Karlsruhe), who suggest me to send out samples to Stuttgart Universität for further measurements.

I would like to thank Herr. Rolf Lehmann and Frau Gertraud Amschliger for their everyday help; Frau G. Kuhn, Frau S. Böcker, Frau Nadja for their help in the chemical stores.

Finally I would like to thank Yuanfeng Cheng, my husband, for his encouragement throughout and the compiling work in the thesis writing. The relaxing hours on the badminton field, on the mountains, in the bars and etc. are wandering in my mind.

Curriculum Vitae

Li Xue

Date of birth 24 June, 1976
Place of birth Daqing, P. R. China
Nationality China

Education

1983-1989 The First Primary School of Daqing Petroleum Refining Industry
1989-1992 The 57th Middle School of Daqing City
1992-1995 The 4th Middle School of Daqing City
1995-1999 B. Sc in Chemistry, Tsinghua University
1999-2002 M. Sc in Chemistry, Tsinghua University
2003-2004 M. Sc in Bioinformatics, Köln Universität
2004-2008 Ph.D. in Chemistry, Universität Karlsruhe (TH)

Experience

Tsinghua University, Beijing, P. R. China / University of Cologne, Germany /
University of Karlsruhe, Germany:

Supervision of final year undergraduate students. Demonstrating for first and second year undergraduate students during their inorganic chemistry practical course. Marking undergraduate students examination.